Abstract

Optical, Mechanical and Thermal Properties of Superfluid Liquid Helium Drops Magnetically-Levitated in Vacuum

Charles Daryl Brown II

2019

The field of optomechanics studies the interactions between light and the motion of an object. One of the goals in this field is to generate and control highly non-classical motion of a massive mechanical oscillator. There has been progress in generating such non-classical motion via coupling the oscillator to a qubit, or by utilizing the non-linearity of single photon detection. However, interest still remains in generating non-classical motion directly via the optomechanical interaction itself. Doing so requires strong coupling between the light and the mechanical oscillator, as well as low optical and mechanical loss and temperature. The unique properties of superfluid helium (zero viscosity, high structural and chemical purity and extremely low optical loss) address some of these requirements.

To exploit the unique properties of superfluid helium we have constructed an optomechanical system consisting entirely of a magnetically levitated drop of superfluid helium in vacuum. Magnetic levitation removes a source of mechanical loss associated with physically clamped oscillators. Levitation also allows the drop to cool itself efficiently via evaporation. The drop's optical whispering gallery modes (WGMs) and its surface vibrations should couple to each other via the usual optomechanical interactions.

In this dissertation we demonstrate the stable magnetic levitation of superfluid helium drops in vacuum, and present measurements of the drops' evaporation rates, temperatures, optical modes and surface vibrations. We found optical modes with finesse ~ 40 (limited by the drop's size). We found surface vibrations with decay rates ~ 1 Hz (in rough agreement with theory). Lastly, we found that the drops reach a temperature $T \approx 330$ mK, and that a single drop can be trapped indefinitely.

Optical, Mechanical and Thermal Properties of Superfluid Helium Drops Magnetically Levitated in Vacuum

A Dissertation
Presented to the Faculty of the Graduate School
of
Yale University
in Candidacy for the Degree of
Doctor of Philosophy

by
Charles Daryl Brown II

Dissertation Director: Jack Harris
December 2019

Acknowledgements

A number of individuals have offered me guidance, support and mentorship throughout my time in graduate school. I will forever be grateful to these individuals. I simply cannot name every person who has had a positive impact on my life because there are too many. However, I wish to directly acknowledge some of those whose presence in my life made the completion of this dissertation possible. I also want to acknowledge the NSF GRFP and Ford Foundation fellowships for support throughout my graduate career. These fellowships provided me with essential resources that helped my graduate research to progress smoothly.

I want to thank my research advisor, Prof. Jack Harris. Jack is a brilliant physicist, communicator and teacher, and I have learned a great deal from him inside and outside of the laboratory. Jack is also an open-minded and compassionate person, who has been a leader in the department on important issues outside of physics. Jack, thank you for your support and mentorship over the last six years; you have had a profound impact on my life. The Yale physics department is fortunate to have someone like you.

I want to thank Prof. Meg Urry, Prof. John Johnson and Prof. Jedidah Isler for their mentorship during the earlier stages of my graduate career. They provided me with the crucial guidance and perspective that I needed as an underrepresented minority physicist, which allowed me to become a successful graduate student. I want to thank Dr. Rona Ramos, Prof. Keith Baker, Prof. Reina Maruyama, Prof. Nick Read, Prof. Ramamurti Shankar, Prof. Paul Tipton, and the Climate and Diversity Committee for supporting my

non-physics endeavors, for the many great conversations, and for helping me to establish a sense of belonging in the physics department. I want to thank the other members of my thesis committee for their time, career advice and insight regarding my dissertation work: Prof. Dave DeMille, Prof. Steve Girvin and Prof. Dave Moore. I want to thank Dr. Maria Parente, Claudia Merson and Prof. Suzie Forster for all of the opportunities I was given to do impactful science outreach events in the New Haven area. I want to thank Dave Johnson, Craig Miller, Russ Bernardo and Vinnie Bernardo for everything that they taught me over the years regarding machining, welding, and vacuum and cryogenic system design.

I want to thank Glen Harris, the postdoc with whom I built the first few generations of the levitated helium drop experiment. Glen is an all-around awesome person and mentor, and he played an important role in my development into an independent scientist. I want to thank Yiqi Wang, Mehdi Namazi and Tuna Uysal for being great colleagues to work with on the levitated drop experiment, and for all of their contributions. I also want to thank the other current Harris Lab members for making our group a fun place to do physics: Luyao Jiang, Parker Henry, Sean Frazier, Lucy Yu, Nenad Kralj and Yogesh Patil. I would like to give a special thanks to Nenad, Mehdi and Yogesh, from whom I have learned a lot during our short overlap in the Harris Lab. Before I worked on the levitated drop experiment I worked with Anna Kashkanova and Alexey Shkarin (when we were all graduate students), from whom I learned about many aspects of experimental physics; thank you for the time and effort you put into teaching me. I also want to thank Dave Mason, Nathan Jacobs-Flowers, Anthony Lollo, Woody Underwood, Ivana Petkovic and Dustin Ngo for welcoming me into the group, and for all the good conversations over the years.

I would like to thank my oldest friends, Anthony Clay and Malik Woods, for decades of support and encouragement. Many thanks to my college friends whom have stayed in close contact, and continue to offer their support and encouragement: Mac Cameron, Hunter Dunbar and Mike Hepler. Many thanks to my friends at Yale that made it an enjoyable place to be: Shanique Alabi, Eustace Edwards, Andy Gasbarro, Gadareth Higgs, James

Ingoldby, Zak Kobos, Adrian Meyers, Zlatko Minev, Danielle Noricini, Brooke Russell, Anthony Scruse, Darryl Seligman, Johnathon Tyson, Lexi Williams, Nathan Williams and Peter Williams.

My mom has always stressed the importance of education, and did everything that she could to ensure that I got a good one. She always supported my scientific aspirations, even when I was destroying her things in my garage laboratory as a child. Mom, thank you for the constant love, support and encouragement. I certainly would not have come this far in life if it were not for all of your effort and sacrifice.

Finally, I want to thank my wife, Lyndsey McMillon-Brown for being such a wholesome, compassionate, loving and supportive person. Lyndsey, your presence in my life made bearable the most difficult times in graduate school, and created many of the most wonderful moments in my life. I love you.

Contents

List of Figures

List of Tables

Chapter 1

Introduction

The main goals of my dissertation research were to construct a new optomechanical system consisting entirely of a superfluid helium drop that is magnetically levitated in vacuum, and to characterize its essential components (i.e., its optical and mechanical modes, as well as its evaporation and temperature). In this dissertation I describe the work that my colleagues and I have done to achieve these goals. Specifically, I provide a historical account of the relevant progress in the field of optomechanics to date, theoretical descriptions of the essential components of our helium drop optomechanical system, a description of the construction of the experiment, and a discussion of measurements of helium drops' optical and mechanical modes and their temperatures. I also discuss prospects for future experiments with levitated helium drops, which extend well beyond the realm of optomechanics. The results reported in this dissertation add to the existing research in the field of superfluid helium physics. They also position the levitated helium drop as a platform that could be useful for experimental studies of optomechanics, quantum turbulence in isolated liquids, and physics beyond the standard model. Furthermore, our results show the coldest and most long-lived trapped helium drops in the literature, with the added ability to trap a drop indefinitely.

The field of optomechanics studies the interactions of light with the motion of a me-

chanical oscillator. The coupling between the two arises because light in the optical resonator exerts a force on the oscillator; the oscillator's motion in response to this force changes the optical resonator's geometry, thereby modifying the light in the resonator and the force on the mechanical oscillator. While there are many interesting directions to pursue using optomechanical systems, our main interest in these systems stems from their ability to provide an avenue to study the quantum behavior of macroscopic objects. All optomechanical systems suffer from optical and mechanical loss, however, which makes it difficult to observe the quantum aspects of a macroscopic oscillator's motion.

The unique properties of a magnetically levitated superfluid ^{4}He in vacuum (i.e., its zero viscosity, extremely low optical loss, and its ability to cool itself efficiently via evaporation) address some important issues that can preclude the observation of quantum effects in an optomechanical system. As a result, liquid helium is an intriguing material from which to construct an optomechanical system, and may allow one to reach new regimes of quantum optomechanics.

In writing this dissertation I hope not only to provide a thorough and accessible description of the important concepts that are necessary for experiments with levitated superfluid helium drops, but also to provide a clear description of the experiments done throughout my graduate career, and the exciting directions that can be pursued after my time in the Harris Lab.

In Chapter 2, I provide a review of the optomechanics literature, including a review of superfluid optomechanics and levitated optomechanics. I also provide a review of experiments with isolated helium drops to date. I provide a brief theoretical description of the canonical optomechanical system, and detailed theoretical descriptions of the magnetic levitation of a helium drop, a drop's evaporation in vacuum, a drop's optical and mechanical modes, and the optomechanical coupling between them.

In Chapter 3, I provide detailed descriptions of the magneto-optical cryostat inside which we levitate helium drops, as well as the experimental chamber that we designed

and constructed. I then describe the process of using this chamber to create drops. I also describe initial measurements of drops' size, shape, evaporation, temperature and center of mass motion via analysis of video images.

In Chapter 4, I describe laser-based measurements of drops' evaporation, temperature, center of mass motion, optical modes and mechanical modes (in particular, their surface modes, which are restored by surface tension).

In Chapter 5, I describe future work, including a re-design of the experimental chamber that should offer several improvements, as well as exciting physics directions to pursue.

In Chapter 6, I summarize the main results of our research with levitated superfluid helium drops.

Chapter 2

Background and Motivation

2.1 Optomechanics

Optomechanical systems mostly consist of harmonic oscillators that are weakly coupled to each other, and that are limited to weak drives. Consequently, such systems are described by Gaussian quantum states and they have been extensively studied. Yet, to measure the associated Gaussian quantum effects in a millimeter-scale helium drop – such as zero-point fluctuations in its motion, or quantum measurement backaction – is interesting because it would amount to an orders-of-magnitude increase in the mass of a system in which such effects have been observed. These measurements could lead to a more thorough understanding of quantum effects in macroscopic objects.

To access the more exotic non-Gaussian quantum effects (e.g. the Wigner function negativity of a mechanical oscillator in an excited Fock state), an optomechanical system must be nonlinear at the single quantum level. Such non-classical states of motion have been achieved via the use of the nonlinearity inherent to single photon detection, or via the interaction of a mechanical oscillator with a superconducting qubit. However, due to the extremely low optical loss and low stiffness of a millimeter-scale helium drop, it could be possible to use the inherent nonlinearity of the optomechanical interaction to observe

non-Gaussian quantum effects in an object with mass ~ 0.5 mg.

In an optomechanical system, light is typically confined in a cavity, and it couples to motion of the mechanical oscillator in the cavity via radiation pressure. Radiation pressure provides a unitary coupling mechanism between light and the mechanical oscillator, so it can be used to explore the quantum motion of macroscopic objects. However, all optomechanical systems suffer from optical and mechanical loss, which makes it difficult to observe the quantum aspects of the mechanical oscillator's motion. Over the last two decades, researchers have put forth much effort toward addressing these challenges and there has been much progress in the study of the quantum motion of mechanical oscillators. Yet, researchers are still working to optimize their systems and push them further into a regime where quantum mechanics dominates the physics.

Levitating the mechanical oscillator and evacuating the space around it is advantageous because it removes a pathway for energy from the environment to leak into the mechanical oscillator and spoil its quantum properties. Furthermore, mechanical energy cannot leak out of it, thereby minimizing mechanical loss. However, the isolation provided by levitation removes the possibility of cooling the object by conventional means and so may result in high temperatures. Despite this, levitated optomechanical systems are making important strides toward studying the quantum motion of macroscopic mechanical oscillators.

Constructing the optical cavity from superfluid liquid ^{4}He addresses the issue of optical loss because because the combination of its chemical and structural purity, along with its large electronic bandgap means that it has vanishing optical loss; because of its low optical loss, it could sustain low-loss optical modes. Because of liquid helium's low surface tension, a drop with a millimeter-scale radius has mechanical modes with frequencies ~ 10 Hz, and large zero-point fluctuations of its mechanical modes for mechanical oscillators of this size. Levitating the liquid in vacuum will allow its optical and mechanical energy to be stored entirely in the drop, which could lead to significant overlap between the light and the motion, and thus large coupling between them. In fact, the coupling could be $\sim 10\times$

larger than the mechanical mode frequency. Levitating the liquid isolates it from its environment, which would still lead to elevated temperatures compared to a system in thermal contact with a dilution refrigerator. However, a liquid helium drop has the added benefit of evaporatively cooling itself to sub-Kelvin temperatures, as compared to other levitated systems. At these temperatures (~ 300 mK) the drop is essentially entirely superfluid, so its viscosity is zero, which has a profound effect on its rotational motion. A superfluid drop could host vortices of quantized circulation to which optical modes within the drop could couple, paving a path towards vortex optomechanics.

Consequently, a levitated superfluid optomechanical system may allow one to reach a new regime of quantum optomechanics.

2.1.1 Radiation Pressure

Radiation pressure is generally defined as the force per unit area exerted on an object as a result of the absorption or reflection of electromagnetic radiation. Since the advent of the notion of radiation pressure, it has been shown to mediate physical processes ranging over many orders of magnitude in mass and length. In 1619, Johannes Kepler conceptualized the idea of radiation pressure in effort to explain the observation that comet tails always point away from the Sun. The concept of radiation pressure remained largely unexplored until 1862 when James Clark Maxwell predicted from first principles that electromagnetic fields carry momentum, providing a fundamental understanding of Kepler's hypothesis. Maxwell's prediction of the precise amount of momentum carried by electromagnetic fields was verified with ground-breaking experiments conducted by Pyotr Lebedev (1900), Ernest Nichols and Gordon Hull (1901).

In 1909, Einstein used Planck's blackbody spectrum to calculate the radiation pressure force fluctuations acting on a movable mirror, as well as the corresponding frictional effects of radiation pressure [1]. In this work, Einstein revealed the wave-particle duality of blackbody radiation, and he argued that this would be important for understanding the quantum

nature of the electromagnetic field.

In the 1930's Frisch and Beth demonstrated the linear and angular momentum transfers of photons to atoms and macroscopic objects [2, 3]. In 1970, Ashkin implemented precise control over radiation pressure for the acceleration and trapping of particles [4]. In 1987, Pritchard and colleagues used radiation pressure to trap atomic clouds with $\sim 10^7$ atoms at densities $\sim 10^{11}$ atoms/cm^3 [5]. More recently, experimental techniques that precisely control radiation pressure have led to several notable results, including observations of Bose-Einstein Condensation in dilute gases of alkali atoms [6, 7], direct laser cooling and trapping of diatomic molecules [8], and laser cooling of a nanomechanical oscillator to its quantum ground state [9].

2.1.2 Cavity Optomechanics

The use of radiation pressure to study quantum features in the motion of macroscopic objects (i.e., much larger than a molecule) is usually explored in devices known as cavity optomechanical systems.

The quintessential cavity optomechanical system is shown in figure 2.1. It consists of an optical Fabry-Perot cavity with one mirror fixed in place, while the other mirror, affixed to a spring, is able to move. The electric field amplitude $\hat{a}$ of a specific electromagnetic mode inside the optical cavity functions as one degree of freedom, and the displacement $\hat{x}$ of the movable mirror functions as a second degree of freedom. When light of wavelength λ impinges on the cavity with mirror separation L, a resonant condition can be met provided $L = n\lambda/2$, where n is an integer. That is, if the mirror separation (cavity length) is an integer number of half-wavelengths of the incident light the electric field amplitude within the cavity can grow to a large value. As such, the resonant frequency of the cavity can be written as $\omega_{\rm c}(\hat{x}) = n\pi c/L(\hat{x})$. Light in the optical cavity exerts radiation pressure on the movable mirror; the mirror's motion in response to this force changes the cavity length, thereby modifying the cavity resonant frequency. The resulting coupling between a and $\hat{x}$

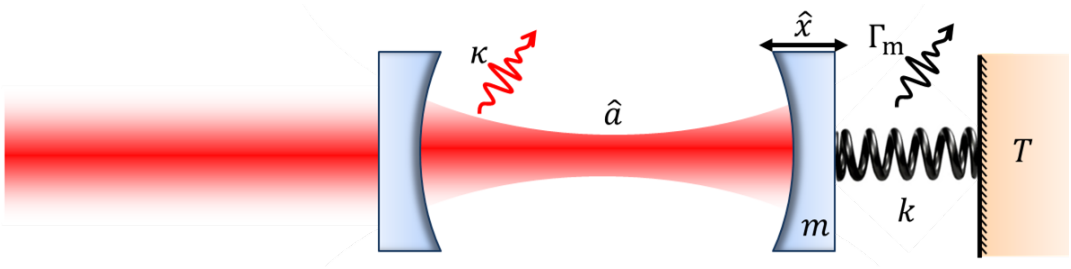

Figure 2.1: A Fabry-Perot optical cavity with a movable end mirror. The optical mode has amplitude $\hat{a}$, and its linewidth and resonance frequency are κ and ω_{c}, respectively. The mechanical linewidth and resonance frequency of the mirror with position $\hat{x}$ is, Γ_m and $\omega_{\mathrm{m}} = \sqrt{k/m}$, respectively. The mechanical oscillator is coupled to a bath with temperature T.

is known as optomechanical coupling.

To further elucidate the details of a typical optomechanical system, one may define a Hamiltonian given by

$$\hat{H} = \hbar\omega_{\mathrm{c}}(\hat{x})\hat{a}^{\dagger}\hat{a} + \hbar\omega_{\mathrm{m}}\hat{b}^{\dagger}\hat{b} \tag{2.1}$$

where $\omega_{\mathrm{c}}(x)$ is the mirror position-dependent cavity resonance frequency, $\hat{a}(\hat{a}^{\dagger})$ is the annihilation (creation) operator for a photon in the cavity mode with frequency $\omega_{\mathrm{c}}(x)$, $\omega_{\mathrm{m}} = \sqrt{k/m}$ is the resonant frequency of the movable mirror with mass m, and $\hat{b}(\hat{b}^{\dagger})$ is the annihilation (creation) operator for a phonon in the mechanical mode with frequency ω_{m}.

A Taylor expansion of the cavity resonance frequency to first order in the mirror position yields

$$\omega_{\mathrm{c}}(\hat{x}) \approx \omega_{\mathrm{c}}(x_0) + \frac{\partial\omega_{\mathrm{c}}(x)}{\partial x}\hat{x} \tag{2.2}$$

where x_0 is the equilibrium position of the mirror, $\hat{x} = x_{zpf}(\hat{b} + \hat{b}^{\dagger})$ and $x_{zpf} = \sqrt{\frac{\hbar}{2m\omega_{\mathrm{m}}}}$ is the zero-point fluctuation of the mirror position. Thus, in consideration of the optomechanical interaction, the Hamiltonian can be rewritten as

$$\hat{H} = \hbar\omega_{\mathrm{c}}(x_0)\hat{a}^{\dagger}\hat{a} + \hbar\omega_{\mathrm{m}}\hat{b}^{\dagger}\hat{b} + \hbar g_0\hat{a}^{\dagger}\hat{a}(\hat{b} + \hat{b}^{\dagger}) \tag{2.3}$$

where the single-photon (vacuum) optomechanical coupling rate is given by

$$g_0 = \frac{\partial \omega_{\mathrm{c}}(x)}{\partial x} x_{\mathrm{zpf}} \tag{2.4}$$

The Heisenberg equations of motion for the electromagnetic and mechanical modes are given by $\dot{\hat{a}} = i/\hbar[\hat{H}, \hat{a}]$ and $\dot{\hat{b}} = i/\hbar[\hat{H}, \hat{b}]$, with commutation relations $[\hat{a}^\dagger, \hat{a}] = -1$, $[\hat{b}^\dagger, \hat{b}] = -1$, $[\hat{a}^\dagger \hat{a}, \hat{a}] = -\hat{a}$ and $[\hat{b}^\dagger \hat{b}, \hat{b}] = -\hat{b}$. As a result, the equations of motion are

$$\dot{\hat{a}} = -i\left(\omega_{\mathrm{c}}\hat{a} + g_0\left(\hat{b} + \hat{b}^\dagger\right)\hat{a}\right) \tag{2.5}$$

$$\dot{\hat{b}} = -i\left(\omega_{\mathrm{m}}\hat{b} + g_0\hat{a}^\dagger\hat{a}\right) \tag{2.6}$$

In general, optomechanical coupling can arise from different physical mechanisms that cause the cavity length to change, such as radiation pressure, electrostriction or thermal expansion. The change in cavity length due to radiation pressure arises because the photons scattering from the mechanically compliant cavity exert a force on it, which is proportional to the intensity of the electric field. The change in cavity length due to electrostriction arises from the polarizability of the cavity material. The electric field polarizes the atoms or molecules in the material, which then experience a force due to the electric field gradient. This force, proportional to the product of the electric field and its gradient, can change the physical cavity length L, or its effective length L_{eff} by changing the index of refraction n of the material filling the cavity ($L_{\mathrm{eff}} = nL$). Lastly, the change in cavity length due to thermal expansion of the material used to construct the cavity results in a photothermal coupling. The thermal expansion arises from the absorption of photons in the material, which causes its temperature to rise.

Radiation pressure and electrostrictive coupling between the electrocmagnetic mode and the mechanical mode are both unitary (lossless) mechanisms, which are described by equations 2.5 and 2.6. On the other hand, photothermal coupling necessarily involves the

loss of photons via their conversion into heat, and so is not unitary. Including this non-unitarity leads to equations of motion somewhat different from equations 2.5 and 2.6. In general, this form of coupling is less suitable to studies of quantum mechanics.

Equations 2.5 and 2.6, however, do not provide a complete picture of optomechanics in the real world, because they do not include electromagnetic or mechanical loss, nor do they include noise. In a more complete picture of optomechanics, which includes loss and noise, the equations of motion are given by [10]

$$\dot{\hat{a}} = -i\left(\omega_{\mathrm{c}} + g_0\left(\hat{b} + \hat{b}^\dagger\right)\right)\hat{a} - \frac{\kappa}{2}\hat{a} + \sqrt{\kappa_{\mathrm{ext}}}\hat{a}_{\mathrm{in}} + \sqrt{\kappa_{\mathrm{int}}}\hat{f}_{\mathrm{int}} \tag{2.7}$$

$$\dot{\hat{b}} = -i\left(\omega_{\mathrm{m}}\hat{b} + g_0\hat{a}^\dagger\hat{a}\right) - \frac{\Gamma_{\mathrm{m}}}{2}\hat{b} + \sqrt{\Gamma_{\mathrm{m}}}\hat{b}_{\mathrm{in}} \tag{2.8}$$

where $\kappa = \kappa_{\mathrm{int}} + \kappa_{\mathrm{ext}}$ is the total energy loss rate of the electromagnetic mode and Γ_{m} is the energy loss rate of the mechanical mode. Here, κ_{int} is the internal loss rate in the cavity, whereas κ_{ext} is the loss rate through the channel used to drive the electromagnetic mode (i.e. the loss through the mirror). The operator $\hat{a}_{\mathrm{in}}$ describes a coherent drive applied to the electromagnetic mode, as well as the input of external electromagnetic noise. The operator $\hat{f}_{\mathrm{int}}$ describes internal electromagnetic noise. Lastly, the operator $\hat{b}_{\mathrm{in}}$ describes noise input to the mechanical mode via its contact with a thermal bath at temperature T. Another quantity that is useful to quantify loss in harmonic modes is the quality factor. The quality factor for the mechanical mode $Q_{\mathrm{mech}} = \omega_{\mathrm{m}}/\Gamma_{\mathrm{m}}$, and the quality factor for the optical mode $Q_{\mathrm{opt}} = \omega_{\mathrm{c}}/\kappa$. A low loss harmonic mode has $Q \gg 1$.

Of crucial importance in optomechanics are the relative rates of loss from the electromagnetic mode, loss from the mechanical mode, and the coupling between the two modes. The physical phenomena that can be accessed with a particular device depend on dimensionless ratios of κ, Γ_{m}, g_0 and ω_{m}. For example, the resolved sideband regime ($\omega_{\mathrm{m}}/\kappa \gg 1$) is particularly useful because it allows the extraction of energy from the mechanical mode by dumping it into a non-resonant electromagnetic mode that escapes the cavity; as will

be described in section 2.1.2, this has been used to cool a mechanical mode to its quantum ground state. This process is called sideband cooling.

The thermal optomechanical cooperatively $C_{\rm th}$ is perhaps the most important figure of merit in determining whether quantum effects are dominant in optomechanics ($C_{\rm th} > 1$), and it is given by

$$C_{\rm th} = \frac{4g_0^2 n_{\rm circ}}{\kappa \Gamma_{\rm m} n_{\rm th}} \tag{2.9}$$

where $n_{\rm circ}$ is the number of photons in the electromagnetic mode and $n_{\rm th} = k_{\rm B}T/\hbar\omega_{\rm m}$ is the thermal occupation of the mechanical mode. The quantity $C_{\rm th}$ can be thought of as the ratio of two rates. The first rate $4g_0^2 n_{\rm circ}/\kappa$ describes the rate at which excitations are exchanged between the optical and mechanical modes. The second rate $\Gamma_{\rm m} n_{\rm th}$ (also known as the thermal decoherence rate) describes the rate at which a thermal phonon from the environment (with which the mechanical mode interacts) will enter. Quantum effects are important when the first rate is larger than the second rate. Throughout the history of cavity optomechanics, researchers have made many attempts to maximize $C_{\rm th}$ by reducing κ, $\Gamma_{\rm m}$ and $n_{\rm th}$ while increasing g_0 and $n_{\rm circ}$. As a result, many different optomechanical systems have been realized, each with their own strengths and weaknesses. In this thesis we are interested in a similar optimization by using the unique material properties of superfluid helium and the advantages of magnetic levitation. This will be elaborated upon in upcoming sections of this thesis.

Review of Cavity Optomechanics

Decades prior to the development of cavity optomechanics into an independent field of research, many of its concepts and techniques were already developed and utilized in gravitational wave detectors. In the 1960's, Gertsenshtein and Pustovoit, and independently, Braginskii, proposed using a laser interferometer as a gravitational wave detector [11, 12]. In the 1970's, the first prototypes of such an interferometer were developed by Forward and Weiss, laying the foundation for modern gravitational wave detectors such as LIGO and

VIRGO [13, 14]. Since the 1970's, researchers have made improvements upon the canonical optomechanical system presented in section 2.1.2 (as well as many other systems). The improvements include higher laser power, longer interferometer arms, and increased vibration isolation from environmental sources of noise. In LIGO and VIRGO, kilometer-scale arms of a Michelson interferometer are designed to measure minuscule dilations of the arm length associated with gravitational waves traversing the interferometer [15]. Despite the fact that the primary interest of these detectors lay in astrophysical gravitational waves, it became important to address optomechanical effects, as they dominate the properties of these detectors and can obscure or enhance the detection of gravitational waves.

The most immediate impact of quantum mechanics on the performance of gravitational wave detectors is photon shot noise. Photon shot noise refers to the Poissonian-distributed arrival time of photons in coherent laser light. To diminish the effect of this noise in the photodetector signal, it is advantageous to use a bright laser beam – this reduces the measurement imprecision of an optical interferometer. However, it was shown that quantum fluctuations of the intra-cavity photon number (distinct from the fluctuations at the detector) represent an additional source of noise, as the radiation pressure associated with these fluctuations can perturb the position of the cavity mirror [16]. This phenomenon, known as quantum back-action, adds imprecision with increased intra-cavity photon number. The balance of these two noise sources results in the minimum achievable measurement imprecision (and an optimal laser intensity) of an optical interferometer. In the field of optomechanics, the balance between measurement imprecision at the detector and quantum back action in the cavity is referred to as the standard quantum limit (SQL). Understanding the SQL in optomechanical systems, and even achieving beyond-SQL measurement imprecision, represents an outstanding challenge and an exciting direction to the field of optomechanics.

In 2009, Lehnert and colleagues at JILA detected the motion of a nanomechanical oscillator near the SQL with a microwave analogue of a Mach–Zehnder interferometer in

a dilution refrigerator at temperatures below 100 mK [17]. They generated a microwave tone, then injected this tone into the two arms of the interferometer so that one arm acted as the local oscillator, while the other arm contained the optomechanical system. The optomechanical system was a resonant microwave circuit with an embedded nanomechanical oscillator whose displacement modulated the capacitance of the circuit, and therefore its resonance frequency. In their system, $\omega_c = 2\pi \times 7.49$ GHz, $\kappa = 2\pi \times 2.88$ MHz, $\omega_{\rm m} = 2\pi \times 1.04$ MHz, coupling $G = g_0/x_{zpf} = 2\pi \times 34$ kHz/nm and $g_0 \approx 2\pi \times 1.3$Hz. With sensitive detection of the phase fluctuations at the output of the interferometer, they inferred the power spectral density of displacement fluctuations of the nanomechanical oscillator S_{xx} and found it to be 80% of the SQL, with $S_{xx} = [(4.8 \pm 0.4)\ \mathrm{fm/Hz^{1/2}}]^2$. Furthermore, their use of a Josephson parametric amplifier with total added noise of 1.3 quanta allowed them to reach a force sensitivity $S_{ff} = (0.26 \pm 0.04)\ \mathrm{aN^2/Hz}$.

In 2019, Schliesser and colleagues at the Niels Bohr Institute demonstrated displacement and force detection below the SQL using a silicon nitride membrane (patterned with a honeycomb lattice of holes to create a phononic crystal with an acoustic bandgap near 1 MHz) coupled to a Fabry-Perot cavity [18]. A "defect" in the pattern of holes near the center of the membrane provided several vibrational modes that lie in the bandgap. The phononic crystal shields these modes from radiative loss and provides a "soft clamp", which dramatically reduces the mechanical loss. Their system operated at T = 10 K, with $\omega_{\rm m} = 2\pi \times 1.135$ MHz, $\Gamma_{\rm m} = 2\pi \times 1.1$ mHz, $\kappa = 2\pi \times 16$ MHz and $g_0 = 2\pi \times 120$ Hz. They made homodyne measurements of the light at the output of the cavity, and used optomechanically-induced correlations in the light to generate destructive interference between the imprecision and backaction noise at particular reference values of the homodyne reference phase. As a result, they demonstrated position measurements 1 dB below the SQL over several kHz of bandwidth. Also, using the sub-SQL measurement technique from above, they achieve $S_{ff} = (11.2\mathrm{aN/Hz^{1/2}})^2$.

In addition to the research on quantum-limited measurement imprecision, there has

been much effort put forth toward cooling a macroscopic mechanical oscillator to its quantum ground state. To date, several groups have cooled mechanical oscillators to the quantum ground state (defined as having the average phonon occupation of the mechanical mode $n_{\mathrm{m}} \approx k_{\mathrm{B}}T/\hbar\omega_{\mathrm{m}} < 1$). In 2010, Cleland and colleagues were the first to demonstrate that a mode of an individual, macroscopic mechanical oscillator was in its quantum ground state [19]. Their system was placed in a dilution refrigerator, and consisted of a piezoelectric cantilever coupled to a superconducting qubit. With $\omega_{\mathrm{m}} = 2\pi \times 6$ GHz, at the base temperature of their dilution refrigerator they achieved $n_{\mathrm{m}} \sim 10^{-2}$. In 2011, Painter and colleagues sideband cooled a nanomechanical oscillator to its quantum ground state [9]. In their work, an optomechahnical crystal with $\omega_{\mathrm{m}} = 2\pi \times 3.68$ GHz, $\Gamma_{\mathrm{m}} = 2\pi \times 35$ kHz and $\omega_{\mathrm{c}} = 2\pi \times 195$ THz was placed in a refrigerator at $T = 20$ K. The mechanical mode was sideband cooled from $n_{\mathrm{m}} \approx 100$ to $n_{\mathrm{m}} = 0.85 \pm 0.08$. In 2015, Harris and colleagues sideband cooled a mechanical mode of a mm-scale silicon nitride membrane coupled to a Fabry-Perot cavity to its quantum ground state [20]. In this work, $\omega_{\mathrm{m}}/2\pi = 705$ kHz, $\Gamma_{\mathrm{m}}/2\pi \sim 10^{-1}$ Hz and $\kappa/2\pi = 165$ kHz. The optomechanical system was placed in a ^{3}He cryostat, and the mechanical mode was sideband cooled from $n_{\mathrm{m}} \approx 10^4$ to $n_{\mathrm{m}} = 0.84 \pm 0.22$. Cooling macroscopic mechanical oscillators to their quantum ground state is interesting in its own right, but the ground state is also a useful starting point from which to generate non-classical motion of a mechanical oscillator.

Significant theoretical and experimental efforts have been made towards the preparation of non-classical mechanical motion in optomechanical systems [21]. One theoretical proposal consists of preparing the optical cavity in a superposition of two Fock states, resulting in radiation pressure driving a movable mirror to a superposition state of different oscillation amplitudes [22]. Another theoretical proposal utilizes the radiation pressure of a single intra-cavity photon to prepare a mechanical oscillator in a superposition state of two oscillation amplitudes [23]. In 2017, Aspelmeyer, Gröblacher and colleagues used an optomechanical crystal with $g_0/2\pi = 869$ kHz, $\omega_{\mathrm{m}}/2\pi = 5.25$ GHz, $\Gamma_{\mathrm{m}}/2\pi 1.4$ kHz and $\kappa/2\pi =$

846 MHz [24]. Their system operated at $T = 35$ mK in a dilution refrigerator, so when the device was thermalized with the refrigerator, $n_{\mathrm{m}} \sim 10^{-1}$. The interaction Hamiltonian in equation 2.3 can be linearized when $g_0\sqrt{n_{\mathrm{circ}}} \ll \kappa$, which Aspelmeyer, Gröblacher and colleagues ensured by exciting the optical mode with ~ 10 fJ pulses (the low power pulses are also necessary to limit the absorptive heating in their system). This linearization gives two terms: $\hat{H}_{\mathrm{dc}} = \hbar g_0\sqrt{n_{\mathrm{circ}}}\left(\hat{a}^\dagger\hat{b}^\dagger + \hat{a}\hat{b}\right)$, which allows for the down-conversion of a photon into a correlated photon-phonon pair, and $\hat{H}_{\mathrm{swap}} = \hbar g_0\sqrt{n_{\mathrm{circ}}}\left(\hat{a}^\dagger\hat{b} + \hat{a}\hat{b}^\dagger\right)$, which allows the state of the optical and mechanical modes to be swapped. They used the down-conversation interaction to create correlated photon-pairs, and used a single photon detector (SPD) at the output of the cavity to project the mechanical mode into a single-phonon Fock state. They then used the state-swap interaction to swap the mechanical Fock state onto the state of the optical mode, and detected the resulting photon. They measured the light exiting the cavity with a Hanbury Brown and Twiss interferometer to measure the mechanical mode's second-order intensity correlation function $g^{(2)}(\tau)$, where τ is the time between subsequent detection events. Measurement of $g^{(2)}(0) < 1$ is direct evidence of the quantum nature of the mechanical mode; it implies sub-Poissonian phonon statistics (a coherent state has $g^{(2)}(0) = 1$ and Poissonian statistics, $g^{(2)}(0) = 2$ for a thermal state), and they measured $g^{(2)}(0) = 0.65$. Experimental realization of such non-classical features of mechanical motion – combined with measurement imprecision at or beyond the SQL – may allow experimental study of exotic decoherence processes such as gravitational self-interaction, in which gravity is postulated to induce the collapse of spatial superpositions [25]. Although experimental tests of gravitational decoherence may be far from realization, the field of quantum optomechanics continues to rapidly advance.

There has also been progress towards generating non-classical motion in electrical analogues of optomechanical systems through coupling mechanical motion to superconducting qubits. Last year, Lenhnert and colleagues at JILA demonstrated electromechanical coupling between a Cooper pair box qubit (which behaves as a non-linear inductor) and the

motion of a compliant capacitor plate [26]. In this work, a single phonon in the mechanical mode dispersively couples to the qubit with transition frequency $\omega_{\rm q}/2\pi = 3.8$ GHz at the rate $g_0/2\pi = 0.52$ MHz, which is 14% of the qubit linewidth $\kappa_{\rm q}/2\pi = 3.7$ MHz. As a result, they were able to detect the phonon distribution of the mechanical mode via qubit spectroscopy and drive phonon number dependent sideband transitions that allow for the generation of non-thermal states of mechanical motion. In parallel, Schoelkopf, Rakich and colleagues, prepared Fock states of mechanical motion in a bulk acoustic-wave resonator, and performed tomographic verification of the quantum motion of the mechanical mode [27]. Here, mechanical modes with $\omega_{\rm m}/2\pi \sim 1$ MHz and $\Gamma_{\rm m}/2\pi \sim 15$ kHz, coupled piezoelectrically to a superconducting transmon qubit with a rate $g_0/2\pi = 350$ kHz. They made measurements of the qubit population after microwave pulse sequences for Fock state generation, and then extracted from it the phonon populations. They then made parity measurements of the phonon populations and used maximum likelihood estimation to reconstruct the Wigner function. The Wigner function negativity they observed is a clear signature of the quantum nature of the motion. Also in 2018, Cleland and colleagues demonstrated the preparation of Fock states of mechanical motion in a surface acoustic wave resonator with $\omega_{\rm m}/2\pi \approx 4$ GHz and $\Gamma_{\rm m}/2\pi \approx 7$ MHz, coupled piezoelectrically to a superconducting qubit with a rate $g_0/2\pi = 7.3$ MHz. They reconstructed the Wigner function that described the mechanical motion and it showed negativity, verifying the quantum nature of the mechanical motion.

However, devices in the optical domain have not gained access to qubit-like two level systems to initialize quantum states of mechanical motion. Researchers who work with these devices must instead rely on maximizing $C_{\rm th}$ by minimizing $\Gamma_{\rm m}$, minimizing κ, and increasing the loaded optomechanical coupling $g = g_0\sqrt{n_{\rm circ}}$. However, larger $n_{\rm circ}$ often leads to heating in the system, which increases $n_{\rm th}$ and tends to move the system away from the quantum regime. As described in section 2.1.3, the unique properties of liquid helium could allow for decreased κ and increased $n_{\rm circ}$, and so could be an excellent material to

use to construct an optomechanical system.

2.1.3 Superfluid Optomechanics

In this section we review the properties of liquid helium that make it especially well-suited to use in quantum optomechanical devices. We also review work with superfluid helium used as a mechanical element.

Optical loss in a material that is used to construct an optomechanical system will increase κ and cause heating, thus decreasing $C_{\rm th}$. Optical loss arises from absorption due to electronic excitations in the host material, structural imperfections or chemical impurities. Optical absorption can be suppressed by using a material with a large bandgap, but even for large bandgap materials structural and chemical impurities remain. Liquid helium simultaneously combats each of these sources of optical loss. First, liquid helium has a bandgap energy $\approx$19.8 eV, so it will not resonantly absorb infrared or visible light. Second, liquid helium is (like any liquid) without structural imperfections. Third, at liquid helium temperatures, any chemical impurities freeze to the walls of the container holding the liquid.

Mechanical loss in a material that is used to construct an optomechanical system will also decrease $C_{\rm th}$. Mechanical loss arises from phonon radiation into the surroundings, phonon absorption by chemical and structural impurities, mode conversion via mechanical non-linearity in the material, and – in liquids – viscosity. Liquid helium addresses these sources of mechanical loss in a number of ways. First, superfluid liquid helium has zero viscosity. Second, it is chemically and structurally pure. Third, although its mechanical non-linearity is significant, the resulting mechanical loss $\propto T^4$, so it is rapidly suppressed with decreasing temperature T. Fourth, the acoustic impedance mismatch between liquid helium and its container will suppress the process of phonons radiating away.

Because a liquid can fill an optical cavity, the mechanical and optical modes can be confined such that they have a high degree of spatial overlap, which increases their mutual

interaction. As a result, it could be possible to have large g_0,

To date, only a few research groups have used optomechanical systems that incorporate superfluid helium. In 2014, De Lorenzo and Scwhwab at Caltech reported the first use of superfluid helium as a mechanical element in an optomechanical system [28]. In their work, they coupled the acoustic mode of superfluid ^{4}He to an electromagnetic mode of a high quality factor superconducting microwave cavity. The microwave resonance frequency was modulated by the modulation of the liquid's density, and the resulting modulation of the permittivity inside the cavity. They observed $Q_{\rm mech} \sim 10^7$, but very small $g_0 \sim 10^{-8}$ Hz between modes with $\omega_{\rm c}/2\pi = 10.6$ GHz and $\omega_{\rm m}/2\pi = 12.2$ kHz. The vibrational mode frequencies of their microwave cavity were larger than $\omega_{\rm c}/2\pi$, so the cavity's motion was in-phase with the liquid's motion. As a result, the mechanical forces the cavity exterted on the liquid did not damp the liquid's motion. They also placed the microwave input couplers and the helium fill line at the first radial mechanical node in the cavity, minimizing leakage of the mechanical mode into the fill line. They observed an acoustic mode with $Q_{\rm mech} \sim 10^8$, limited by ^{3}He impurities [29]. Interestingly, the most recent work from those authors explores how such an optomechanical system could achieve strain sensitivities similar to that of LIGO [30].

In 2015, John Davis' group at the University of Alberta also reported experiments which use superfluid helium as a nanomechanical resonator, in pursuit of studying quantum nanofluidics [31]. They measured a Helmholtz resonator constructed from a borosillicate channel through which the superfluid can flow, and part of which is contained between the plates of a capacitor. As the superfluid flowed in and out of the capacitor, the permittivity of the capacitor changed, which allowed studies of superfluid motion in the nanoscale channel. They demonstrated mechanical modes with $Q_{\rm mech} \approx 300$. They drove the mechanical modes and studied the temperature dependence of $Q_{\rm mech}$, and found that larger drive voltages led to decreased $Q_{\rm mech}$, likely due to the onset of quantum turbulence. In further work using devices made from quartz (with better surface quality) they observed

a mechanical mode with $Q_{\mathrm{mech}} \sim 10^6$ [32]. In 2016, Warwick Bowen's group at the University of Queensland reported measurements of microtoroid optical resonators coated with a thin superfluid ^{4}He film. Waves in the film restored by the van der Waals force – third sound – couple to the evanescent portions of the microtoroid's optical whispering gallery modes [33]. Here, $\omega_{\mathrm{c}}/2\pi \sim 200$ THz and $\kappa/2\pi = 22.3$ MHz. They used sensitive homodyne detection to measure the thermal motion of the third sound modes with $\Gamma_{\mathrm{mech}} \approx 4$ kHz and $\omega_{\mathrm{m}}/2\pi \sim 500$ kHz, and they demonstrated the ability to cool and heat these modes primarily via photothermal coupling. In a 2019 paper published on arXiv, the group demonstrated the ability to use their microtoroid resonators to create confined clusters of superfluid vortices, and use the vortices' coupling to the third sound modes to study metastable states involving vortices orbiting the center of the resonator. The orbiting vortices break a degeneracy between the mechanical modes, and generate a splitting that can be measured via the mechanical modes' detuning of the optical modes [34].

Lastly, in recent work from Jack Harris' group at Yale, we demonstrated the coherent coupling of an acoustic mode in superfluid liquid helium to an optical mode of a miniature Fabry-Perot optical cavity [35, 36]. In this work, the coupling arises due to the acoustic mode modulating the helium density, giving the effect of modulating the optical cavity resonance frequency. Here, $Q_{\mathrm{mech}} \approx 6 \times 10^4$, $\omega_{\mathrm{m}}/2\pi \approx 317$ MHz, $\omega_{\mathrm{c}}/2\pi \sim 200$ THz, $\kappa/2\pi = 46$ MHz and $g_0/2\pi = 3$ kHz. We demonstrated the ability to cool the mechanical mode to near its quantum ground state, $n_m \approx 5$ phonons, and directly detected quantum features in its motion by studying correlations in the light at the output of the cavity [37]. Our group has also proposed the use of an isolated liquid helium drop as an optomechanical system, in which optical whispering gallery modes of the drop couple to the drop's vibrations, possibly providing access to new regimes of optomechanics [38].

2.1.4 Levitated Optomechanics

Mechanical oscillators must be supported against Earth's gravity. They are typically clamped to a structure that facilitates coupling the mechanical oscillator to a fixed cavity (or other probes). This structure also forms a solid link between the mechanical oscillator and its environment, which has three immediate consequences. First, the clamping introduces mechanical loss by allowing mechanical energy to radiate out of the oscillator and into the environment. Second, the form of the clamp may change the mechanical eigenmodes of the oscillator in such a way that concentrates stress and increases loss from internal friction. Third, the clamping allows the mechanical oscillator's bulk to remain in thermal equilibrium with its surroundings.

Removal of the clamp (i.e. by levitation of the mechanical oscillator) provides a solution to two of these consequences. First, mechanical energy cannot flow out of the oscillator and into the environment. Second, the mechanical eigenmodes are not disturbed in such a way that increases internal friction. However, because a levitated mechanical oscillator is not in thermal contact with a refrigerator, it is potentially vulnerable to heating.

In current levitated optomechanics experiments, the mechanical mode of interest is the levitated object's center-of-mass motion. The most important parameters in levitated optomechanics are the diameter of the mechanical oscillator d, its oscillation frequency ω_{m}, the damping rate of its motion Γ_{m}, the pressure P of the chamber in which it is levitated, the motional temperatures $\{T_{\mathrm{x}}, T_{\mathrm{y}}, T_{\mathrm{z}}\}$, and its bulk temperature T_{bulk}. Levitation of the mechanical oscillator is currently achieved by several different means: optical tweezers, radio frequency quadrupole traps and diamagnetic levitation [39].

In 2010, Geraci and colleagues at NIST Boulder proposed using an optically levitated nanoscale silica sphere to measure forces between the sphere and another object at distances $\lesssim 1$ μm to search for non-Newtonian, gravity-like forces at small length scales [40]. However, it should be mentioned that in the pursuit of measuring forces at such small length scales, the main challenge is usually removing other unwanted forces, such as electrostatic

forces.

In further work, Geraci and colleagues trapped silica spheres with $d \approx 300$ nm in an optical lattice formed by two counter-propagating laser beams with total power $P_{\mathrm{L}} \sim 2$ W and beam waist radius $w \approx 8$ μm, and demonstrated force sensitivity $S_{ff} = (1.63 \pm 0.37\mathrm{aN/Hz}^{1/2})^2$ [41]. The particles were loaded into the optical lattice by first applying them to a cantilever, then driving cantilever motion to eject the spheres from the surface and into the three-dimensional trap at $P \sim 10$ mbar. After evacuating to $P \sim 1$ mbar, they measured $\{\omega_{\mathrm{m}}^{(\mathrm{x})}/2\pi, \omega_{\mathrm{m}}^{(\mathrm{y})}/2\pi, \omega_{\mathrm{m}}^{(\mathrm{z})}/2\pi\}$ = $\{2.8\ \mathrm{kHz}, 3.4\ \mathrm{kHz}, 7.3\ \mathrm{kHz}\}$, with $\Gamma_{\mathrm{m}}/2\pi = 1.4$ kHz. After evacuating to $P \sim 10^{-6}$ mbar, and applying feedback damping (forces proportional to the particle's velocity), they cooled the three center of mass modes to $\{T_{\mathrm{x}}, T_{\mathrm{y}}, T_{\mathrm{z}}\}$ to $\{460\ \mathrm{mK}, 610\ \mathrm{mK}, 8\ \mathrm{K}\}$. They studied the trap instabilities and found that at $P \sim 10^{-2}$ mbar, feedback cooling was necessary to have the sphere remain trapped as the chamber was evacuated. They also reported an exponential reduction in the trap lifetime with laser power, which was unexpected. While the exact mechanism that caused this behavior is unknown, they noted that it could be due to optical absorption. From the optical absorption, they estimated the bulk temperature $600\ \mathrm{K} \lesssim T_{\mathrm{bulk}} \lesssim 1,000$ K, which could cause annealing, glass-crystalline phase transition or evaporation of the particle. Such changes could cause a change in density, size or refractive index of the particle, which would lead to the particle receiving a sudden kick.

In 2014, Gratta and colleagues at Stanford used an optical tweezer with $P_{\mathrm{L}} \approx 300$ mW to trap silica spheres with with $d \approx 5$ μm at $P \sim 10^{-7}$ mbar [42]. They also demonstrated the capacity to resolve tiny forces, with a reported force sensitivity $S_{ff} = 5 \times 10^{-17}\mathrm{N/Hz}^{1/2}$. They cooled the motion of the sphere to $\{T_{\mathrm{x}}, T_{\mathrm{y}}, T_{\mathrm{z}}\} \sim 10$ mK using feedback cooling. Though their system was originally intended for testing gravity at small length scales, they instead conducted a direct search for millicharged particles. These are fractionally charged (ηe, where e is the electron charge) predicted by some dark matter models that include interactions with baryonic matter. As a result, they needed to take care

in understanding at what level their spheres were neutral (in the absence of millicharged particles). They found that after loading the trap with particles (using the same method described above) the spheres typically had charge $q \sim 10^2 - 10^3 e$. To remove this charge, they illuminated the spheres with ultraviolet light from a fiber-coupled xenon flash lamp, which provided photoelectric ejection of electrons from the spheres and completely removed the surplus electrons. Next, they applied an oscillating 500 V across electrodes separated by 1 mm, between which the sphere was trapped. They searched for oscillations of the trapped sphere due to this voltage by studying the center of motion of nominally neutral spheres. They placed an upper bound on the abundance of millicharged particles per nucleon of $< 2.5 \times 10^{-14}$ for $\eta \sim 10^{-1} - 10^{-5}$. In 2016, Gratta and colleagues proposed using these levitated silica spheres to search for exotic new forces associated with dark energy [43]. In 2017, Moore and colleagues at Yale demonstrated a levitated silica sphere system with acceleration sensitivity $S_{aa} \sim (1\mu g/\mathrm{Hz}^{1/2})^2$ [44].

Alongside the effort to study foundational physics in levitated systems, a large amount of important work has been done with the goal of pushing levitated optomechanical systems into the quantum regime. Goals in the field of levitated optomechanics include cooling the center-of-mass motion of a levitated object into its quantum ground state, and initializing non-classical states of motion (for example, a quantum superposition). However, ground state cooling may be difficult to achieve due to blackbody emission from silica spheres with high T_{bulk}. Furthermore, such emission would cause recoil noise in the position of the levitated object, placing a limit on the smallest resolvable displacement.

In 2015, the Barker group at University College London demonstrated the cooling of a charged silica sphere with $q \sim e$ confined within a Paul trap and interacting with a Fabry-Perot cavity [45]. The trapped sphere had $d \approx 400$ nm and $\omega_{\mathrm{m}}/2\pi \approx 18$ kHz, and the cavity had $\kappa \approx 270$ kHz. They cooled the motion of the sphere to 10 K at $P \sim 10^{-4}$ mbar. In further work, they demonstrated the levitation of crystalline ytterbium-doped yttrium lithium fluoride (Yb:YLF), which is able to cool its bulk temperature when exposed to

laser light [46]. They showed that Yb:YLF nanocrystals in an optical dipole trap with $P_{\mathrm{L}} \approx 200$ mW could reach $T_{\mathrm{bulk}} \approx 130$ K through anti-Stokes scattering of the trap light at $P \sim 10$ mbar. The crystals were asymmetric and birefringent, so when exposed to linearly polarized light they underwent pendulum-like motion at $\omega_{\mathrm{m}}/2\pi \approx 24$ kHz, and when exposed to circularly polarized light they rotated at $\omega_{\mathrm{m}}/2\pi \approx 52$ kHz, both with $\Gamma_{\mathrm{m}}/2\pi \approx 15$ kHz.

In 2017, the Vamivakas group at the University of Rochester demonstrated coherent control of the spin of a nitrogen-vacancy (NV) center in optically levitated nanodiamonds [47]. The nanodiamonds had $d \approx 40$ nm, $\omega_{\mathrm{m}} \approx 100$ kHz and were trapped with an optical tweezer with $P_{\mathrm{L}} \approx 200$ mW at $P \approx 25$ mbar. The NV spin was initialized by a 1 μs pulse from a $\lambda = 532$ nm beam, then rotated by a microwave pulse, before a final 1 μs pulse from the $\lambda = 532$ nm beam converted the spin state into photoluminescence that could be measured. They measured oscillations in the photoluminescence with increasing microwave pulse length, and used this data to extract the spin dephasing time $T_2 = 109.6 \pm 5.5$ ns. Their works provides a platform to couple spin to mechanical motion, and to potentially use this interaction to initialize quantum states of motion.

In 2018, the Novotny group at ETH Zurich reported free fall experiments with silica spheres with $d = 60$ nm at $P \sim 10^{-5}$ mbar [48]. They first trapped the spheres with $P_{\mathrm{L}} = 140$ mW, which gave $\{\omega_{\mathrm{m}}^{(\mathrm{x})}/2\pi, \omega_{\mathrm{m}}^{(\mathrm{y})}/2\pi, \omega_{\mathrm{m}}^{(\mathrm{z})}/2\pi\} = \{195\ \mathrm{kHz}, 160\ \mathrm{kHz}, 60\ \mathrm{kHz}\}$. They used feedback to cool the sphere to motional temperatures $\{T_{\mathrm{x}}, T_{\mathrm{y}}\} = \{63, 47\}$ mK before dropping it, quickly recapturing it, and measuring the kinetic energy it acquired during its gravitational acceleration. They extracted a force $F_{\mathrm{y}} = 21 \pm 4$ aN, which, with their particle of mass $m = 2.0 \pm 0.7$ fg, implied a gravitational acceleration $g = 10.4 \pm 1.8$ m/s^2 that agrees with the known value. This is an important result because the measured force is static. In contrast, other experiments measure oscillating forces at mechanical resonance, so their sensitivity is enhanced by a factor of Q_{mech}. In addition, the demonstration of rapidly repeated free fall experiments marks an important step toward matter wave interferometry

experiments with macroscopic objects [49]. This is because there is no physical contact between the sphere and its environment, and thus the decoherence of a quantum state of motion is limited, and because rapid time-of-flight measurements of the position of a sphere after its initialization into a quantum state of motion would allow one to reconstruct the Wigner function.

In 2018, the D'Urso group at Montana State University reported measurements of a magnetically levitated micron-scale silica sphere at $P \sim 10^{-10}$ Torr [50]. In this work, they circumvented the heating associated with optical traps by using a DC magnetic quadrupole trap to balance the sphere against gravity, owing to its diamagnetic response. They measured $\{\omega_{\mathrm{m}}^{(\mathrm{x})}/2\pi, \omega_{\mathrm{m}}^{(\mathrm{y})}/2\pi, \omega_{\mathrm{m}}^{(\mathrm{z})}/2\pi\} = \{59.6\ \mathrm{Hz}, 96.9\ \mathrm{Hz}, 7.01\ \mathrm{Hz}\}$. Like the other experiments, they implemented feedback cooling and cooled the sphere's center of mass degrees of freedom to $\{T_{\mathrm{y}}, T_{\mathrm{z}}\} = \{1.2\ \mathrm{mK}, 0.6\ \mathrm{mK}\}$, with $\{\Gamma_{\mathrm{y}}/2\pi, \Gamma_{\mathrm{z}}/2\pi\} = \{7.0\ \mathrm{Hz}, 1.5\ \mathrm{Hz}\}$. They noted that, sometimes, they weakly cooled the motion in the x-direction, but they did not calibrate the motion, so they could not provide T_{x}. They mentioned that such a system with a levitated superconductor would have much lower thermal occupation of its motion (the trap would be much more tightly confining because its magnetic susceptibility would be much larger), which, with their ultra-high vacuum capability and zero optical absorption, may place their system well on its way to the quantum regime.

Finally, the Aspelmeyer group at the University of Vienna recently reported measurements of a silica sphere with $d \approx 150$ nm, trapped in an optical tweezer with $P_{\mathrm{L}} = 170$ mW and $\{\omega_{\mathrm{m}}^{(\mathrm{x})}/2\pi, \omega_{\mathrm{m}}^{(\mathrm{y})}/2\pi, \omega_{\mathrm{m}}^{(\mathrm{z})}/2\pi\} = \{190\ \mathrm{kHz}, 170\ \mathrm{kHz}, 90\ \mathrm{kHz}\}$ at $P \sim 10^{-2}$ mbar [51]. The motion of the sphere was cooled to $\{T_{\mathrm{x}}, T_{\mathrm{y}}, T_{\mathrm{z}}\} \sim 1$ K by scattering photons into a mode of an optical cavity with $\kappa/2\pi = 193$ kHz. They were able to measure loaded optomechanical couplings $g_{\mathrm{x}}/2\pi = 60$ kHz and $g_{\mathrm{z}}/2\pi = 120$ kHz. Given the sideband resolution in this experiment, and the large optomechanical coupling, they could immediately sideband-cool the center-of-mass motion of the sphere to its quantum ground state if they could operate at the lowest operating pressures shown in other levitated optomechan-

ics experiments. At lower pressures, increasing the laser power may increase the coherent scattering into the cavity mode, so as to enable even larger loaded coupling rates to the cavity. This may pave a path toward the "ultra-strong" coupling regime where the loaded coupling rate exceeds both mechanical frequency and cavity decay rate, and quantum effects dominate in the interaction between the light and the mechanical motion.

2.2 High-Finesse Optical Resonators

An optical resonator can be made from low loss materials arranged into a geometry that confines the electromagnetic field. Such a resonator will host a number of modes, each of which can be approximately represented as an independent harmonic oscillator. The accuracy of this approximation increases as the mode loss decreases, or, equivalently, as the mode finesse increases.

The finesse $\mathcal{F}$ of a mode is defined as the free spectral range $\Delta\omega_{\mathrm{FSR}}$ (the frequency spacing between the confined modes) divided by the full-width-half-max bandwidth κ of the modes, and it is an important figure of merit for a resonator. A useful physical definition of the finesse is the average number of round-trips a photon would traverse in the resonator before being lost.

In practice, the finesse is limited by losses arising from light scattering out of the resonator or being absorbed by it. If a fraction ϱ of the optical power in the resonator remains in the resonator after one round-trip, the round-trip loss is $\varphi = 1 - \varrho$. The finesse is then given by

$$\mathcal{F} \approx \frac{2\pi}{\varphi}, \tag{2.10}$$

which is an excellent approximation when $\varphi \ll 1$ (low loss). The finesse is related to the mode quality factor such that $Q_{\mathrm{opt}} = (\omega_{\mathrm{c}}/\Delta\omega_{\mathrm{FSR}})\mathcal{F}$.

In experiments in which optical resonators are coupled to other systems (e.g. an atom, or a mechanical oscillator), it is often useful to not only have a large finesse, but also to

have a small mode volume, which increases the interaction strength between the optical mode and the other system.

High finesse optical resonators can be operated as optical interferometers that are sensitive to phase variations of the light. In optomechanics, where the phase of light leaving the optical resonator is sensitive to the motion of a mechanical oscillator, its often useful to have larger finesse because the light will pick up more phase variation for a given oscillator displacement, and thus it can allow for more sensitive measurement of a mechanical oscillator.

There are several types of optical resonators, each having strengths and weaknesses for various applications. In the next section, I will review the main types of optical resonators, with a special emphasis placed on whispering gallery mode resonators.

2.2.1 Fabry-Perot Resonators

In 1899, Fabry and Pérot invented an optical resonator consisting of two parallel reflecting surfaces that are separated by some distance. In the first paragraph of section 2.1.2, I describe the properties of this resonator – see figure 2.1. Since its creation, the Fabry-Pérot interferometer has been used to build: optical wavemeters, optical spectrum analyzers, laser resonators, dichroic filters and wave division multitplexers for telecommunications [52, 53, 54, 55, 56]. Furthermore, these resonators have been useful for terrestrial and non-terrestrial atomic spectroscopy and metrology, as well as for measuring gravitational waves [57, 58, 59, 15]. Also, as I describe in section 2.1.2, these resonators have been highly successful at optically probing mechanical systems and studying the quantum mechanics of light-matter interactions in optomechanical systems.

The maximum finesse of Fabry-Pérot a resonator is limited by loss in the mirror coatings. It seems that the highest reported finesse of an optical Fabry-Pérot resonator is 1.9×10^6 [60].

2.2.2 Photonic Crystal Resonators

In a crystal, the periodicity of the lattice restricts the motion of electrons such that the electrons experience bands of allowed and forbidden energies. The bands of forbidden energies are known as bandgaps. In direct analogy with an electron in the periodic potential of a crystal lattice, light confined in a dielectric material with periodic regions of low and high refractive index is subjected to allowed and forbidden frequencies, and thus a photonic band gap exists; a structure that exhibits this property is called a photonic crystal. Although it is not often spoken about in this manner, the well-known Bragg mirror, first studied by Lord Rayleigh in 1888, is an example of a one-dimensional photonic crystal.

Photonic crystals are typically fabricated in a photonic crystal slab geometry. This geometry uses a periodic arrangement of holes in a thin (thickness $t \leq \lambda$, where λ is the wavelength of the light) material. The holes provide the necessary periodic index of refraction to realize a photonic crystal (PhC) [61]. Intentionally placed "defects" in the hole locations can form a region in which light is strongly confined to a volume $\sim \lambda^3$. Houdre and colleagues at EPFL fabricated a PhC slab using silicon with index of refraction $n = 3.46$ and thickness $t = 220$ nm, and on the slab they patterned holes with diameter $d = 0.5a$ and lattice constant $a = 435$ nm. However, in the fabrication they slightly displaced the holes of one intersecting row and column, which provided a region where light with $\lambda = 1.59$ μm, could be confined. The confinement region was centered at the intersection of the row and column, and the mode intensity rapidly decreased over just a few lattice constants away from the intersection. They measured a confined optical mode with $Q_{\rm opt} = 4 \times 10^5$ and mode volume $V = 0.34(\lambda/n)^3$. Painter and colleagues at Caltech fabricated a 2D PhC cavity by implementing defects in the hole pattern an demonstrated a resonance with $\lambda \sim 1.5$ μm, $Q_{\rm opt} = 1.2 \times 10^6$ and $V = 0.04\lambda^3$, which seems to be the largest $Q_{\rm opt}$ demonstrated in the literature among PhC cavities [62].

The loss in PhC cavities is typically limited by impurities in the material used to construct the cavity (or on its surface), or by fabrication errors in the holes' size, shape and

position. While PhC cavities serve as high quality optical resonators, a large part of the utility of PhC cavities is their small mode volumes. To date, the compact nature of high quality factor photonic crystal resonators, and the strong light-matter interactions afforded to them due to the small electromagnetic mode volume, has resulted in several important technical and scientific applications, such as low threshold lasing, ultra-small filters and quantum optomechanics [63, 64, 9, 65, 66, 37].

2.2.3 Whispering Gallery Mode Resonators

In the late 1870's, Lord Rayleigh observed that whispers initiated at the periphery of the dome of St Paul's Cathedral could be heard across the dome, but only along the periphery; if the listener moved closer to the center of the dome, the whispers could not be heard [67]. In Lord Rayleigh's example, the whispering gallery phenomenon was caused by the smooth, curved dome walls guiding the acoustic waves around the periphery of the room with minimal scattering of the acoustic wave toward the center of the dome. Such whispering gallery modes exist (WGMs) for electromagnetic waves confined within curved dielectrics, and have, for example, been observed in micron-scale glass spheres and tori, calcium fluoride crystals and liquid drops [68, 69, 70, 71, 72]. In silica spheres and liquid drop resonators, $\mathcal{F} \gtrsim 10^6$ has been observed, whereas in calcium fluoride resonators $\mathcal{F} \sim 10^7$ has been observed. Thus far, optical whispering gallery mode resonators have been especially useful for applications in sensing, lasing, and frequency comb generation.

Whispering Gallery Modes: The Ray-Optical Picture

To understand the origin of whispering gallery modes, we can begin with a ray-optics picture. In such a picture, the light rays are nearly perfectly confined within the periphery of the dielectric resonator via total internal reflection. However, the total internal reflection (TIR) is imperfect because rays with a given $\mathbf{k}$ may meet the criteria for TIR at some locations on the dielectric, but not others, and thus optical modes in whispering gallery

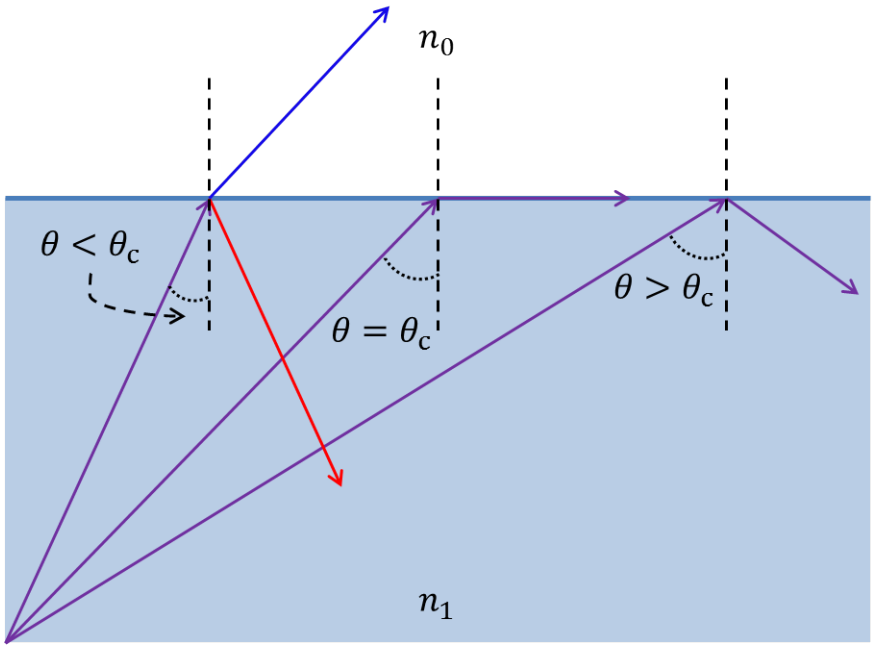

Figure 2.2: Light rays traveling in a medium with index of refraction n_1, which strike a flat interface with another medium with index of refraction n_0. When $n_1 > n_0$, the light will undergo total internal reflection if the light strikes the interface at an angle $\theta > \theta_c = \sin^{-1}(n_0/n_1)$. Otherwise, the light ray will be partially transmitted across the interface.

resonators are inherently lossy. One may expect that this loss decreases for larger spheres, as the surface appears flatter, in which case rays with a given $\mathbf{k}$ can satisfy TIR over a wider area on the sphere. The fact that there are no true bound states of light in whispering gallery mode resonators means that even with idealized material properties, these modes undergo leakage.

More quantitatively, we note that when a plane wave of light traveling in a medium with index of refraction n_1 approaches a flat interface with a second medium with index of refraction n_0, total internal reflection (TIR) will occur if the angle of incidence relative to the normal to the interface $\theta > \theta_c = \sin^{-1}(n_0/n_1)$. For light approaching flat surfaces this reflection is perfect. Figure 2.2 provides an illustration of rays with various values of θ approaching the interface. However, when light approaches a curved interface between the two media, electromagnetic field leakage can occur across the interface. Although the curved interface seems locally flat, the plane wave of light is actually composed of rays that

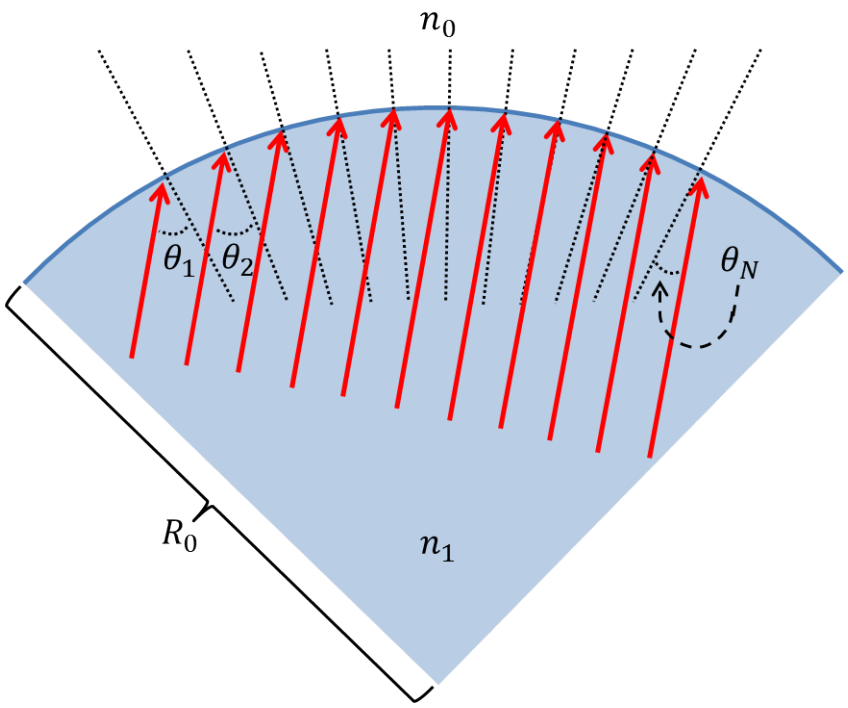

Figure 2.3: Ray-optical picture of total internal reflection at a curved dielectric interface. Light rays traveling in a medium with index of refraction n_1 strike a curved interface with radius of curvature R_0 between the n_1 medium and another medium with index of refraction n_0. Each light ray is understood to represent one portion of a plane wave, which has infinite transverse extent. Consequently, a plane wave can be thought of as having many angles of incidence θ_i with respect to the interface, and so it cannot be perfectly reflected.

spread over an infinite extent in the transverse directions, and these will have many different angles of incidence to the interface, as shown in figure 2.3. Thus, a convex dielectric can support highly confined modes of the electromagnetic field, provided the radius of the dielectric is sufficiently large that a large number of optical rays undergo TIR. As shown below in a more quantitative treatment, the active figure of merit for determining WGM loss is the ratio of the resonator's radius of curvature to the wavelength of the light.

Whispering Gallery Modes: Exact Theory

In order to determine the electromagnetic fields and the resonant WGM frequencies inside a dielectric, one can solve Maxwell's equations. For a source-free region, with linear

electric and magnetic susceptibility we can write

$$\nabla \times \mathbf{E} = -i\omega\mu\mathbf{H} \tag{2.11}$$

$$\nabla \times \mathbf{H} = -i\omega\epsilon\mathbf{E} \tag{2.12}$$

where I have assumed a time dependence of $e^{-i\omega t}$.

In the following derivation, I follow reference [73] closely and solve Maxwell's equations in a generalized orthogonal coordinate system, before switching to spherical coordinates to find the radial and angular electromagnetic field components.

Consider the position vector $\mathbf{r} = x\hat{x} + y\hat{y} + z\hat{z}$ in Cartesian coordinates that points from the origin to the point $(x, y, z) = (x_1, x_2, x_3)$. The same point can be identified with orthogonal curvilinear coordinates (u_1, u_1, u_3) by scaling them with the factors (also known as Lamé coefficients) $\{h_1, h_2, h_3\}$. The scale factors are given by

$$h_i = \left|\frac{\partial \mathbf{r}}{\partial u_i}\right| = \left(\sum_{k=1}^{3} \frac{\partial x_k}{\partial u_i}\right)^{1/2} \tag{2.13}$$

Then, in terms of (u_1, u_2, u_3), the electric and magnetic fields can be written as $\mathbf{E} = E_1\hat{u}_1 + E_2\hat{u}_2 + E_3\hat{u}_3$, $\mathbf{H} = H_1\hat{u}_1 + H_2\hat{u}_2 + H_3\hat{u}_3$, respectively. The six differential equations represented by equations 2.11 and 2.12 can be written as

$$\frac{\partial(h_3E_3)}{\partial u_2} - \frac{\partial(h_2E_2)}{\partial u_3} = -i\omega\mu h_2h_3H_1 \tag{2.14}$$

$$\frac{\partial(h_1E_1)}{\partial u_3} - \frac{\partial(h_3E_3)}{\partial u_1} = -i\omega\mu h_3h_1H_2 \tag{2.15}$$

$$\frac{\partial(h_2E_2)}{\partial u_1} - \frac{\partial(h_1E_1)}{\partial u_2} = -i\omega\mu h_1h_2H_3 \tag{2.16}$$

$$\frac{\partial(h_3H_3)}{\partial u_2} - \frac{\partial(h_2H_2)}{\partial u_3} = i\omega\epsilon h_2h_3E_1 \tag{2.17}$$

$$\frac{\partial(h_1 H_1)}{\partial u_3} - \frac{\partial(h_3 H_3)}{\partial u_1} = i\omega\epsilon h_3 h_1 E_2 \tag{2.18}$$

$$\frac{\partial(h_2 H_2)}{\partial u_1} - \frac{\partial(h_1 H_1)}{\partial u_3} = i\omega\epsilon h_1 h_2 E_3 \tag{2.19}$$

If the scale factors h_1, h_2, h_3 satisfy the conditions

$$h_3 = 1 \tag{2.20}$$

$$\frac{\partial}{\partial u_3}\left(\frac{h_1}{h_2}\right) = 0 \tag{2.21}$$

then two scalar functions U and V, known as Borgnis potentials (also known as Debye potentials) can be found such that E_3 is a function of U only, and H_3 is a function of V only [74, 73]. Borgnis potentials are useful because they provide a convenient method to solve the vector Helmhotz equation. In terms of the Borgnis potentials and wavenumber $k = \omega/c$, the fields can be expressed as

$$E_1 = \frac{1}{h_1}\frac{\partial^2 U}{\partial u_3 \partial u_1} - i\omega\mu\frac{1}{h_2}\frac{\partial V}{\partial u_2} \tag{2.22}$$

$$E_2 = \frac{1}{h_2}\frac{\partial^2 U}{\partial u_2 \partial u_3} + i\omega\mu\frac{1}{h_1}\frac{\partial V}{\partial u_1} \tag{2.23}$$

$$E_3 = \frac{\partial^2 U}{\partial {u_3}^2} + k^2 U \tag{2.24}$$

$$H_1 = \frac{1}{h_1}\frac{\partial^2 V}{\partial u_3 u_1} + i\omega\epsilon\frac{1}{h_2}\frac{\partial U}{\partial u_2} \tag{2.25}$$

$$H_2 = \frac{1}{h_2}\frac{\partial^2 V}{\partial u_2 u_3} - i\omega\epsilon\frac{1}{h_1}\frac{\partial U}{\partial u_1} \tag{2.26}$$

$$H_3 = \frac{\partial^2 V}{\partial {u_3}^2} + k^2 V \tag{2.27}$$

The functions U and V satisfy

$$\frac{1}{h_1 h_2}\left[\frac{\partial}{\partial u_1}\left(\frac{h_2}{h_1}\frac{\partial}{\partial u_1}\right) + \frac{\partial}{\partial u_2}\left(\frac{h_1}{h_2}\frac{\partial}{\partial u_2}\right)\right]U + \frac{\partial^2 U}{\partial {u_3}^2} + k^2 U = 0 \tag{2.28}$$

$$\frac{1}{h_1 h_2}\left[\frac{\partial}{\partial u_1}\left(\frac{h_2}{h_1}\frac{\partial}{\partial u_1}\right)+\frac{\partial}{\partial u_2}\left(\frac{h_1}{h_2}\frac{\partial}{\partial u_2}\right)\right]V+\frac{\partial^2 V}{\partial {u_3}^2}+k^2V=0 \tag{2.29}$$

Note that equation 2.28 and equation 2.29 are nearly the Helmholtz Equation.

Since we are interested in finding the modes of a spherical (or nearly spherical) dielectric body, spherical polar coordinates will be a useful orthogonal coordinate system, and thus we take $u_1 \to \theta, u_2 \to \phi, u_3 \to r$.

Then the associated scale factors are

$$h_\theta = \left|\frac{\partial \vec{r}}{\partial \theta}\right| = \sqrt{r^2\cos^2\theta\cos^2\phi + r^2\cos^2\theta\sin^2\phi + r^2\sin^2\theta} = r \tag{2.30}$$

$$h_\phi = \left|\frac{\partial \vec{r}}{\partial \phi}\right| = \sqrt{r^2\sin^2\theta\sin^2\phi + r^2\sin^2\theta\cos^2\phi} = r\sin\theta \tag{2.31}$$

$$h_r = \left|\frac{\partial \vec{r}}{\partial r}\right| = \sqrt{\sin^2\theta\cos^2\phi + \sin^2\theta\sin^2\phi + \cos^2\theta} = 1 \tag{2.32}$$

where $\vec{r} = r\sin\theta\cos\phi\hat{x} + r\sin\theta\sin\phi\hat{y} + r\cos\theta\hat{z}$ in Cartesian coordinates. Applying the coordinates $u_1 \to \theta, u_2 \to \phi, u_3 \to r$ with scale factors h_θ, h_ϕ, h_r to equation 2.28 and equation 2.29 yields

$$\frac{1}{r^2\sin\theta}\left[\frac{\partial}{\partial\theta}\left(\sin\theta\frac{\partial}{\partial\theta}\right)+\frac{\partial}{\partial\phi}\left(\frac{1}{\sin\theta}\frac{\partial}{\partial\phi}\right)\right]U+\frac{\partial^2 U}{\partial r^2}+k^2U=0 \tag{2.33}$$

$$\frac{1}{r^2\sin\theta}\left[\frac{\partial}{\partial\theta}\left(\sin\theta\frac{\partial}{\partial\theta}\right)+\frac{\partial}{\partial\phi}\left(\frac{1}{\sin\theta}\frac{\partial}{\partial\phi}\right)\right]V+\frac{\partial^2 V}{\partial r^2}+k^2V=0 \tag{2.34}$$

Equation 2.33 and equation 2.34 are not scalar Helmholtz equations because the r-derivative terms are not scaled correctly. As such, these equations are separable, but difficult to solve. However, a simple substitution can be used to find analytic solutions for U and V.

Defining $U = krF$, substitution into equation 2.33 yields

$$\frac{1}{r^2\sin\theta}\left[\frac{\partial}{\partial\theta}\left(\sin\theta\frac{\partial F}{\partial\theta}\right)+\frac{1}{r^2\sin^2\theta}\frac{\partial^2 F}{\partial\phi^2}+\frac{1}{r^2}\frac{\partial}{\partial r}\left(r^2\frac{\partial F}{\partial r}\right)+k^2F=0\right. \tag{2.35}$$

Note that the substitution $V = krF$ yields the same result for equation 2.34. Now assume $F = R(r)\Theta(\theta)\Phi(\phi)$. Multiplying equation 2.35 by $r^2 \sin\theta$ and dividing by F yields

$$\frac{\sin}{\Theta}\frac{\mathrm{d}}{\mathrm{d}\theta}\left(\sin\theta\frac{\mathrm{d}\Theta}{\mathrm{d}\theta}\right) + \frac{1}{\Phi}\frac{\mathrm{d}^2\Phi}{\mathrm{d}\phi^2} + \frac{\sin^2\theta}{R}\frac{\mathrm{d}}{\mathrm{d}r}\left(r^2\frac{\mathrm{d}R}{\mathrm{d}r}\right) + k^2r^2\sin^2\theta = 0 \tag{2.36}$$

Equation 2.36 can only be satisfied if each of the four terms are equal to constants; this equation can now be separated into three parts to be solved individually. Due to its simplicity, we start with the equation for Φ:

$$\frac{1}{\Phi}\frac{\mathrm{d}^2\Phi}{\mathrm{d}\phi^2} = -m^2 \implies \Phi(\phi) = A_m e^{im\phi} + B_m e^{-im\phi} \tag{2.37}$$

Equation 2.36 becomes

$$\frac{\sin\theta}{\Theta}\frac{\mathrm{d}}{\mathrm{d}\theta}\left(\sin\theta\frac{\mathrm{d}\Theta}{\mathrm{d}\theta}\right) - m^2 + \frac{\sin^2\theta}{R}\frac{\mathrm{d}}{\mathrm{d}r}\left(r^2\frac{\mathrm{d}R}{\mathrm{d}r}\right) + k^2r^2\sin^2\theta = 0 \tag{2.38}$$

Dividing equation 2.38 by $\sin\theta$ yields

$$\frac{1}{\Theta\sin\theta}\frac{\mathrm{d}}{\mathrm{d}\theta}\left(\sin\theta\frac{\mathrm{d}\Theta}{\mathrm{d}\theta}\right) - \frac{m^2}{\sin^2\theta} + \frac{1}{R}\frac{\mathrm{d}}{\mathrm{d}r}\left(r^2\frac{\mathrm{d}R}{\mathrm{d}r}\right) + k^2r^2 = 0 \tag{2.39}$$

The r-terms and the θ-terms must be constants of opposite sign which sum to zero. Assuming the absolute value of the constant is $\ell(\ell+1)$, the equations for R and Θ are

$$\frac{1}{R}\frac{\mathrm{d}}{\mathrm{d}r}\left(r^2\frac{\mathrm{d}R}{\mathrm{d}r}\right) + k^2r^2 = \ell(\ell+1) \tag{2.40}$$

$$\frac{1}{\Theta\sin\theta}\frac{\mathrm{d}}{\mathrm{d}\theta}\left(\sin\theta\frac{\mathrm{d}\Theta}{\mathrm{d}\theta}\right) - \frac{m^2}{\sin^2\theta} = -\ell(\ell+1) \tag{2.41}$$

The equation for Θ is the associated Legendre equation, a generalization of the Legendre

equation. The solution is

$$\Theta(\theta) = C_{\ell m} P_\ell^m(\cos\theta) + D_{\ell m} Q_\ell^m(\cos\theta) \tag{2.42}$$

where the P_ℓ^m are called Legendre polynomials of the first kind and the Q_ℓ^m are called Legendre polynomials of the second kind.

Substitutions must be made in order to solve the equation for R. Let $R = f/\sqrt{kr}$ and $r = u/k$ (this u has no connection to the orthogonal coordinates in the beginning of this document). Equation 2.40 becomes

$$u\frac{\mathrm{d}}{\mathrm{d}u}\left(u\frac{\mathrm{d}f}{\mathrm{d}u}\right) + \left[u^2 - \left(\ell + \frac{1}{2}\right)^2\right] f = 0 \tag{2.43}$$

which is Bessel's equation with solution

$$\begin{aligned} f(u) &= \alpha_{q\ell m} J_{\ell+\frac{1}{2}}(u) + \beta_{q\ell m} N_{\ell+\frac{1}{2}}(u) \\ &= \alpha_{q\ell m} H^{(1)}_{\ell+\frac{1}{2}}(u) + \beta_{q\ell m} H^{(2)}_{\ell+\frac{1}{2}}(u) \end{aligned} \tag{2.44}$$

where $J_{\ell+\frac{1}{2}}(u)$ is a Bessel Function of the first kind, $N_{\ell+\frac{1}{2}}(u)$ is a Bessel Function of the second kind (also known as the Neumann function), $H^{(1)}_{\ell+\frac{1}{2}}(u) = J_{\ell+\frac{1}{2}}(u) + iN_{\ell+\frac{1}{2}}(u)$ is a Hankel function of the first kind and $H^{(2)}_{\ell+\frac{1}{2}}(u) = J_{\ell+\frac{1}{2}}(u) - iN_{\ell+\frac{1}{2}}(u)$ is a Hankel function of the second kind. A solution for $R(r)$ can now be determined

$$\begin{aligned} R(r) &= \alpha_{q\ell m}\frac{J_{\ell+\frac{1}{2}}(kr)}{\sqrt{kr}} + \beta_{q\ell m}\frac{N_{\ell+\frac{1}{2}}(kr)}{\sqrt{kr}} \\ &= \alpha_{q\ell m}\frac{H^{(1)}_{\ell+\frac{1}{2}}(kr)}{\sqrt{kr}} + \beta_{q\ell m}\frac{H^{(2)}_{\ell+\frac{1}{2}}(kr)}{\sqrt{kr}} \end{aligned} \tag{2.45}$$

For now, I will suppress the fact that the wavenumber $k = k_{q\ell m}$. The index q tracks the number of nodes in the radial component of the electric field. I will elaborate on $k = k_{q\ell m}$ in section 2.2.4.

Recalling the relationship $U = krF$, a solution for U(or, equivalently, V) is given by

$$U = \left(\alpha_{q\ell m}\sqrt{kr}H^{(1)}_{\ell+\frac{1}{2}}(kr) + \beta_{q\ell m}\sqrt{kr}H^{(2)}_{\ell+\frac{1}{2}}(kr)\right) \times \left(C_{\ell m}P^m_\ell(\cos\theta) + D_{\ell m}Q^m_\ell(\cos\theta)\right)\left(A_m e^{im\phi} + B_m e^{-im\phi}\right) \tag{2.46}$$

In order to make U (or V) a Borgnis potential whose derivatives provide an appropriate representation of the fields inside the dielectric sphere, some coefficients should be set to zero. In general, the spatial distribution of the field in the dielectric sphere contains $\theta = 0$ and $\theta = \pi$. However, at $\theta = 0, \pi$ the associated Legendre polynomial of the second kind, $Q^m_\ell(\cos\theta)$ diverges so we take $D_{\ell m} = 0$. Furthermore, the origin of the spherical polar coordinate system is at the center of the dielectric sphere, so the fields cannot diverge at $r = 0$. As a result, since $N_{\ell+\frac{1}{2}}(kr)$ has divergent behavior at the origin, we set $\beta_{q\ell m} = 0$, so the radial dependence inside the sphere is described by $J_{\ell+\frac{1}{2}}(kr)$.

Next, we apply the general solutions for U and V to the case of a dielectric sphere of radius a. For $r < a$, the index of refraction is $n_1 = \sqrt{\epsilon_{\rm r}\mu_{\rm r}}$ and in what follows we will assume $\mu_{\rm r} = 1$. For $r > a$, we have vacuum so $n_0 = 1$.

Inside the sphere, one can use the following as a solution for V

$$\begin{aligned} V^{(\rm in)} &= A^{(\rm in)}_{q\ell m}\sqrt{k^{(\rm in)}r}J_{\ell+\frac{1}{2}}(k^{(\rm in)}r)P^m_\ell(\cos\theta)e^{-im\phi} \\ &= A^{(\rm in)}_{q\ell m}\sqrt{k^{(\rm in)}r}J_{\ell+\frac{1}{2}}(k^{(\rm in)}r)Y^m_\ell(\theta,\phi) \end{aligned} \tag{2.47}$$

where $Y^m_\ell(\theta,\phi)$ are spherical harmonics, $k^{(\rm in)} = n_1 k_0$ and k_0 is the wavenumber in vacuum. On the other hand, outside of the dielectric sphere ($r > a$), V takes the following form

$$V^{(\rm out)} = A^{(\rm out)}_{q\ell m}\sqrt{k_0 r}H^{(1)}_{\ell+\frac{1}{2}}(k_0 r)Y^m_\ell(\theta,\phi) \tag{2.48}$$

As I explicitly show in section 2.2.4, in the limit $r \to \infty, R(r) \sim \sin(k_0 r)/\sqrt{k_0 r}$, which corresponds to radiation outwards from the sphere and is in agreement with the asymptotic

behavior of $H^{(1)}_{\ell+\frac{1}{2}}(k_0 r)$ for $r \to \infty$. However, for $r \to \infty$, $H^{(2)}_{\ell+\frac{1}{2}}(k_0 r)$ is asymptotic to a waveform which radiates inwards, toward the sphere, which should not occur for a resonant mode. As a result, we take $\beta_{q\ell m} \to 0$ outside the dielectric sphere. Note that U takes the same form as V inside and outside of the dielectric sphere.

The boundary conditions between the two regions are usually given in terms of the fields $\mathbf{H}$ and $\mathbf{E}$, rather than U and V. For a sphere with radius a the boundary conditions are

$$B^{(\text{in})}_{\perp}|_{r=a} = B^{(\text{out})}_{\perp}|_{r=a} \tag{2.49}$$

$$D^{(\text{in})}_{\perp}|_{r=a} = D^{(\text{out})}_{\perp}|_{r=a} \tag{2.50}$$

$$E^{(\text{in})}_{\parallel}|_{r=a} = E^{(\text{out})}_{\parallel}|_{r=a} \tag{2.51}$$

$$H^{(\text{in})}_{\parallel}|_{r=a} = H^{(\text{out})}_{\parallel}|_{r=a} \tag{2.52}$$

Solving these boundary value problems allows us to find the vacuum wavenumber k_0 associated with these modes, and hence the corresponding angular frequency $\omega = ck_0$.

TE Modes

We can satisfy the boundary conditions in two ways. In the first, we take $E_r = 0, H_r \neq 0$ (this corresponds to transverse electric (TE) modes). For these modes, $U = 0, V \neq 0$. Using equations 2.22-2.27

$$E_\theta = i\omega\mu \frac{1}{r\sin\theta}\frac{\partial V}{\partial \varphi} \tag{2.53}$$

$$E_\phi = \mathrm{i}\omega\mu \frac{1}{r}\frac{\partial V}{\partial \theta} \tag{2.54}$$

$$E_r = 0 \tag{2.55}$$

The radial component of the auxiliary field must satisfy equation 2.27.

$$H_r = \frac{\partial^2 V}{\partial r^2} + k^2 V \tag{2.56}$$

Using equation 2.34,

$$H_r = \frac{1}{r^2 \sin\theta}\left[\frac{\partial}{\partial\theta}\left(\sin\theta\frac{\partial}{\partial\theta}\right) + \frac{\partial}{\partial\phi}\left(\frac{1}{\sin\theta}\frac{\partial}{\partial\phi}\right)\right]V \tag{2.57}$$

Maxwell's equations applied to the boundary between a dielectric sphere and its surrounding require that the perpendicular component of the magnetic induction **B** must be continuous across the boundary ($r = a$). Substituting V into equation 2.57 and applying the condition $\mu_{\mathrm{r}} H_r^{(\mathrm{in})} = H_r^{(\mathrm{out})}$ (this is the auxiliary field, **H**, not a Hankel function) at the boundary $r = a$ yields

$$\mu_{\mathrm{r}}\sqrt{n_1 k_0 a}\,J_{\ell+\frac{1}{2}}(n_1 k_0 a) = B_{q\ell m}^{(\mathrm{out})}\sqrt{k_0 a}\,H_{\ell+\frac{1}{2}}^{(1)}(k_0 a) \tag{2.58}$$

Both E_θ and E_ϕ and their derivatives must be continuous across the boundary $r = a$, but both components are parallel to the interface so each component provides the same boundary condition information as the other. In order to achieve our goal of finding values of k_0 that satisfy equation 2.58, it suffices to write the boundary condition equation for either E_θ or E_ϕ. In combination with the boundary condition equation 2.58, we will be able to cancel the amplitude $B^{(\mathrm{out})}$, and derive an equation with only k_0 unknown. Matching the spatial derivative of E_θ across the boundary $r = a$ yields

$$\left[\sqrt{n_1 k_0 a}\,J_{\ell+\frac{1}{2}}(n_1 k_0 a)\right]' = B_{q\ell m}^{(\mathrm{out})}\left[\sqrt{k_0 a}\,H_{\ell+\frac{1}{2}}^{(1)}(k_0 a)\right]' \tag{2.59}$$

where the prime denotes differentiation with respect to argument of the Bessel or Hankel functions ($k_0 a$ or ka). Dividing equation 2.58 by equation 2.59 removes $B_{q\ell m}^{(\mathrm{out})}$ and yields the following characteristic equation that defines the allowed values of k_0, and thus the electromagnetic mode frequencies

$$\frac{\left[\sqrt{n_1 k_0 a}\,J_{\ell+\frac{1}{2}}(n_1 k_0 a)\right]'}{\sqrt{n_1 k_0 a}\,J_{\ell+\frac{1}{2}}(n_1 k_0 a)} = \sqrt{\frac{\mu_{\mathrm{r}}}{\epsilon_{\mathrm{r}}}}\frac{\left[\sqrt{k_0 a}\,H_{\ell+\frac{1}{2}}^{(1)}(k_0 a)\right]'}{\sqrt{k_0 a}\,H_{\ell+\frac{1}{2}}^{(1)}(k_0 a)} \tag{2.60}$$

There are countably infinitely many k_0 that satisfy this equation, and they are indexed by q, where $q-1$ is the number of zeros of the Bessel functions occurring for $r < a$. Thus, one must specify q when identifying values of the wave number that satisfy equation 2.60. For each value of q, there are two additional indices: $\ell \in \mathbb{N}$ (including 0) and $m \in \mathbb{Z}$, where $|m| \leq \ell$. Consequently, for each q there are $2(\ell+1)$ degenerate modes with wavenumber k_0.

It is also important to note that in this derivation, U, V, $\mathbf{E}$, $\mathbf{H}$ and k_0 are complex-valued, which is unphysical because the electromagnetic fields and the wavenumber are real-valued in nature. Moreover, as derived above, the spectrum of $k_0 \in \mathbb{C}$ is discrete. This is also unphysical, as in actuality, electromagnetic radiation with any $k_0 \in \mathbb{R}$ can occupy the space in and around the dielectric sphere. However, not all electromagnetic waves with $k_0 \in \mathbb{R}$ are guaranteed to have significant amplitude within the sphere. Only a smaller set of electromagnetic modes with $\ell \sim k_0 a$ and small q have large amplitudes in the dielectric sphere; these correspond to the "nearly bound" modes of the sphere. We restricted our solution to these modes (described phenomenologically by $k_0 \in \mathbb{C}$) by setting $\beta_{q\ell m} = 0$ outside the sphere. Solving equation 2.60 over the complex numbers is equivalent to finding the poles of the scattering matrix.

If we define

$$Q_{\text{opt}} = \frac{\text{Re}[k_0]}{\text{Im[k}_0\text{]}} \tag{2.61}$$

then when $Q_{\text{opt}} \gg 1$, $\text{Re}[k_0]$ is understood to give the frequency of oscillations of a (nearly) bound mode, while $\text{Im}[k_0]$ can be understood to give the mode's decay rate [74].

TM modes

Following the same steps for $H_r = 0, E_r \neq 0$, (corresponding to the transverse magnetic (TM) modes) we have $U \neq 0, V = 0$. Using equations 2.22-2.27

$$H_\theta = \text{i}\omega\epsilon \frac{1}{r\sin\theta}\frac{\partial U}{\partial \varphi} \tag{2.62}$$

$$H_\phi = \mathrm{i}\omega\epsilon\frac{1}{r}\frac{\partial U}{\partial\theta} \tag{2.63}$$

$$H_r = 0 \tag{2.64}$$

Similar to the derivation of TE modes, inside the sphere,

$$U^{(\mathrm{in})} = A^{(\mathrm{in})}_{q\ell m}\sqrt{k^{(\mathrm{in})}r}J_{\ell+\frac{1}{2}}(k^{(\mathrm{in})}r)Y^m_\ell(\theta,\phi) \tag{2.65}$$

while outside the sphere U is given by

$$U^{(\mathrm{out})} = A^{(\mathrm{out})}_{q\ell m}\sqrt{k_0 r}H^{(1)}_{\ell+\frac{1}{2}}(k_0 r)Y^m_\ell(\theta,\phi) \tag{2.66}$$

The radial component of the electric field must satisfy equation 2.24.

$$E_r = \frac{\partial^2 U}{\partial r^2} + k^2 U \tag{2.67}$$

Using equation 2.33,

$$E_r = \frac{1}{r^2\sin\theta}\left[\frac{\partial}{\partial\theta}\left(\sin\theta\frac{\partial}{\partial\theta}\right) + \frac{\partial}{\partial\phi}\left(\frac{1}{\sin\theta}\frac{\partial}{\partial\phi}\right)\right]U \tag{2.68}$$

Similar to the case for TE modes, Maxwell's equations applied to a boundary between a dielectric sphere and its surroundings require that the perpendicular component of the electric displacement **D** must be continuous across the boundary. Substituting the expressions for U inside and outside of the sphere into equation 2.68 and applying the condition $\epsilon_{\mathrm{r}}E_r^{(\mathrm{in})} = E_r^{(\mathrm{out})}$ at the boundary ($r = a$) yields

$$\epsilon_{\mathrm{r}}\sqrt{n_1 k_0 a}J_{\ell+\frac{1}{2}}(n_1 k_0 a) = A^{(\mathrm{out})}_{q\ell m}\sqrt{k_0 a}H^{(1)}_{\ell+\frac{1}{2}}(k_0 a) \tag{2.69}$$

Furthermore, both H_θ and H_ϕ and their derivatives must be continuous across the boundary $r = a$ in the absence of surface charge on the dielectric sphere. For the reason-

ing provided in the TE modes section, only the boundary equation for H_θ will be written explicitly. Matching the derivative of H_θ across the boundary $r = a$ yields

$$\left[\sqrt{n_1 k_0 a} J_{\ell+\frac{1}{2}}(n_1 k_0 a)\right]' = A^{(\text{out})}_{q\ell m}\left[\sqrt{k_0 a} J_{\ell+\frac{1}{2}}(k_0 a)\right]' \tag{2.70}$$

Again, dividing to eliminate $A^{(\text{out})}_{q\ell m}$ we have

$$\frac{\left[\sqrt{n_1 k_0 a} J_{\ell+\frac{1}{2}}(n_1 k_0 a)\right]'}{\sqrt{n_1 k_0 a} J_{\ell+\frac{1}{2}}(n_1 k_0 a)} = \sqrt{\frac{\epsilon_\text{r}}{\mu_\text{r}}} \frac{\left[\sqrt{k_0 a} H^{(1)}_{\ell+\frac{1}{2}}(k_0 a)\right]'}{\sqrt{k_0 a} H^{(1)}_{\ell+\frac{1}{2}}(k_0 a)} \tag{2.71}$$

which has no solutions for $k_0 \in \mathbb{R}$. However, there are a countably infinite number $k_0 \in \mathbb{C}$ that satisfy this characteristic equation. Thus, one must specify a root number, q when identifying values of the wavenumber that satisfy equation 2.71. Furthermore, the resulting k_0 exhibit the same $(2\ell + 1)$-fold degeneracy that was described in the TE modes section.

2.2.4 Solving the WGM Characteristic Equations

Using Bessel function identities for derivatives of the Bessel function, one can re-express 2.60 and 2.71 as root-finding problems. For TE modes

$$\begin{aligned} H^{(1)}_{\ell+\frac{1}{2}}(k_0 a)\left[J_{\ell-\frac{1}{2}}(n_1 k_0 a) - \frac{\ell}{n_1 k_0 a} J_{\ell+\frac{1}{2}}(n_1 k_0 a)\right] \\ - \sqrt{\frac{\mu_\text{r}}{\epsilon_\text{r}}} J_{\ell+\frac{1}{2}}(n_1 k_0 a)\left[H^{(1)}_{\ell-\frac{1}{2}}(k_0 a) - \frac{\ell}{k_0 a} H^{(1)}_{\ell+\frac{1}{2}}(k_0 a)\right] = 0 \end{aligned} \tag{2.72}$$

and for TM modes

$$\begin{aligned} H^{(1)}_{\ell+\frac{1}{2}}(k_0 a)\left[J_{\ell-\frac{1}{2}}(n_1 k_0 a) - \frac{\ell}{n_1 k_0 a} J_{\ell+\frac{1}{2}}(n_1 k_0 a)\right] \\ - \sqrt{\frac{\epsilon_\text{r}}{\mu_\text{r}}} J_{\ell+\frac{1}{2}}(n_1 k_0 a)\left[H^{(1)}_{\ell-\frac{1}{2}}(k_0 a) - \frac{\ell}{k_0 a} H^{(1)}_{\ell+\frac{1}{2}}(k_0 a)\right] = 0 \end{aligned} \tag{2.73}$$

TM/TE	q	ℓ	$\omega_{\rm opt}/2\pi$ [$\times 10^{14}$ Hz]	$Q_{\rm opt}$ [$\times 10^{13}$]	$\mathcal{F}$ [$\times 10^{9}$]
TM	1	6,430	2.998708	756	1,172
TE	1	6,430	2.998610	492	762
TM	1	6,429	2.998243	834	1,292
TE	1	6,429	2.998145	6,693	10,362
TM	1	6,428	2.997778	16,615	25,725
TE	1	6,428	2.997680	1,318	2,042
TM	1	6,427	2.997313	3,274	5,070
TE	1	6,427	2.997215	1,231	1,906
TM	2	6,404	2.998568	380	589
TE	2	6,404	2.998479	808	1,250
TM	2	6,403	2.998103	840	1,300
TE	2	6,403	2.998013	381	590
TM	2	6,402	2.997637	992	1,536
TE	2	6,402	2.997548	372	576
TM	2	6,401	2.997171	2,364	3,661
TE	2	6,401	2.997082	559	866
TM	3	6,383	2.998573	2.93	4.55
TE	3	6,383	2.998492	3.10	4.80
TM	3	6,382	2.998107	2.92	4.52
TE	3	6,382	2.998026	3.07	4.76
TM	3	6,381	2.997641	2.91	4.51
TE	3	6,381	2.997560	3.06	4.75
TM	3	6,380	2.997175	2.88	4.47
TE	3	6,380	2.997094	3.06	4.74

Table 2.1: Tabulated optical WGM parameters with wavelengths near $\lambda = 1$ μm for a drop with $a = 1$ mm.

It is straightforward to implement a computer program to numerically find the roots of equation 2.72 and equation 2.73, and thus find the wavenumber (or equivalently, the frequency) associated with a given WGM. Note that the equation has no dependence on the azimuthal mode index m, reflecting the $(2\ell + 1)$-fold degeneracy of WGMs for a dielectric sphere. There exists multiple roots that satisfy these equations for the same value of ℓ, which are indexed by the radial mode number q. Furthermore, there exists a mode with the smallest value of k_0 allowable for a dielectric sphere of radius a, that can be obtained from solving these equations. This mode is the most tightly confined WGM, and thus the WGM which exhibits the smallest amount of leakage out of the dielectric sphere. This smallest-k_0

root is given the index $q = 1$.

Table 2.1 contains parameters for WGMs with $\lambda \approx 1$ μm, which were determined by solving equations 2.72 and 2.73.

Insights on WGMs in a Dielectric Sphere

In what follows, I explain the important features of WGMs using a heuristic picture of WGMs based on a physically intuitive combination of ray optics and paraxial wave optics. For large spheres (i.e. $r \gg \lambda$) and small q, the light confined within the WGM propagates close to the surface and traverses a distance $2\pi a$ in a single round trip. If one round trip equals ℓ wavelengths, a running electromagnetic wave is resonant with the dielectric sphere; mathematically, $2\pi a = \ell\frac{\lambda}{n_1}$. In consideration of a photon with momentum $p = \hbar k = \hbar\frac{2\pi n_1}{\lambda}$, if its angle of incidence to the dielectric interface is $\approx \pi/2$ with respect to a diameter line, its angular momentum $\mathbf{L}$ is such that $|\mathbf{L}| = ap = a\hbar\frac{2\pi n_1}{\lambda} = \hbar\ell$. Thus, ℓ can be identified as the angular momentum number. Then, $\ell = n_1\frac{2\pi a}{\lambda}\sin\theta$, and due to TIR – with critical angle $\theta_c = \sin^{-1}(n_0/n_1)$ – the angular momentum number is bounded such that $\frac{2\pi a}{\lambda} \leq \ell \leq n_1\frac{2\pi a}{\lambda}$. Thus, for $\frac{2\pi a}{\lambda} \gg 1$, ℓ and $\frac{2\pi a}{\lambda} = k_0 a$ are, at least, of the same order, if not nearly exactly equal. Consequently, one associates ℓ with the number of wavelengths that fit along the circumference of the dielectric sphere.

For each value of ℓ, there are $2\ell + 1$ degenerate optical WGM modes (corresponding to the allowed values of m), which reflects the ray-optics picture of optical WGMs traversing different great circles of the dielectric sphere. Note that in the spherical coordinate system used here, $\theta = 0$ refers to the north pole of the sphere, while $\theta = \pi/2$ refers to the sphere's equator; in the ray-optics picture, the WGM with $\ell = m$ traverses the great circle along the equator. Additionally, each value of ℓ has an index q associated with it, which corresponds to a WGM with $q - 1$ radial nodes of the electric field within the sphere. As mentioned in sections 2.2.3 and 2.2.3, this value q arises from solving the characteristic equation for some specific value of ℓ; there will be multiple solutions labeled by q that correspond

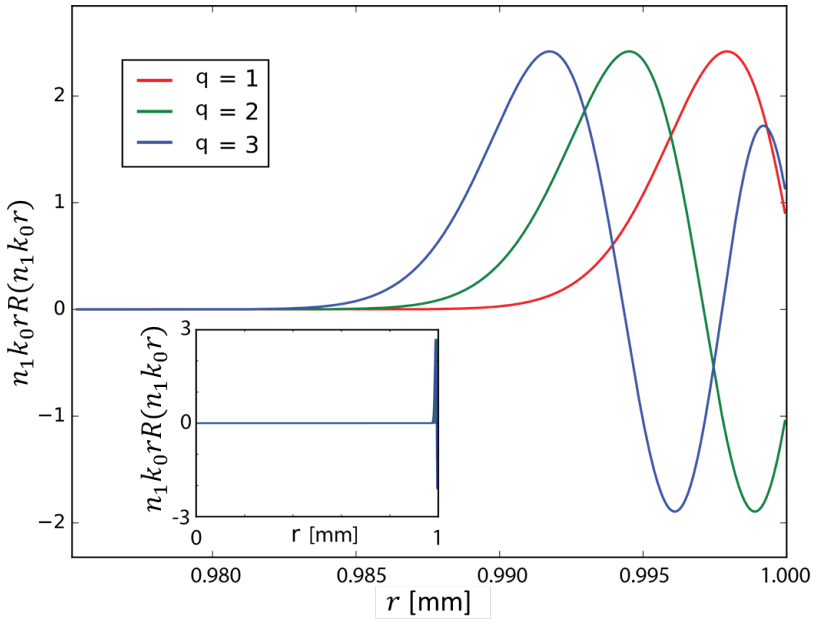

Figure 2.4: The radial component of the Borgnis potential $n_1 k_0 r R(r)$ for WGMs with $q = 1, 2, 3$ in a helium drop with $n_1 = 1.028$, $a \approx 1$ mm and $m = \ell \sim n_1 k_0 a \approx 6,000$. The inset shows that the potential is zero until just near the drop's periphery.

to different values of $k_0 = k_{q\ell m}$, and thus correspond to different radial functions with different numbers of radial nodes. The solutions with $q = 1$ correspond to the lowest value of k_0 that solves the characteristic equation, and to WGMs with no nodes in the electric field. These WGMs exhibit the tightest confinement near the periphery of the sphere. The next set of solutions have $q = 2$, and thus have one radial node. The third set of solutions have $q = 3$, and thus have two radial nodes, and so on. As it turns out, the lowest-q solutions exhibit the lowest leakage out of the dielectric sphere, with the leakage rapidly increasing with increasing q. Figure 2.4 shows a plot of the full radial part of the Borgnis potential $n_1 k_0 r R(kr)$ for WGMs with $q = 1, 2, 3$ in a helium drop with $n_1 = 1.028$, $a = 1$ mm and $m = \ell \sim k_0 a \approx 6000$. The inset shows $n_1 k_0 r R(kr)$ over the entire drop radius, and illustrates that the electromagnetic field is indeed tightly confined near the periphery of the sphere, as we would expect for WGMs with small q and large ℓ.

Figure 2.5 shows polar plots (r, θ) of the $\ell = 10, m = 10$ TM WGM electric field intensity in a helium drop with $n_1 = 1.028$, $a = 1$ mm and $\lambda \approx 100$ μm for $q = 1$

(figure 2.5a), $q = 2$ (figure 2.5b $q = 3$figure 2.5c) and $q = 4$ (figure 2.5d). The $\ell = 10$ mode is shown solely for illustrative purposes; this would correspond to $\lambda = 100$ μm. The mode with $\ell \sim 2\pi n_1 a/\lambda$ is tightly confined to the periphery and difficult to see clearly in a plot that is to scale. The $\ell = 10$ mode shows the important qualitative features of the WGM. One should just note that as ℓ increases, the electromagnetic field for $q = 1, m = \ell$ becomes more and more tightly confined near the periphery and near $\theta = \pi/2$. Figure 2.6 shows polar plots (r, θ) of the $q = 1, \ell = 10$ TM WGM electric field intensity with $\lambda = 100$ μm within in a helium drop with $n_1 = 1.028$, $a = 1$ mm for with $m = \pm 10$ (figure 2.6a), $m = \pm 9$ (figure 2.6b), $m = \pm 8$ (figure 2.6c). Finally, figure 2.7 shows a polar plot (r, ϕ) of the TE WGM electric field intensity with $q = 1, \ell = 10, m = 10$. If one referred to the (r, θ) plot as a "side view" then the (r, ϕ) plot is the "top view."

By inspecting figure 2.5, figure 2.6 and figure 2.7, one will notice that the WGM with the smallest mode volume corresponds to the mode with $m = \ell$. Thus, for optomechanics experiments that benefit from large $\mathcal{F}$ and small mode volume (e.g. our future optomechanics experiments with levitated drops), the optimal WGM is the one with $\lambda \ll a$, $q = 1, \ell \sim 2\pi n_1 a/\lambda, m = \ell$.

To further emphasize the relationship between ℓ and the confinement of optical WGMs, figure 2.8 shows polar plots (r, θ) of the $\ell = 6,232, m = 6,232$ TM WGM electric field intensity within in a helium drop with $n_1 = 1.028$, $a = 1$ mm for (figure 2.8a) $q = 1, \lambda \approx 1.000$ μm, (figure 2.8b) $q = 2, \lambda \approx 0.999$ μm, (figure 2.8c) $q = 3, \lambda \approx 0.996$ μm and (figure 2.8d) $q = 4, \lambda \approx 0.993$ μm. Figure 2.9 shows polar plots (r, θ) of the $q = 1, \ell = 6,232$ TM WGM electric field intensity with $\lambda = 1\mu$m within in a helium drop with $n_1 = 1.028$, $a = 1$ mm for with (figure 2.9a) $m = \pm 6,232$, (figure 2.9b) $m = \pm 6,231$, (figure 2.9c) $m = \pm 6,230$ and (figure 2.9d) $m = \pm 6,229$. Lastly, figure 2.10 shows a polar plot (r, ϕ) of the TM WGM electric field intensity with $q = 1, \ell = 6,232, m = 6,232$.

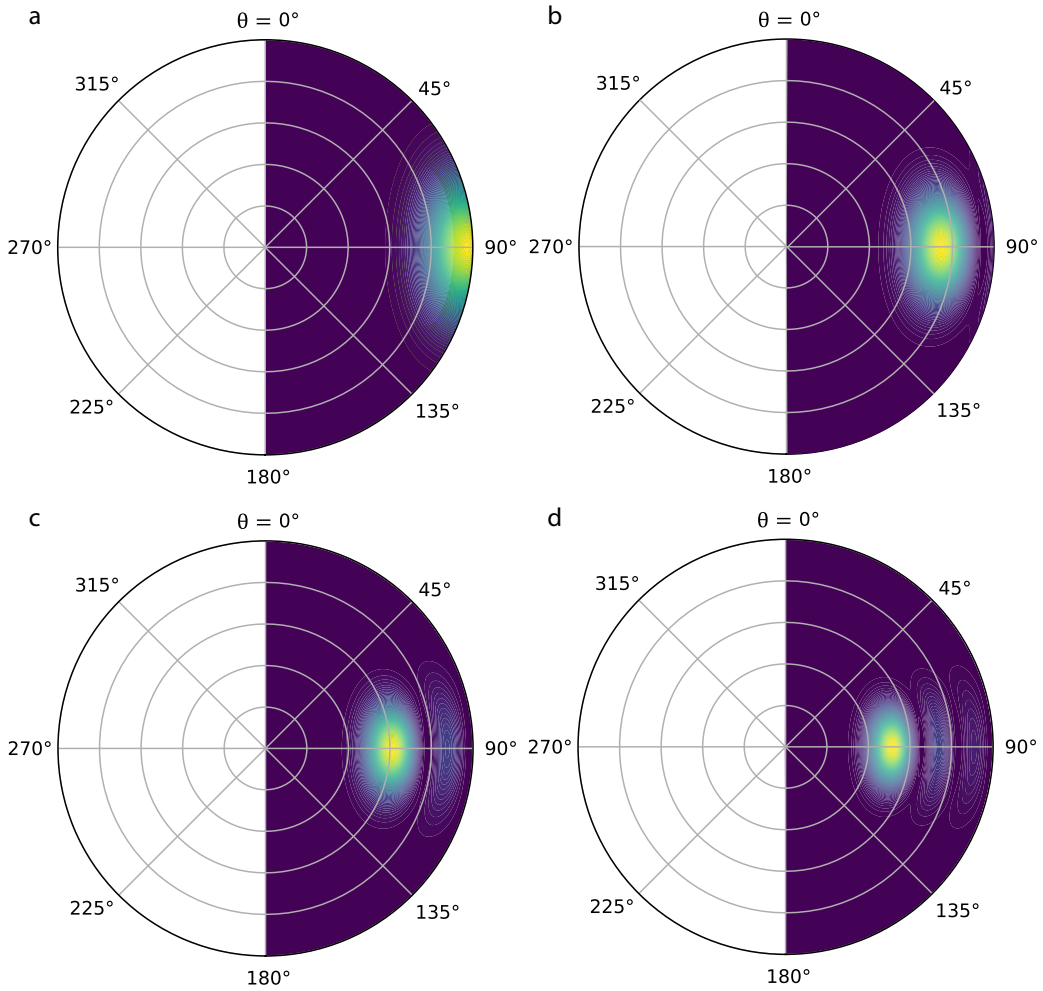

Figure 2.5: A plot of the $\ell = 10, m = 10$ TM WGM electric field intensity with $\lambda \approx 100$ μm within a helium drop with $n_1 = 1.028$ and $a = 1$ mm for (a) $q = 1$, (b) $q = 2$, (c) $q = 3$ and (d) $q = 4$.

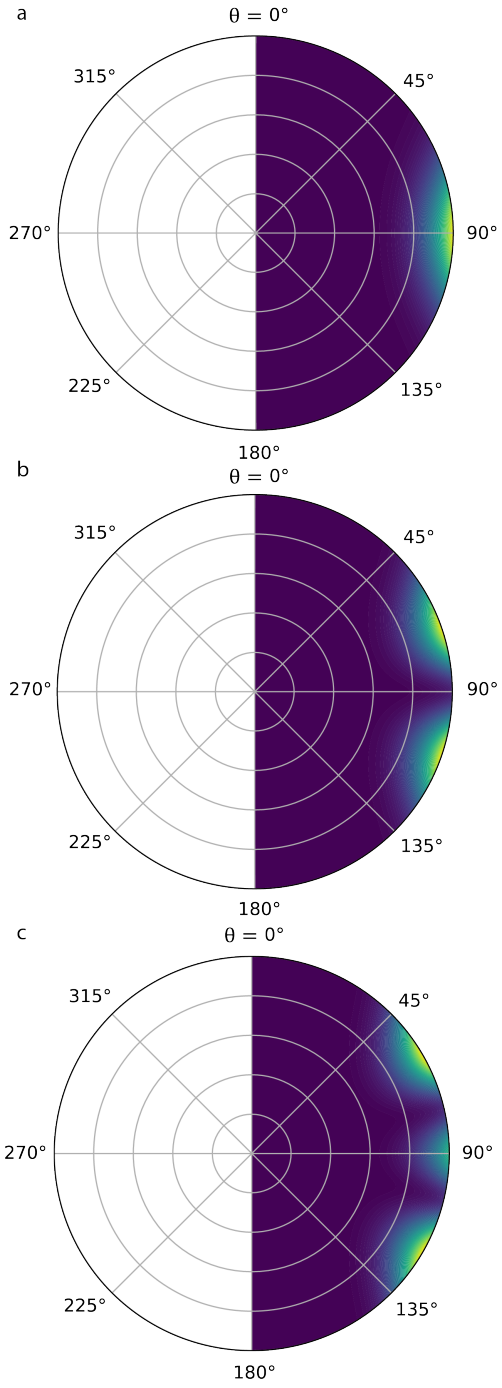

Figure 2.6: A plot of the $q = 1, \ell = 10$ TM WGM electric field intensity with $\lambda = 100$ μm within a helium drop with $n_1 = 1.028$ and $a = 1$ mm for (a) $m = \pm 10$, (b) $m = \pm 9$, (c) $m = \pm 8$.

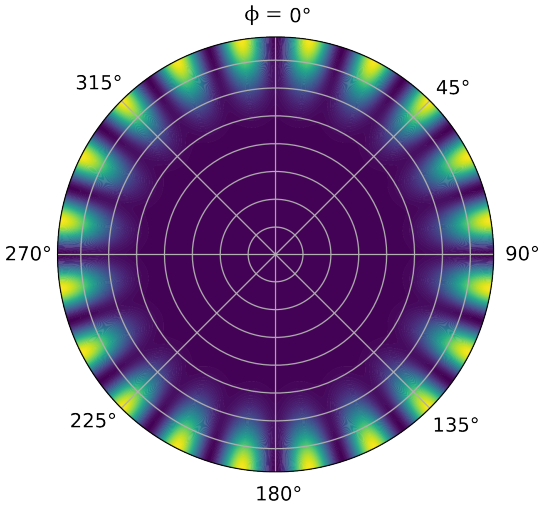

Figure 2.7: The TM WGM electric field intensity ($\theta = \pi/2$) for a WGM with $\lambda = 100$ μm and $q = 1, \ell = 10, m = 10$ within a helium drop with $n_1 = 1.028$, and $a = 1$ mm.

WGM Radiation Loss and Pseudo-Bound States

The characteristic equations 2.60 and 2.71 define complex wavenumbers k_0, which arise due to the fact that a WGM will decay due to radiation loss (also known as bending loss). Intuition about the leakage of WGMs can be gained by studying the behavior of the full r-coordinate dependence of the Borgnis potential $Z(r) = krR(kr)$ for $r \to \infty$. The differential equation that $Z(kr)$ must satisfy can be written in the following form

$$\left(\frac{\mathrm{d}^2}{\mathrm{d}r^2} + (n_1^2(r) - n_0^2(r))k_0^2 - \frac{\ell(\ell+1)}{r^2}\right) Z(r) = n_0^2(r)k_0^2 Z(r) \tag{2.74}$$

where $n_1(r)$ is the spatially-dependent, piecewise-defined index of refraction of the dielectric sphere, $n_0(r)$ is the spatially-dependent, piecewise-defined index of refraction of the medium surrounding the dielectric sphere, and k_0 is the wavenumber in vacuum.

One can make a useful mathematical analogy between equation 2.74 and the one-dimensional time-independent Schrödinger equation (TISE) $\hat{H}\Psi = E\Psi$. The term on the left hand side of equation 2.74 that multiplies $Z(r)$ corresponds to $\hat{H}$ from the TISE, which I will now refer to as H_{eff}. On the right hand side of equation 2.74, $n_0^2 k_0^2$ corresponds to E from the TISE, which I will refer to as the pseudoenergy. The second-derivative term

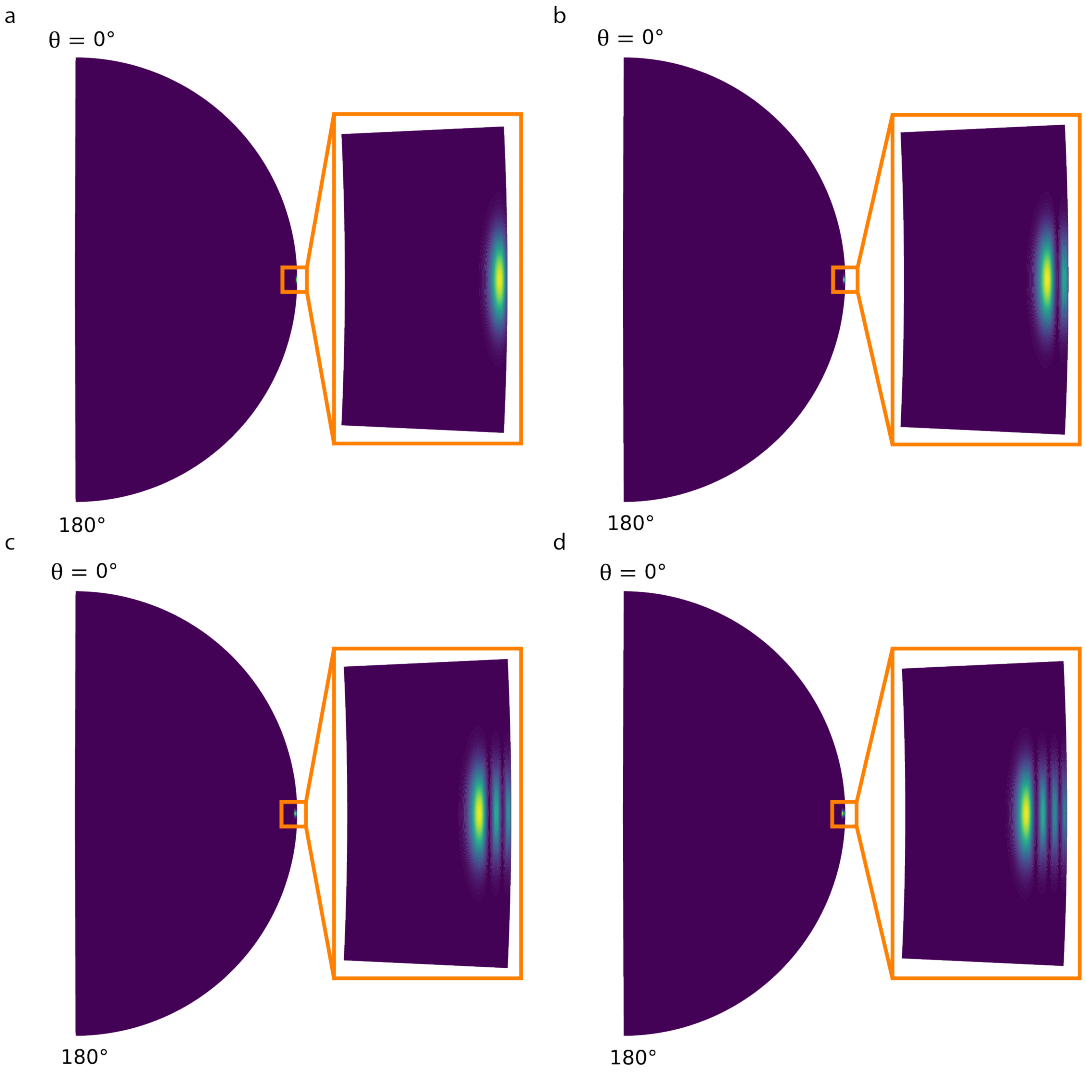

Figure 2.8: A plot of the $\ell = 6,232, m = 6,232$ TM WGM electric field intensity within a helium drop with $n_1 = 1.028$ and $a = 1$ mm for (a) $q = 1, \lambda \approx 1.000$ μm, (b) $q = 2, \lambda \approx 0.999$ μm, (c) $q = 3, \lambda \approx 0.996$ μm and (d) $q = 4, \lambda \approx 0.993$ μm.

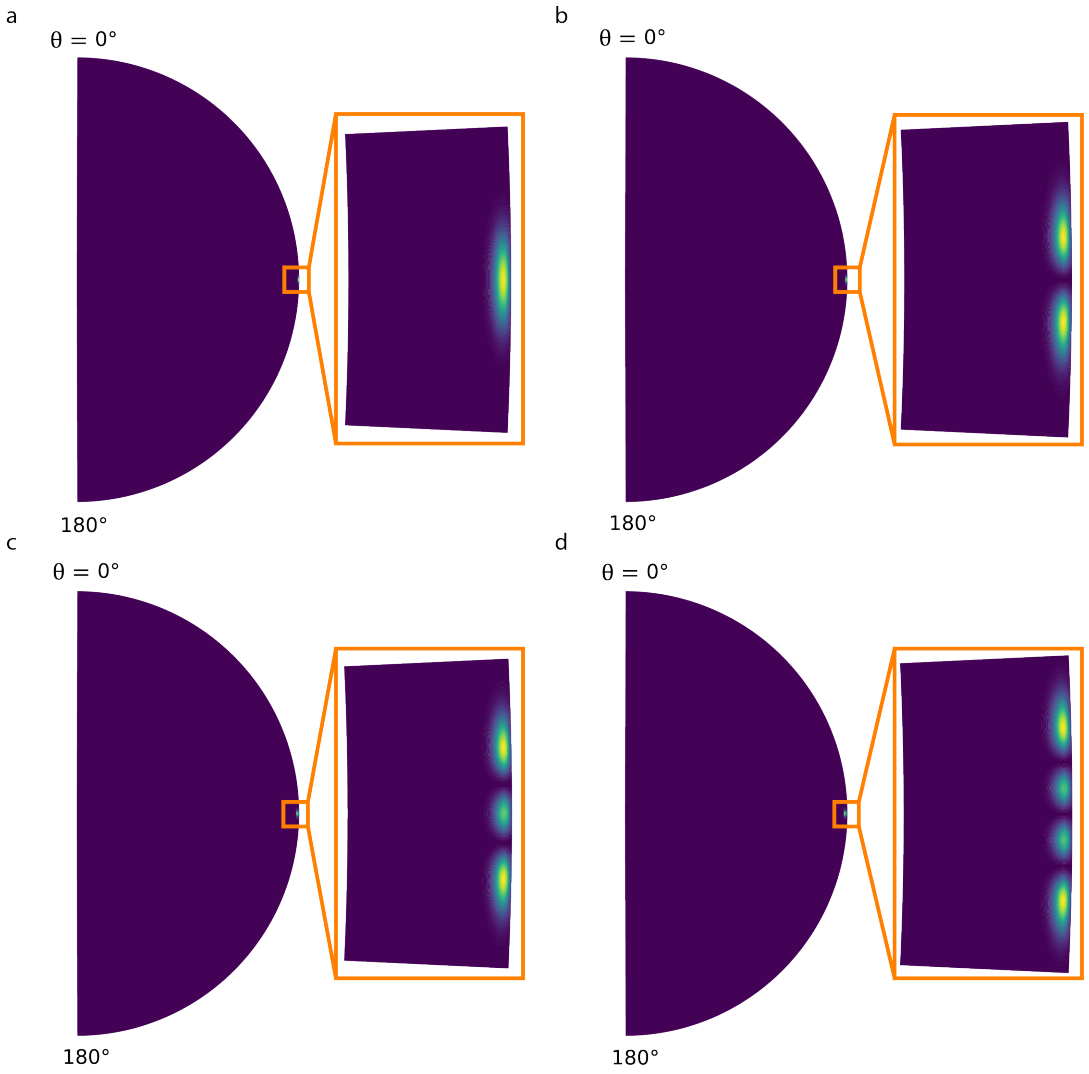

Figure 2.9: A plot of the $q = 1, \ell = 6, 232$ TM WGM electric field intensity with $\lambda = 1$ μm within a helium drop with $n_1 = 1.028$ and $a = 1$ mm for (a) $m = \pm 6, 232$, (b) $m = \pm 6, 231$, (c) $m = \pm 6, 230$ and (d) $m = \pm 6, 229$.

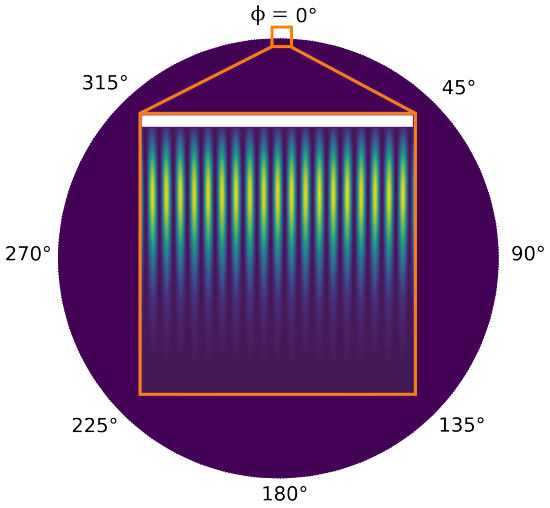

Figure 2.10: A plot of the TM WGM electric field intensity ($\theta = \pi/2$) for a WGM with $\lambda = 1$ μm and $q = 1, \ell = 6, 232, m = 10$ within a helium drop with $n_1 = 1.028$, and $a = 1$ mm.

in H_{eff} corresponds to kinetic energy in the TISE. The two remaining terms in H_{eff} correspond to the potential energy in the TISE, which I will refer to as the pseudopotential V_{eff}. We may interpret the second term in V_{eff} as the centrifugal barrier that arises if the spatial coordinate r is in fact the radial coordinate in a spherical coordinate system and we have performed separation of variables to focus on a component of the full wave function with angular momentum $\hbar\ell$. In this case, the first term is a radially-varying potential energy.

The pseudopotential $V_{\text{eff}}(r)$ is given by

$$V_{\text{eff}}(r) = (n_0^2(r) - n_1^2(r))k_0^2 + \frac{\ell(\ell+1)}{r^2} \tag{2.75}$$

Figure 2.11 includes a plot of $V_{\text{eff}}(r)$. Also shown in the figure are the radial components of the Borgnis potential for WGMs with $q = 1, 2, 3$.

Because $V_{\text{eff}}(r) \to 0$ as $r \to \infty$ (and is nowhere < 0), there are no true bound states of electromagnetic modes in the dielectric sphere, and the higher pseudoenergy modes (larger q) exhibit faster leakage out of the dielectric sphere than the lower pseudoenergy modes (smaller q) in part because the pseudopotential barrier becomes thinner at higher pseudoenergies. Also, higher pseudoenergy makes it easier to tunnel through a barrier of constant

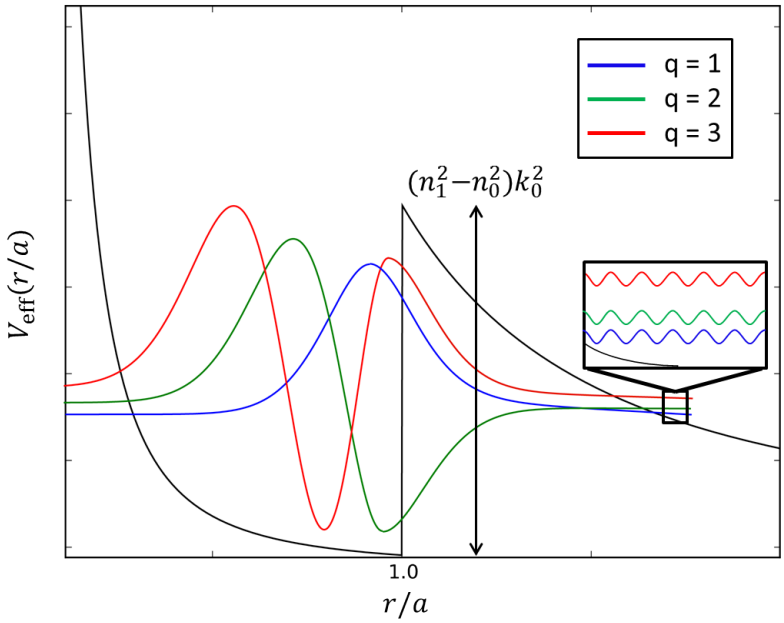

Figure 2.11: Black: The pseudopotential $V_{\text{eff}}(r/a)$ a WGM experiences as a function of position r/a, where r is the radial coordinate and a is the dielectric sphere's radius. Blue, Green, Red: The radial component of the real part of the Borgnis potential for WGMs with $q = 1, 2, 3$. The WGMs have different vertical offsets relative to $V_{\text{eff}}(r/a)$ at large r/a because modes with higher q (higher leakage) have will have more energy outside the sphere.

height. The Hankel function description of the WGMs outside the sphere also shows the lack of a true bound state in that the Hankel functions decay over a wide range of r, but finally oscillate again as $r \to \infty$. Furthermore, the size of the step in the pseudopotential is given by the index of refraction contrast between the dielectric sphere and its surrounding medium. As a result, for a given sphere radius a, larger index of refraction contrast leads to tighter confinement of the WGM within the sphere, and thus slower leakage of the WGM into free space.

The rate of radiation leakage can be extracted from the exact solutions described in sections 2.2.3 and 2.2.3. However, we can also describe an approximate expression for this loss rate that is much more compact and convenient. To do this, we study solutions to equation 2.74 for a distance x away from the dielectric's surface that is small compared to a. See figure 2.12 for visual details of the problem at hand. Using the relationships $r = a(1 + x/a)$, $1/r \approx 1/a(1 - x/a)$, $1/r^2 \approx 1/a^2(1 - 2x/a)$, equation 2.74 can be written to lowest order in x/a as

$$\frac{\mathrm{d}^2 Z}{\mathrm{d}x^2} + \left(n_0^2 k_0^2 - \frac{\ell(\ell+1)}{a^2} \right) Z = 0 \tag{2.76}$$

Equation 2.76 is an ordinary differential equation with general solution $R = \exp(bx)$. Substituting this general solution into equation 2.76 yields a characteristic quadratic equation for b, given by $b^2 + c^2 = 0$, where $c = n_0 k_0^2 - \ell(\ell+1)/a^2$. Thus $b = \pm\sqrt{c}$ and for $x \ll a$, the radial function takes the form

$$Z(x) = A_0 e^{-\sqrt{n_0^2 k_0^2 - \frac{\ell(\ell+1)}{a^2}} x} \tag{2.77}$$

Given that $k_0 = 2\pi/\lambda_0$, for $x \ll a$ one can see that not only does the electromagnetic field of the WGM decay exponentially, but also that this decay depends on a/λ_0. As one learns through studying the one dimensional time-independent Schrödinger equation, the wave function exponentially decays while inside the potential barrier; this is in exact analogy

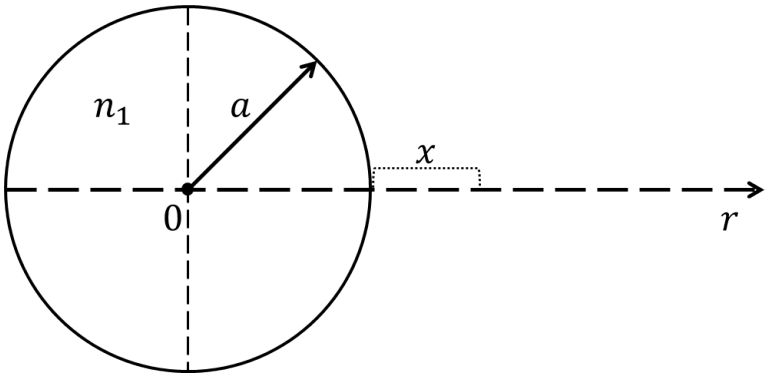

Figure 2.12: A sketch of a dielectric sphere with radius a and index of refraction n_1 centered at the origin of a coordinate system. The small distance x starts at the outer edge of the dielectric sphere, and extends towards larger values of the radial coordinate r.

with the exponentially decaying solution to equation 2.77.

Alternatively, in the limit that $r \to \infty$ equation 2.74 takes the form

$$\frac{\mathrm{d}^2 Z}{\mathrm{d}x^2} + n_0^2 k_0^2 Z = 0 \tag{2.78}$$

Solutions to equation 2.78 take the form of complex exponential functions which oscillate and have infinite radial extent. This, again, shows that there are no true bound states of WGMs in a dielectric.

2.3 Isolating Drops of Liquid Helium

Isolated liquid helium drops are model systems for addressing a myriad of outstanding scientific questions. ^{4}He drops isolated in vacuum exist in the superfluid state, and thus function as many-body quantum systems near absolute zero temperature, which may be suitable to study open questions in fluid dynamics, such as the connection between the onset and decay of turbulence in quantum fluids and the dynamics of vortex lines. In 1974, experiments reported observed of parallel arrays of quantum vortices in a bucket of superfluid ^{4}He [75], but until recent experiments in 2014 with free—flying superfluid nanodroplet beams, little was known about quantum vortices in isolated superfluids [76].

Studying isolated helium drops may even shed light on astrophysical phenomena such as the dynamics of neutron stars due to their superfluid crust or core [77, 78, 79]. ^{3}He drops isolated in vacuum are unlikely to cool below their superfluid transition; as a result, they can be used to study outstanding questions in normal fluid mechanics, such as the longstanding problem of the equilibrium shape of a drop undergoing rigid-body rotation [80](it is known that a normal drop undergoes a series of spontaneous symmetry breaking events as its rotation rate increases, but it is unknown if this series is finite or infinite, or if it includes equilibrium shapes that are topologically distinct from the sphere [81, 82]).

Embedding dopants within liquid helium drops (such as atoms, molecules, or electrons) provides an avenue to study the dopants in a cold isolated environment. Due to vanishing optical absorption from the far-infrared to the vacuum ultraviolet range and the fact that dopants typically exist in their (ro)vibrational and electronic ground states, superfluid nanodroplets have been powerful systems in which to conduct such experiments. Free-flying nanodroplets have been useful for spectroscopy of single cold molecules and atomic/molecular clusters, as well as for studies of cold chemical reactions [83]. An electron injected into liquid ^{4}He produces a cavity inside which it becomes trapped, forming a one-of-a-kind quantum dot that changes size significantly depending on the trapped electron's quantum state. From the perspective of pushing into the regime of quantum optomechanics, which requires low optical and mechanical loss, the vanishing optical absorption and zero viscosity of superfluid helium make it an ideal material to use to construct an optomechanical system. In this section, I will describe the unique material properties of superfluid helium and the history of experiments with isolated superfluid drops. I place a special emphasis on the diamagnetic levitation of liquid helium, which may enable the use of an isolated helium drop as both the optical resonator and the mechanical resonator of an optomechanical system.

2.3.1 The Superfluid Phase of Helium

Liquid ^{4}He undergoes a second-order phase transition from a normal liquid to a superfluid at $T_\lambda = 2.17$ K. Superfluid ^{4}He has zero viscosity and a thermal conductivity that varies strongly with temperature and is larger than that of pure copper for $1\ \mathrm{K} \lesssim T < T_\lambda$. Through van der Waals attraction, helium will wet the surface of a container and form a thin film, but in its normal state the film is clamped by its viscosity (many other materials will wet a container, but helium is special as it wets all materials but cesium). However, when the helium film is cooled to $< T_\lambda$, its viscosity vanishes and the film – called a Rollin film – is able to move freely at speeds up to the critical Landau velocity $v_L = 60$ m/s. Superfluid ^{4}He also passes through tiny capillaries too small to pass any other material, and forms lattices of vortices with quantized angular momentum when rotated. Quantized vorticies arise due to the irrotational velocity field of a superfluid, which I discuss in section 2.4.5. Finally, provided a object moving through the superfluid doesn't exceed v_L, it will not dissipate energy into the superfluid.

At temperatures $T < T_\lambda$, the behaviour of liquid helium is well-described by a two-fluid model with a total density $\rho_0 = \rho_\mathrm{n} + \rho_\mathrm{s}$, where ρ_n is the density of the viscous, normal fluid component and ρ_s is the density of the superfluid component. The superfluid fraction exhibits a power law dependence on the ratio T/T_λ. Specifically, for $T \ll 0.8$ K, $\rho_\mathrm{n}/\rho_0 \approx 1.2 \times 10^{-4} T^4$ [84]. Figure 2.13 shows ρ_n/ρ_0 and ρ_s/ρ_0 for $0 < T < T_\lambda$. The drops the we levitate in vacuum reach $T \approx 330$ mK, so they are essentially pure superfluid. For temperatures $T > T_\lambda$, $\rho_0 = \rho_\mathrm{n}$, equal to 125 kg/m^3. Whereas, as T decreases from T_λ to absolute zero, the normal fraction ρ_n/ρ_0 decreases from 1 to 0, while the superfluid fraction ρ_s/ρ_0 increases from 0 to 1, with $\rho_\mathrm{s} \approx 145$ kg/m^3 for $T < T_\lambda$ [84].

The dispersion relation for excitations in liquid helium allows for the existence of phonons at any $T > 0$. An object in the liquid can scatter from these phonons; this interaction provides a mechanism for energy to be exchanged. (Note that at $T \approx 8$ K, another excitation called a roton appears, but for $T < 0.57$ K, roton scattering processes

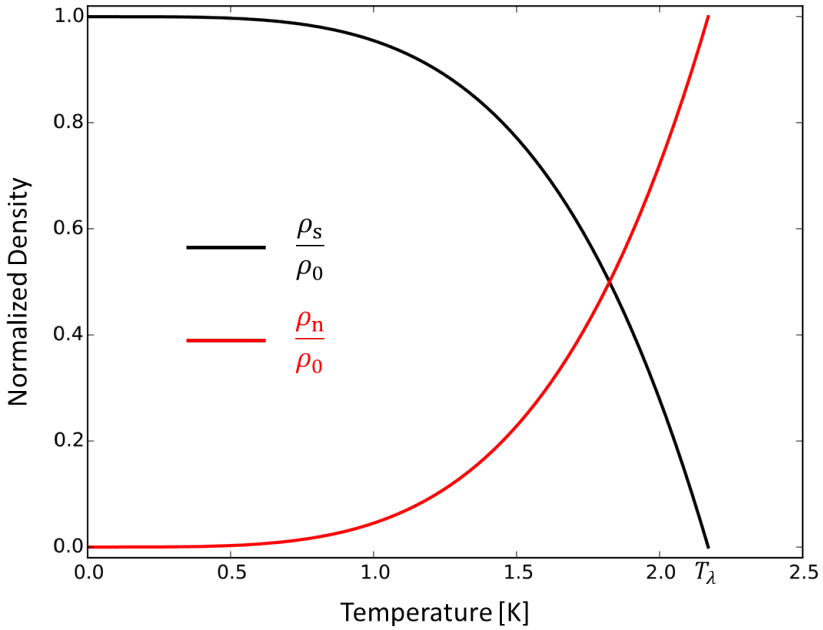

Figure 2.13: The normal fluid fraction ρ_n/ρ_0 and superfluid fraction ρ_s/ρ_0 for $0 < T < T_\lambda = 2.17$ K with $\rho_0 = \rho_n + \rho_s$.

are negligible [84, 85]).

^{3}He, a fermion with nuclear spin 1/2, also can exhibit superfluidity. For $T \gtrsim 3$ K, ^{3}He behaves as a degenerate Fermi liquid, but it is not in a superfluid state. However, for $T \lesssim 3$ mK, ^{3}He can undergo a phase transition into one of two superfluid states, which are referred to as the A and B phases. For $T < 3$ mK, ^{3}He atoms form bosonic quasiparticles called Cooper pairs, highly similar to Cooper pairs in the BCS theory of superconductivity. Superfluid ^{3}He also exhibits unusual properties, including vortex configurations which are distinct from superfluid ^{4}He [84].

Optical Loss in ^{4}He

As I mentioned above, superfluid helium is an ideal material from which to construct an optomechanical system due to its nearly vanishing optical loss. Here we will discuss the optical loss suffered by WGMs in a levitated liquid ^{4}He drop.

^{4}He samples have high chemical purity because all other atoms or molecules (with the exception of ^{3}He) will freeze on the surface of the container that holds the liquid. The

natural abundance of ^{3}He relative to all helium is 1.37×10^{-6} [86]. Because liquid ^{4}He has high chemical purity and its first electronic excited state of has an energy $\mathcal{E}_1 \approx 19.8$ eV, helium does not absorb light from the far-infrared to the vacuum ultraviolet ($\lambda = 100$ nm). range. However, non-zero optical loss in liquid helium arises due to elastic and inelastic scattering processes – Rayleigh (elastic), Raman (inelastic), Brillouin (inelastic). Furthermore, as described in section 2.2.4, radiation loss in optical WGMs occurs due a dielectric sphere's inability to perfectly confine a WGM. Finally, loss in an optical WGM can arise due to light scattering from thermally-populated surface waves on the levitated drop. However, for helium drops with radius $R \approx 250$ μm (the typical drop radius in the experiments described in this thesis), this source of loss is expected to be negligible in comparison to the radiation loss; the opposite is expected to be the case for $R \sim 1$ mm [38].

In reference [87], Landau and Lifshitz provide a formula for the extinction coefficient for the combined Rayleigh and Brillouin scattering μ_{comb} due to thermodynamic fluctuations of pressure or temperature in a material:

$$\mu_{\mathrm{comb}} = \frac{\omega^4}{6\pi c^4}\left(k_{\mathrm{B}} T \rho^2 \beta_{\mathrm{T}} \left(\frac{\partial \epsilon_{\mathrm{r}}}{\partial \rho}\right)_T^2 + \frac{k_B T^2}{\rho C_{\mathrm{V}}}\left(\frac{\partial \epsilon_{\mathrm{r}}}{\partial T}\right)_\rho^2\right) \tag{2.79}$$

where ω is the angular frequency of the light impinging on the scatterer, c is the speed of light, k_{B} is Boltzmann's constant, β_{T} is the isothermal compressibility, ϵ_{r} is the relative permittivity of the material, T is the temperature of the material, ρ is the density of material, and C_{V} is the heat capacity of the material at constant volume.

In reference [88], Seidel and colleagues calculate the Rayleigh scattering lengths for several materials. They note that, for liquid helium, the second term in equation 2.79 is several orders of magnitude smaller than the first; I, too, will neglect the second term since I am concerned with scattering in levitated helium drops. We are left only with scattering induced by light interaction with phonons (the term that was neglected is associated with

second sound). Using equation 2.192, equation 2.79 can be written in the following form

$$\mu_{\rm comb} = \frac{(2\pi)^3}{27\lambda^4}(\epsilon_{\rm r}-1)^2(\epsilon_{\rm r}+2)^2 k_{\rm B} T \beta_{\rm T} \tag{2.80}$$

where λ is the wavelength of the light in the liquid helium. The extinction coefficient $\mu_{\rm comb}$ has units of [$\rm m^{-1}$], which can now be used to determine the Rayleigh scattering-limited finesse of a WGM. For a helium drop with radius R_0, the round-trip loss $\varphi_{\rm comb}$ that a WGM with $q = 1, R_0 \gg \lambda$ would experience due to $\mu_{\rm comb}$ as it propagates around the drop's periphery is given by

$$\varphi_{\rm comb} = 2\pi n_1 R_0 \mu_{\rm comb} \tag{2.81}$$

where n_1 is the index of refraction of helium. Using equation 2.10, the Rayleigh scattering-limited finesse of the WGM is given by

$$\begin{aligned} \mathcal{F}_{\rm comb} &\approx \frac{2\pi}{\varphi_{\rm comb}} \\ &\approx \frac{27\lambda^4}{(2\pi)^3 n_1 (\epsilon_{\rm r}-1)^2(\epsilon_{\rm r}+2)^2 R_0 k_{\rm B} T \beta_{\rm T}} \end{aligned} \tag{2.82}$$

This result includes the mode loss due to both Rayleigh and Brillouin scattering. For a WGM with $\lambda \approx 1550$ nm and large ℓ ($\sim 2\pi R_0/\lambda$) in a ^{4}He drop with $R_0 = 250$ μm at $T = 350$ mK, $\mathcal{F}_{\rm comb} \approx 1.4 \times 10^{11}$. The Rayleigh scattering component refers to scattered light that, after the scattering event, retains its pre-scattering energy. The Brillouin scattering component, however, refers to scattered light that has a different energy after scattering from phonons. In 1934, Landau and Placzek theorized (referred to as the Landau-Placzeck theory) that the light intensity of the combined Rayleigh and Brillouin scattering to just the light intensity due to Brillouin scattering is given by the ratio of the isothermal compressibility $\beta_{\rm T}$ to the isentropic compressibility $\beta_{\rm S}$ of the liquid from which light is scattered. In 1966, Cummins and Gammon experimentally tested the Landau-Placzeck theory on 11 liquids and found that their results were in good agreement with the theory [89].

One can split $\mu_{\rm comb}$ into two components: the Rayleigh component $\mu_{\rm Rayleigh}$ and the Brillouin component $\mu_{\rm Brillouin}$, which sum to $\mu_{\rm comb}$. Using the Landau-Placzeck theory,

$$\frac{\mu_{\rm comb}}{\mu_{\rm Brillouin}} = \frac{\beta_{\rm T}}{\beta_{\rm S}} \tag{2.83}$$

In reference [90], Brooks and Donnelly provide for liquid helium at $T \approx 350$ mK, $\beta_{\rm T} \approx 1.21 \times 10^{-7}[{\rm ms^2 kg^{-1}}]$. Along with $\beta_{\rm S} = 1/\rho u_{\rm c}^2$, where and $u_{\rm c}$ is the speed of sound in liquid helium, one finds that for liquid helium at $T \approx 350$ mK, $\beta_{\rm T}/\beta_{\rm S} \approx 1.01$. As a result, $\mu_{\rm Brillouin} \approx 0.99\mu_{\rm comb}$, which suggests that the Rayleigh-limited WGM finesse $\mathcal{F}_{\rm comb}$ is dominated by loss due to scattering from phonons in the liquid helium. I will now refer to $\mathcal{F}_{\rm comb}$ as $\mathcal{F}_{\rm phonon}$.

Another scattering process that could lead to optical loss is Raman scattering, in which light creates excitations in the liquid. In superfluid helium Raman scattering results in the creation of rotons. In 1969, Greytak and Yan measured the Raman scattering of light with $\lambda = 514.5$ nm from rotons in liquid at $T = 1.16$ K [91]. They measured an extinction coefficient $\mu_{\rm Raman} = 4\pi \times (6 \pm 2) \times 10^{-12}$ cm^{-1}. Again, for a helium drop with radius R_0, the round-trip loss $\varphi_{\rm Raman}$ that a WGM with $q = 1, R_0 \gg \lambda$ would experience due to $\mu_{\rm Raman}$ as it propagates around the drop's periphery is given by $\varphi_{\rm Raman} = 2\pi n_1 R_0 \mu_{\rm Raman}$. As a result,

$$\mathcal{F}_{\rm Raman} \approx \frac{2\pi}{\varphi_{\rm Raman}} \tag{2.84}$$

For such a WGM in a ^{4}He drop with $R_0 = 250$ μm, $\mathcal{F}_{\rm Raman} \approx 5 \times 10^{11}$.

Optical WGMs also experience loss due to the non-zero curvature of the dielectric around which they propagate, which I will refer to as radiation loss. In 2002, Oraevsky published work in which he solved Maxwell's equations and derived the optical WGMs of a dielectric sphere in a manner that is similar to the derivation I provided in section 2.2.3 [74]. Oraevksy found the same characteristic equation whose solutions yield complex WGM wavenumbers $n_1 k_{q\ell}$, and he gives an approximate expression (valid for $\ell \sim k_0 a \gg 1$) for

the WGM quality factor:

$$Q_{q\ell} = \frac{\mathrm{Re}[k_{q\ell}]}{\mathrm{Im}[k_{q\ell}]} = \frac{\ell + \frac{1}{2}}{2} \left(\frac{\epsilon_\mathrm{r}(\epsilon_\mathrm{r}\mu_\mathrm{r} - 1)}{\mu_\mathrm{r}} \right)^{1/2} e^{2T_{q\ell}} \tag{2.85}$$

where

$$T_{q\ell} = \left(\ell + \frac{1}{2}\right) \left[\cosh^{-1}(\sqrt{\epsilon_\mathrm{r}\mu_\mathrm{r}}) - \left(\frac{\epsilon_\mathrm{r}\mu_\mathrm{r} - 1}{\epsilon_\mathrm{r}\mu_\mathrm{r}} \right)^{1/2} \right] + \xi_q \left(\frac{\ell + \frac{1}{2}}{2} \right)^{1/3} \left(\frac{\epsilon_\mathrm{r}\mu_\mathrm{r} - 1}{\epsilon_\mathrm{r}\mu_\mathrm{r}} \right)^{1/2} + \frac{1}{\epsilon_\mathrm{r}} \tag{2.86}$$

Here, ξ_q is the q-th root of the Airy function. I have written the expression in the notation that is being used in this thesis. The real part of the wavenumber $\mathrm{Re}[k_{q\ell 0}]$ is related to the WGM angular frequency such that $\omega_\mathrm{opt} = ck_{q\ell 0}$. The imaginary part of the wavenumber $\mathrm{Im}[k_{q\ell 0}]$ is the WGM radiation loss rate. $Q_{q\ell}$ does not depend on m due to the $(2\ell+1)$-fold degeneracy of WGMs in a spherical dielectric. The radiation limited finesse $\mathcal{F}_{q\ell}$ is given by

$$\begin{aligned} \mathcal{F}_{q\ell} &= \frac{\Delta\omega_\mathrm{FSR}}{\omega_\mathrm{opt}} Q_{q\ell} \\ &= \frac{Q_{q\ell}}{\ell} \end{aligned} \tag{2.87}$$

with $\Delta\omega_\mathrm{FSR} = c/(2\pi n_1 R_0)$. Here $n_1 = \sqrt{\epsilon_\mathrm{r}\mu_\mathrm{r}}$ is the index of refraction and R_0 is the radius of the sphere. For a helium drop with radius R_0 and index of refraction n_1, figure 2.14 shows plots of $\mathcal{F}_{1\ell}$ for various ℓ and for various values of R_0/λ, where λ is the WGM wavelength for $q = 1$.

Finally, loss in an optical WGM can arise due to light scattering from the thermally-populated surface modes of a levitated drop. However, for helium drops with radius $R \approx 250$ μm and $\lambda = 632.8, 1,550$ nm (the typical R and λ in the experiments described in this thesis), this source of loss is expected to be negligible in comparison to the radiation loss. Surfaces defined by surface tension are typically smooth, yet for $T > 0$ the drop's surface modes have non-zero thermal occupation. Consequently, the drop can be thought to have

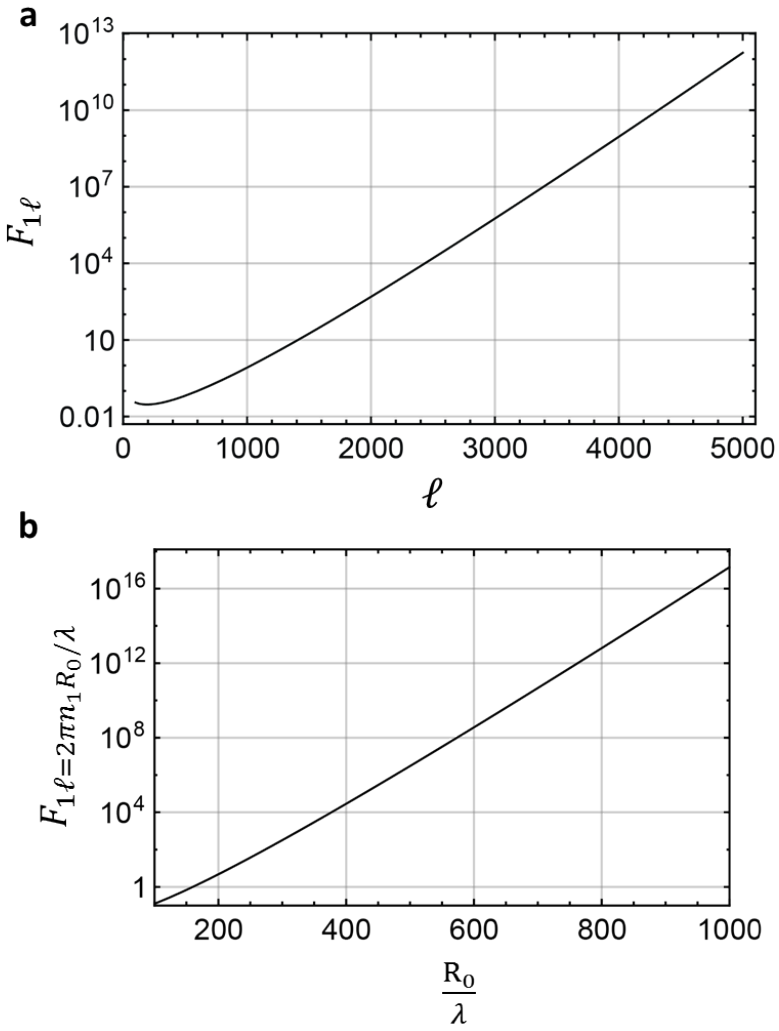

Figure 2.14: The calculated finesse of optical WGMs in a ^{4}He drop. (a) The finesse of the $q = 1$ WGMs plotted against the angular momentum number ℓ. (b) The finesse of the $q = 1$ WGMs plotted against R_0/λ, where R_0 is the drop's radius and λ is the WGM wavelength. In these calculations, only radiation loss is considered.

an effective surface roughness that scatters light. In reference [38], we assume that over the lifetime $2\pi/\kappa$ of an optical WGM, the random thermal surface deformations due to the surface modes are frozen. In this case, we find the following lower bound for the surface roughness-limited Q:

$$Q_{\rm rough} \approx \frac{\lambda_0 R}{\pi^2\sqrt{\epsilon_{\rm r}-1}}\frac{\sigma}{k_{\rm B}T} \tag{2.88}$$

For a ^{4}He drop with $R = 250$ μm (1 mm), $\sigma = 3.75 \times 10^{-4}$, $\epsilon_{\rm r} = 1.057$, $T = 300$ mK and $\lambda_0 = 1$ μm, $Q_{\rm rough} \approx 9.7 \times 10^9$ ($Q_{\rm rough} \approx 4 \times 10^{10}$).

2.3.2 Jets of Liquid Helium Nanodroplets in Vacuum

Droplet formation in gas expansions of helium was reported by Kammerling Onnes in 1908, at Leiden University, during initial attempts of helium liquefaction [92]. Due to technological limitations of the time, unfortunately, it was exceedingly difficult to verify the existence of helium nanodroplets in the expansion experiments, so such experiments were not pursued further.

In the 1960's, researchers revisited droplet formation. The method that has typically been employed to produce helium nanodroplets with approximate diameters $d \sim 10 - 100$ nm is homogeneous nucleation of high pressure helium gas in supersonic nozzle expansions [93, 94, 95, 96, 97, 98, 83]. Pre-cooled helium gas, initially at rest in a stagnation region at pressure $P_0 \lesssim 10^2$ bar, is made to expand through a nozzle assembly with nozzle diameter $\leq$ 100 μm at temperature $3.5 \leq T_0 \leq 20$ K and into a vacuum system. The stagnation pressure and the nozzle temperature are critical experimental parameters that control the eventual average size of the nanodroplets in the beam. The expanding gas accelerates through the nozzle and adiabatically cools. In general, it is possible for the local thermodynamic state of the expanding gas to pass into the liquid-gas coexistence region before internal collisions effectively stop, and thus phase separation may take place, leaving a mixture of nanodroplets and helium vapor in the jet. Depending on T_0 and P_0, the jet

can undergo subcritical or supercritical expansion, yielding relatively small or large nanodroplets, respectively [83]. The mixture is then collimated by a skimmer, or pinhole-like orifice, and a helium nanodroplet beam is formed, with nanodroplets reaching temperatures $T_{\mathrm{d}} \approx 380$ mK after a typical droplet lifetime $t_{\mathrm{d}} \lesssim 25$ ms for ^{4}He [83].

In 1961, Becker and colleagues at the University of Karlsruhe reported time-of-flight measurements of helium nanodroplet beams subjected to a mechanical chopper in order to measure the velocity distribution of the beam [99, 100]. They expanded helium gas through a tapered nozzle at $T_0 = 4.2$ K and $P_0 = 0.98$ Bar and observed a velocity distribution whose center peaked at 165 m/s, and whose narrow width could only be explained by cluster formation in the liquid jet.

A large collection of studies by Gspann and colleagues on atomic and molecular bombardment of ^{3}He and ^{4}He nanodroplet beams continued into the 1980's at the University of Karlsruhe [101]. In this body of work, nanodroplet beams with $N_{\mathrm{d}} \sim 10^6$ atoms of either helium isotopes were bombarded (normal to the nanodroplet beam's propagation direction) with cesium or xenon atomic jets. The cesium atoms' momentum was completely absorbed by the nanodroplets, which could be directly detected by striking a surface ionization detector (a hot tungsten strip) with the bombarded nanodroplet beam. It was important to use heavy atoms because their low thermal velocities at vapor pressures high enough to ensure frequent interactions with the ^{4}He beams would not exceed the Landau critical velocity, and thus not spoil superfluidity. In nanodroplets of both helium isotopes the momentum of the xenon atoms intercepted by the beam was not completely transferred to them, and thus the xenon atoms were not captured. Gspann explained the inability to capture xenon with high capture efficiency by deep penetration into the nanodroplet, followed by anisotropic ejection of helium atoms.

In the 1990's, experiments from the Toennies group at the University of Göttingen in collaboration with Northby at the University of Rhode Island used similar nanodroplet bombardment techniques to those of Gspann's work. They found that helium nanodroplets

with $N_{\rm d} \leq 10^9$ and $t_{\rm d} \leq 25$ ms could capture one or more neon, ^{3}He or ^{4}He atoms [102, 103, 104]. They also captured the same atoms using a new technique where the nanodroplet beam propagated through a pick-up chamber with gaseous atomic or molecular dopants. Also in the 1990's, the Scoles group at Princeton University used the combined pick-up chamber technique with laser-induced evaporation and were thus able to make spectroscopic measurements where they could detect the infrared absorption of sulfur hexafluoride molecules captured within helium nanodroplets with $N_{\rm d} \sim 10^4$ atoms [105]. After Scoles's work, Toennies and Vilesov performed high-resolution measurements of sulfur hexafluoride molecules captured within helium nanodroplets with $N_{\rm d} \sim 10^3 - 10^4$ which revealed that the sodium hexaflouride spectral lines were unusually sharp and presented evidence of rotational fine structure, indicating that the embedded molecules can rotate freely inside the ^{4}He nanodroplets [106]. Furthermore, fitting the rotational spectra data yielded a temperature $T_{\rm d} = 370 \pm 50$ mK, which was interpreted as the internal nanodroplet temperature.

Alongside the work with neutral nanodroplet beams, there was a great deal of work done on bombarding ^{3}He and ^{4}He nanodroplet beams with electrons, thus creating beams of charged nanodroplets. One of the first such experiments was conducted by Gspann, in which neutral nanodroplet beams were bombarded with $\mathcal{E}_{\rm bomb} \approx 200$ eV electrons, which ionized the nanodroplets (the ionization energy $\mathcal{E}_{\rm I} \approx 24.6$ eV), thus creating positively charged nanodroplets that would reflect from highly polished metallic surfaces [107]. In this work, the nanodroplets were found to have an atom number-to-charge ratio $Z_{\rm d} \sim 10^5$. In a subsequent set of publications, Gspann and Vollmar reported measurements of large ^{3}He and ^{4}He nanodroplets with a single positive charge, consisting of $N_{\rm d} \sim 10^6 - 10^8$ atoms ($Z_{\rm d} \sim 10^6 - 10^8$); they also reported evidence for the existence of large multiply charged nanodroplets [108, 109, 110]. Upon bombardment with electrons, the ^{3}He nanodroplets were found to eject charged mini-clusters with $N_{\rm d} = 85$ atoms, whereas ^{4}He nanodroplets would eject charged mini-clusters with $N_{\rm d} = 68$.

The existence of negatively charged ^{4}He nanodroplets was first reported by Gspann [111].

Gspann utilized a time-of flight method and found that negatively charged clusters with $N_{\rm d} \gtrsim 10^6$ atoms, no less, could be detected in his apparatus. It is known that there is no stable, negatively charged monoatomic helium ion or diatomic molecule. From studies on bulk liquid helium samples, it is well known that electrons are weakly bound to a planar helium surface (but that there must also be repulsion at short range). The binding is the result of an attractive image charge induced in the liquid helium due to its polarizability [112]. It had been predicted that similar surface-bound electron states should exist on nanodroplets, as long as they were large enough [113, 114].

Following Gspann's work, more in-depth studies of negatively charged nanodroplets with $N_{\rm d} \sim 10^3 - 10^6$ atoms were conducted by Northby and colleagues. The droplets were bombarded by electrons with $\mathcal{E}_{\rm bomb} \approx 35$ eV (so that a single electron could not ionize multiple He atoms), then they measured the energy of the nanodroplets by using an in-line stopping potential method and by a deflection method; these methods gave them a tool with which to measure the size distribution of nanodroplets in beams [115]. In their next set of experiments, they bombarded nanodroplets with $N_{\rm d} \approx 10^5$ atoms with electrons with $\mathcal{E}_{\rm bomb} < \mathcal{E}_{\rm I}$, and suggested that the resulting negatively charged nanodroplets were due to an electrons in bubble states within the nanodroplets, which is a state consisting of an electron being bound in the interior of the nanodroplet by the polarization force arising from the liquid's polarizability [116]. Northby and colleagues realized that if the electron bubble model was the correct interpretation of the negative charge found on the nanodroplets, this negatively charged cluster would be optically active and thus detectable by electron detachment spectroscopy [117, 118]. As a result, in further work, they created an infrared beam with $\lambda \geq 800$ nm from an optically filtered tungsten bulb and used it to interrogate a negatively charged nanodroplet beam above an electron multiplier detector sensitive to detached electrons. They observed that without infrared illumination, there was still a significant spontaneous electron detachment signal. When the infrared illumination was turned on, the electron detachment count rate doubled, consistent with the

thought that infrared optical transitions of the electron in the bubble potential could lead to enhanced detachment rates of electrons from the nanodroplets [119]. Lastly, in a further study, Northby and colleagues used a monochromator in an attempt to measure the wavelength dependence of the optically enhanced electron emission from the nanodroplets, for which they found a peak in the emission signal at $\lambda \approx 1.5$ μm [120]. In this work, they mentioned that an electron confined in a bubble potential well of radius $R_{\mathrm{B}} = 18.7$ Å with a depth $V_{\mathrm{B}} = 0.7$ eV would have a transition to the conduction band at with an excitation wavelength $\lambda = 1.5$ μm, but that other bound state transitions could play a role in the enhanced electron emission.

Also in the 1990's, but tangential to the work on doped or charged helium nanodroplets, Schöllkopf and Toennies used nanostructured transmission gratings to study the diffraction of helium nanodroplet beams [121]. Because the velocity distribution of nanodroplets was quite narrow, the deBroglie wavelength of nanodroplet clusters within the beam were inversely proportional to the number of atoms it contained. As a result, each cluster was diffracted at different angles as it passed through the grating. One highlight of this work is that, with a 200 nm grating period and 100 nm slit widths, they clearly identified diffraction peaks corresponding to He_2 and He_3 molecules, providing unambiguous proof of the existence of these extremely weakly bound helium molecules, which before their work was open to debate.

In 2014, Vilesov and collaborators at S.L.A.C. detailed an experiment where ^{4}He nanodroplet beams with $N_{\mathrm{d}} \sim 10^8 - 10^{11}$ were imaged with a bright pulsed x-ray beam with $\lambda = 8.2$ Å [76], in which they report several interesting observations. They observed that approximately 98% of the droplets in the beam had elliptical cross-sections, with aspect ratio $b/a \leq 2.3$. Further, after doping the nanodroplets with xenon atoms and imaging the nanodroplet beam with x-ray pulses, they observed filaments that were consistent with xenon atoms trapped along the cores of quantized vortices, and observed the presence of vortex arrays with a period of approximately 200 nm. From an x-ray image of a droplet

with $d = 2.2$ μm, they observed a vortex density $n_{\rm v} = 4.5 \times 10^{13}$ m^{-2}, corresponding to the presence of 170 vortices in the droplet.

To date, large numbers of the noble gas atoms, alkali and alkaline earth atoms, transition metal atoms, lathnanide atoms, organic molecules, and even amino acids have been studied in the infrared, visible, or near ultraviolet within helium nanodroplets [83, 95]. Experiments carried out at the University of Göttingen have even shown that metal atoms can be captured within a nanodroplet. Other experiments have found that chemical reactions in nanodroplets can exhibit much larger reaction rates due to the low temperature. An example of such a reaction is Ba + $N_2O \rightarrow BaO^*$+N_2. Studies of bimolecular interactions in a liquid helium nanodroplet may facilitate the in-depth study of multi-step chemical reactions, and even allow for the control of reaction pathways [122, 95].

2.3.3 Electrostatic Levitation of Liquid Helium Drops

In 1997, Niemela of the University of Oregon demonstrated the electrostatic levitation of charged superfluid ^{4}He droplets [123]. These experiments were the first to demonstrate the trapping of a drop for $t_{\rm d} \gg 25$ ms. By using a fountain pump, he could deliver the superfluid to a vessel out of which the superfluid would creep in the form of a thin film. The superfluid film would then flow over an electrode before dripping off the end, under the acceleration of gravity. He used the electrode to initiate a weak coronal discharge, ionizing helium atoms in the liquid as they dripped off the end of the electrode. He was left with positively charged ^{4}He drops with $d \leq 150$ μm with a total charge $Q_{\rm d} \sim +10^5 e$, which would fall, under gravity, into a region between a set of levitation electrodes. Using active control of the vertical component of the electric field between the levitation electrodes, he could stably levitate the drops for up to 20 minutes.

The force balance condition for electrostatic levitation is given by $m\mathbf{g} = Q_{\rm d}\mathbf{E}$, where m is the drop's mass, $\mathbf{g}$ is the acceleration of gravity, and $\mathbf{E}$ is the electric field. It is worth noting that one would expect the electrostatic levitation of charged drops to require

active control of the electric field, due to Earnshaw's theorem, which essentially states that electric charges cannot be stably bound in an electrostatic potential well. Earnshaw's theorem concerns local minima in any vector component of an electrostatic field. Because vector components of the electric field have no local minima, a charge cannot be stably bound in the associated potential. Niemela was able to levitate the drops by manually tuning the electric field strength that counteracts the gravitational force on the charged drop on a 10-minute timescale.

On the other hand, an electrostatic (magnetostatic) field can be used to levitate an object, provided the levitation condition depends on a local minimum in the magnitude of the electric (magnetic) field. In 1995, the Maris and Seidel groups at Brown University demonstrated the use of an optical dipole trap to levitate superfluid ^{4}He droplets with $d \approx 10 - 20$ μm in ^{4}He vapor at $P \sim 1$ bar and $T \approx 2$ K for up to 3 minutes [124]. They applied a strong drive to a hemispherical, concave piezoelectric transducer submerged ≈2 mm beneath the surface of a liquid helium bath. When the transducer was driven near resonance by a signal with drive frequency $f_{\rm drive} \approx 1.1$ MHz and amplitude $V_{\rm drive} \approx 10$ Vrms, a mist of superfluid droplets was ejected. Some of those droplets were captured by a trap formed by two focused counter-propagating lasers with total $P_{\rm L} = 4$ W, $\lambda = 1,064$ nm and beam radius $w = 40$ μm at the focal plane. For $V_{\rm drive} > 10$ Vrms, they observed a fountain of drops with $d \approx 500$ μm emerge from the liquid surface in the vicinity of the acoustic focus. However, the drops created with the fountain technique were too large to be levitated with their laser trap.

In directions transverse to the trapping beams' propagation axis, the transverse trap frequency $f_{\rm trap}^{\rm (trans)} \approx 200$ Hz and along the propagation axis the axial trap frequency $f_{\rm trap}^{\rm (axial)} \approx 2.5$ Hz. They mention that, while single drops with levitation lifetimes $t_{\rm d} = 3$ minutes were observed, $t_{\rm d} \approx 30$ s was most common. They estimated that for the largest droplets $t_{\rm d} \approx 200$ s. However, the droplets were generally lost from the trap before evaporating completely, due to instabilities in the trap or disturbances in the levitation chamber.

They believed the trap instabilities arose due to vibrations of their cryostat which couple to the droplet's motion through viscous interaction with the gaseous environment, while liquid drops from condensation of gas on cold surfaces above the trap could drip and interrupt the beam path, allowing the axial force from one of the trap beams to push the previously trapped droplet out of the trap. Importantly, they provide detailed explanations regarding why the observation of droplets with small t_{d} were not due to optical absorption (which is negligible in liquid helium), but to a non-equilibrium thermodynamic effect. More specifically, the curved surface of a trapped droplet and the planar surface of liquid helium beneath it necessarily cannot be at the same temperature, resulting in heat flow from the warmer planar surface into the colder trapped droplet.

2.3.4 Diamagnetic Levitation of Liquid Helium Drops

The same groups at Brown University also reported the use of diamagnetic levitation to trap neutral or charged drops [125, 126]. The basic principle of this approach is that a powerful magnetic field will create a magnetic moment in the liquid helium, while a field gradient will apply a force to the moment. If the magnetic force is balanced against gravity, a helium drop can be suspended. Further details on the theory of diamagnetic levitation are provided in section 2.3.4.

The groups at Brown University used a superconducting magnet to generate the magnetic field necessary for trapping helium. In a first attempt to magnetically levitate helium drops, they tried the same droplet production method from their work on laser levitation. They found that the production of droplets had a strong dependence on the liquid helium surface height above the transducer; in combination with the transducer limiting optical access, this method was deemed unsuitable for their purposes. The next method they tried was to allow liquid helium to flow down the levitation chamber's wall, before being pulled into the trap via magnetic forces. This process generated drops uncontrollably, and, more often than not, would lead to the liquid flowing to the bottom of the chamber instead of into

the trap. In their next attempt they generated a liquid helium mist via two methods. In the first method, they rapidly cooled the levitation chamber's walls while adding helium gas to the chamber, causing the gaseous helium to condense into a mist of tiny liquid drops that coalesced to form a larger drop. In the second method, they pumped on a liquid helium puddle in their levitation chamber, causing it to boil and eject a liquid helium mist. Again, this mist could then coalesce into a larger drop. The helium mist method was not suitable for their purposes because they found that they could not control the agglomerated drop's size or temperature at the level they would have liked. Their last, and preferred, method was to introduce liquid helium directly into the trap via a capillary tube whose end was situated at the edge of the trap. They used a capillary line that was thermally anchored to both the helium bath of their cryostat and an internal ^{4}He pot. Upon pressurizing this capillary with He gas at its room temperature, and liquid would emerge from the end of the capillary in the cryostat and flow onto a thin wire of diameter 0.1 mm before being pulled into the trap. Drop formation with the capillary method was not easily controlled by varying the gas pressure applied to the room temperature end of the capillary, due to the unintentionally large impedance of the line. However, the flow of liquid through the capillary depended on the relative temperatures of ^{4}He pot and the levitation chamber walls, allowing them to produce drops with the size control they desired. This capillary delivery method allowed the groups at Brown University to create and levitate liquid helium drops with $d \leq 2$ cm at $T \geq 650$ mK in a gaseous environment. These drops exhibited oscillation frequencies ~ 1 Hz, in agreement with what one would expect from theory described in section 2.3.4.

Initially, the groups at Brown University mainly focused on the non-coalescence of liquid helium drops in the trap. They observed that when one drop was held in the trap and another drop was added to the trap, the two drops would occasionally appear to remain in contact without coalescing. They found the non-coalescence of levitated drops to be the result of a layer of vapor between the drops, which kept the liquid surfaces from making direct contact with each other. Due to the non-equilibrium conditions present in the levitation

chamber, the vapor layer was sustained by continued evaporation as the drops cooled. Occasionally, the drops would bounce off of one another before coming to rest. At sufficiently low magnet current (where the equipotentials shift from oblate to prolate), two small non-coalescing drops would stack themselves vertically in the trap, as opposed to resting horizontally side-by-side at larger currents. They observed the area of contact to appear planar, where each drop exhibited a shape similar to that of a liquid drop resting on a non-wettable flat surface; there were no sharp corners at the edges of the contact region. Coalescence of a pair of drops was observed to result from mechanical disturbance to the trapped drops, such as an additional drop colliding with the trapped pair, or sudden increases in the pressure in the levitation chamber. Non-coalescence was only observed above the superfluid transition temperature, which is to be expected because the non-uniform pressure distribution forcing the drops apart in the trap means that there must also be a non-uniform temperature distribution on the surface of the liquid; such non-uniform surface temperature is strongly suppressed by the large thermal conductance of superfluid helium.

In another set of experiments by the groups at Brown University, they measured the shape oscillations of magnetically levitated, positively-charged superfluid ^{4}He drops with $d \approx 5$ mm [127, 128]. Helium is only weakly polarizable, making it difficult to use electric fields to induce shape oscillations in liquid helium. As a result, the groups at Brown University used electrodes surrounding the levitation region to initiate an electrical discharge through the levitated drop, ionizing many helium atoms and leaving the drop charged with approximately 10^6 He^+. With this level of charge, they could apply to the levitated drop an AC electric field of magnitude $E_{\text{drive}} = 100$ V/m, resonant with the shape oscillation's natural frequency, and induce shape oscillations with amplitudes $\sim 10^{-1}d$. They illuminated the drop with a laser, and collected the light that exited the cryostat on a photodetector. The drop's changing local radius of curvature would cause a varying amount of divergence of the laser, resulting in power fluctuations at the photodiode. The current from the photodiode was fed into a lock-in amplifier, allowing them to measure changes in a drop's

radius $\sim 5 \times 10^{-5} d$. They reported measurements of driven surface waves on the levitated drops, which are a discrete set of oscillation modes whose restoring force is provided by the surface tension; these modes are described in detail in section 2.4.2.

The groups at Brown University mention that they observed the first 15 of these oscillation modes. They do not explicitly show measurements of them most of them, but do show the resonance of the lowest order surface mode, along with a measurement of its ring-down. They observed the lowest order surface mode to have an oscillation frequency ≈ 8.8 Hz with a decay rate ≈ 20 mHz. They found that the charges on the drop do not significantly contribute to the surface wave decay rates. Further, they measured the decay rate of the lowest order surface mode and found that it agreed well with predictions of a hydrodynamic model, which took into account the two fluids within the drop (superfluid and normal fluid) and the effects of the vapor surrounding the drop.

Lastly, in work reported in 2002, the groups at Brown University used measurements of the lowest order surface modes of a levitated drop with $d \approx 2$ mm to measure the surface tension σ of liquid ^{4}He as a function of temperature, for $0.6 < T < 1.6$ K. They found $\sigma = (3.75 \pm 0.004) \times 10^{-4}$ N/m^2.

In their 2002 paper, the groups at Brown University also showed the broken degeneracy of the $\ell_{\rm d} = 2$ (fundamental) surface mode, induced by the trap anisotropy (discussed in section 2.3.4). The broken degeneracy resulted in a resonance spectrum with three doubly-degenerate resonances.

Theory of Diamagnetic Levitation

Owing to the non-zero magnetic susceptibility of ^{4}He, a magnetic field can be used to generate a magnetic moment in ^{4}He. In addition, a field gradient can be used to apply a force on this magnetic moment. With suitable values of the magnetic field and magnetic field gradient, one can balance the magnetic force acting on the ^{4}He with the gravitational force acting on it. It is the diamagnetism of ^{4}He that provides the equilibrium point with

stability.

Magnetic levitation of a helium drop enables the creation of an optomechanical system made entirely of helium. Levitating a drop in vacuum allows the optical mode to be stored entirely in the drop/vacuum. As a result, the optical modes are expected to have very low loss, and not to contribute to heating of the optomechanical system. Levitation also removes the clamping loss associated with many mechanical oscillators. The very low optical loss and absence of clamping positions a levitated helium drop as an intriguing system with which one could possibly reach new regimes of quantum optomechanics. Furthermore, magnetic levitation of a liquid helium drop may allow the drop to be used as a tool to study open question in fluid dynamics. In what follows, I derive the conditions necessary to trap a ^{4}He drop by balancing the gravitational force acting on it with a repulsive diamagnetic force, and to ensure three dimensional stability.

The potential energy density of an object with mass density ρ, under the influence of gravitational acceleration g, with permeability $\mu = \mu_0\mu_\mathrm{r}$, and magnetic induction $\mathbf{B}$ due to an external auxiliary field $\mathbf{H}$ can be written as

$$U(x,y,z) = U_\mathrm{G}(z) + U_B(x,y,z) \tag{2.89}$$

where

$$U_\mathrm{G}(z) = \rho g z \tag{2.90}$$

and

$$U_\mathrm{B}(x,y,z) = \frac{1}{2}\mathbf{H}\cdot\mathbf{B} \tag{2.91}$$

Noting that

$$\mathbf{B} = \mu\mathbf{H} \tag{2.92}$$

the magnetic potential energy U_{B} can be rewritten as

$$U_{\mathrm{B}}(x,y,z) = \frac{B^2}{2\mu} = \frac{B^2}{2\mu_0\mu_{\mathrm{r}}} = \frac{B^2}{2\mu_0(1+\chi_{\mathrm{vol}})} \tag{2.93}$$

where χ_{vol} is the unitless volume magnetic susceptibility. For diamagnetic materials, $\chi_{\mathrm{vol}} < 0$, and it is this fact that mathematically suggests the possibility of stable levitation by a balance between the gravitational force and diamagnetic repulsion of the external auxiliary field. In the case that $|\chi_{\mathrm{vol}}| \ll 1$, which is the case for liquid ^{4}He ($\chi_{\mathrm{vol}} \approx -8.6 \times 10^{-7}$),

$$\frac{1}{1+\chi_{\mathrm{vol}}} \approx 1 - \chi_{\mathrm{vol}} \tag{2.94}$$

Substituting equation 2.94 into equation 2.93, one finds that the magnetic potential energy density takes the form

$$U_{\mathrm{B}}(x,y,z) = \frac{B^2}{2\mu_0} - \chi_{\mathrm{vol}}\frac{B^2}{2\mu_0} \tag{2.95}$$

One can interpret the first term in equation 2.95 as the energy density stored in the auxiliary field, and the second term as the energy density stored in the diamagnet through magnetic induction. The second term in equation 2.95 is of interest, as it produces diamagnetic repulsion, which can be balanced against gravity.

I define a new quantity U_{D} which contains the potential energy density responsible for the forces on the diamagnet

$$U_{\mathrm{D}}(x,y,z) = \rho g z - \chi_{\mathrm{vol}}\frac{B^2(x,y,z)}{2\mu_0} \tag{2.96}$$

With the exception of superconductors, materials which exhibit diamagnetism have small values of χ_{vol}, making them difficult to levitate. As such, the levitation of non-superconducting diamagnets typically requires the use of powerful solenoids to generate the field strengths required for levitation. In what follows, I consider levitation in a powerful solenoid. In a region near the central axis of a solenoid there are no free charges, and so

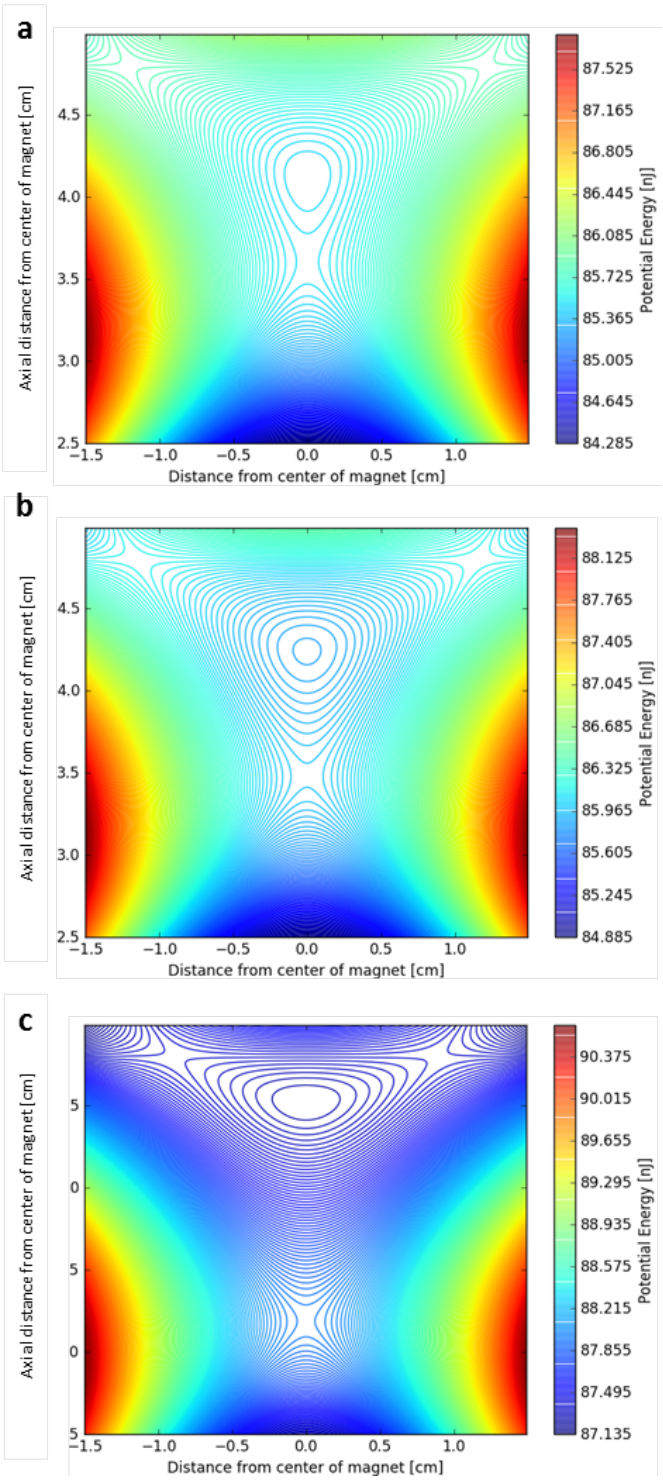

Figure 2.15: The potential energy contours of a levitated ^{4}He drop with radius $R_0 = 1$ mm, with contributions from the gravitational field and the diamagnetic response of the ^{4}He. The contours are plotted for magnet current a) $I = 115.8$ A, b) $I = 116.4$ A and c) $I = 118.0$ A.

the magnetic field produced is irrotational:

$$\nabla \times \mathbf{B} = \mathbf{0} \tag{2.97}$$

Equation 2.97 allows one to express $\mathbf{B}$ as the gradient of a magnetic scalar potential Φ

$$\mathbf{B} = \nabla\Phi(x, y, z) \tag{2.98}$$

Due to the fact that $\nabla \cdot \mathbf{B} = 0$,

$$\nabla^2\Phi(x, y, z) = 0 \tag{2.99}$$

In the ideal case of rotational symmetry about the axis of the solenoid, the second derivatives of the potential with respect to x and y must be equal. Noting this, equation 2.99 suggests

$$\frac{\partial^2}{\partial x^2}\Phi(x, y, z) = \frac{\partial^2}{\partial y^2}\Phi(x, y, z) = -\frac{1}{2}\frac{\partial^2}{\partial z^2}\Phi(x, y, z) \tag{2.100}$$

If the coordinate system is defined such that the levitation point occurs at the origin, one may begin inspecting the equilibrium and stability by Taylor expansion of $\Phi(x, y, z)$ around the point $(0, 0, z)$:

$$\begin{aligned}\Phi(x, y, z) =& \Phi(0, 0, z) + \\ & \frac{\partial}{\partial x}\Phi(0, 0, z)x + \frac{\partial}{\partial y}\Phi(0, 0, z)y + \\ & \frac{1}{2!}\left(\frac{\partial^2}{\partial x^2}\Phi(0, 0, z)x^2 + \frac{\partial^2}{\partial y^2}\Phi(0, 0, z)y^2 + 2\frac{\partial^2}{\partial x \partial y}\Phi(0, 0, z)xy\right) + \\ & \frac{1}{3!}\left(\frac{\partial^3}{\partial x^3}\Phi(0, 0, z)x^3 + \frac{\partial^3}{\partial y^3}\Phi(0, 0, z)y^3 + 3\frac{\partial^2}{\partial x^2}\frac{\partial}{\partial y}\Phi(0, 0, z)x^2y \right. \\ & \left. + 3\frac{\partial}{\partial x}\frac{\partial^2}{\partial y^2}\Phi(0, 0, z)xy^2\right)\end{aligned} \tag{2.101}$$

I define $\Phi(0, 0, z) = \phi(z)$. In efforts to completely describe the magnetic potential in terms of its on-solenoid-axis components, and their derivatives, one can Taylor expand $\phi(z)$ to

third order as

$$\phi(z) = \phi(0) + \frac{\partial\phi(0)}{\partial z}z + \frac{1}{2}\frac{\partial^2\phi(0)}{\partial z^2}z^2 + \frac{1}{6}\frac{\partial^3\phi(0)}{\partial z^3}z^3 \tag{2.102}$$

As described in the first section, the potential energy density of the diamagnetic sphere in the solenoid's magnetic field **B** depends on B^2, which can conveniently be described using the magnetic scalar potential:

$$B^2(x,y,z) = \mathbf{B}\cdot\mathbf{B} = \left(\frac{\partial}{\partial x}\Phi(x,y,z)\right)^2 + \left(\frac{\partial}{\partial y}\Phi(x,y,z)\right)^2 + \left(\frac{\partial}{\partial z}\Phi(x,y,z)\right)^2 \tag{2.103}$$

Up to second order in the coordinates, substitution of equations 2.101 and 2.102 into equation 2.103 yields after a great deal of algebraic manipulation

$$\begin{aligned} B^2(x,y,z) =& \left(\frac{1}{4}\Big(\frac{\partial^2\phi(0)}{\partial z^2}\Big)^2 - \frac{1}{2}\frac{\partial\phi(0)}{\partial z}\frac{\partial^3\phi(0)}{\partial z^3}\right)x^2 \\ &+ \left(\frac{1}{4}\Big(\frac{\partial^2\phi(0)}{\partial z^2}\Big)^2 - \frac{1}{2}\frac{\partial\phi(0)}{\partial z}\frac{\partial^3\phi(0)}{\partial z^3}\right)y^2 \\ &+ \left(\frac{\partial\phi(0)}{\partial z}\right)^2 + 2\frac{\partial\phi(0)}{\partial z}\frac{\partial^2\phi(0)}{\partial z^2}z + \left(\Big(\frac{\partial^2\phi(0)}{\partial z^2}\Big)^2 + \frac{\partial\phi(0)}{\partial z}\frac{\partial^3\phi(0)}{\partial z^3}\right)z^2 \end{aligned} \tag{2.104}$$

Equation 2.104 can be simplified in the following manner, yielding

$$B^2(r,z) = B^2 + 2BB'z + \left(\frac{1}{4}B'^2 - \frac{1}{2}BB''\right)r^2 + \left(B'^2 + BB''\right)z^2 \tag{2.105}$$

where the radial coordinate $r = \sqrt{x^2+y^2}$ and $B = \frac{\partial\phi(0)}{\partial z}$, $B' = \frac{\partial^2\phi(0)}{\partial z^2}$, and $B'' = \frac{\partial^3\phi(0)}{\partial z^3}$ are the z-components of the on-axis magnetic field, the first z-derivative of the on-axis magnetic field, and the second z-derivative of the on-axis magnetic field at the levitation point, respectively.

Figure 2.15 shows a plot of the potential energy of a ^{4}He drop with radius $R_0 = 1$ mm in Earth's gravitational and the magnetic field produced by the superconducting solenoid used in this thesis. What can be noticed immediately is that there are local potential minima

– levitation points – at each of the three solenoid currents used to generate the plots in figure 2.15. The magnetic trap is ~ 10 pJ deep, corresponding to a trap depth of $\sim 10^{12}$ Kelvin. As the current flowing through the solenoid is increased from 115.8 A to 118.0 A, the levitation point moves upward against gravity, and the shape of the contours near the levitation point change from prolate to oblate. Note that for the potential energy contours shown, the conversion between current and magnetic field strength is 7.81 A/T at the magnet's center. The ability to change the shape of the trap is useful because it allows one to change the shape of the levitated drop.

At the levitation point $(r = 0, z = 0)$, the z-direction equilibrium condition can be explicitly written down as

$$-\frac{\partial U_{\mathrm{D}}}{\partial z}\bigg|_{z=0} = \frac{\chi_{\mathrm{vol}}}{2\mu_0}\frac{\partial}{\partial z}B^2(r,z) - \rho g\bigg|_{z=0} = 0 \tag{2.106}$$

From equation 2.106, one finds that in order to suspend a magnet object in a gravitational field

$$\frac{\mu_0 \rho g}{\chi_{\mathrm{vol}}} = BB' \tag{2.107}$$

The necessary $|BB'| = 20.7\ \mathrm{T}^2/\mathrm{cm}$ for a ^{4}He drop.

To achieve stability of the equilibrium point defined by equation 2.106, one must ensure $\frac{\partial^2}{\partial r^2}U_{\mathrm{D}}(r,z), \frac{\partial^2}{\partial z^2}U_{\mathrm{D}}(r,z) > 0$; i.e., that the r-direction and z-direction curvatures of the potential energy density are positive. Positive curvature is guaranteed for a diamagnet with $\chi_{\mathrm{vol}} < 0$.

For sufficiently low magnet currents, the gravitational force is not balanced by the magnetic force, so there is no levitation point. For sufficiently high magnet currents, radial stability is lost and a drop cannot be trapped (note the trend for increasing current in figure 2.15).

It is worth noting that it may be possible to levitate drops of ^{3}He, as well. However, the diamagnetic response (which results from the electronic orbitals) is partially offset by

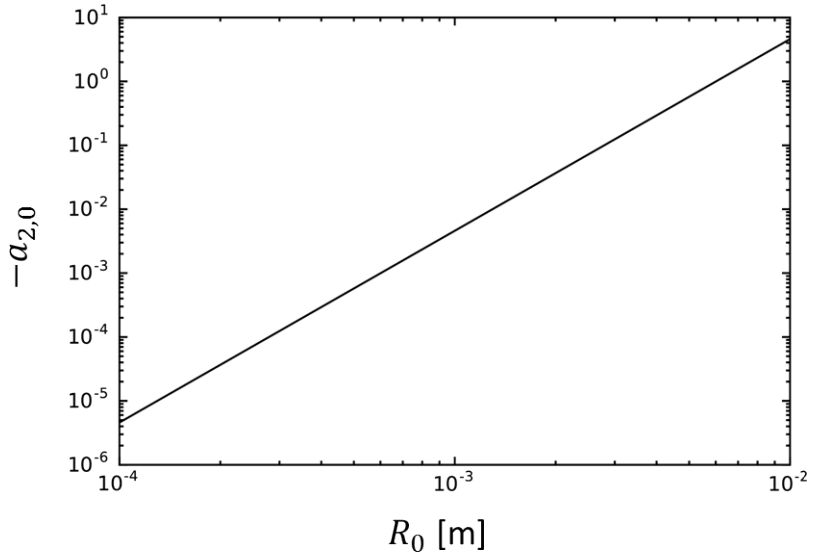

Figure 2.16: The $Y_2^0(\theta, \phi)$ spherical harmonic deformation amplitude of a drop versus the drop's unperturbed radius. This curve was generated using a magnet current of 118 A.

the paramagnetic response of the ^{3}He nucleus, which has spin 1/2. In thermal equilibrium, the paramagnetic response increases as the temperature is decreased, and would render the liquid ^{3}He paramagnetic ($\chi_{\text{vol}} > 0$), and hence untrappable, for $T \sim 1$ K [129, 130, 131]. Thus, it could become necessary to drive the ^{3}He sample with microwaves to effectively average out the nuclear spin before diamagnetic levitation becomes possible.

Magnetic Field-Induced Static Deformations of a Levitated Helium Drop

By inspecting figure 2.15, it is clear that it is possible to change the shape of the levitated drop by varying the current in the solenoid. As elaborated upon in section 2.6.1, the shape of the levitated drop can affect the frequencies of the WGMs in a significant manner and lift a huge degeneracy of WGMs. To determine the shape of the drop, the surface tension contribution to the drop's energy must be added to the gravitational and magnetostatic energy contributions and the resulting total energy must be minimized. Next, I follow reference [126] and review a derivation of the distortion of a levitated drop due to the magnetic trap. Using the expansion from 2.169, and assuming that the distortions cause a change in the radius that is small compared to the radius itself, the radius $R(\theta, \phi)$ of the

drop can be expressed as

$$R(\theta,\phi) = R_0\left(1 + a_{0,0}Y_0^0(\theta,\phi) + a_{2,0}Y_2^0(\theta,\phi)\right) \tag{2.108}$$

where the term $a_{0,0}Y_0^0$ is necessary to ensure the volume of the drop remains constant when $a_{2,0} \neq 0$. To second order in the expansion amplitudes $a_{0,0}$ and $a_{2,0}$, the volume of the drop can be written as

$$V = \frac{4}{3}\pi R_0^3\left(1 + \frac{3a_{0,0}}{2\sqrt{\pi}} + \frac{3a_{0,0}^2}{4\pi} + \frac{3a_{2,0}^2}{4\pi}\right) \tag{2.109}$$

The volume of the drop should be independent of $a_{2,0}^2$ up to second order, which can be achieved by setting $a_{0,0} = -a_{2,0}^2/(2\sqrt{\pi})$. The energy stored in the drop as a result of surface tension $E_\mathrm{s} = \sigma S$, where S is the surface area. This can be written as

$$E_\mathrm{s} = 4\pi\sigma R_0^2\left(1 + \frac{a_{2,0}^2}{2\pi}\right) \tag{2.110}$$

to lowest order in $a_{2,0}$. On the other hand, the volume energy, which can be found by integrating the potential energy density of equation 2.95 is

$$E_\mathrm{V} = \frac{4\pi r_0^5}{15}\left((k_z + 2k_r) - \sqrt{5\pi}\,(k_\mathrm{r} - k_\mathrm{z})\,a_{2,0} + (2k_\mathrm{r} + 5k_\mathrm{z})\,\frac{a_{2,0}^2}{7}\right) \tag{2.111}$$

where I have made use of the spring constants k_r and k_z associated with the center-of-mass motion and defined in equations 2.114 and 2.115.

Minimization of the total energy $E_\mathrm{s} + E_\mathrm{V}$ as a function of of $a_{2,0}$ gives

$$a_{2,0} = \frac{14}{3}\sqrt{\frac{\pi}{5}}\frac{(k_\mathrm{r} - k_\mathrm{z})\,R_0^3}{(2k_\mathrm{r} + 5k_\mathrm{z})\,R_0^3 + 14\sigma}, \tag{2.112}$$

which is plotted in figure 2.16 for a magnet current of 118 A. As can be seen in figure 2.16, the amplitude of the deformation is sensitive to the unperturbed radius R_0 of the drop.

It's useful to remember that because the potential energy density was used, the spring

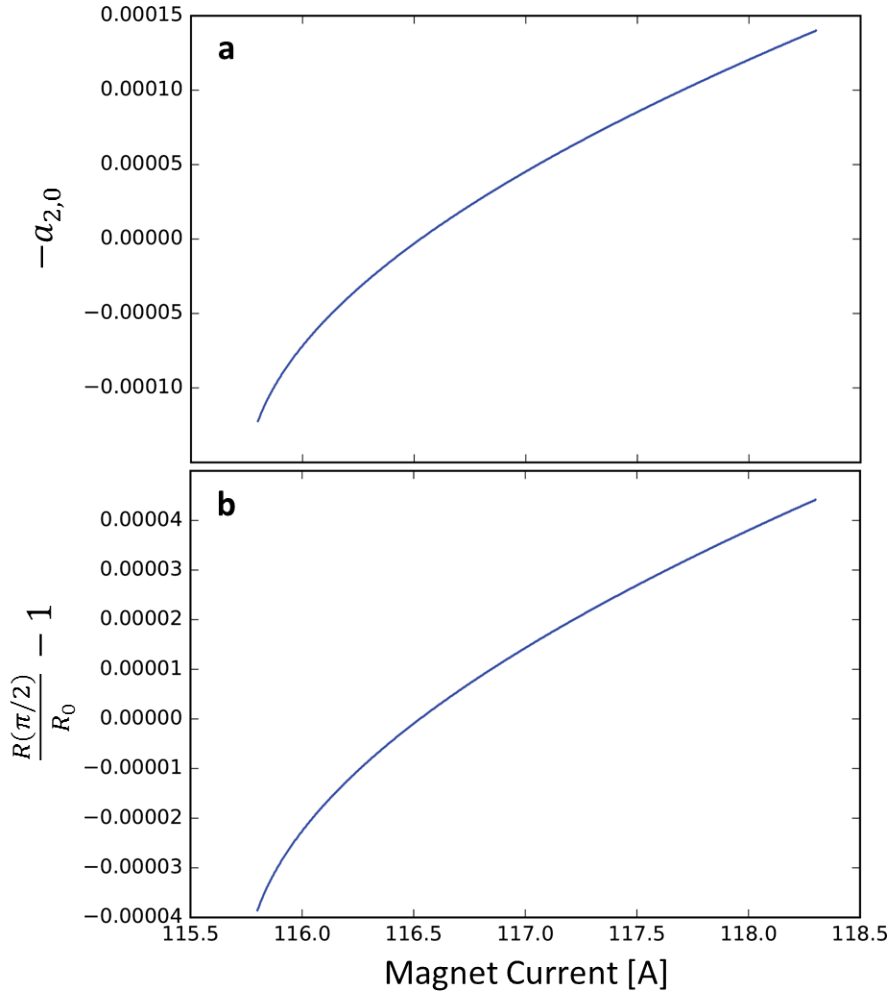

Figure 2.17: The $Y_2^0(\theta, \phi)$ spherical harmonic deformation amplitude of a drop versus the magnet current. This curve was generated for a drop with a radius of 250 μm. These plots indicate that the drop changes from oblate to prolate at a magnet current ≈ 116.5 A.

constants k_r and k_z have been defined per unit volume. For radial deflection amplitudes that are small compared to the drop radius, the volume-conserving term in equation 2.108 can be neglected. Then, the drop radius can be expressed as $R(\theta) = R_0(1 + \delta R(\theta))$, where the deflection of the drop radius $\delta R(\theta)$ can be written (using equation 2.158) as

$$\delta R(\theta) = \frac{7}{6} \frac{(k_\mathrm{r} - k_\mathrm{z})\, R_0^3}{(2k_\mathrm{r} + 5k_\mathrm{z})\, R_0^3 + 14\sigma} \left(3\cos^2\theta - 1\right) \tag{2.113}$$

For clarity, in this coordinate system when $\theta = \pi/2$, a vector that is normal to the surface of the drop at that location is orthogonal to the symmetry axis of the levitation magnet.

Using equations 2.112 and 2.113, figure 2.17a shows the Y_2^0-deflection amplitude plotted against the current flowing through the magnet and figure 2.17b shows the corresponding radial bulge at the equator ($\theta = \pi/2$) for a drop with $R_0 = 250$ μm.

2.4 Mechanical Motion of a Levitated Helium Drop

A levitated liquid helium drop can undergo several types of mechanical motion. The five types of mechanical motion that will be discussed in this thesis are: center of mass (COM) motion, surface modes, bulk modes, acoustic WGMs and rotation. Here, we give a brief overview of these modes; more detailed discussion can be found in sections 2.4.1-2.4.5.

The COM of a levitated ^{4}He drop with magnetic susceptibility $\chi_{\rm vol}$ can undergo harmonic motion in a magnetic field that traps the drop. The restoring force for this motion is provided by the magnetic trap. In practice, the COM frequency $\omega_{\rm COM}/2\pi \sim 1$ Hz, and it has no direct coupling to the optical WGMs. However, understanding the COM motion is useful for characterizing the trapping potential, and because COM motion can spoil the alignment between a laser beam and the drop's optical WGMs.

Surface modes experience a restoring force set by the drop's surface tension σ. For a drop with $R_0 \sim 1$ mm, the surface mode frequencies are $\omega_{\rm surf}/2\pi \approx 23$ Hz and "harmonics" thereof. These modes couple to optical WGMs by changing the drop circumference that the optical WGM experiences. The resulting optomechanical coupling is described by the standard optomechanical Hamiltonian. These modes are of particular interest for this thesis.

Bulk modes experience a restoring force set by the drop's bulk modulus B. For $R_0 \sim 1$ mm, the bulk mode frequencies are $\omega_{\rm bulk}/2\pi \approx 120$ kHz and "harmonics" thereof. These modes couple to optical WGMs via a combination of density *and* shape changes, and the resulting optomechanical coupling is described by the standard optomechanical Hamilto-

nian. However, they are not the main interest in this thesis.

Acoustic WGMs are bulk modes that have optimal spatial overlap with optical WGMs. The coupling g_0 between acoustic and optical WGMs is estimated in section 2.6.3, and is optimized when $\lambda_{\rm opt} = 2\lambda_{\rm aWGM}$. For $\lambda_{\rm opt} = 1550$ nm, the acoustic WGM frequency $\omega_{\rm aWGM}/2\pi \approx 315$ MHz.

The drop's rotational motion deforms the drop's shape via the centrifugal force, and thus detunes the optical WGMs. However, rotational motion is not equivalent to a harmonic oscillator, and the interaction of rotation with optical WGMs is not described by the standard optomechanical coupling Hamiltonian.

2.4.1 Center of Mass Motion in a Magneto-Gravitational Trap

To achieve stability of the equilibrium point defined by equation 2.106, one must ensure $\frac{\partial^2}{\partial r^2}U_{\rm D}(r,z), \frac{\partial^2}{\partial z^2}U_{\rm D}(r,z) > 0$; i.e., that the r-direction and z-direction curvatures of the potential energy density are positive. Then, for small displacements from equilibrium, $-\frac{\partial^2}{\partial r^2}U_{\rm D}(r,z)$ and $-\frac{\partial^2}{\partial z^2}U_{\rm D}(r,z)$ give the spring constants $k_{\rm r}$ and $k_{\rm z}$, associated with the restoring forces of the magnetic trap. As a result, the radial and axial angular frequencies of small oscillations about the equilibrium point are given by

$$\omega_{\rm r} = \sqrt{\frac{k_{\rm r}}{\rho}} = \sqrt{-\frac{\chi_{\rm vol}}{\mu_0 \rho}\left(\frac{1}{2}(B')^2 - BB''\right)} \tag{2.114}$$

and

$$\omega_{\rm z} = \sqrt{\frac{k_{\rm z}}{\rho}} = \sqrt{-\frac{2\chi_{\rm vol}}{\mu_0 \rho}\left((B')^2 + BB''\right)} \tag{2.115}$$

The drop's volume does not appear in equations 2.114 or 2.115, so the drop's oscillation frequencies are independent of its size.

The values for the axial magnetic field and its derivatives are obtained by fitting axial magnetic field strength data provided by Oxford Instruments for the solenoid used in the experiments discussed in this thesis. A magnet current $I = 116$ A is predicted to provide

$B \approx 11$ T, $B' \approx -188$ T/m, and $B'' \approx -2270$ T^2/m^2 at the levitation point $z_{\rm lev} \approx 4$ cm above the magnet's center for a ^{4}He drop with $\chi_{\rm vol} \approx -8.6 \times 10^{-7}$ ($\chi^{(\rm CGS)} \approx 1.89 \times 10^{-6}$) and $\rho = 145$ kg/m^3. In this case, we expect $\omega_{\rm r}/2\pi \approx 1.7$ Hz and $\omega_{\rm z}/2\pi \approx 1.2$ Hz.

Note that in the literature, values for the magnetic susceptibility of different elements are often given in CGS units and defined per mole (and the units are sometimes not specified clearly). The conversion to $\chi_{\rm vol}$ is given by

$$\chi_{\rm vol} = 4\pi \times 10^{-6} \frac{\rho}{M} \chi_{\rm mol}^{(\rm CGS)} \tag{2.116}$$

where M is the molar mass.

2.4.2 Surface Waves on a Levitated Helium Drop

Surface modes in a levitated drop are approximately volume-conserving and have an effective mass $\sim$ the drop's total mass. Their restoring force is set by surface tension σ, which is much weaker than the restoring force set by the bulk modulus B. As a result, one would expect $\omega_{\rm surf}$ to be small compared to $\omega_{\rm bulk}$. The drop shape distortions induced by surfaces modes are well-suited to detune optical WGMs because the surface modes alter the drop's (local) radius by an amount δR, leading to $\Delta\omega_{\rm opt} \propto \partial\omega_{\rm opt}/\partial\delta R$. This coupling between the surface modes and the optical WGMs is conceptually equivalent to the movable end-mirror optomechanical system in section 2.1.2. Small $\omega_{\rm surf}$ leads to large zero-point fluctuations $x_{\rm zpf}$, and since $g_0 = x_{\rm zpf}\partial\omega_{\rm opt}/\partial\delta R$, g_0 is large. More specifically, g_0 is large with respect to the couplings found in other mm-scale WGM resonators, and it is large compared to $\omega_{\rm surf}$.

To provide a quantitative derivation of these features, we begin with the Navier Stokes equation, which describes the behavior of a fluid with mass density field $\rho(\mathbf{r}, t)$, viscosity ν, pressure field $P(\mathbf{r}, t)$ and velocity field $\mathbf{v}(\mathbf{r}, t)$, and we apply it to the case of a levitated

^{4}He drop whose COM is at rest:

$$\rho\left(\frac{\partial \mathbf{v}}{\partial t} + \mathbf{v}\cdot\nabla\mathbf{v}\right) = -\nabla\bar{P} + \nu\nabla^2\mathbf{v} + \frac{1}{3}\nu\nabla(\nabla\cdot\mathbf{v}) \tag{2.117}$$

where

$$\bar{P} = P - \zeta\nabla\cdot\mathbf{v} \tag{2.118}$$

and $\zeta \propto \nu$ is the volume viscosity. It is useful to note the vector identity

$$\mathbf{v}\cdot\nabla\mathbf{v} = (\nabla\times\mathbf{v})\times\mathbf{v} + \frac{1}{2}\nabla\mathbf{v}^2 \tag{2.119}$$

Liquid ^{4}He becomes pure superfluid for $T \lesssim 800$ mK (which is expected for a ^{4}He drop levitated in vacuum – see section 2.5.1), so we set $\nu = 0$. Furthermore, superfluids undergo irrotational flow, which means $\nabla\times\mathbf{v} = \mathbf{0}$. In this case, equation 2.117 simplifies to

$$\rho\left(\frac{\partial \mathbf{v}}{\partial t} + \frac{1}{2}\nabla\mathbf{v}^2\right) = -\nabla P \tag{2.120}$$

The drop's normal modes of oscillation consist of small density and pressure fluctuations about their equilibrium values, such that

$$P(\mathbf{r},t) = P_0 + \delta P(\mathbf{r},t) \tag{2.121}$$

$$\rho(\mathbf{r},t) = \rho_0 + \delta\rho(\mathbf{r},t) \tag{2.122}$$

where P_0 and ρ_0 are the equilibrium pressure and density, respectively, and $\delta P \ll P_0,\ \delta\rho \ll \rho_0$. Because δP and $\delta\rho_0$ result only in small velocities, and terms that are quadratic in the fluctuations are also small, substituting equations 2.121 and 2.122 into equation 2.120 gives a further simplified form of the Navier Stokes equation:

$$\rho_0\frac{\partial \mathbf{v}}{\partial t} = -\nabla\delta P \tag{2.123}$$

The fluid flow in the drop must also satisfy the mass conservation equation

$$\frac{\partial \rho}{\partial t} = -\nabla \cdot (\rho \mathbf{v}) \tag{2.124}$$

which after substitution of equations 2.121 and 2.122 into equation 2.124 gives

$$\frac{\partial}{\partial t}\delta\rho = -\rho_0 \nabla \cdot \mathbf{v} \tag{2.125}$$

Equations 2.123 and 2.125 determine the fluid flow, and they are connected through the relation

$$\delta P(\mathbf{r}, t) = \left(\frac{\partial P_0}{\partial \rho_0}\right)_S \delta\rho(\mathbf{r}, t) \tag{2.126}$$

where the subscript S denotes constant entropy; here, we are considering oscillations that are adiabatic with respect to microscopic thermal fluctuations.

In what proceeds, I follow references [59, 132] and derive the surface mode spectrum. Since $\nabla \times \mathbf{v} = \mathbf{0}$, the velocity field $\mathbf{v}$ can be described by a scalar potential such that

$$\mathbf{v} = \nabla\psi(\mathbf{r}, t) \tag{2.127}$$

Equations 2.123, 2.125 and 2.126 can be combined to find the following wave equation for $\psi(\mathbf{r}, t)$:

$$\frac{\partial^2}{\partial t^2}\psi(\mathrm{r}, \theta, \phi, t) - u_\mathrm{c}^2 \nabla^2 \psi(\mathrm{r}, \theta, \phi, t) = 0 \tag{2.128}$$

where we have used the gauge invariance of ψ to absorb a spatially constant offset [59], and $u_\mathrm{c} = \sqrt{\left(\frac{\partial P_0}{\partial \rho_0}\right)_S}$ is the speed of sound in the liquid.

Because the liquid drop is levitated, one would expect the drop's surface tension to minimize its surface area and thus yield a spherical drop. As a result, it is natural to use a spherical polar coordinate system with its origin at the drop's center. In this case, it is

well-known that the eigenmodes of equation 2.128 are given by

$$\psi_{q_d\ell_d m_d}(\mathrm{r},\theta,\phi,t) = A_{q_d\ell_d m_d} j_{\ell_d}(k_{q_d\ell_d}\mathrm{r}) Y_{\ell_d}^{m_d}(\theta,\phi) e^{-i\omega_{q_d\ell_d}t} \tag{2.129}$$

where $A_{q_d\ell_d m_d}$ is the mode amplitude, $j_{\ell_d}(k_{q_d\ell_d}\mathrm{r})$ is a spherical Bessel function, $Y_{\ell_d}^{m_d}(\theta,\phi)$ is a spherical harmonic and $\omega_{q_d\ell_d}$ is the surface mode frequency. The quantity q_d indexes the radial nodes of the velocity potential in the drop. For surface modes, there are no radial nodes, so $q_d = 0$; I will suppress it during the subsequent derivation of the surface mode spectrum and restore it when we consider bulk modes.

There are two boundary conditions that can now be applied to ψ, in order to find ω_{ℓ_d}. The first boundary condition relates the velocity at the drop's surface to the time-derivative of its surface distortion, and the second boundary condition relates the pressure at the drop's surface to the additional pressure from surface tension that is caused by the surface distortion. Towards the goal of finding ω_{ℓ_d}, it is useful to parameterize the drop's shape distortion in terms of its local radius R in the following manner

$$R(\theta,\phi,t) = R_0 + \delta R(\theta,\phi,t) \tag{2.130}$$

where R_0 is the equilibrium drop radius and δR describes the drop's surface distortion.

For $\delta R \ll R_0$, the first boundary condition requires that

$$\frac{\partial}{\partial r}\psi(\mathrm{r},\theta,\phi,t)\bigg|_{r=R_0} = \frac{\partial}{\partial t}\delta R(\theta,\phi,t) \tag{2.131}$$

In order to apply the second boundary condition, one must account for the pressure inside and outside the drop. The pressure inside the drop must equal the pressure outside the drop p_{out} plus the contribution from the surface tension σ. The Young-Laplace equation

expresses this equality as

$$P(\mathbf{r},t) = P_{\text{out}} + \sigma\left(\frac{1}{R_1} + \frac{1}{R_2}\right) \tag{2.132}$$

where R_1 and R_2 are the principle radii of curvature that describe the curvature at the point $\mathbf{r}$ lying on the drop's surface. Here, I set $P_{\text{out}} = 0$, since the drop is in vacuum. In reference [133], Landau and Lifshitz provide an expansion of $1/R_1 + 1/R_2$ to leading order in δR:

$$\frac{1}{R_1} + \frac{1}{R_2} = \frac{2}{R_0} - \frac{1}{R_0^2}\left(2 + \nabla^2_{\theta\phi}\right)\delta R \tag{2.133}$$

where $\nabla^2_{\theta\phi}$ is the angular part of the Laplacian in a spherical coordinate system. Linearizing equation 2.132 by substituting into it equation 2.121, then substituting into it equation 2.133 gives

$$P_0 = \frac{2\sigma}{R_0} \tag{2.134}$$

$$\delta P = -\frac{\sigma}{R_0}\left(2 + \nabla^2_{\theta\phi}\right)\delta R \tag{2.135}$$

The velocity potential ψ allows δP to be expressed as [59]

$$\delta P = -\rho_0 \frac{\partial \psi}{\partial t} \tag{2.136}$$

At the drop's surface, equations 2.135 and 2.136 should be equal, which gives:

$$\rho_0 \left.\frac{\partial \psi}{\partial t}\right|_{\mathrm{r}=R_0} = \frac{\sigma}{R_0^2}(2 + \nabla^2_{\theta\phi})\delta R \tag{2.137}$$

After taking the time derivative of equation 2.137 and substituting into it the first boundary condition (equation 2.131), we find the second boundary condition:

$$\rho_0 \left.\frac{\partial^2 \psi}{\partial t^2}\right|_{\mathrm{r}=R_0} = \frac{\sigma}{R_0^2}(2 + \nabla^2_{\theta\phi}) \left.\frac{\partial \psi}{\partial \mathrm{r}}\right|_{\mathrm{r}=R_0} \tag{2.138}$$

Recalling the fact that

$$\nabla^2_{\theta\phi} Y^{m_d}_{\ell_d}(\theta,\phi) = -\ell_d(\ell_d+1) Y^{m_d}_{\ell_d}(\theta,\phi) \tag{2.139}$$

substituting the expression for the normal mode's velocity potential (equation 2.129) into equation 2.138 allows one to read off the surface wave frequencies $\omega_{\rm surf}$

$$\omega_{\ell_d} = \omega_{\rm surf} = \sqrt{\frac{\ell_d(\ell_d-1)(\ell_d+2)\sigma}{\rho_0 R_0^3}} \tag{2.140}$$

For a superfluid ^{4}He drop with $\rho = 145$ kg/m^3, $\sigma = 3.75\times10^{-4}$ J/m^2 and $R_0 = 1$ mm, the fundamental surface mode has $\omega_{\ell_d=2}/2\pi \approx 23$ Hz. Similar to the optical WGMs, these surface modes are $(2\ell_d+1)$-fold degenerate in a spherical drop. It is important to note that $\ell_d \geq 2$. This is because $\ell_d = 0$ corresponds to breathing modes, which are restored by B. The $\ell_d = 1$ mode corresponds to translation of the drop's COM, which equation 2.140 correctly predicts to be zero (i.e. in the absence of a trap).

The $(2\ell_d+1)$-fold degeneracy of surface modes can be broken by deforming the drop from a sphere to an oblate or prolate spheroid. Such deformation can occur depending on the magnetic field that is used to levitate the drop. For more details on static deformation of a levitated drop induced by the magnetic trap, see section 2.3.4.

For a surface mode with index $\ell_{\rm d}$, $2\pi R_0 = \ell_{\rm d}\lambda_{\rm d}$, where $\lambda_{\rm d}$ is the surface mode wavelength. The index $\ell_{\rm d}$ is associated with the surface mode angular momentum, and there is another index $m_{\rm d}$ that is associated with the projection of the angular momentum onto the symmetry axis of the levitation magnet. The index $m_{\rm d}$ takes on all integer values such that $|m_{\rm d}| < \ell_{\rm d}$, so there are $2\ell_{\rm d}+1$ modes for each $\ell_{\rm d}$. The index $m_{\rm d}$ can be associated with the wave traversing different great circles around the drop. In a spherically-symmetric drop, the circumference is the same for all great circles, so all $2\ell_{\rm d}+1$ modes satisfy $2\pi R_0 = \ell_{\rm d}\lambda_{\rm d}$ with the same $\lambda_{\rm d}$, and thus all the modes are degenerate (which is why $m_{\rm d}$ was suppressed in the derivation of equation 2.140). However, in a non-spherical drop every great circle

does not have the same circumference, but the $\pm m_{\rm d}$ mode pair does. Then, for each $\pm m_{\rm d}$ mode pair, $\ell_{\rm d}\lambda_{\rm d}^{(m)}$ must equal the drop circumference at the corresponding great circle. As a result of the drop's shape deformation, a surface mode that was $(2\ell_d + 1)$-fold degenerate in a spherical drop is split into $\ell_d + 1$ modes in a spheroidal drop. The $\ell_d + 1$ modes consist of a non-degenerate mode with $m_{\rm d} = 0$ and ℓ_d doubly degenerate mode pairs with index $\pm m_{\rm d}$. This double degeneracy is a result of time-reversal symmetry, and would not be present in a spinning drop.

Surface Mode Loss in a ^{4}He Drop

At temperatures $T < 450$ mK (which is expected for a liquid helium drop levitated in vacuum – see section 2.5.1), surface modes are expected to decay primarily via interactions with phonons in the bulk. However, for a drop with radius R, the form of the surface mode (ripplon) damping depends on where or not the mean-free-path $L_{\rm mfp}$ of phonons in the liquid is such that $L_{\rm mfp} \ll R$ (viscous regime of phonon propagation) or $L_{\rm mfp} \gg R$ (molecular regime of phonon propagation). A drop with $T < 450$ mK has $L_{\rm mfp} \gg R$. In what follows, we estimate $L_{\rm mfp}$, and briefly describe the ripplon-phonon interactions that lead to surface mode damping in the molecular (ballistic) phonon propagation regime.

$L_{\rm mfp}$ is temperature dependent and given by [83]

$$L_{\rm mfp} \approx \frac{3\mu(T)\rho_0}{\rho_{\rm n}(T)u_{\rm c}} \tag{2.141}$$

where $\mu(T)$ is the dynamic viscosity (associated with the liquid helium's normal fluid component, which is non-zero for $T > 0$), ρ_0 is the liquid's mass density, $\rho_{\rm n}(T)$ is the mass density associated with the liquid helium's normal fluid component and $u_{\rm c}$ is the speed of sound.

For $T < 450$ mK, the roton contribution to $\rho_{\rm n}(T)$ is negligible (see section 2.3.1) [84],

leaving only the contribution from phonons, which is given by

$$\frac{\rho_{\rm n}(T)}{\rho_0} = \frac{2\pi^2 k_{\rm B}^4}{45\hbar^3 u_{\rm c}^5 \rho_0} T^4 \tag{2.142}$$

As reported in reference [134, 135], Whitworth and Shoenberg measured the heat flow of liquid helium in narrow tubes and found $L_{\rm mfp} \approx 1.4$ mm at $T \approx 455$ mK, and it agrees well with three-phonon scattering theory. Using equations 2.142 and 2.141 in order to estimate $L_{\rm mfp}$ for phonons in a levitated drop we can write

$$L_{\rm mfp}(T_2) = \frac{\mu_2(T_2)}{\mu_1(T_1)} \left(\frac{T_1}{T_2}\right)^4 L_{\rm mfp}(T_1) \tag{2.143}$$

Using Whitworth and Shoenberg's measured value $L_{\rm mfp}(T_1 = 455{\rm mK}) = 1.4$ mm, then for a helium drop with $T_2 = 330$ mK (which is the temperature of the coldest drop we have measured via optical modes to date - see section 4.3), $L_{\rm mfp} \approx 4.5$ mm, where we have assumed $\mu_2(T_2)/\mu_1(T_1) \approx 1$. This suggests that phonons propagate ballistically in a drop with $T = 330$ mK and $R = 250$ μm.

Roche and colleagues studied the damping of ripplons on a flat surface of liquid helium due to their scattering interactions with ballistic phonons in the liquid's bulk. In this model, ripplons decay via a one-ripplon-two-phonon scattering process, in which a thermal phonon scatters from the liquid's surface, and is Doppler-shifted to a higher energy [136]. The scattered phonon then carries away the energy it acquired from the ripplon, and thermalizes with a vessel at temperature T, inside which the liquid helium is contained. Roche and colleagues calculated the resulting surface mode lifetime $\tau_{\rm molecular}$, and found

$$\tau_{\rm molecular} = \frac{60\rho_0}{\pi^2 \hbar \mathcal{K}} \left(\frac{\hbar u_{\rm c}}{k_{\rm B} T}\right)^4 \tag{2.144}$$

where the ripplon wavenumber $\mathcal{K}$ is given by [83]

$$\mathcal{K} = \frac{\sqrt[3]{\ell_d(\ell_d-1)(\ell_d+2)}}{R} \tag{2.145}$$

If we apply this model to a ^{4}He drop with $R = 250$ μm, $T = 330$ mK, and $\rho_0 \approx 145$ kg/m^3, then $\tau_{\rm molecular} \approx 1$ s for the $\ell_d = 2$ surface mode.

2.4.3 Bulk Oscillations of a Levitated Helium Drop

Another class of oscillations are bulk modes, which are restored by the bulk modulus of the drop. Bulk modes are not volume-conserving and, as mentioned earlier, have a restoring force set by B, which is much stronger than the restoring force set by σ. Consequently, one would expect bulk modes to have $\omega_{\rm bulk} \gg \omega_{\rm surf}$. The drop shape distortions induced by bulk modes are also suited to detune optical WGMs because they produce shape *and* density distortions in the drop. Since $\omega_{\rm bulk} > \omega_{\rm surf}$, one might expect bulk modes to have smaller zero-point fluctuations $x_{\rm zpf}$, and hence smaller g_0.

To provide a quantitative description of bulk modes in superfluid ^{4}He, we can start with equation 2.129, since a bulk mode is also a solution to the linearized Navier Stokes equation. Combining equation 2.123 with the time derivative of equation 2.125 gives

$$\nabla^2\delta\rho(r,\theta,\phi,t) - \frac{1}{u_{\rm c}^2}\frac{\partial^2}{\partial t^2}\delta\rho(r,\theta,\phi,t) = 0, \tag{2.146}$$

A bulk mode that satisfies equation 2.146 is given by

$$\delta\rho = \rho_0 B_{q_d\ell_d m_d} j_{\ell_d}(k_{q_d\ell_d}\mathrm{r}) Y_{\ell_d}^{m_d}(\theta,\phi) e^{-i\omega_{q_d\ell_d}t} \tag{2.147}$$

Substituting equation 2.147 into equation 2.146 gives the dispersion relation $\omega_{q_d\ell_d} = u_{\rm c} k_{q_d\ell_d}$.

The bulk modes are investigated in the limit that the restoring force from surface tension is negligible with respect to the restoring force from the bulk modulus. As a result, there

is no excess pressure at the free surface of the drop, and equation 2.135 gives $\delta\rho = 0$ at $r = R_0$ for $\sigma = 0$ [132]. Setting equation 2.147 to zero requires

$$j_{\ell_d}(k_{q_d\ell_d}R_0) = 0, \tag{2.148}$$

which specifies the spectrum of bulk oscillations of the drop. In order to find the frequencies that satisfy equation 2.148, $k_{q_d\ell_d}R_0$ must equal ξ_{q_d,ℓ_d}, the zeros of the ℓ_d-th spherical Bessel function. Then,

$$\omega_{q_d,\ell_d} = \frac{u_c}{R_0}\xi_{q_d,\ell_d} \tag{2.149}$$

ξ_{q_d,ℓ_d} can be found numerically (e.g. using Mathematica), but reference [137] (page 317) gives a useful expansion for $\xi_{q_d=1,\ell_d}$ for $\ell_d \gg 1$. Using this expansion, the expression for the $q_d = 1$ bulk mode frequency is

$$\omega_{q_d=1,\ell_d} \approx \frac{u_c}{R_0}\left[\ell_d + \frac{1}{2} + 1.86\left(\ell_d + \frac{1}{2}\right)^{1/3} + 1.03\left(\ell_d + \frac{1}{2}\right)^{-1/3} - 0.004\left(\ell_d + \frac{1}{2}\right)^{-1}\right] \tag{2.150}$$

For a ^{4}He drop with $R_0 = 1$ mm and $u_c = 238$ m/s, the lowest order sound mode with $\{q_d = 1, \ell_d = 0\}$, has a frequency $\omega_{1,0}/2\pi \approx 120$ kHz, which is $\sim 10^4$ larger than the frequency of the lowest order surface mode. Similar to the optical WGMs, these sound modes are $(2\ell_d + 1)$-fold degenerate in a spherical drop. There are a countably infinite number of bulk (sound) modes $q_d = 1, 2, 3...$ for each $\ell_d = 0, 1, 2, ...$

2.4.4 Acoustic WGMs in a Levitated Helium Drop

An acoustic whispering gallery mode is an acoustic normal mode with pressure antinodes confined near the periphery of the resonator. As for optical WGMs, acoustic WGMs have large $\ell_d \sim 2\pi R_0/\lambda_{\mathrm{aWGM}}$, and only have significant coupling to optical WGMs when $\lambda_{\mathrm{opt}} = 2\lambda_{\mathrm{aWGM}}$, where λ_{aWGM} is the acoustic WGM wavelength. This is because otherwise the optical WGM intensity antinodes would overlap with an equal number of acoustic

WGM pressure nodes and antinodes. The issue of mode orthogonality necessitating the relationship $\lambda_{\rm opt} = 2\lambda_{\rm aWGM}$ has been discussed in detail in the Harris group's published work with superfluid-filled fiber cavities [35, 36, 37]. Physically, the coupling arises because the acoustic WGM modulates the index of refraction (by modulating the pressure, and so the density) along the path of the optical WGM. Although these modes are not studied here, we note that for $\lambda_{\rm opt} = 1550$ nm, $\omega_{\rm aWGM}/2\pi \approx 315$ MHz.

2.4.5 Rotations of Liquid Drops

The rotational motion of a levitated helium drop depends on which helium isotope is used, because at the expected temperatures (see section 2.5.1) ^{3}He will not be superfluid, but ^{4}He will be. What they do have in common is that their rotational motion is not described by a simple harmonic oscillator, because it does not have a restoring force. As a result, coupling between rotation and optical WGMs is not described by the standard optomechanical Hamiltonian.

A levitated ^{3}He drop in its normal state will be able to undergo rigid-body rotation. The resulting centrifugal force will lead to a deflection of the drop's radius, which will detune optical WGMs.

On the other hand, the velocity field in a superfluid ^{4}He drop must be irrotational, so it cannot undergo rigid-body rotation. Instead, angular momentum in superfluid ^{4}He exists in the form of vortices with quantized circulation. The resulting velocity field throughout the drop will still be non-zero at the drop's surface, and so will still result in a centrifugal force-induced radial bulge, and thus optical WGMs will be detuned.

For both ^{3}He and ^{4}He, the coupling between the drop's rotation and optical WGMs is not described by the standard optomechanical coupling Hamiltonian. More specifically, $\Delta\omega_{\rm opt}^{\rm (rot)} \propto \delta R \propto L_{\rm z}^2$ is the drop's radial deflection that results from its rotation.

Rigid-Body Rotation of a Normal Liquid

In 1863, Plateau was the first to study the dynamics of a rotating liquid drop bound together by surface tension [138]. He submerged a liquid drop into another liquid with which it could not mix. The two liquids had approximately the same density, but the drop had a significantly larger viscosity than the surrounding liquid. Matching the density of the drop with the surrounding liquid ensured that the drop would not fall during experiments. A rod that penetrated the drop was used to define the rotation axis, and was rotated at a rate Ω. Consequently, the drop rotated as well, and could undergo significant deviations from its spherical equilibrium shape at $\Omega = 0$. As Ω was increased, Plateau observed a set of equilibrium shapes of the drop. Beyond a certain Ω, he observed toroid-shaped configurations that would tend to break into smaller droplets. Due in part to qualitative similarities between Plateau's rotating liquid drop held together by surface tension, and self-gravitating astrophysical bodies, there have been many theoretical studies of the equilibrium configurations of rotating drops and their stability [80, 81, 82, 139].

It is known from numerical simulations that when undergoing rigid body rotation, an isolated drop whose shape is determined by surface tension evolves from a spherical configuration when it is stationary, through a family of axisymmetric configurations that progressively flatten at the poles while developing a bulge at the equator. However, axisymmetric isolated drops are only stable up to a certain values of Ω, beyond which a series of bifurcations occur that lead to non-axisymmetric stable equilibrium shapes referred to as two-lobe (peanut-like), three-lobe, four-lobe, five-lobe and six-lobe [81, 139]. Furthermore, at sufficiently large Ω, a drop can evolve into an unstable torus configuration, topologically distinct from spheroids. However, there is no analytic theory which predicts this rich bifurcation behavior. It is not known if the series of spontaneous bifurcations is finite or infinite, or if it includes stable equilibria that are topologically distinct from the sphere.

In order to describe the shape distortion that a levitated drop with angular velocity $\mathbf{\Omega}$ experiences, we again start with the Navier Stokes equation (equation 2.117). For small

$\mathbf{\Omega}$, the deformation of the drop δR is small compared to the drop's radius R_0, which leads to small $\mathbf{v}$. Consequently, the non-linear velocity terms in equation 2.117 are neglected. Assuming an incompressible fluid, the drop's volume is conserved and equation 2.124 gives $\nabla \mathbf{v} = 0$, which further simplifies equation 2.117. Here, we study the drop's shape in a frame rotating at $\mathbf{\Omega}$, in which we must take into account the apparent forces on the liquid from centripetal acceleration. In this frame, the motion of the fluid is determined by

$$\frac{\partial}{\partial t}\mathbf{v} + \frac{1}{\rho_0}\nabla P = -\mathbf{\Omega} \times (\mathbf{\Omega} \times \mathbf{r}) + 2\mathbf{v} \times \mathbf{\Omega} \tag{2.151}$$

where the first and second terms on the right hand side are the acceleration associated with the centrifugal force and the Coriolis force, respectively. From here, I will essentially review a derivation in reference [133]. Using vector identities, the centrifugal force term can be written as the gradient of a scalar in the following manner

$$-\mathbf{\Omega} \times (\mathbf{\Omega} \times \mathbf{r}) = \nabla \frac{1}{2}(\mathbf{\Omega} \times \mathbf{r})^2 \tag{2.152}$$

and the pressure can be written in terms of a reduced pressure

$$\mathcal{P} = P - \frac{\rho_0}{2}(\mathbf{\Omega} \times \mathbf{r})^2 \tag{2.153}$$

Equation 2.151 can now be written in a simpler form:

$$\frac{\partial}{\partial t}\mathbf{v} + \frac{1}{\rho_0}\nabla \mathcal{P} - 2\mathbf{v} \times \mathbf{\Omega} = 0 \tag{2.154}$$

It is useful to solve this problem in spherical coordinates. In the coordinate system of the problem, $\mathbf{\Omega}$ is parallel to the z-axis in a Cartesian system, so θ is the angle between $\mathbf{\Omega}$ and r. In the rotating frame (assuming the drop is undergoing rigid-body rotation) $\mathbf{v} = 0$ and

the pressure in the drop is

$$P(\mathbf{r}) = P_0 + \frac{\rho_0}{2}\Omega^2 r^2 \sin^2\theta \tag{2.155}$$

Here we have made use of the fact that the term ∇P allows the addition of an arbitrary pressure constant p_0, which is to be determined by the appropriate boundary conditions [59]. As in section 2.4.2 (equation 2.130, but now dropping the time dependence), the radial deflection δR can be expressed in terms of spherical harmonics in the following manner

$$\delta R(\theta,\phi) = \sum_{\ell_\mathrm{d}\geq 2} a_{\ell_\mathrm{d}} Y_{l,m_\mathrm{d}=0}(\theta,\phi) \tag{2.156}$$

Here, $m_\mathrm{d} = 0$ is chosen to restrict the deflections to be axisymmetric. Substituting the deflection into the Young-Laplace equation provides the deflection amplitude a_{ℓ_d}. The substitution is valid at $r = R_0$, where R_0 is the unperturbed drop radius, for small deflection amplitudes. As a result, the deflection amplitude at small rotation rates is given by

$$a_{\ell_\mathrm{d}=2} = -\frac{\sqrt{\pi}}{6\sqrt{5}}\frac{\rho_0 R_0^4 \Omega^2}{\sigma} \tag{2.157}$$

where σ is the surface tension and ρ_0 is the unperturbed density of the fluid. Since

$$Y_2^0(\theta,\varphi) = \frac{1}{4}\sqrt{\frac{5}{\pi}}\left(3\cos^2\theta - 1\right) \tag{2.158}$$

the deflection of the radius $\delta R(\theta)$ at the equator ($\theta = \pi/2$) is given by

$$\delta R(\pi/2) = \frac{1}{24}\frac{\rho_0 R_0^4 \Omega^2}{\sigma} \tag{2.159}$$

A normal fluid drop undergoing rigid-body rotation will experience a static distortion due to centrifugal forces, which will cause the equator to change in circumference, and thus induce a static detuning of the optical WGMs. In addition, as described in section 2.3.4, a sufficiently large levitated drop can be statically distorted into a prolate or oblate spheroid

with the appropriate tuning of the magnetic field strength. A static distortion of this sort– induced by rotation, or by tuning the shape of the magneto-gravitational trap – is similar in effect to an $\hat{S}_z^2$ term in a spin Hamiltonian and breaks the $(2\ell + 1)$-fold degeneracy of an optical WGM. If in equation 2.178, the term $\delta R_{\rm zpf}$ is replaced by a change of radius δR that is the result of rotation or trap-induced asphericity, one can estimate the impact of this static distortion on the optical WGM frequencies. A family of WGMs with index ℓ splits into $\ell+1$ WGMs with distinct frequencies. There is one non-degenerate mode with $m = 0$, but the rest of these remain doubly degenerate because this splitting is only sensitive to$|m|$; the resulting frequency shifts are proportional to m^2.

Rotation in a Superfluid

As mentioned in section 2.3.1, superfluid liquid helium exhibits many unique qualities. Perhaps one of the most striking features is the presence of quantized vortices in a superfluid with angular momentum. In the 1970's and 1980's, Packard and colleagues at U.C. Berkeley reported the presence of arrays of quantized vortex lines in rotating cylindrical vessels of ^{4}He [75, 140]. In this work, they injected electrons into the liquid helium, which formed electron bubbles that were trapped at the locations of vortex lines for a small amount of time. The electrons could then be pulled out of the liquid with an electric field and made to strike a phosphor screen, which would emit light that could be captured for photographs. In 2014, Vilesov and colleagues at S.L.A.C. produced beams of superfluid ^{4}He nanodroplets, and scattered from them pulsed x-rays produced by a free-electron laser. They also observed vortex arrays in the superfluid [76].

When a container filled with liquid helium at temperature $T < T_\lambda$ rotates with constant angular velocity $\mathbf{\Omega}$, the two-fluid model suggests that both the normal and superfluid components can take part in the rotational motion. However, the two fluid components of the liquid in the container will behave quite differently. The normal fluid component rotates with the container, undergoing rigid-body rotation. As mentioned in section 2.4.5, the

velocity of the normal fluid $\mathbf{v}_{\rm n} = \mathbf{\Omega} \times \mathbf{r}$ and the vorticity of the normal fluid is given by $\nabla \times \mathbf{v}_{\rm n} = 2\mathbf{\Omega}$, with the origin of the coordinate system positioned on the rotation axis of the container. In the language of quantum mechanics, an atom with mass m in the normal fluid component is in a state $\Psi(\mathbf{r}) = \left|\Psi(\mathbf{r})\right| \exp\left(i\Phi(\mathbf{r})\right)$, and using the momentum operator the velocity of the particle is given by $\mathbf{v} = \hbar/m\nabla\Phi(\mathbf{r})$. Because the curl of a gradient is identically zero, the vorticity is zero. However, the result of zero vorticity for the atom does not prevent uniform rotation of the normal liquid because each particle has its own distinct velocity, each of which can combine together to mimic uniform rotation on a scale that is larger than the inter-particle spacing [141].

On the other hand, superfluids are different in that they are characterized by a single macroscopic wave function. As such, all atoms in the superfluid component occupy the same quantum state. All of the particles have the same velocity $\mathbf{v}_{\rm s}$, so the vorticity $\nabla \times \mathbf{v}_{\rm s} = \mathbf{0}$ on a macroscopic scale. Therefore, the superfluid in the container cannot rotate like a normal fluid.

At small rotation rates, the superfluid is in the Landau state, where $\mathbf{v}_{\rm s} = \mathbf{0}$ everywhere [142, 141]. However, a stationary liquid in thermal contact with a rotating vessel has a high free energy [143]; as the angular velocity of the container increases, the Landau state becomes unstable and system tends toward a lower energy state which has vortex lines of quantized circulation.

A vortex line is defined by the property that the superfluid phase $\Phi(\mathbf{r})$ changes by an integer multiple of 2π around the line. As a result, the superfluid circulates around a vortex line with a velocity that is inversely proportional to the distance from the line. Due to this scaling with distance, the superfluid density should $\rightarrow 0$ in the vortex core. Due to the evolution of the phase of a superfluid around a vortex, the line integral of the superfluid velocity around a contour P which encloses a vortex line is given by

$$\oint_P \mathbf{v}_{\rm s} \cdot {\rm d}\mathbf{l} = n\frac{h}{m} = n\kappa_0 \tag{2.160}$$

In bulk superfluid ^{4}He, vortex lines of $|n| > 1$ are unstable against decay into multiple vortex lines each with $|n| = 1$ [84].

2.5 Evaporation of Helium Drops

When a sample of liquid helium is adjacent to vacuum, the evaporation of helium atoms into the vacuum will tend to lower the temperature of the remaining liquid. This effect is widely utilized in conventional cryogenics by confining liquid helium at the bottom of a solid container and pumping the space directly above the liquid. This same evaporative cooling also occurs naturally for drops of liquid helium completely surrounded by vacuum. In experiments in which liquid helium drops are doped with atoms or molecules, the low temperatures provided by the drops serves to cool the atoms or molecules; likewise, spectroscopy of the embedded atoms or molecules has been used to determine the drop's temperature. To date, these studies have used freely-falling sub-μm drops and, before the work done in this thesis, there have been no direct studies of evaporative cooling of trapped helium drops.

In perfect vacuum, helium drops are predicted to reach $T < 0.5$ K in time $t \sim 1$ms. In an experiment with a trapped drop, however, the vacuum is imperfect. Consequently, helium gas will surround the drop and impart a heat load on the drop

Light incident on the drop (or trapped in an optical WGM) is another potential heat load, but due to the low optical absorption in liquid helium (see section 2.3.1) this source of heating is negligible.

2.5.1 Evaporation in Vacuum

In 1990, Brink and Stringari calculated the evaporation rate of ^{3}He and ^{4}He droplets in perfect vacuum by considering how the total energy of these droplets changes as an atom evaporates from the droplet's surface and carries away the latent heat of evaporation [144].

They found that ^{4}He droplets with more than 10^3 atoms should cool to $\sim$300 mK in 1 ms of evaporation. Droplets with less than 10^3 atoms shouldn't cool below 450 mK because at that temperature the atom cluster's total energy is less than the binding energy of a single atom to the cluster; in this case, an atom cannot attain the required kinetic energy to escape the cluster. On the other hand, the behavior of ^{3}He droplets is different because they are a degenerate Fermi liquid. Brink and Stringari's model predicts that ^{3}He droplets should cool to about 150 mK after 1 ms of evaporation. There are not similar constraints that limit the ability for small ^{3}He droplets to evaporate.

The Brink and Stringari model gives an evaporation rate (in atoms/second) in perfect vacuum and with no external heat load of

$$\Gamma_{\rm evap}(T) = \frac{g k_{\rm B} m N_a^{2/3} r_0^2}{\pi \hbar} T^2 e^{-E_0/T} \tag{2.161}$$

where in units with $\hbar = k_{\rm B} = 1$, $m = 0.0825$ K^{-1} Å^{-2} is the mass of a ^{4}He, g is the sticking probability (accommodation coefficient) of an atom striking the droplet, $k_{\rm B}$ is Boltzmann's constant, $E_0 = 7.14$ (2.5) K is the binding energy of a ^{4}He (^{3}He) atom to the droplet, N_a is number of helium atoms in the droplet and $r_0 = 2.22$ (2.25) Å is the interatomic spacing of ^{4}He (^{3}He) atoms in the droplet.

We can also write $N_a = R^3/r_0^3$, where R is the drop radius. By taking the time derivative of N_a, the evaporation rate (also in atoms/second) can be re-expressed as

$$\Gamma_{\rm evap}(T) = \frac{{\rm d}N_a(t)}{{\rm d}t} = -\frac{3}{r_0^3} R(t)^2 \frac{{\rm d}R(t)}{{\rm d}t} \tag{2.162}$$

By equating the right hand sides of equation 2.161 and equation 2.162, we see that ${\rm d}R(t)/{\rm d}t$ does not depend on the droplet's size N_a and takes the following form:

$$\frac{{\rm d}R(t)}{{\rm d}t} = -\frac{g k_{\rm B} m r_0^3}{3\pi\hbar} T(t)^2 e^{-E_0/T(t)} \tag{2.163}$$

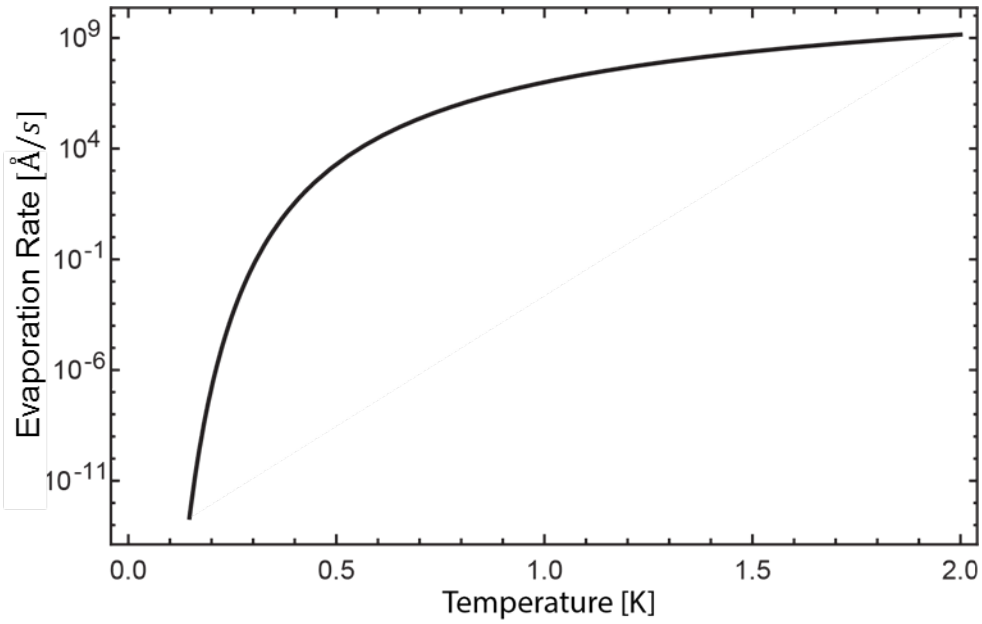

Figure 2.18: The time derivative of the radius of a ^{4}He drop in vacuum as a function of the drop's temperature.

A plot of the rate of change of the drop radius versus temperature is provided in figure 2.18.

The rate of change of a drop's energy is $-E_0\Gamma_{\rm evap}(t)$; to convert this into the evolution of the drop's temperature requires knowledge of its heat capacity. Brink and Stringari assume that the drop's heat capacity is due to its surface modes: $C_{\rm surf}(T) = \alpha k_{\rm B} T^{7/3} N_a^{2/3}$, where $\alpha = 0.39\ [\mathrm{K}]^{-4/3}$ (they neglect the energy contribution from bulk (phonon) modes because the associated energy is $\propto T^4$, which is negligible for drops with $T < 1$ K)

To model the full range of temperatures attained during cooling, we extend Brink and Stringari's model by also accounting for the phonon contribution to the heat capacity $C_{\rm bulk}(T)$. We do this by using measured values of the specific heat and latent heat [145, 146, 147, 148]; these measurements were performed on bulk samples of liquid helium, and so reflect the contribution of bulk modes rather than surface modes. The total heat capacity of the droplet is given by $C_{\rm drop} = C_{\rm surf} + C_{\rm bulk}$.

The tabulated values of the latent heat per atom ΔH and the heat capacity of the drop can be combined with equation 2.161, yielding the differential equation that describes the

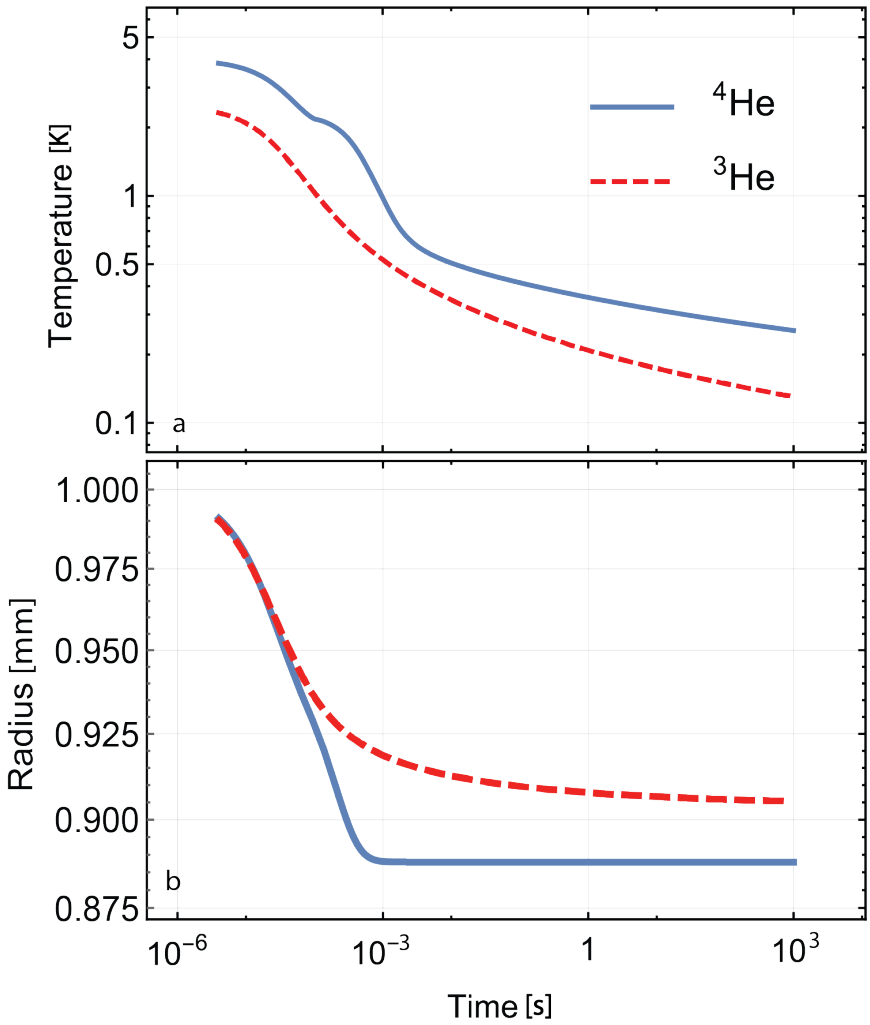

Figure 2.19: Evaporation of a helium drop in perfect vacuum. (a) The temperature and (b) the radius of ^{3}He and ^{4}He drops as a function of time for drops evaporating in perfect vacuum. The initial drop radii are 1 mm.

temperature evolution of the drop over time:

$$\frac{\mathrm{d}T(t)}{\mathrm{d}t} = -\frac{\Delta H(T(t))}{C_{\mathrm{drop}}(T(t))}\Gamma_{\mathrm{evap}}(T(t)) \tag{2.164}$$

Numerical integration of equation 2.164 can be used to find $T(t)$ and $R(t)$, which are shown in figure 2.19 for ^{3}He and ^{4}He drops with initial radii $R_0 = 1$ mm.

For ^{4}He (^{3}He), the drop temperature reaches $\approx$ 350 mK ($\approx$ 200 mK) after approximately one second of evaporation time, before slowly cooling to $\approx$ 290 mK ($\approx$ 150 mK)

after approximately one minute. Because ^{3}He has a smaller latent heat of evaporation, it cools more effectively. The complete evaporative cooling process shrinks the radius of both types of drops by about 10%.

In the absence of an external heat load, the drop's temperature will continually decrease, although the rate of decrease continually slows. However, in a real experiment we expect a non-zero heat load to arise from imperfect vacuum. This will cause the drop's temperature to asymptote to an equilibrium value, which is defined by balancing the external heat load with the cooling power of evaporation. The drop's cooling power can be expressed by $dE/dt = -\Delta H \Gamma_{\text{evap}}$, since each atom carries away the latent heat of evaporation (the latent heating being defined per atom). Figure 2.20a shows the cooling power of a helium drop in vacuum with $R = 1$ mm.

The asymptotic value of the temperature is of interest because it will determine the quality factor of the optical and mechanical modes of the drop, as discussed in section 2.3.1. Furthermore, it will set the rate at which the drop radius will drift during an experiment. The expected drift rate will not result in an appreciable change in the mechanical mode frequencies; however, it will result in a drift in the optical mode frequency large enough to require tracking with laser-locking techniques. As mentioned in section 2.2.4, the frequencies of the optical modes are given by $f = \ell c/2\pi n_1 R$, where c is the speed of light and R_0 is the radius of the drop. Taking the time derivative of the drop radius gives the following expression for the drift of the optical modes

$$\frac{\mathrm{d}f}{\mathrm{d}t} = -\frac{1}{3}\frac{c}{\lambda}\left(\frac{r_0}{R}\right)^3 \Gamma_{\text{evap}} \tag{2.165}$$

which is shown in figure 2.20b for an optical mode with wavelength $\lambda = 1$ μm.

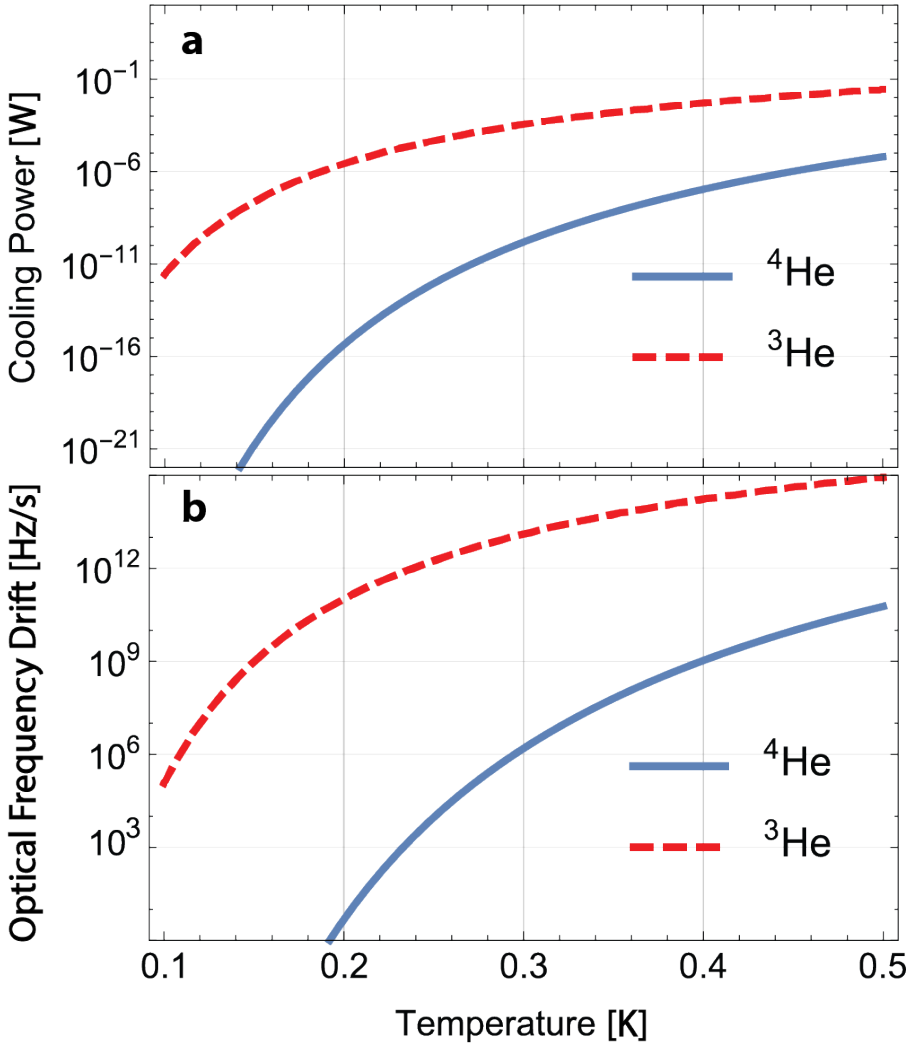

Figure 2.20: Temperature-dependent quantities of helium drops in perfect vacuum. (a) The cooling power of helium drops evaporating in perfect vacuum, and (b) the rate of change of the frequency of optical modes confined within the drops. The initial drop radii are 1 mm.

2.5.2 Evaporation in Non-Zero Background Pressure

In our experiments we expect a non-zero heat load on the drop, which will cause the temperature to asymptote to some equilibrium value. This heat load is expected to arise primarily from imperfect vacuum. Here we consider the drop's equilibrium temperature as a function of the background pressure, by assuming that either it is constant, or time-varying (due to gas that is sourced by the drop's evaporation).

In practice the evaporated atoms cannot be instantly removed. In fact, the atoms that evaporate from the drop will be pumped away at a speed limited by the pumping speed of the vacuum system in which the drop is levitated. As a result, the drop will be levitated in a non-zero background of helium atoms. Additionally, a liquid helium layer coating the walls of the experimental chamber will outgas and generate gas around the drop. In both cases, the drop will experience heating from atoms that thermalize the drop with the chamber walls.

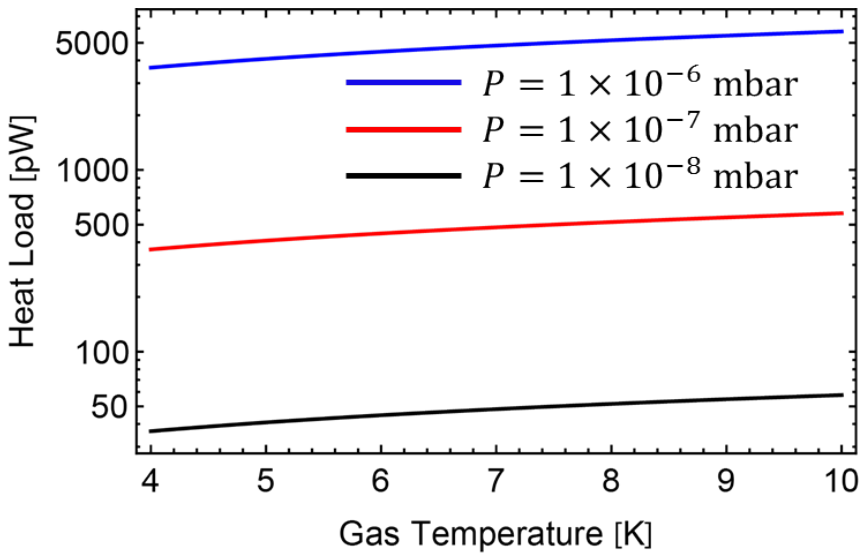

Figure 2.21: The heat load conducted into a levitated ^{4}He drop with a radius of 0.25 mm versus the temperature of ^{4}He gas surrounding it.

The rate of collisions between a levitated drop of cross-sectional area $A_c = \pi R^2$ and a surrounding gas with particle density n and an average velocity of gas atoms $\bar{v}$ is given by $nA_c\bar{v}$, where $\bar{v} = \sqrt{8k_B T_g/\pi m_g}$, T_g is the temperature of the gas and m_g is the mass of

an atom in the gas. On the other hand, the collision rate can be defined by the heat load $\dot{Q}$ the gas imparts onto the drop, with each impinging gas atom providing $(1/)2m_{\rm g}g\bar{v}^2$; here g is the accommodation coefficient, which quantifies how much kinetic energy an atom deposits into the drop. In what follows, I set $g = 1$, which means that an atom that strikes the drop is always absorbed. The collision rate is given by $\dot{Q}/((1/2)m_{\rm g}\bar{v}^2)$. Equating these two collision rates are equal and using the ideal gas law for the particle density n allows the heat load to be written in terms of the pressure of the gas:

$$\dot{Q} = PR^2\sqrt{\frac{128k_{\rm B}T_{\rm g}}{\pi m_{\rm g}}} \tag{2.166}$$

Figure 2.21 shows the heat load on a ^{4}He drop with $R = 0.25$ mm versus the temperature of ^{4}He gas at a pressure $P = 1 \times 10^{-6}$, $P = 1 \times 10^{-7}$ and $P = 1 \times 10^{-8}$ mbar. The value $P = 1 \times 10^{-8}$ mbar was chosen because these this is the typical pressure reached in our experiments. By comparing figure 2.21 with figure 2.20a, one would expect ^{4}He gas with $T_{\rm g} = 5$ K at a pressure of 1×10^{-8} mbar to result in a drop with $T \sim 300$ mK.

Equation 2.166 can be added directly to equation 2.164 and solved numerically to illustrate the effect of a constant background pressure on a levitated drop. Figure 2.22 shows the temperature evolution of a ^{4}He drop with an initial $R = 0.25$ mm that is levitated in constant background pressures $P = 0$, $P = 1 \times 10^{-6}$, $P = 1 \times 10^{-7}$ and $P = 1 \times 10^{-8}$ mbar with $T_{\rm g} = 7$ K (the typical temperature of the chamber walls surrounding the drop). At ~ 1 s of evaporation, the model suggests the drop's temperature should equilibrate to $T \approx 393$ mK, $T \approx 354$ mK and $T \approx 319$ mK for background pressures of $P = 1 \times 10^{-6}$, $P = 1 \times 10^{-7}$ and $P = 1 \times 10^{-8}$ mbar, respectively.

As mentioned before, the background pressure of helium will result from the finite speed at which gas can be evacuated from the region where the drop is trapped. In order to calculate the expected background pressure in the levitation region, we note that the atom flux $\dot{N}$ through a pumping line is proportional to the difference in particle number density

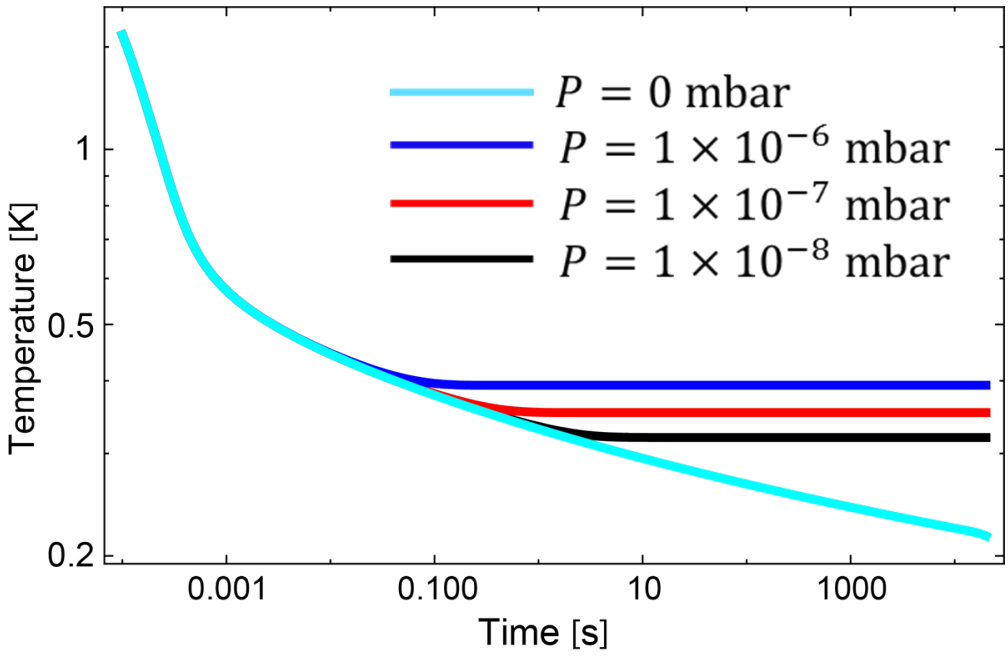

Figure 2.22: The temperature evolution of a ^{4}He drop, with an initial radius of 0.25 mm, levitated in a constant background pressure of helium gas with $T = 7$ K.

between two points of the line, which can be expressed as $\dot{N} = C(N_1 - N_2)$, where C is the pumping speed and $N_1(N_2)$ is the particle number density at position 1(2). By taking $N_2 = 0$ (e.g. at the location of the pump) and using the ideal gas law, the pumping-speed-limited pressure P_{C} in the chamber is given by

$$P_{\mathrm{C}} = \frac{k_{\mathrm{B}}T}{C}\dot{N} \tag{2.167}$$

If the atom flux through the line is sourced by the drop's evaporation, $\dot{N} = \Gamma_{\mathrm{evap}}$, and the pumping-speed-limited self-heating $\dot{Q}_{\mathrm{C}}$ of the drop is given by substituting equation 2.167 into equation 2.166:

$$\dot{Q}_{\mathrm{C}} = \frac{k_{\mathrm{B}}T}{C}R^2\Gamma_{\mathrm{evap}}\sqrt{\frac{128k_{\mathrm{B}}T_{\mathrm{g}}}{\pi m_{\mathrm{g}}}} \tag{2.168}$$

The heat load $\dot{Q}_{\mathrm{C}}$ arises from gas that is emitted from the levitated drop, then thermalizes with the walls of the experimental chamber before striking the drop. At sufficiently

low chamber pressures, gas will travel in the molecular flow regime, in which case an atom in the gas has a mean-free-path that is greater than the size of the chamber. As a result, the atoms in the gas have equal probability of scattering in any direction, not necessarily in the direction of flow that would be induced by a pump in the laminar flow regime. Gas emitted from the drop may linger, undergoing multiple reflections from the chamber walls before striking or wandering away from the drop.

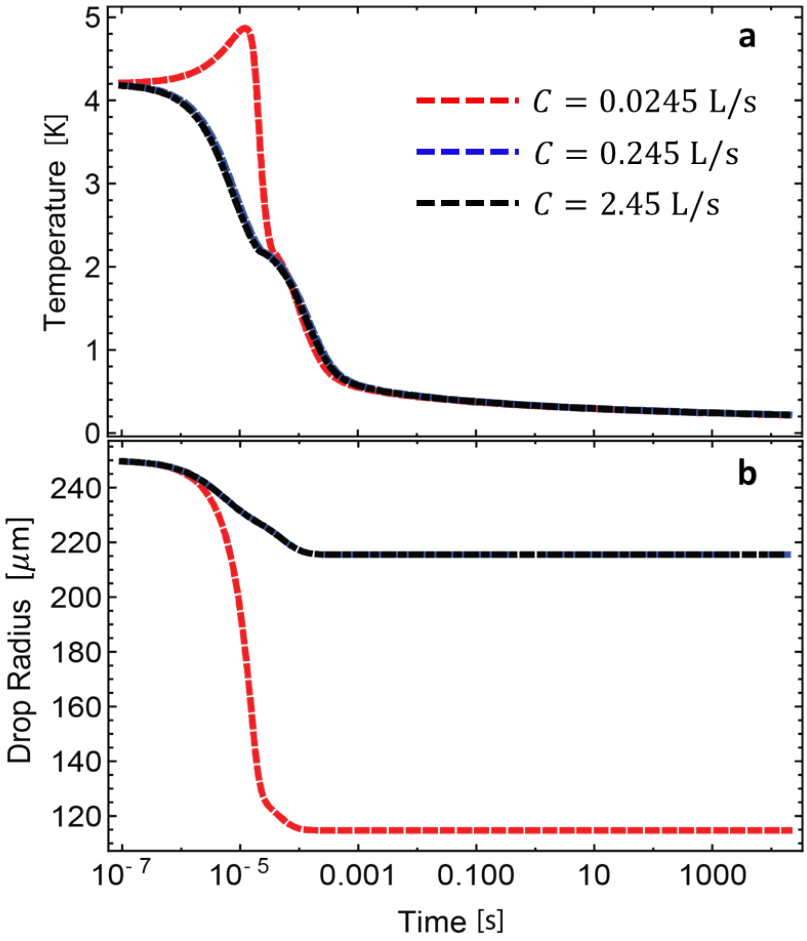

Figure 2.23: Evaporation in imperfect vacuum as a result of the finite speed C that a drop's evaporated atoms can be removed from the experimental chamber. (a) The temperature and (b) the radius evolution of a ^{4}He drop, with an initial radius of 0.25 mm and temperature of 4.2 K.

Equation 2.168 can be added directly to equation 2.164 and solved numerically to illustrate the effects of the finite speed at which gas emitted from a levitated drop can be pumped away. The numerical solution for a ^{4}He drop with an initial radius of 0.25 mm and

temperature of 4.2 K is shown in figure 2.23. In figure 2.23a, the temperature curves with an experimental chamber pumping speed of 0.0245 L/s (red) and 0.245 L/s (blue) nearly exactly overlap, yet a pumping speed of 0.0245 L/s (red) leads to a brief period of heating. Note that as $C \to \infty$, the evaporative cooling model approaches that of evaporation in perfect vacuum. In figure 2.23b, it becomes clear that a pumping speed of 0.0245 L/s leads to a significant decrease of the drop's radius, as compared to evaporation in perfect vacuum. Instead of the typical 10% decrease in radius over the evaporative cooling process, there is over 50% reduction in the radius of the drop. For our experiment, we expect $C \approx 0.8$ L/s with $T_{\mathrm{g}} = 7$ K.

Evaporation from Optical Absorption

Typical lasers used in experiments with optical resonators (which is the case for our levitated ^{4}He drop experiments) operate at wavelengths $\lambda \approx 500 - 1,550$ nm. Helium does not have electronic transitions with $\lambda \approx 500 - 1,550$ nm, due to its bandgap energy ≈ 19.8 eV, so it does not resonantly absorb light. However, energy can be absorbed from light through the inelastic Brillouin and Raman scattering mechanisms, as described in section 2.3.1.

In section 2.3.1, we found the Brillouin scattering-limited optical mode finesse $\mathcal{F}_{\mathrm{phonon}}$, which has approximately equal contributions from Stokes and anti-Stokes scattering of light; this is because the momentum change of the incident light via scattering from phonons is small [149]. Consequently, half of the extinction coefficient μ_{comb} that results in $\mathcal{F}_{\mathrm{phonon}}$ is due to higher energy phonons being created by scattering from the incident light. This process heats the liquid. The other half cools the liquid, but I will momentarily ignore the cooling contribution. If one were to illuminate a levitated ^{4}He drop in perfect vacuum with a laser with power P_{L}, the drop is heated due to the absorbed laser power $P_{\mathrm{abs}} = 1/2 I_{\mathrm{L}} V \mu_{\mathrm{heat}}^{\mathrm{phonon}}$, where I_{L} is the laser intensity, V is the helium volume that overlaps with the laser and $\mu_{\mathrm{heat}}^{\mathrm{phonon}} = 1/2 \mu_{\mathrm{comb}}$. For a laser with $\lambda = 1,550$ nm, $P_{\mathrm{L}} = 1$ W

and diameter $d = 2R_0$ illuminating a drop with radius $R_0 = 250$ μm and $T = 300$ mK, $P_{\rm abs} \sim 1$ pW. Here, $P_{\rm L} = 1$ W was used for illustrative purposes; in our experiments to date $P_{\rm L} \lesssim 30$ mW. Even with $P_{\rm L} = 1$ W, $P_{\rm abs}$ is $\lesssim 10^2$ times less than the heat load on the drop from surrounding gas with $P \sim 1 \times 10^{-8}$ mbar and $T_{\rm g} = 7$ K (see section 2.5.2). For a drop levitated in perfect vacuum, $P_{\rm L} = 1$ W would lead the drop to equilibrate at $T \approx 250$ mK with a radius evaporate rate $\mathrm{d}R/\mathrm{d}t \sim 10^{-3}$Å/s. Comparing this evaporation rate to the initial drop size gives a lifetime $t_{\rm d} \approx 80$ years. However, I have ignored the phonon scattering that results in cooling in nearly equal proportion to heating. Additionally, the drop's evaporation slows as a function of time as it cools. Overall, one finds $t_{\rm d} \gg 80$ years.

The heating due to inelastic Raman scattering is expected to be lower than the heating due to Brillouin scattering. As described in section 2.3.1, Greytak and Yan measured the Raman scattering of light with $\lambda = 514.5$ nm from rotons in liquid ^{4}He at $T = 1.16$ K. They measured an extinction coefficient $\mu_{\rm Raman} = 4\pi \times (6 \pm 2) \times 10^{-12}$ cm^{-1}. For a laser with $\lambda = 514.5$ nm, $P_{\rm L} = 1$ W and diameter $d = 2R_0$ illuminating a drop with radius $R_0 = 250$ μm and $T = 1.16$ K, $P_{\rm abs} \sim 1$ pW. However, levitated ^{4}He drops have $T \lesssim 400$ mK; at these temperatures the rotons are negligible with respect to phonons. Also, the Raman scattering intensity scales with λ^{-4}, so with $\lambda = 1,550$ nm the heating via Raman scattering will be significantly suppressed compared to $\lambda = 514.5$ nm. Overall, it is likely that $P_{\rm abs} \ll 1$ pW.

2.6 Optomechanical Coupling

Optical WGMs couple to four of the five types of mechanical motion described in section 2.4 (the type of mechanical motion that optical WGMs do not couple to is the drop's COM motion). Here we briefly summarize the coupling of optical WGMS to the various mechanical modes of a levitated drop. For detailed information on the mechanical modes, see section 2.4.

The drop's equilibrium shape is that which minimizes the sum of its gravitational, magnetostatic and surface energies. When a levitated drop undergoes COM motion it experiences a uniform gravitational field, but non-uniform magnetic field (see section 2.3.4). Consequently, the drop's shape can change from significant COM motion. However, for small amplitude COM motion the drop's shape will approximately remain unchanged (this approximation becomes better for smaller drops). As a result, we assume the COM optomechanical coupling $g_0/2\pi \approx 0$.

Surface modes couple to optical WGMs via the standard optomechanical coupling Hamiltonian, and are of particular interest for this thesis. Surface modes with frequency $\omega_{\rm surf}$ couple to optical WGMs with frequency $\omega_{\rm opt}$ via an intuitive stretching effect that changes the drop circumference that the optical WGM experiences. This stretching can be characterized by a radial deflection δR. If $\delta R_{\rm zpf}^{\rm (surf)}$ is the result of the zero-point amplitude fluctuation $x_{\rm zpf}^{\rm (surf)}$ of a surface mode, then $g_0 = \omega_{\rm opt}(\delta R_{\rm zpf}^{\rm (surf)}/R_0)$. As described in section 2.4, $x_{\rm zpf}$ can be quite large due to the low surface tension of liquid helium. For a drop with $R_0 \sim 1$ mm, the fundamental surface mode frequency is $\omega_{\rm surf}/2\pi \approx 23$ Hz and it couples to optical WGMs with optomechanical coupling rate $g_0/2\pi \approx 213$ Hz .

Bulk modes also couple to optical WGMs via the standard optomechanical coupling Hamiltonian, but they are of less interest for this thesis. Bulk modes with frequency $\omega_{\rm bulk}$ experience a restoring force set by the drop's bulk modulus B, which is much stronger than the restoring force for surface modes (set by the drop's surface tension). Consequently, one might expect $x_{\rm zpf}^{\rm (bulk)} < x_{\rm zpf}^{\rm (surf)}$. For a drop with $R_0 \sim 1$ mm, assuming the effective mass of the fundamental surface and bulk modes are equal, the fundamental bulk mode coupling to optical WGMs is estimated to be $g_0 \approx \omega_{\rm opt}(\delta R_{\rm zpf}^{\rm (surf)}/R_0)\sqrt{\omega_{\rm surf}/\omega_{\rm bulk}} \approx 10$ Hz.

As mentioned before, rigid-body rotational motion is not a simple harmonic oscillator. Consequently, the coupling between the drop's rotation and optical WGMs is not described by the standard optomechanical coupling. More specifically, $\Delta\omega_{\rm opt}^{\rm (rot)} \propto \delta R \propto L_{\rm z}^2$, where δR is the drop's radial deflection that results from its rotation. For a ^{3}He drop with R_0 = 1

mm, $\Delta\omega_{\rm opt}^{(\rm rot)} = 1.3 \times 10^{-47} \times \omega_{\rm opt} \times (L_z/\hbar)^2$.

Acoustic WGMs are large ℓ_d bulk modes with optimal spatial overlap with optical WGMs. The coupling g_0 is optimized for the case $\lambda_{\rm opt} = 2\lambda_{\rm aWGM}$. For $\lambda_{\rm opt} = 1550$ nm, the relevant acoustic WGM has resonant frequency $\omega_{\rm aWGM}/2\pi \approx 315$ MHz and $g_0 \sim 3$ kHz.

2.6.1 Optical WGMs Coupled to a Drop's Capillary Waves

For surface modes, one would expect an energy change ΔE associated with a change in curvature of the form $\Delta E = \sigma \Delta S$, where σ is the surface tension and ΔS is the change in the surface area. If ΔS arises from a surface mode's zero-point fluctuation, then $\sigma \Delta S_{\rm zpf} = \hbar\omega_{\rm surf}/4$, and there is a corresponding radial fluctuation $\delta R_{\rm zpf}$ at the drop's equator, along which the optical WGM's intensity antinodes lie. The deflection $\delta R_{\rm zpf}$ detunes the optical WGM and gives the single-quantum optomechanical coupling $g_0 = \omega_{\rm opt}\delta R_{\rm zpf}/R_0$, where R_0 is the drop's equilibrium radius.

In order to calculate ΔS due to a surface mode, one may first expand the drop's radius $R(\theta, \phi)$ in terms of spherical harmonics:

$$R(\theta,\phi) = R_0\Big(1 + \sum_{\ell_d=2}^{\infty}\sum_{m_d=-\ell_d}^{\ell_d} a_{\ell_d,m_d} Y_{\ell_d}^{m_d}(\theta,\phi)\Big) \tag{2.169}$$

where $a_{\ell_d m_d}$ is the amplitude of mode $Y_{\ell_d}^{m_d}(\theta,\phi)$.

Using the standard formula, the surface area of the perturbed drop is given by

$$S = \int_0^{2\pi}\int_0^{\pi} \sin\theta \mathrm{d}\theta\mathrm{d}\phi \sqrt{R^2 + \left(\frac{\partial R}{\partial\theta}\right)^2}\sqrt{R^2 + \frac{1}{\sin^2\theta}\left(\frac{\partial R}{\partial\phi}\right)^2} \tag{2.170}$$

For small surface perturbations, the polar derivatives of R are smaller than R itself, allowing the integrand to be expanded to second order in the amplitude of the spherical

harmonics [150]

$$S \approx 4\pi r_0^2 + \frac{r_0^2}{2}\sum_{\ell_d=2}^{\infty}\sum_{m_d=-\ell_d}^{\ell_d}(-1)^{m_d}(\ell_d(\ell_d+1)+2)a_{\ell_d,m_d}a_{\ell_d,-m_d} \tag{2.171}$$

where, since the volume of the droplet is not changed by surface waves, a useful quantity r_0 is related to R_0 in the following manner

$$r_0 \approx R_0 - \frac{R_0}{4\pi}\sum_{\ell_d=2}^{\infty}\sum_{m_d=-\ell_d}^{\ell_d}(-1)^{m_d}r_{\ell_d,m_d}r_{\ell_d,-m_d} \tag{2.172}$$

Substituting equation 2.172 into equation 2.171 and keeping terms to second order in the amplitude of the spherical harmonics yields for the surface area

$$\Delta S \approx \frac{R_0^2}{2}\sum_{\ell_d=2}^{\infty}\sum_{m_d=-\ell_d}^{\ell_d}(\ell_d(\ell_d+1)-2)\left|r_{\ell_d,m_d}\right|^2 \tag{2.173}$$

In consideration of the $\ell_d = 2, m_d = 0$ surface wave mode, which is of particular interest in this work, substituting $a_{\text{zpf}} = r_{\ell_d,m_d}R_0$ into equation 2.173 yields

$$\Delta S_{\ell_d=2,m_d=0} = 2a_{\text{zpf}}^2 \tag{2.174}$$

where a_{zpf} is the zero-point fluctuation of the $\ell_d = 2, m_d = 0$ surface wave mode. Since the surface mode is a harmonic oscillator, its average kinetic and potential energy are equal, so half of the zero point energy should go into the potential energy of changing the surface area. As a result,

$$\sigma\Delta S_{\ell_d=2,m_d=0} = \frac{1}{4}\hbar\omega_{\text{surf}} \tag{2.175}$$

which, using equation 2.140, gives

$$\begin{aligned} a_{\mathrm{zpf}} &= \sqrt{\frac{\hbar\omega_{\mathrm{surf}}}{8\sigma}} \\ &= \left(\frac{\hbar^2}{16\sigma\rho R_0^3}\right)^{\frac{1}{4}} \end{aligned} \tag{2.176}$$

Using equation 2.158, equation 2.176 can be used to write the fluctuation of the radius at the equator of the drop due to the zero point fluctuation of the $\ell_d = 2, m_d = 0$ surface wave, which is given by

$$\delta R_{\mathrm{zpf},\ell_d=2,m_d=0} = \sqrt{\frac{5}{16\pi}} a_{\mathrm{zpf}} \tag{2.177}$$

Each optical WGM in the drop is specified by the indices ℓ, m and q, which specify the WGM's total angular momentum, its projection along the z axis, and the number of radial nodes of the WGM's electric field, respectively. The WGM that lies closest to the drop's equator has $\ell = m$, and an optical path length that is proportional to the equatorial circumference of the drop, as described in section 2.2.3. As a result, the single quantum optomechanical coupling between an equatorial optical WGM with radius R_0 = 1 mm and wavelength λ = 1 μm, and the $\ell_d = 2, m_d = 0$ surface wave mode is $g_0/2\pi \approx 213$ Hz.

In general, optical WGMs with arbitrary ℓ, m couple linearly to a drop's $\ell_d = 2, m_d = 0$ surface mode of the drop with single quantum optomechanical coupling rates determined exactly by [151]

$$g_0^{(\ell,m)} = \frac{\omega_{\mathrm{opt}}}{2}\frac{\delta R_{\mathrm{zpf}}}{R_0}\left(\frac{3m^2}{\ell(\ell+1)} - 1\right) \tag{2.178}$$

As can be seen from equation 2.178, optical WGMs that propagate near the equator (that is, with $\ell \approx m$) experience a decrease of optical frequency upon expansion of the equator. On the other hand, WGMs for which $|m|$ is small are modes where the light propagate closer to the poles, and these experience an increase in their optical frequencies; in a ray-optical picture, the light travels along great circles passing near the poles, and when the equator expands, since the volume is conserved, the path length they propagate through

must shorten.

2.6.2 Optical WGMs Coupled to a Drop's Rotation

The dynamical coupling between WGMs in a liquid drop and rotations is an exciting new direction of quantum optomechanics. For both ^{4}He and ^{3}He, the rotational motion of the drop is expected to interact with the optical WGMs because the velocity field associated with the rotation of the liquid will deform the drop and thereby detune the WGMs. This coupling should allow measurements of the optical WGM to provide information about the drop's rotational motion.

To write down the optorotational Hamiltonian we work in a coordinate system where the drop is rotating with angular velocity $\hat{\Omega}_{\rm z}$, and the z-component of the drop's angular momentum is $\hat{L}_{\rm z} = I\hat{\Omega}_{\rm z}$, where the moment of inertia of the drop I is

$$I = \frac{8\pi}{15}\rho R_0^5 \tag{2.179}$$

which is a good approximation for a drop that is nearly spherical. Because we already know the first order correction to the optical WGM frequency at the equator due to a change of equator circumference, we can immediately write down the interaction part of the Hamiltonian $\hat{H}_{\rm O.R.}$, which takes the form

$$\hat{H}_{\rm O.R.} = \hbar\omega_{\rm opt}\frac{\delta R}{R_0}\hat{a}^\dagger\hat{a} \tag{2.180}$$

where $a^\dagger a$ is the number of photons occupying the WGM. Upon substitution of equation 2.159 into equation 2.180 and using the relationship $\hat{L}_{\rm z} = I\hat{\Omega}_{\rm z}$, the optorotational Hamiltonian takes the form

$$\hat{H}_{\rm O.R.} = \frac{1}{24}\hbar\omega_{\rm opt}\frac{\rho R_0^3}{\sigma}\left(\frac{\hat{L}_{\rm z}}{I}\right)^2\hat{a}^\dagger\hat{a}. \tag{2.181}$$

After substitution of the expression for the moment of inertia into equation 2.181, the optorotational Hamiltonian can be written in the form

$$\hat{H}_{\mathrm{O.R.}} = \hbar g_L \left(\frac{\hat{L}_z}{\hbar}\right)^2 \hat{a}^\dagger \hat{a}, \tag{2.182}$$

where the optorotational coupling is given by

$$g_L = \frac{1}{24}\left(\frac{15}{8\pi}\right)^2 \frac{\hbar^2}{\rho\sigma R_0^7}\omega_{\mathrm{opt}} \tag{2.183}$$

For a ^{3}He drop with R_0 = 1 mm, $\rho \approx 81\mathrm{kg/m}^3$, and $\sigma = 1.52 \times 10^{-4}\mathrm{N/m}$, the optorotational coupling $g_{\mathrm{rot}} = 1.3 \times 10^{-47} \times \omega_{\mathrm{opt}}$ [37].

2.6.3 Optical WGMs Coupled to a Drop's Acoustic WGMs

Acoustic whispering gallery modes are examples of the bulk modes described in section 2.4, in which the pressure antinodes are confined near the perimeter of a dielectric acoustic resonator. More specifically, they correspond to modes with $q_d = 1, \ell_d \gg 1, m_d \sim \ell_d$. As such, they are highly similar to their optical counterparts. Regions of higher pressure will have higher density, which alters the energy stored in the optical WGM.

Because an acoustic WGM is a pressure wave (with a corresponding shape deformation of the dielectric), it is the pressure change in the dielectric that detunes the optical WGMs. As a result, in order to find the optomechanical coupling one can Taylor expand the WGM frequency ω_{opt} to first order in the amplitude of the pressure change δP. The single quantum optomechanical coupling is defined by the frequency shift induced by the zero point pressure fluctuations δP_{zpf}:

$$g_0 = \frac{\partial \omega_{\mathrm{opt}}}{\partial P}\delta P_{\mathrm{zpf}} \tag{2.184}$$

By the chain rule, the change in the optical WGM frequency per change in pressure from

the acoustic WGM can be expressed as

$$\frac{\partial \omega_{\rm opt}}{\partial P} = \frac{\partial \omega_{\rm opt}}{\partial \epsilon_{\rm r}} \frac{\partial \epsilon_{\rm r}}{\partial \rho} \frac{\partial \rho}{\partial P} \tag{2.185}$$

In what follows, I will calculate each of the partial derivatives that appear in equation 2.185.

Small shape perturbations of the dielectric in which an electromagnetic mode is confined results in a change in permeability $\Delta\mu$ and permittivity $\Delta\epsilon$ within the dielectric. The frequency shift $\Delta\omega_{\rm opt}$ of an electromagnetic mode with frequency $\omega_{\rm opt}$ that is caused by such a perturbation is given by [152, 153]

$$\frac{\Delta\omega_{\rm opt}}{\omega_{\rm opt}} = -\frac{\int \Delta\mu |\mathbf{H}_0|^2 + \Delta\epsilon |\mathbf{E}_0|^2 \, \mathrm{d}V}{\int \mu |\mathbf{H}_0|^2 + \epsilon |\mathbf{E}_0|^2 \, \mathrm{d}V} \tag{2.186}$$

where the integration is taken over the entire volume V of the dielectric and $\{\mathbf{E}_0, \mathbf{H}_0\}$ are the unperturbed modes. The energy of the electromagnetic mode is equally split between the electric and magnetic fields, so the two terms in the denominator of equation 2.186 are equal, and can be written solely in terms of the electric field. Assuming a linear relationship between the density ρ of the dielectric and both its permeability and permittivity, $\Delta\mu/\mu_0 = \chi_M \Delta\rho/\rho$ and $\Delta\epsilon/\epsilon_0 = \chi_E \Delta\rho/\rho$ where χ_M and χ_E are the magnetic and electric susceptibilities, respectively. As a result, the ratio of the magnetic part to the electric part of the numerator of equation 2.186 is equal to χ_M/χ_E, which is very small for many linear dielectrics. In the specific case of ^{4}He, $\chi_M/\chi_E \sim 10^{-5}$, so I will neglect the perturbation of the optical mode due to a shift of permeability. As a result, in spherical coordinates equation 2.186 can be re-written as [153]

$$\frac{\Delta\omega_{\rm opt}}{\omega_{\rm opt}} = -\frac{\epsilon_0}{2} \frac{\int \Delta\epsilon_{\rm r}(r,\theta,\phi) |\mathbf{E}_0|^2 \, \mathrm{d}V}{\int \epsilon |\mathbf{E}_0|^2 \, \mathrm{d}V}, \tag{2.187}$$

where ϵ_0 is the permittivity of free space and the dielectric constant $\epsilon = \epsilon_0 \epsilon_{\rm r}$, where $\epsilon_{\rm r}$ is the relative permittivity of the dielectric. In equation 2.187, $\Delta\epsilon_{\rm r}(r,\theta,\phi) = \Delta\epsilon_{\rm r} f(r,\theta,\phi)$,

where the dimensionless function $f(r, \theta, \phi)$ describes the functional form of bulk modes, as described in section 2.4. Then, equation 2.187 can be rearranged into the following form:

$$\frac{\Delta\omega_{\text{opt}}}{\Delta\epsilon_{\text{r}}} = -\epsilon_0 \frac{\omega_{\text{opt}}}{2} \frac{\int f(r,\theta,\phi)|\mathbf{E}_0|^2 \,\mathrm{d}V}{\int \epsilon |\mathbf{E}_0|^2 \,\mathrm{d}V}. \tag{2.188}$$

In the limit that $\Delta\omega, \Delta\epsilon_{\text{r}} \to 0$, the following partial derivative describes the frequency shift due to a change in relative permittivity

$$\frac{\partial\omega_{\text{opt}}}{\partial\epsilon_{\text{r}}} = -\epsilon_0 \frac{\omega_{\text{opt}}}{2} \frac{\int f(r,\theta,\phi)|\mathbf{E}_0|^2 \,\mathrm{d}V}{\int \epsilon |\mathbf{E}_0|^2 \,\mathrm{d}V}. \tag{2.189}$$

The Clausius-Mosotti equation provides the relationship between a material's ϵ_{r} and ρ, which is given by

$$\frac{\epsilon_{\text{r}} - 1}{\epsilon_{\text{r}} + 2} = \frac{4\pi\alpha_M \rho}{3M}, \tag{2.190}$$

where M is the molar mass and α_M is the molar polarizability. Solving the Clausius-Mosotti equation for the permittivty yields

$$\epsilon_{\text{r}} = \frac{1 + 2\eta\rho}{1 - \eta\rho}, \tag{2.191}$$

where $\eta = 4\pi\alpha_M\rho/3M$. Then, partial differentiation with respect to the density gives

$$\begin{aligned} \frac{\partial\epsilon_{\text{r}}}{\partial\rho} &= \frac{3\eta}{(1-\eta\rho)^2} \\ &= \frac{(\epsilon_{\text{r}} + 2)(\epsilon_{\text{r}} - 1)}{3\rho}. \end{aligned} \tag{2.192}$$

The pressure P in the dielectric is related to its density through the compressibility β, which is given by

$$\beta = -\frac{1}{V}\frac{\partial V}{\partial p}. \tag{2.193}$$

Partial differentiation of the density $\rho = m/V$ gives

$$\begin{aligned}\frac{\partial \rho}{\partial V} &= \frac{m}{V}\left(-\frac{1}{V}\right) \\ &= \beta\rho\left(\frac{\partial V}{\partial P}\right)^{-1},\end{aligned} \tag{2.194}$$

where I have made use of equation 2.193. Since the partial derivatives commute, multiplying this equation by $\partial V/\partial P$ and making use of the chain rule, gives the relation between the density and the pressure:

$$\frac{\partial \rho}{\partial P} = \beta\rho. \tag{2.195}$$

Substituting equations 2.189, 2.192, and 2.195 into equation 2.185, the change in the optical WGM frequency per change in pressure is given by

$$\frac{\partial \omega_{\mathrm{opt}}}{\partial P} = -\frac{1}{6}\left(\epsilon_{\mathrm{r}}+2\right)\left(\epsilon_{\mathrm{r}}-1\right)\beta\omega_{\mathrm{opt}}\frac{\int f(r,\theta,\phi)|\mathbf{E}_0|^2\,\mathrm{d}V}{\int \epsilon_{\mathrm{r}}|\mathbf{E}_0|^2\,\mathrm{d}V} \tag{2.196}$$

The total energy stored in the acoustic mode is given by [154]

$$E = \frac{1}{2}\beta\int \left|Pf(r,\theta,\phi)\right|^2\,\mathrm{d}V. \tag{2.197}$$

The zero point pressure fluctuations are given by setting the total energy in the acoustic WGM mode with frequency ω_{aWGM} to be $1/2\hbar\omega_{\mathrm{aWGM}}$. Using the expression $\Lambda = \int(f(r,\theta,z))^2\mathrm{d}V$, the zero point pressure fluctuation amplitude is given by

$$\delta P_{\mathrm{zpf}} = \sqrt{\frac{\hbar\omega_{\mathrm{aWGM}}}{\beta\Lambda}}, \tag{2.198}$$

where the isentropic compressibility $\beta = \beta_{\mathrm{S}} = 1/\rho u_{\mathrm{c}}^2$ and u_{c} is the speed of sound in the dielectric material where the modes are confined.

We are interested in optical modes that have $q = 1, \ell \gg 1, m \sim \ell$. For the case $m = \ell$, the optical mode intensity $|\mathbf{E}_0|^2$ will be $\propto \sin^2(\ell\phi)$ and/or $\propto \cos^2(\ell\phi)$. For the case

$q_d = 1, \ell_d \gg 1, m_d = \ell_d$, the functional form of the acoustic WGM $f(r, \theta, \phi) \propto \cos(\ell_d \phi) + i \sin(\ell_d \phi)$. As a result, when we evaluate the integral in the numerator of equation 2.196 (by using the real part of the spherical harmonics) it will be proportional to the product of the optical and acoustic WGM ϕ-components. An example of one of the products that appears in the numerator is

$$\int_{\phi=0}^{\phi=2\pi} \cos^2(\ell\phi)\cos(\ell_d\phi)\mathrm{d}\phi = \frac{\pi}{2}\delta_{2\ell,\ell_d} \tag{2.199}$$

where $\delta_{2\ell,\ell_d}$ is the Kronecker delta function. All terms that appear in the numerator of equation 2.196 will have an integral that is non-zero only if $2\ell = \ell_d$. Since for a drop with radius R_0 the optical and acoustic WGMs were are considering satisfy the condition $\ell\lambda_{\mathrm{opt}} = R_0 = \ell_d\lambda_{\mathrm{mech}}$, and $2\ell = \ell_d$, we find that optomechanical coupling is non-zero when $\lambda_{\mathrm{opt}} = 2\lambda_{\mathrm{mech}}$.

Figure 2.24 shows the estimated single quantum optomechanical coupling between the $q_d = 1$,$m_d = \ell_d$ acoustic WGM and the $q = 1$,$m = \ell$, $\lambda \approx 1$ μm optical WGM versus $\ell = \ell_d/2$. Figure 2.25 shows the optomechanical coupling between the same modes, but it is plotted versus the drop radius R.

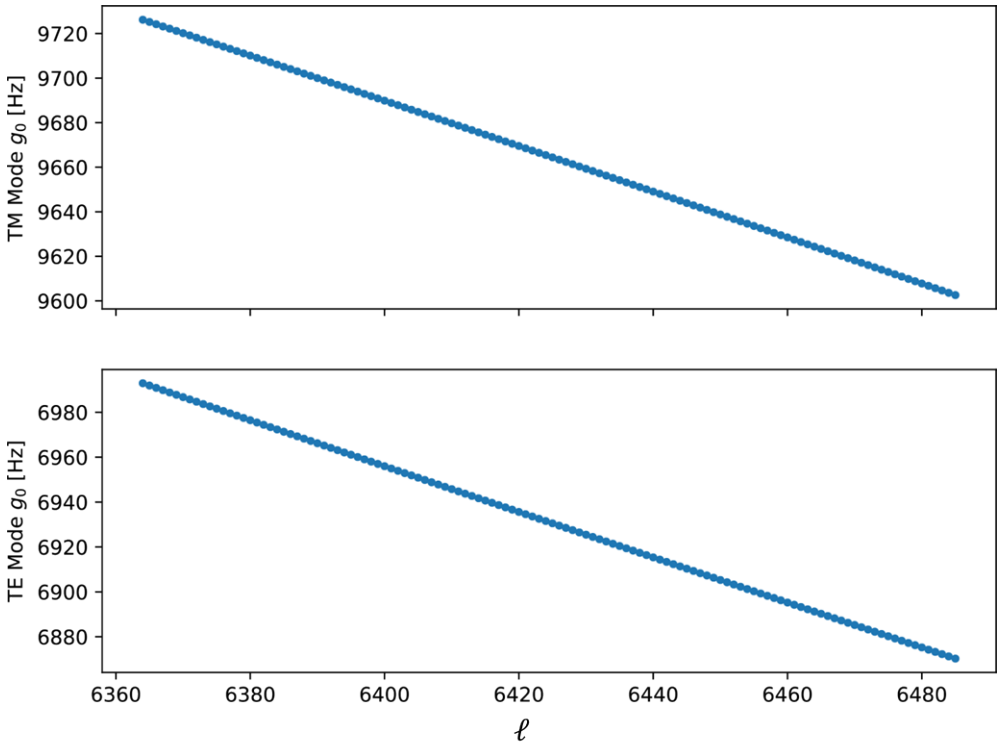

Figure 2.24: The single quantum optomechanical coupling between the $q_d = 1$,$m_d = \ell_d$ acoustic WGM and the $q = 1$,$m = \ell$, $\lambda \approx 1$ μm optical WGM versus $\ell = \ell_d/2$.

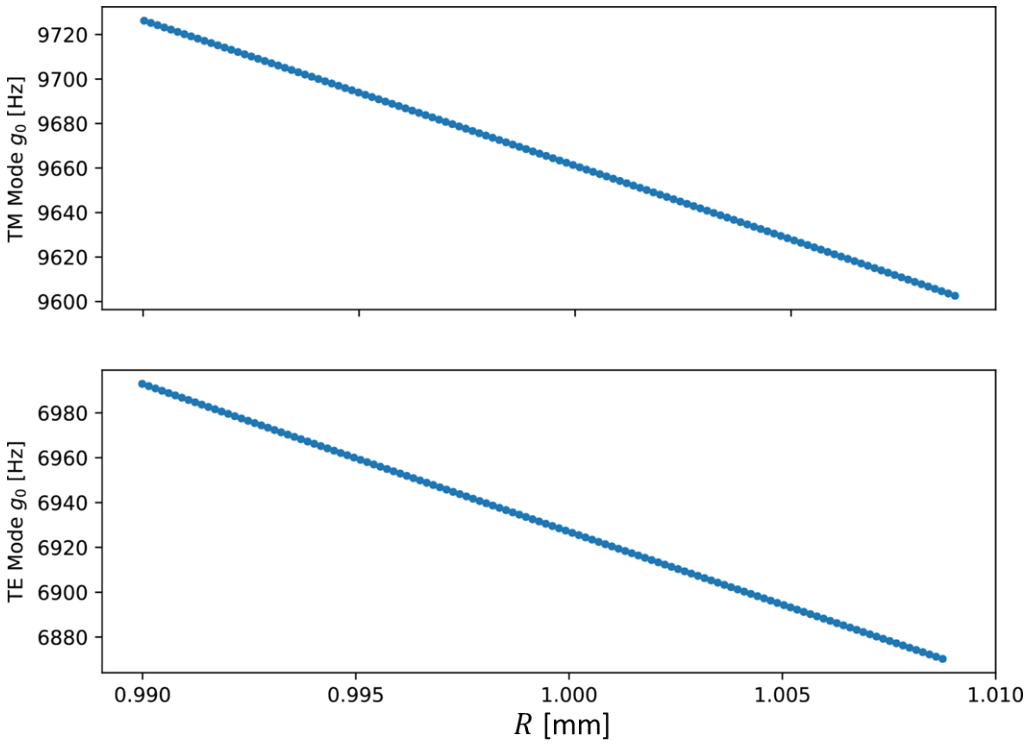

Figure 2.25: The single quantum optomechanical coupling between the $q_d = 1$,$m_d = \ell_d$ acoustic WGM and the $q = 1$,$m = \ell$, $\lambda \approx 1$ μm optical WGM versus the drop radius R.

Chapter 3

Experiment Design and Initial Characterizations

In this chapter I describe in detail the cryostat and experimental chamber that is used to perform experiments with levitated ^{4}He drops. I describe, via analysis of recorded video of levitated drops, the drops' typical size and shape, the properties of the trapping potential that is used to levitate the drops, and the drop's evaporation rate and temperature. I also provide brief details on the shift of a drop's levitation point due to changes in its size. Lastly, I provide brief details on producing charged drops.

3.1 Description of Levitation Cryostat

In order to levitate helium drops, we have constructed a custom experimental chamber that fits inside a commercially available ^{4}He magneto-optical cryostat from Oxford Instruments. A superconducting magnet rests at the bottom of the cryostat's helium bath space. The magnet consists of a number of coaxial solenoid sections which are wound using multi-filament superconducting wire. The magnet is constructed using Oxford Instruments' propriety Magnabond system, which provides a structure that is thermally stable and physically stable against the large Lorentz forces that are generated when the magnet

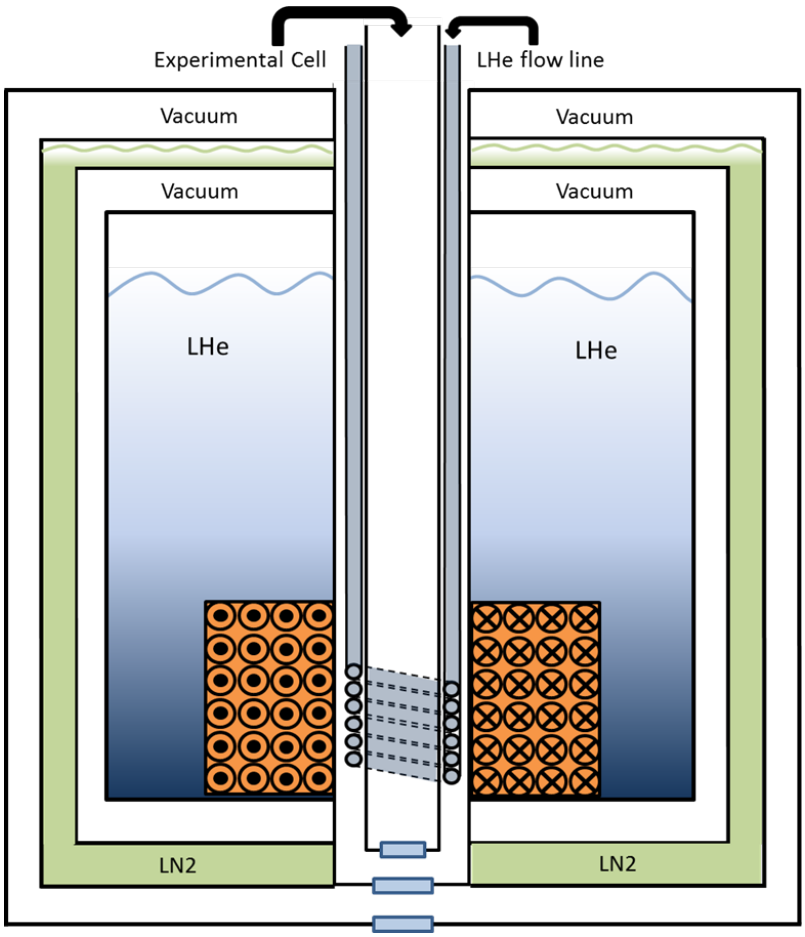

Figure 3.1: The levitation cryostat, which is a ^{4}He cryostat with a superconducting magnet resting in the helium bath. Also depicted is the experimental cell inserted into the cryostat. The experimental cell has its own window for optical access, and liquid helium flows through a coil around the cell to keep its walls cold.

is under operation.

Figure 3.1 provides an illustration of the levitation cryostat, with our experimental cell inserted. There is a clear-shot opening through the cryostat that is parallel to the symmetry axis of the magnet. The opening has a diameter of 68 mm at the top of the cryostat, before switching to 66 mm just inside the top plate of the cryostat, then to 32 mm at the top of the magnet. The top of this opening in the cryostat is fitted with an o-ring seal, whereas the bottom of the opening is sealed by two windows that have anti-reflection coatings for 1.55 μm light. The outer-most window is thermally anchored to room temperature, but the inner window is thermally anchored to the cryostat's liquid nitrogen bath to limit black-

body radiation emission into the opening. The opening, which is part of the vacuum jacket of the cryostat, passes through a liquid nitrogen shield that surrounds the helium bath of the cryostat, and thus it passes through the bore of the magnet. The helium bath volume is 20 L, while the liquid nitrogen bath volume is 24 L. The cryostat is outfitted with a superconducting helium level meter and a capacitive liquid nitrogen level meter with electrical feed-through connections that are accessible on top of the cryostat.

The magnet generates ≈ 1 Tesla at its center per 7.8 Amperes of electrical current that flows through its coils. The magnet is outfitted with a resistive persistent switch heater that allows the magnet to be operated in standard mode, or persistent mode. In standard mode, the persistent switch heater is on, which allows the magnet to be driven with current from leads that connect to the magnet's power supply. When the magnet has been ramped up to the desired current, the persistent switch can be turned off, which electrically (not physically) severs the connection between the magnet and the power supply. With the persistent switch heater off, the current to the magnet leads can be ramped down to zero, placing the magnet in persistent mode, in which case the current only flows through the magnet. We have found that the persistent switch heater should be allowed to cool for at least three minutes before ramping down the magnetic leads to place the magnet in persistent mode. In fact, we have found that for less than three minutes of cooling time, it can be difficult to place the magnet in persistent mode. An even longer cooling time, such as five minutes, would be a good idea for future operation of the crysotat. The cooling time can be set using the power supply controller. It is also useful to note that the specified rate of current decay when the magnet is in persistent mode is 0.006% per hour, which is in decent agreement with what has been observed in the laboratory ($\approx 0.009\%$ per hour).

The specified evaporation rate of the cryostat's helium bath is 0.2 L/hour. When the cryostat has the experimental chamber inside of it, but the magnet field and liquid helium continuous flow are off, the evaporation rate is ≈ 0.45 L/hour. When the magnet is in driven mode and the liquid helium continuous flow is on, the evaporation rate is ≈ 1 L/hour. When

the magnet is in persistent mode and the liquid helium continuous flow is on (described below in section 3.2.1) the evaporation is ≈ 0.25 L/hour.

3.2 Experimental Cell Design

The experimental cell consists of four main parts: the cell body, the baffle stack, the brass cage assembly and the titanium can. In this section I will describe in detail each of these components.

3.2.1 The Cell Body

The cell body is constructed from a ≈ 2.5 feet long section of extruded 316 stainless steel alloy tubing, with a wall thickness of 0.066" and an outer diameter (OD) of 1.00", to which a cap is welded. The bottom of the cap mates with a hydro-formed bellows via an ISO80 flange seal, and the other end of the bellows mates with the top of the cryostat via an o-ring seal, as shown in figure 3.2. Though the bellows is not incredibly flexible, it does allow for a couple of centimeters of compression and a few millimeters of expansion, which can be used to *in situ* re-position the experimental cell. The length of the bellows is controlled with thick steel legs of adjustable height that span the gap between the two flanges of the bellows.

The combination of the small wall thickness and the low thermal conductivity of stainless steel limits the conduction of heat from room temperature down the tube to regions of the cell and cryostat at cryogenic temperatures. Another benefit of 316 stainless steel alloy is that it has a small volume magnetic susceptibility $\chi_{\rm vol} \sim 10^{-3}$), so it can be treated as a non-magnetic material for many purposes [155]. The top of the tube is welded to a cap with multiple KF flanges welded to it, which are used for electrical feed-throughs and connections for the inlet and outlet of a continuous flow line of liquid helium. The bottom of the tube has a flange welded to it for an indium seal, and this flange has a lip into which

brass rods can be screwed (these rods form the brass cage, as described in section 3.2.3). The bottom of the stainless steel tube is shown in figure 3.3. When in operation, the cell body is joined with the titanium can (section 3.2.4) via an indium seal. For the last six" of the 1.00" OD stainless steel tube (stopping before the flange), there is a copper coil made from a copper tube with a 0.125" OD that wraps around the 1.00" OD stainless tube. The coil is brazed to the 1.00" OD stainless steel tube to ensure that they are in strong thermal contact with each other. Both ends of the coil are brazed to stainless steel tubing with an OD of 0.25", which lead up to KF ports on the cap at the top of the cell body.

The KF port on top of the cap is made with a KF 25 flange, which remains connected to a four-way KF reducing cross. The KF cross has two KF 25 ports and two KF 40 ports. One KF 40 port is used for a 24-lead vacuum-tight electrical feed-through. The other KF 40 port is connected to a pumping system consisting of a turbo pump that is backed by a dry roughing pump. Then entire experimental cell placed into the cryostat is shown in figure 3.2.

The continuous flow helium line consists of the 0.125" OD copper coil brazed to the 0.25" stainless steel tubing that leads to the KF ports on the cap of the cell body. One of the KF ports is used as a liquid helium inlet port, to which a vacuum-jacketed liquid helium transfer line from Janis Inc. is connected. The vacuum-jacketed transfer line (bayonet) is brazed to one of the stainless steel tubes that connects to the copper coil, and it is shown in figure 3.2 jutting out of the cap of the cell body at an angle. As a result, we are able to flow liquid helium through the coil, and thereby cooling the bottom of the cell body to liquid helium temperatures. The helium that exits the coil through a KF port on the cap of the cell body is collected by lines that lead into a helium recycling system made by Quantum Design Inc. During experiments, we use a liquid helium transfer line with an adjustable needle valve to control the flow of helium into the bayonet. With a head pressure of 3 PSI on the liquid helium dewar providing the liquid helium to the continuous flow line, having the needle valve on the adjustable flow transfer line open just one revolution from

Figure 3.2: A partially-exploded view of the experimental cell inside the cryostat.

its closed position provides enough cooling power to cool the bottom of the cell to liquid helium temperatures.

There are also three custom two-piece shaft collars attached to the 1.00” OD stainless tube. However, these shaft collars are not depicted in the images shown in this section. The first shaft collar is clamped tightly to the 1.00” OD tube a few inches beneath the bottom edge of the cap of the cell body. The collar has flat regions to which four oxygen-free copper braids with diameters of about 0.25” can be strongly clamped. The opposite ends of these copper braids are strongly clamped to the top plate of the cryostat’s liquid nitrogen bath. As a result this shaft collar allows some heat conducted from room temperature to be dumped into the liquid nitrogen bath, and thus helps keep the bottom of the cell body cold. The second shaft collar is about one foot lower on the 1.00” OD stainless steel tube than the first shaft collar, and it has an OD ≈ 60 mm. Sections of beryllium copper spring finger strips (purchased from Omega Shielding Products) are wrapped around the second shaft

collar and secured with 2850 Stycast epoxy. The spring fingers protrude just over three millimeters from the surface of the second shaft collar. As a result, when the second shaft collar is clamped to the cell body, the entire experimental cell assembly fits snugly into the cryostat and is centered in the cryostat's opening. The second collar is positioned such that the spring fingers are in physical contact with the helium bath, but the spring fingers are small and the force they exert of the helium bath wall is small, so the helium bath provides negligible cooling of the cell body through the spring fingers. Another benefit of the second shaft collar is that it blocks blackbody radiation from room temperature from impinging on the coldest parts of the cryostat. The third and final collar is located ≈ 6" above the top of the copper coil. The third collar is strongly clamped to the 1.00" OD stainless steel tube, and an oxygen-free copper braid with a diameter ≈ 0.25" is clamped to the collar. The opposite end of the braid is clamped to a small shaft collar that is affixed to the stainless steel tube, which is brazed to the copper coil. As a result, the third shaft collar thermally anchors the cell body to the cold helium gas that exits the coil on the way to the helium recycling system. This allows us to use the enthalpy of the cold helium gas to further cool the cell body.

Lastly, a cartridge heater and a Cernox temperature sensor are affixed to the flange at the bottom of the 1.00" OD stainless steel tube. The electrical leads from the two sensors, made of low thermal conductivity phosphor bronze, are spiraled around the continuous flow line all the way up the 1.00" OD stainless steel tube before the reach the electric feed-through port on the cap at the top of the cell body, which limits the heat conduction down from room temperature.

3.2.2 The Baffle Stack

The KF reducing cross connected to the cap at the top of the cell body has a spare KF 25 port that is used to position a series of baffles that block blackbody radiation from room temperature on the way to the region where drops are levitated. This part, which is being

called the baffle stack, is slid into the cell body from the top.

A commercially-available KF 25 blank with a thickness of 0.5" was modified to include a hole with a diameter of 0.125" and a length of 0.25" along the symmetry axis of the blank. A segment of G-10 rod with a length $\approx$ 2 feet and a diameter of 0.125" is epoxied into the hole on the modified KF blank. A series of polished, aluminum semi-circular pieces (baffles) are mounted on the rod at different locations, every one rotated by 180° with respect to its neighbor. The radii of the baffles is $\approx$ 0.010" smaller than the inner radius of the cell body. The baffles are mounted to the rod using small set screws, allowing their positions to be changed. In total, there are seven baffles and each one is separated by $\approx$ 2". There are a few exceptions to this spacing, though, because of the inclusion of three special objects mounted to the rod. These three objects center the rod in the cell body, and provide thermal contact between the rod and the cell body; these objects are round mounts that are affixed to the G-10 rod, which have beryllium copper spring fingers wrapped around them, and thus they make physical contact with the chamber wall. Furthermore, one of the objects has a temperature sensor epoxied to it, while another has a cartridge heater epoxied to it.

When the baffle stack is inserted into the cell body through the KF reducing cross, this orientation of baffles blocks the line-of-sight blackbody radiation from room temperature, while providing a high-conductance path to evacuate the experimental cell with a pumping system. Blocking the line-of-sight radiation from room temperature is important to ensure the walls of the experimental cell near the levitated drop can reach liquid helium temperatures.

Four phosphor bronze electrical leads (36 gauge) from the electrical feed-through on the KF reducing cross spiral down the baffle stack, connecting to the cartridge heater and a Cernox temperature sensor. Another six phosphor bronze leads spiral down the baffle stack and connect to a Cernox temperature sensor and four electrodes in the brass cage.

3.2.3 The Brass Cage

The brass cage is formed by four brass rods (free-machining yellow brass) with a segment of 4-40 screw threading on one of their ends. These are screwed into threaded holes on an internal lip of the stainless steel indium seal flange on the bottom of the cell body. Brass was chosen because it is non-magnetic, and it has larger thermal conductivity than 316 stainless steel (this is useful because we want the entire cage to be well-thermalized with the continuous flow line). Figure 3.3 provides an illustration of the brass cage. Mounted to these rods with set screws are several brass mounts that can hold Cernox temperature sensors, cartridge heaters or other components. The brass mounts are shaped like annuli, with OD of 0.89" and inner diameter of 0.59". We tried to keep the inner diameter as large as possible because we evacuate the experimental cell through these brass mounts. One of the mounts has a countersunk hole, inside which an aspheric lens rests. Two of the mounts are highly unique and will be explained in detail below.

Figure 3.4 shows both unique mounts together as they are in the experimental cell. The first unique mount includes electrodes that can apply electrostatic forces to a levitated drop. The mount is nearly identical to the one described above, with the exception that it has a lip. A G-10 annulus (green colored in figure 3.4) fits around this lip and rests on the brass mount. Electrodes (copper colored in figure 3.4) protrude from the G-10 annulus, and are soldered to phosphor bronze leads that run up to the electrical feed-through on the KF reducing cross. The other unique brass mount holds right-angled prism mirrors, which are used to illuminate levitated drops for imaging, or to steer lasers to the drops. The prisms are made of silica, with their angled surface coated with protected silver (although the coating is depicted as gold in figure 3.4). In the experiment, we slide the entire experimental cell up or down relative to the levitation point, which allows us to position the two mirrors around the drop. This brass mirror mount includes titanium platforms to which the prism mirrors are epoxied. Again, the epoxy we used was 2850 Stycast, which forms robust glue joins between titanium and glass due to their similar thermal contraction properties.

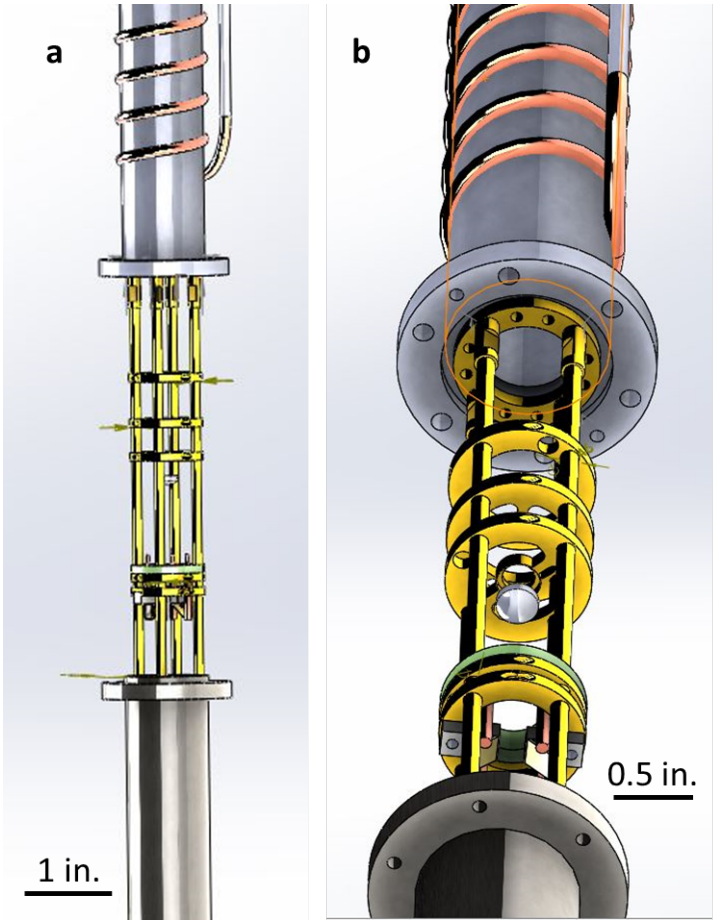

Figure 3.3: The bottom of the experimental cell. Image (a) and image (b) provide different viewpoints. The brass cage assembly is connected to the bottom of the cell body. The copper continuous flow line is affixed to the stainless steel 1" OD tube. Various brass-annulus mounts are connected to the brass cage. The titanium can slides over the brass cage to mate with the stainless steel tube via an indium seal.

Based on the magnetic field profile of the superconducting magnet, we know where the levitation should be (theoretically) when the magnet is producing its maximum specified magnetic field strength ≈ 15 T. With this information, we placed the center of the mirror surfaces at the approximate location of the levitation point before we insert the experimental cell into the cryostat. This positioning is accurate enough that it requires only slight adjustments (1-2 mm) to the vertical position of the mirrors once the drop is levitated. Adjusting the height of the legs that control the length of the bellows that is connected to the cap of the cell body (figure 3.2) allows us to make fine adjustments of the mirrors' position

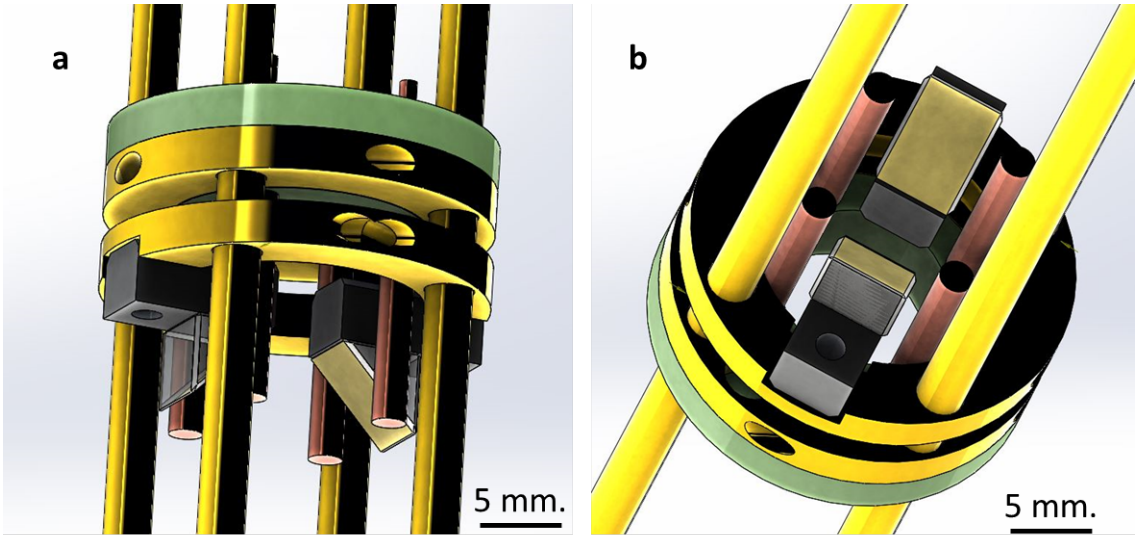

Figure 3.4: The mirror mount inside the experimental cell. (a) and (b) show the mirror mount assembly in the brass cage from different viewpoints. The electrodes (copper colored) allow for the application of electric fields to the levitated drop. In the experiment, the drop is positioned between these mirrors for imaging and laser measurements.

in situ.

3.2.4 The Titanium Can

The titanium can is made from a seamless tube with a 1.02" OD and wall thickness of 0.035", which is shown in figure 3.5. A flange for an indium seal is welded to the top of the titanium tube. This flange mates with the indium seal flange on the 1.00" OD stainless steel tube on the bottom of the cell body. A sapphire window with a thickness of 0.080", a diameter of 0.93", and an anti-reflection coating for 1.55 μm light is brazed into the bottom of the titanium tube. The braze work was done by Applied Vacuum Tech and MPF Products. Titanium and sapphire have similar thermal conductivity and thermal contraction, which allows them to be brazed together and cooled to cryogenic temperatures without the window being crushed by the thermally-contracted metal tube.

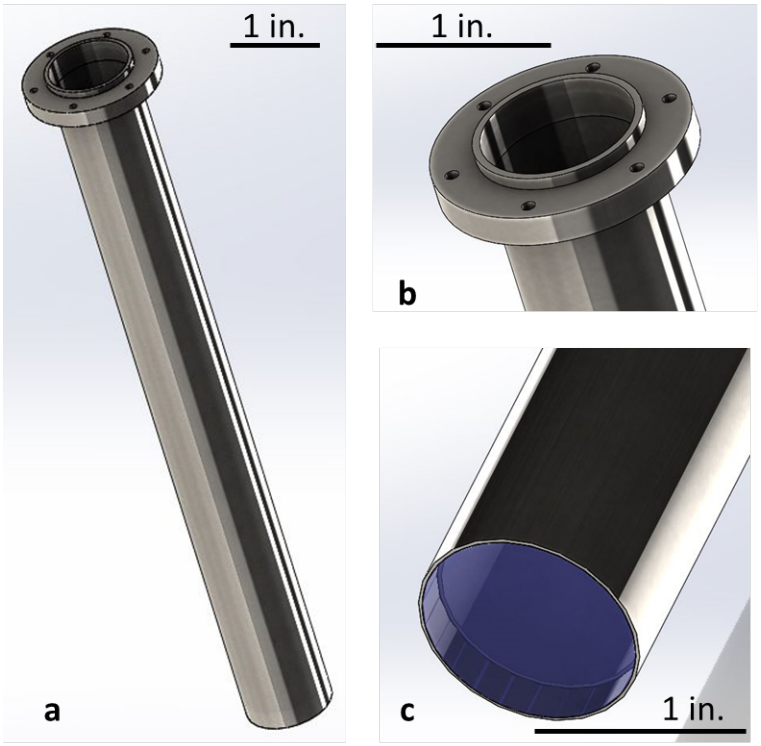

Figure 3.5: The titanium can of the experimental cell. (a) The entire titanium can, which is about 8" long. (b) A zoom-in of the flange use to mate with the flange at the bottom of the cell; (c) a zoom-in of the bottom of the titanium can, into which an anti-reflection coated sapphire window is brazed.

3.3 Procedure for Generating a Levitated ^{4}He Drop

In this section, I describe how we assemble the cell and mount it inside the cryostat. I also describe the process of cooling the cryostat from $T = 300$ K to $T = 4$ K, and how we create and trap levitated drops.

To assemble the experimental cell, the brass cage is first affixed to the cell body. Then the titanium can slides over the brass cage and mates with the flange at the bottom of the cell body. The connection between the bottom of the cell body and the titanium can is made with an indium seal. Next, the experimental cell is slid into the opening of the cryostat, and the cap of the cell body mates with the bellows on top of the cryostat via an ISO80 connection, which is shown in figure 3.2. Next, the experimental cell is connected to a turbo pump station through a KF 40 port. The cell is now inside the cryostat, and it is ready

to be used to study levitated drops. However, the cryostat is at room temperature, so it must be cooled before experiments begin.

3.3.1 Cooling the Cryostat to 4 K

To cool down the cryostat, we evacuate its internal vacuum can to a pressure $P \approx 10^{-6}$ mbar, which thermally isolates the innards of the cryostat from room temperature. We continue to pump on the cryostat's vacuum can while we fill its liquid helium bath with liquid nitrogen. We let the liquid nitrogen sit in the helium bath space for one day to ensure that the innards of the cryostat (especially the large thermal mass of the magnet) is cooled to $T = 77$ K. Next, we connect the outlet port of the liquid helium bath to the inlet port of the liquid nitrogen bath, and insert a transfer line into the bottom of the liquid helium bath space. Upon pressurizing the transfer line, liquid nitrogen exits the liquid helium bath and fills the liquid nitrogen bath. The helium bath is mostly emptied with this method, but to ensure all of the liquid nitrogen has been removed, we blow warm helium gas through the helium bath for 3 hours with the pressure regulator set to 2 PSI. The magnet is in thermal contact with an Allen Bradley resistor, which allows us to monitor its temperature through calibrated resistance measurements. Next, we alternate between pumping on the helium bath space and flushing it with warm helium gas. When there is still liquid nitrogen in the liquid helium bath space, pumping on it will decrease the magnet's temperature by several Kelvin (the Allen Bradley resistance might increase by $\lesssim 10\ \Omega$). We know the liquid nitrogen has been completely removed from the liquid helium bath space when pumping on the bath results in no change of the magnet's temperature. Next we transfer liquid helium into the liquid helium bath of the cryostat and stop pumping on the internal vacuum can of the cryostat. Now, the cryostat is cold and we can prepare for measurements. At this point, the brass cage has $T \approx 130$ K.

3.3.2 Creating a Levitated ^{4}He Drop

When the cryostat is cold, we ramp the magnet up to the typical levitation current of 115.6 A. The ramp takes 15 minutes to complete, and it is controlled by the power supply controller. After the magnet is at full field, we pressurize the experimental cell to $P \approx 200$ mbar of 99.9999% purity ^{4}He gas (note that the ^{4}He gas is passed through a liquid nitrogen cold trap for additional purification before entering the cell), and begin flowing liquid helium through the continuous flow line to cool the cell walls. The slow continuous flow (needle valve open only one revolution) of liquid helium around the cell walls cools its base to $T \approx 4.2$ K in ≈ 40 minutes.

When the cell walls reach $T \approx 4.2$ K at its base, we fill the cell to $P \approx 840$ mbar of 99.9999% purity ^{4}He gas and then immediately shut off the gas supply. The gas in the experimental cell liquefies, reducing the cell pressure, and produces a small puddle of liquid helium at the bottom of the cell. After 15 minutes of liquefaction, the cell pressure asymptotes to $P \approx 720$ mBar (this 15 minute period ensures that there is a significant puddle at the base of the cell, i.e. on top of the sapphire window). Next, we open the cell to a scroll pump and simultaneously spin up a turbo pump, which causes the helium puddle to aggressively boil, at which point a dense fog of micron-sized drops emerge from the liquid (the fog typically appears ≈ 5 s after we begin pumping on the liquid helium puddle in the cell). The fog moves upward into the magneto-gravitational trap, where it coalesces into a single drop. Figure 3.8b shows a 3 mm diameter levitated drop created ≈ 10 s after pumping on the experimental cell. At this point, the drop is levitated above a puddle of superfluid helium and it is surrounded by walls coated with a thin layer of superfluid helium. The vapor pressure of the liquid helium puddle at the bottom of the cell damps the levitated drop's motion. After 2-3 minutes, the drop appears to be motionless with an imaging resolution of 7.1 μm/pixel (see section 3.4.1). Figure 3.6 shows and illustration of the experimental cell immediately the levitated drop is generated.

If the cell is pressurized with an additional 100 mbar of gas up to $P = 940$ mbar

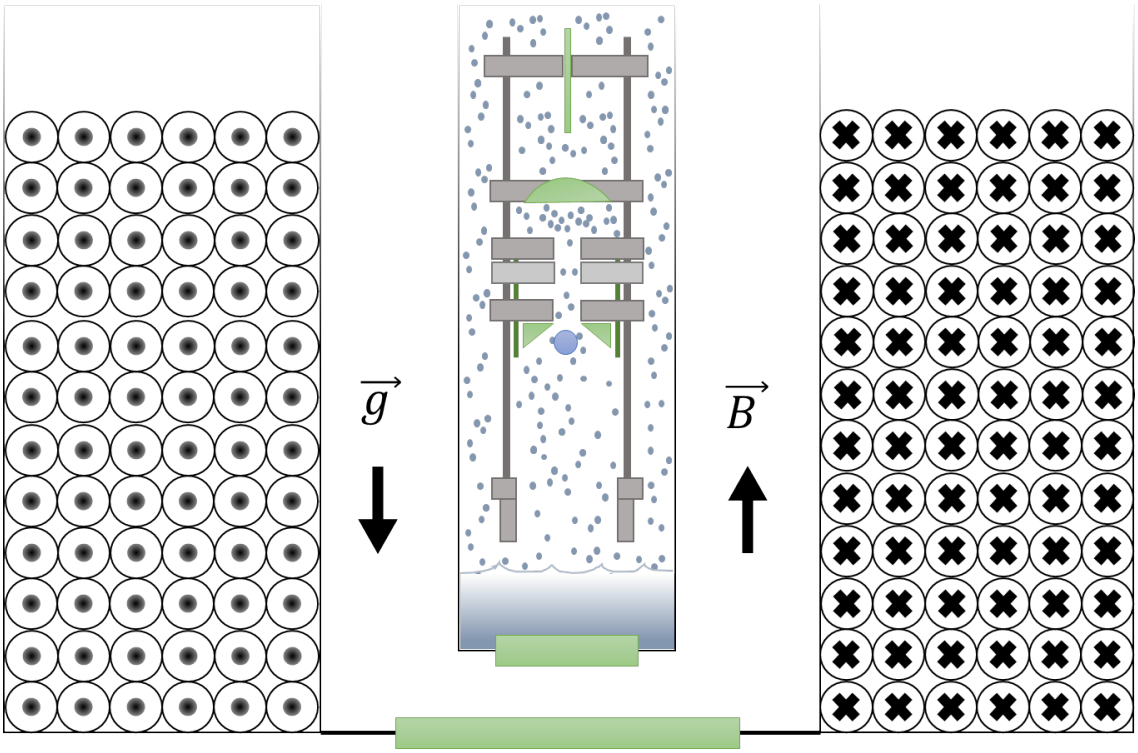

Figure 3.6: The experimental chamber after drop generation. Atop the bottom of the cell is a puddle of liquid helium. The cell contains residual helium gas. A levitated drop is centered between the right-angle prism mirrors (green triangles). The cell is surrounded by the superconducting magnet that surrounds it; the circles and crosses show the direction of the magnet current.

before it is allowed to cool for 15 minutes, too much liquid will be in the cell, which makes producing a drop difficult. When the cell is overfilled with liquid and pumped to make a drop, the fog will tend to condense on cold objects above the levitated drop, and drip from these surfaces. These drips tend to knock the levitated drop out of the trap. If the cell is overfilled, we normally turn on a heater to evaporate the puddle, and then start the puddle formation process from the beginning.

3.4 Video Analysis of Levitated Drops

In this section we discuss our use of the calibrated imaging of levitated drops. Through recording video of levitated drops, we can determine its size and learn about its shape. We

have found that, using the drop production method described in section 3.3, drops typically begin with $R \gtrsim 1$ mm, but evaporate rapidly for a short while before stabilizing around $R \approx 250$ μm. The drops' shape deviations from a perfect sphere induced by the magnetic trap are predicted to be $\sim 10^{-4}$ (see section 2.3.4). We find that the drops described in this section are consistent with sphericity at the level 10^{-3}.

We have used video analysis to measure drops' center of mass (COM) motion and found three normal modes of oscillation with frequencies ~ 1 Hz, which are in good agreement with what was predicted in equations 2.114 and 2.115. However, we found that the COM modes are coupled, and that an asymmetry in our trap leads to a broken degeneracy of the drop's radial motion.

We have also used video imaging to study the drop's evaporation over many hours. With this measurement technique, we have measured the drops' evaporation to be as low as ≈ 0.19 μm/hour; from this evaporation rate we infer a drop temperature $T \approx 330$ mK, and a cell pressure $P \sim 10^{-8}$ mbar. Once a levitated drop had stabilized with $R \approx 250$ μm, we trapped it for more than 24 hours (but we could trap them for much longer if we so choose).

We have found that a drops' levitation point depends on its size. This phenomenon seems to occur due to an additional non-volume-dependent force, which likely arises due to the non-thermal equilibrium state of our experimental chamber.

Lastly, we briefly describe experiments with positively charged helium drops.

3.4.1 Sizes and Shapes of Levitated ^{4}He Drops

The imaging system used to record images and the video of levitated drops consists of an adjustable focus and adjustable magnification Navitar 12X Zoom Lens System connected to a Thorlabs CMOS camera. The lens system has a fine focus adjustment range of 3 mm and an adjustable magnification of up to 12X. Furthermore, the working distance used for image collection was ≈ 30 cm. When imaging a drop, the imaging system is nearly coaxial with a bright green LED light source. The bright green LED is directed towards a

dichroic mirror, which reflects the light into the cryostat. Images of the drop are recorded through the reflection of light exiting the cryostat from the dichroic mirror and into the imaging system.

In order to determine the size of a levitated drop, we calibrated our imaging system using a resolution test target from Thorlabs. Figure 3.7a shows an image of the target that was taken with our imaging system, where the red line is a marker that corresponds to the location of the line cut of the image shown in figure 3.7b. The lines on the resolution test target are spaced by 100 μm, so by counting peaks in figure 3.7b, we are able to relate the displacement between pixels on the camera to a physical distance. In figure 3.7b, the first peak is approximately located at pixel 5, whereas the final peak is approximately located at pixel 708. Consequently, the calibration is 7.1 μm/pixel.

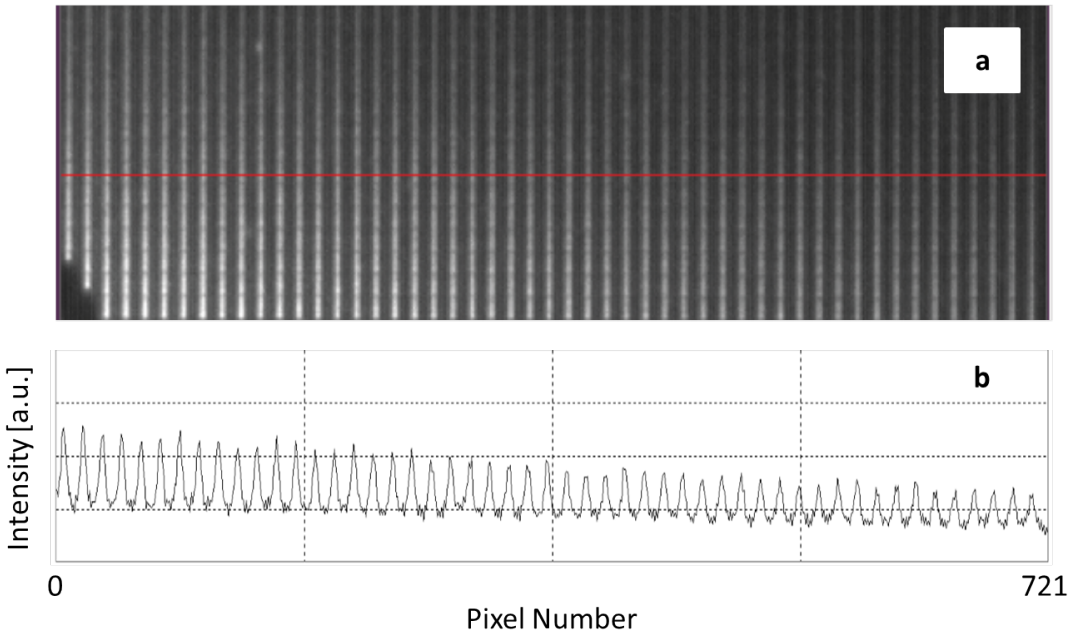

Figure 3.7: The calibration of the imaging system. (a) An image of a Thorlabs resolution test target with 100 μm periodicity. (b) A line cut through the image that shows the intensity versus pixel number. The resulting calibration is 7.1 μm/pixel.

Drop Size

At the end of the levitated drop creation process described in section 3.3, the remaining vapor liquid helium puddle has been cooled to T $\approx$ 1.5 K by the turbo pump. The vapor pressure above the puddle ($P \sim 10^{-1}$ mbar) keeps the experimental cell walls and the levitated drop in thermal contact. After 5-10 minutes, the puddle completely evaporates and the environmental heat load on the cell causes the walls to quickly warm up to $T \approx$ 7 K. When the walls reach this temperature the liquid helium film desorbs from the cell walls. At this time in the chamber $P \sim 10^{-2}$ mbar, and this pressure provides enough thermal contact between the cell walls and the levitated drop to cause, for a short time, rapid evaporation of the drop. The rapid evaporation is exacerbated by the fact that it is difficult to evacuate a chamber of helium, and we evacuate the chamber through ≈ 2.5 feet of 1.00" OD tubing (several inches of which are cryogenic), which severely limits the pumping speed. After 2-3 minutes, the pump has removed enough of the helium vapor to significantly reduce the thermal contact between the levitated drop and the cell walls, resulting in much less drop evaporation. At the end of this rapid evaporation process, we are left with a drop with a radius $R = 250 - 300$ μm that we can trap for many hours. Figure 3.8b shows the drop after the short period of rapid evaporation. Note that the camera looks into the experimental cell from the bottom, so a direct view of the drop is obtained in the middle of the image, whereas side views are obtained from the reflections of the drop in the mirrors on the right and left sides of the image.

In order to extract the size of a levitated drop, we use a script written in the Python language to fit circles to images of drops. Figure 3.9 provides an illustration of the steps undertaken to extract the size and position of a levitated drop. First, the script splits a typical video (figure 3.9a) that is used for data analysis into individual frames (figure 3.9b). The color scale applied to the image in figure 3.9b is an artifact of how it was plotted; the image is gray-scale. Next, the script implements the well-known Canny algorithm to detect all edges in the image (figure 3.9c). The algorithm requires thresholding to make

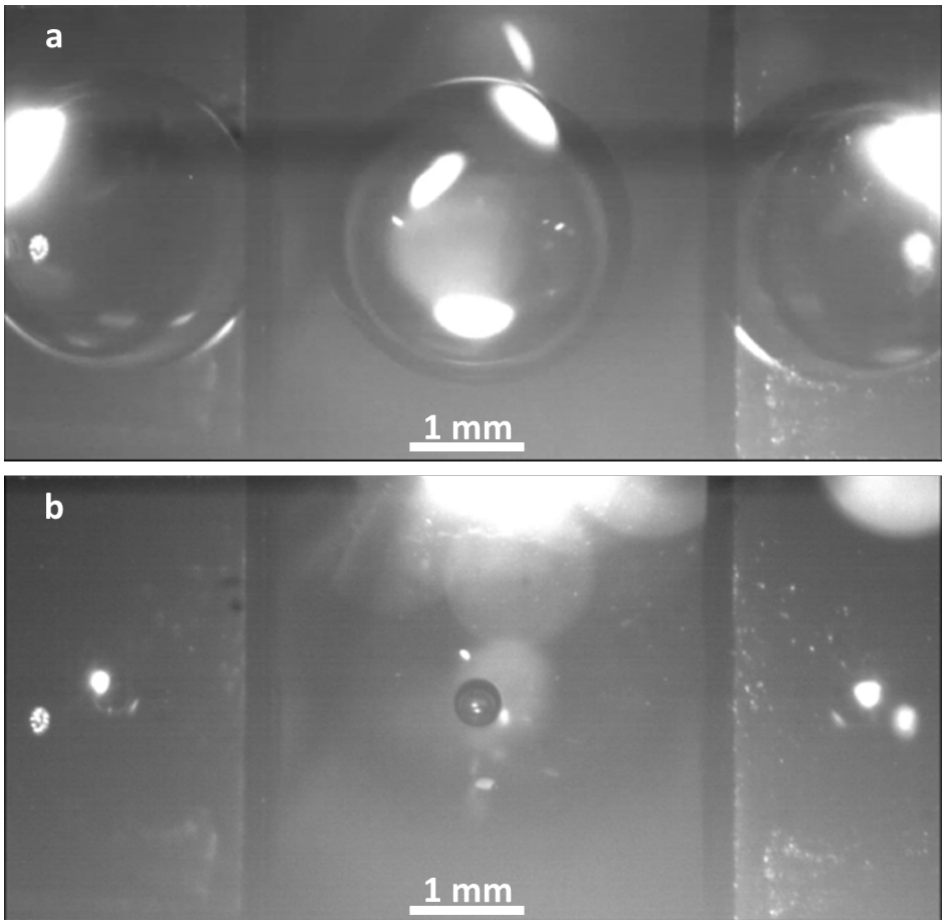

Figure 3.8: A ^{4}He drop magnetically levitated in vacuum. (a) An image of a levitated drop immediately after it is created. (b) The same drop after undergoing an ≈ 3 minute period of rapid evaporation due to the desorbtion of the liquid helium film on the experimental cell walls. In (a) the drop has a radius ≈ 1.5 mm, whereas in (b) the radius is ≈ 250 μm.

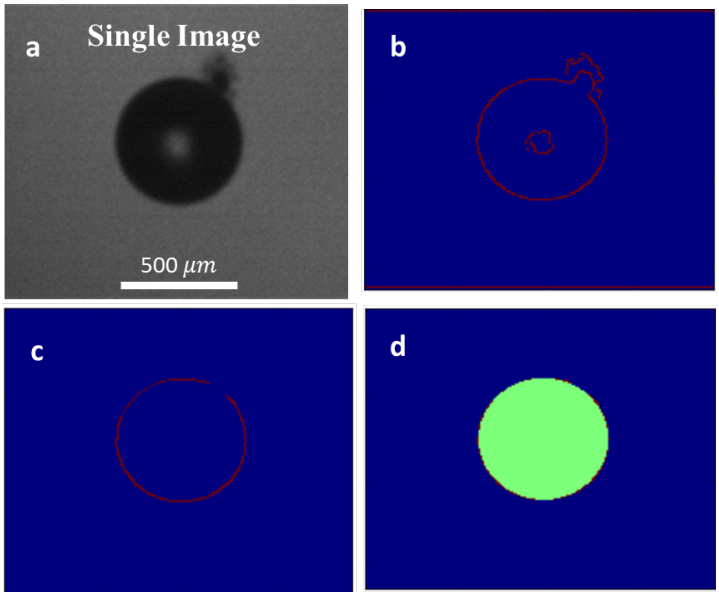

Figure 3.9: Extraction of a drop's position and radius via image analysis. (a) The original video file; (b) One frame from the video file. (c) The Canny algorithm is applied to the image to detect its edges. (d) The image is cleaned by application of an annulus-shaped filter. (e) The cleaned image is fit to a circle to extract the position and radius of the drop.

decisions regarding what is, and what is not, an edge. Because we are consistent with the lighting in our images, the threshold was chosen over a year ago, and has not needed to be changed (it was chosen such that the drop's edges are visible, but other edges are minimal). Next, the image is cleaned using an annulus-shaped filter (figure 3.9d). The filter is implemented with a doubly-nested for-loop that scans over the image. The radii of the filter are chosen manually by visually inspecting the first image in the sequence. Because the drop's evaporation rate is slow, an annulus-shaped filter with a width of only a few pixels can be applied to the same sequence of images of a drop, even over several hours of video. After the image has been cleaned, we are left with a clear image of the edge of the drop. Finally, we use the least-squares method to fit a circle to the drop's edge (figure 3.9e). For each image, the fit returns the coordinates of the drop's center, as well as the the drop's radius in pixels. The calibration determined in section 3.4.1 is used to convert the extracted values from pixels to microns.

Drop Shape

Except at the magnet current at which the radial and axial COM motion spring constants are predicted to be equal, the magneto-gravitational trap tends to cause the drop to take on the shape of an oblate or prolate spheroid. The trap will cause the drop to elongate or shorten along the symmetry axis of the magnet, depending on the shape of the trap, and thus on the magnet current. However, as is described by equation 2.113, the degree of the deviation of the shape of a drop away from a perfect sphere depends on the drop's size. As a result, levitated drops with radii $R = 250 - 300$ μm are highly spherical at the magnet currents needed for levitation. Figure 2.17a suggests that for all magnet currents we should expect to observe a high degree of sphericity of the levitated drop due to the small drop size.

With a description of the radius of a levitated drop given by $R(\theta) = R_0(1 + \delta R(\theta))$, we can use equation 2.113 to define the ellipticity $e = R(0)/R(\pi/2)$. Ellipticity refers to the shape of the drop's perimeter, as would be seen by a cross-sectional cut through the magnet's symmetry axis with a plane whose normal is perpendicular to the axis. As such, direct imaging of the drop along the magnet's symmetry axis is not sufficient to visually detect ellipticity; direct images of the drop along the symmetry axis should have a circular cross-section ($e = 1$) if the ellipticity is generated by the trap (in the limit that the trap is not perturbed significantly, e.g. by nearby magnetic materials). Consequently, we analyze images of levitated drops from reflections in the prism mirrors on the brass cage. Such images provide a side-view of the drop. Figure 3.10 shows the expected ellipticity for drops of different radii and the ellipticity for drops levitated at different currents. In particular, figure 3.10b shows that with a drop with $R = 250$ μm, for all magnet currents that we would potentially use ($I = 115.6 - 118$ A), $-10^{-5} \leq e - 1 \leq 10^{-4}$.

In many cases, it is difficult to record images of levitated drops with high contrast relative to the background. Additionally, glares around the drop's edge will appear depending on the direction of illumination. The glares obscure the drop's edge in images. We devel-

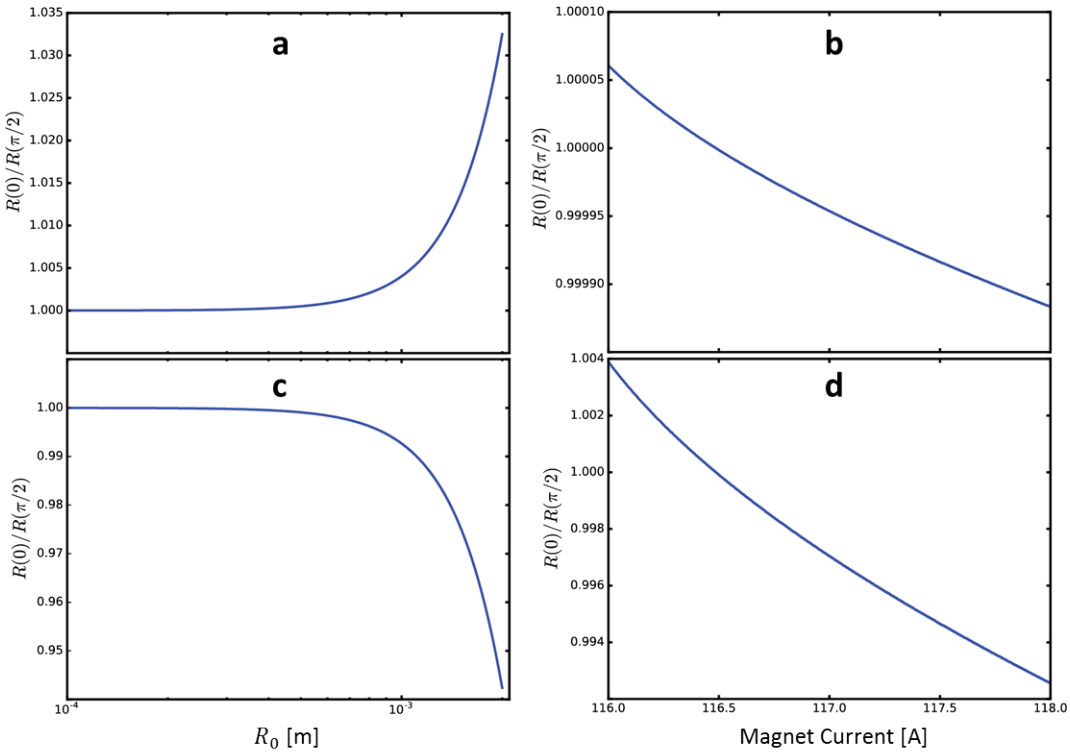

Figure 3.10: The magnetically-induced ellipticity of a levitated ^{4}He drop. (a) and (c) The ellipticity of a drop plotted against its unperturbed radius, for magnet current of 116 A and 118 A, respectively. (b) and (d) The ellipticity of a drop versus the magnet current for a drop with radius $R = 250$ μm $R = 1$ mm.

oped a more sophisticated fitting routine to extract ellipticity in the presence of edge glares. This is particularly useful when simultaneously recording direct-view and side-view images of a levitated drop, because it has been the case that there is a trade-off between contrast and edge glares between the two vantage points. For ellipse fitting, the same edge detection algorithm is applied to images of a levitated drop, but instead of applying an annulus-shaped filter (which would diminish our ability to detect ellipticity by throwing away useful data that don't fall on a circle), an ellipse is fit to all the detected edges. Next, any edge data that lie more than two standard deviations away from the ellipse fit are thrown away, then the remaining data are fit to an ellipse once more. This process is applied recursively until the only remaining edge data fall within two standard deviations of the previously fitted ellipse.

In order to test our ability to resolve a small degree of ellipticity, we purchased highly spherical sapphire balls (grade 25, B0.60S sapphire balls) from Swiss Jewel Co and analyzed images of them. The sapphire spheres' have $R = 300$ μm, and in a coordinate system whose origin is located at the center of the sapphire spheres, the spheres' perimeters (as defined above) in any plane on which the origin lies are specified to have $|1 - e| < 10^{-3}$. Figure 3.11 shows the steps of the recursive ellipse fitting routine; figure 3.11a shows the detected edges in an image of a sapphire sphere; figure 3.11b shows the final fit (blue) overlaid with the final edge data (red), which is surrounded by background edges (green); figure 3.11c shows the final edge data overlaid by the final fit; figure 3.11d shows the original image of the sapphire sphere overlaid with the final ellipse fit. In the end, the fit to the sapphire sphere image yields an ellipticity $e = 0.99 \pm 0.07$. While the manufacturer-specified ellipticity falls within the uncertainty range of our measurement, our measurement uncertainty suggests that its difficult for us to use this method to detect ellipticity at the level of 1 ± 10^{-3} in a 600 μm diameter sphere. Given our imaging system's inability to detect the ellipticity of a 600 μm diameter sapphire sphere, figure 3.10c suggests that the expected ellipticity of a levitated drop with $R = 250 - 300$ μm would be much too small to resolve.

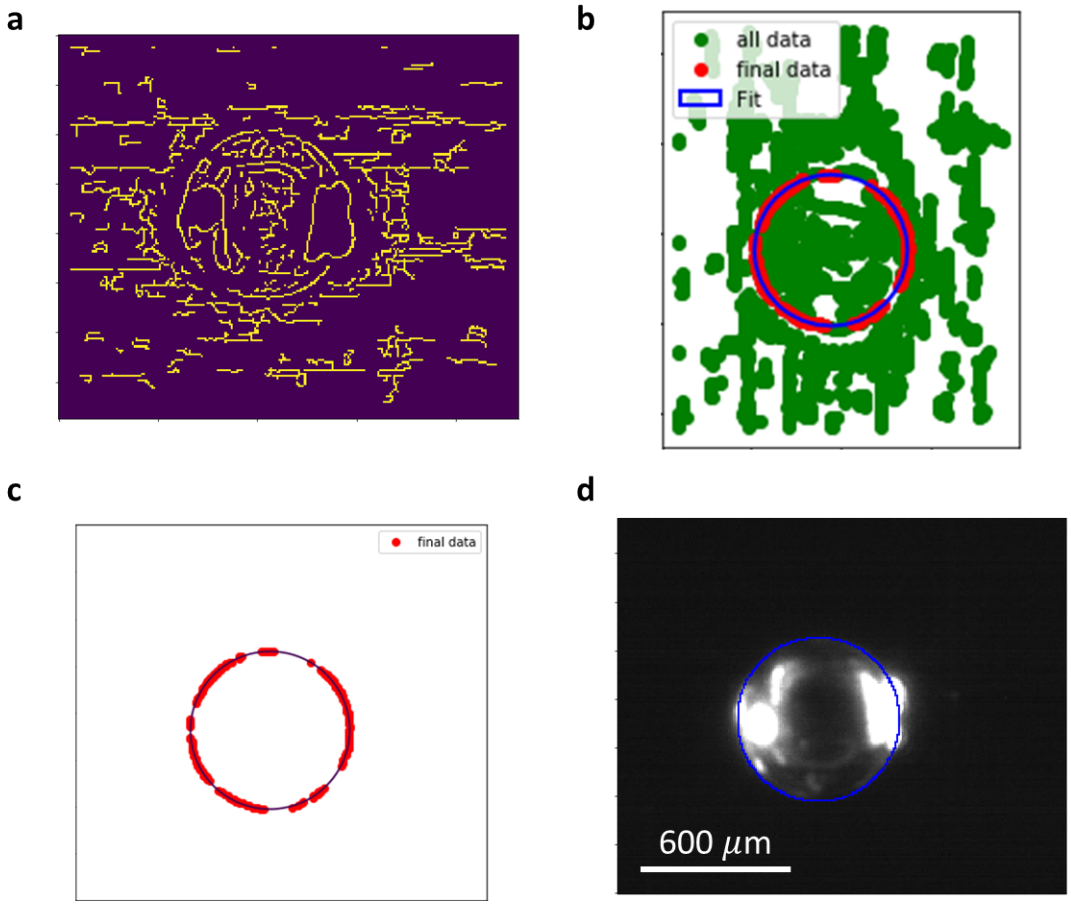

Figure 3.11: The extraction of a sapphire ball's ellipticity via image analysis. (a) The detected edges in an image of a sapphire ball. (b) The final fit (solid blue line) overlaid with the final edge data (red circles), which is surrounded by background edges (green circles). (c) The final edge data overlaid by the final fit. (d) The original image of the sapphire ball overlaid with the final ellipse fit.

In order to observe larger ellipticity in a drop, we simultaneously recorded video of a large drop's direct and side views immediately after its creation (before the short period of rapid-evaporation) at ≈ 1 frame/second (FPS). The drop had $R \approx 0.85$ mm, which was expected to exhibit larger ellipticity as the magnet current (trap shape) was changed, according to figure 3.10. Figure 3.12a shows a fitted direct view image of the drop, while figure 3.12b shows a fitted side view. During the recording, we incremented the magnet current in 100 mA steps from $I = 115.4 - 116.2$ A, which caused the drop's levitation point to move upward against gravity, as shown in figure 3.12g with the following correspondences: $I =$ (i) 115.4 A, (ii) 115.5 A, (iii) 115.6 A, (iv) 115.7 A, (v) 115.8 A, (vi) 115.9 A, (vii) 116.0 A, (viii) 116.1 A, (ix) 116.2 A. As a result of applying the ellipse fitting analysis to the drop's direct view images, figure 3.12c and figure 3.12d show the extracted e and axis lengths (i.e. semi-major and semi-minor) versus the video frame number, respectively. Figure 3.12e and figure 3.12f show the extracted e and axis lengths versus the video frame number, respectively. Here the semi-major axis is parallel to the magnet's symmetry axis, while the semi-minor axis is perpendicular to it. The reason that we observed a decrease in the drop's radius over time in the direct view is because when we increased the current, the drop moved up, and away from the camera (this decreases its apparent size). If, however, the decrease in drop's radius in the direct view was the result of some Δe induced by the magnet, then Δe should have been observable in the side view. Yet, as shown in figure 3.12f, $e \approx 0.96$ appears to be constant throughout the entire range of magnet currents.

From this analysis, we see that the drops are very spherical, but given systematic errors in imaging, such as background glaring in the images, we are unable to use video analysis at the current imaging quality and resolution of 7.1 μm/pixel to detect a deviation $< 1\%$ from a perfect sphere. It is important to note that the measurement of ellipticity could tell us about how much angular momentum the drop has (which would lead to $e \neq 1$ – see section 2.3.4), if the deviation from perfect sphericity were clearly measurable.

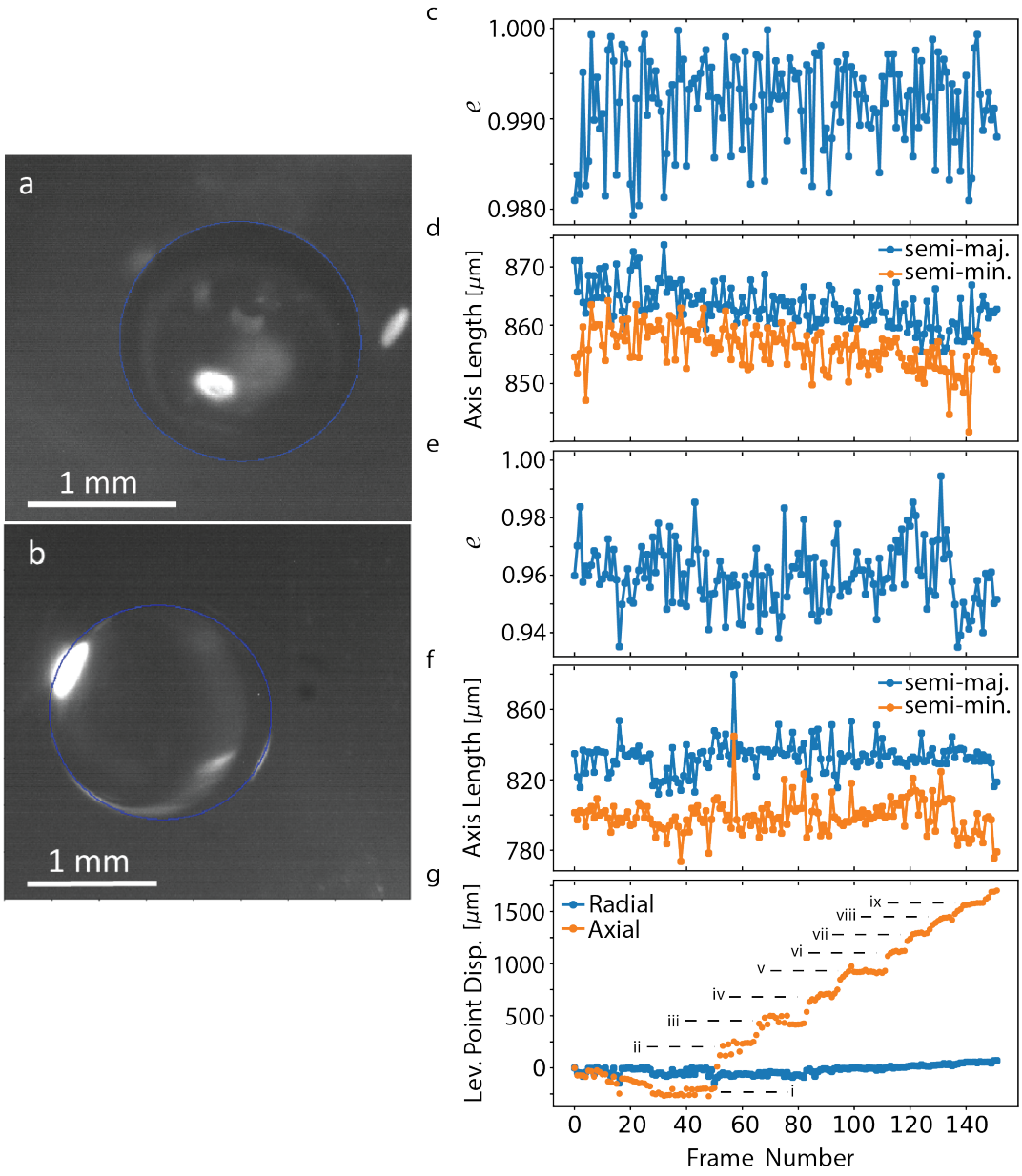

Figure 3.12: Measurements of a large ^{4}He drop's ellipticity via image analysis. (a) A fitted direct view image of a ≈ 1.6 mm diameter levitated drop. (b) The fitted side view image of the drop. (c) The direct view ellipticity extracted from the video recording. (d) The drop's direct view axis lengths. (e) The side view ellipticity extracted from the video recording. (f) The drop's side view axis lengths. (g) The displacement of the drop's equilibrium induced by changing the magnet current I throughout the recording. In (g), I = (i) 115.4 A, (ii) 115.5 A, (iii) 115.6 A, (iv) 115.7 A, (v) 115.8 A, (vi) 115.9 A, (vii) 116.0 A, (viii) 116.1 A, (ix) 116.2 A.

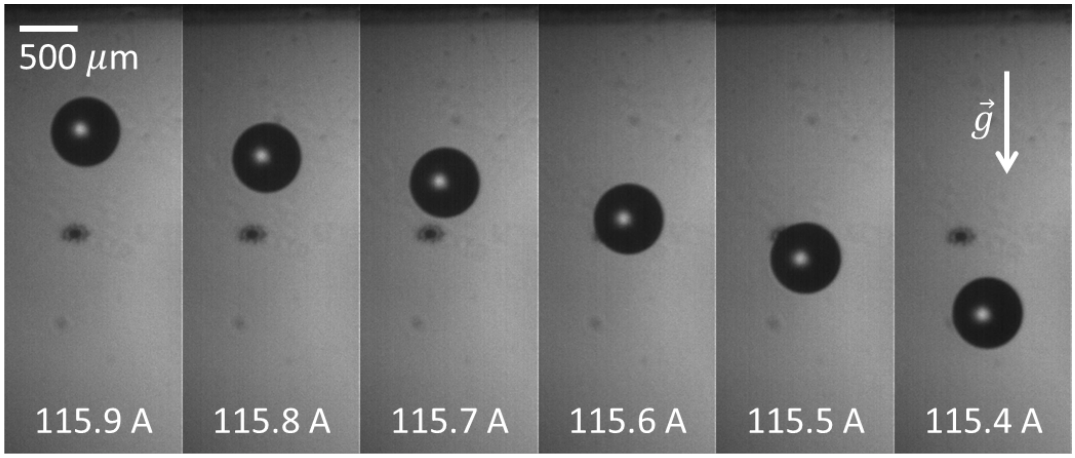

Figure 3.13: A series of still images of a levitated ^{4}He drop, which show displacement of the drop's equilibrium position via changing the magnet current. As indicated in the picture, the direction of gravity points downwards in the images. The fixed ellipse-shaped object near the images' centers is a piece of debris that adhered to the prism mirror surface.

3.4.2 Center-of-Mass Motion of Levitated ^{4}He Drops

The same technique used to extract the size of the drops through video analysis was used to study their center-of-mass (COM) motion. A slight bump to the optical table on which the cryostat rests will set the drop into motion, and this is how the motion was generated for the following measurements. In these measurements we set I to some value, wait for 5 minutes to let the magnet settle, then record video of the drop's motion for ten minutes before repeating the process for a range of I. Figure 3.13 shows a series of still images (obtained from the video that was analyzed to study the drop's COM motion) of a drop that was levitated with various I (the shift in the drop's equilibrium position with I is clear). Video of the drop's motion was recorded by viewing the drop's reflection from one of the right-angle prism mirrors in the brass cage. As a result, the camera records a side view of the drop, which allows for the simultaneous recording of axial and radial motion.

The magnet has a large inductance L_{magnet} $\approx$14 H. Since the voltage V_{magnet} across the magnet is such that $V_{\mathrm{magnet}} \propto L_{\mathrm{magnet}}\mathrm{d}I/\mathrm{d}t$, applying voltages to change the magnet current in a safe manner (to avoid magnet quenches) is a slow process (the current ramp speed is controlled to be $\approx$ 8 A/minute). Furthermore, the power supply that drives the

magnet has a P.I.D. controller that will overshoot and undershoot the target current before settling to the target. After waiting for ≈ 5 minutes, the magnet is well-settled at the target current applied by the power supply.

Figure 3.14 shows a drop's "axial" and "radial" motion with $I = 115.4$ A, which was obtained from video recorded at 20 FPS. The drop's radius was 272.2 ± 0.7 μm. Axial motion refers to motion that appears to be parallel to the magnet's symmetry axis, whereas radial motion appears to be perpendicular to its symmetry axis. Figure 3.15 shows the power spectral density (PSD) of the same drop's axial and radial COM motion. The PSDs of both the radial and axial motion have two peaks, which correspond to two COM normal modes with oscillation frequencies $\omega_1/2\pi \approx 1.0$ Hz and $\omega_2/2\pi \approx 1.6$ Hz. Despite the fact that each PSD shows the presence of two normal modes, the peak heights (which differ by a factor $\sim 10^2$) correspond to the primary motion that is visible in the axial and radial directions. It could be that the camera's imperfect viewing angle (not exactly parallel to the magnet's symmetry axis) projects some of the axial or radial motion onto the other, or that the COM modes are coupled.

Given the working distance of our imaging system, it was difficult to place the camera in a location where the magnetic field would not cause it to malfunction and drop frames during the recording of video. If the camera (standard Thorlabs visible wavelength CMOS camera) was exposed to a magnetic field strength $B_{\mathrm{cam}} = B_{\mathrm{malf}} \approx 600$ gauss, it would shut itself off. When $B_{\mathrm{cam}} < B_{\mathrm{malf}}$, the camera would work, but it would drop more and more frames as $B_{\mathrm{cam}} \to B_{\mathrm{malf}}$. Because of the camera's proximity to the superconducting magnet, when we increased the the magnet current from 115.4 to larger values, the camera would begin to drop frames, and thus the effective video capture frame rate decreased.

As mentioned, we recorded video of the drop's motion while driving the magnet with various values of I. During these measurements, the camera's frame rate was set to 20 FPS. We used an independent clock to count ten minutes, and the video capture time was based on the independent clock's time. As a result, the video capture frame rate was in-

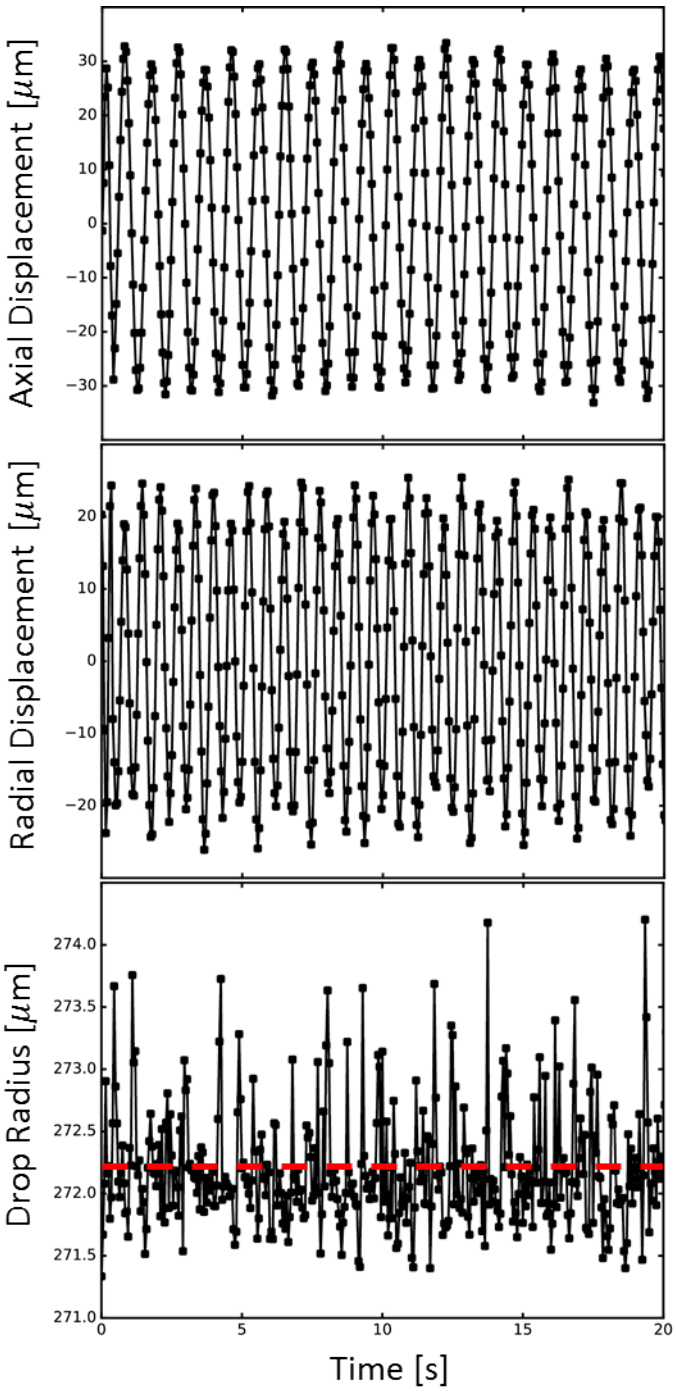

Figure 3.14: The radial and axial center-of-mass motion of a trapped ^{4}He drop with $R = 272.2 \pm 0.7$ μm (dashed red line marks the average radius). The current flowing through the magnet is 115.4 A.

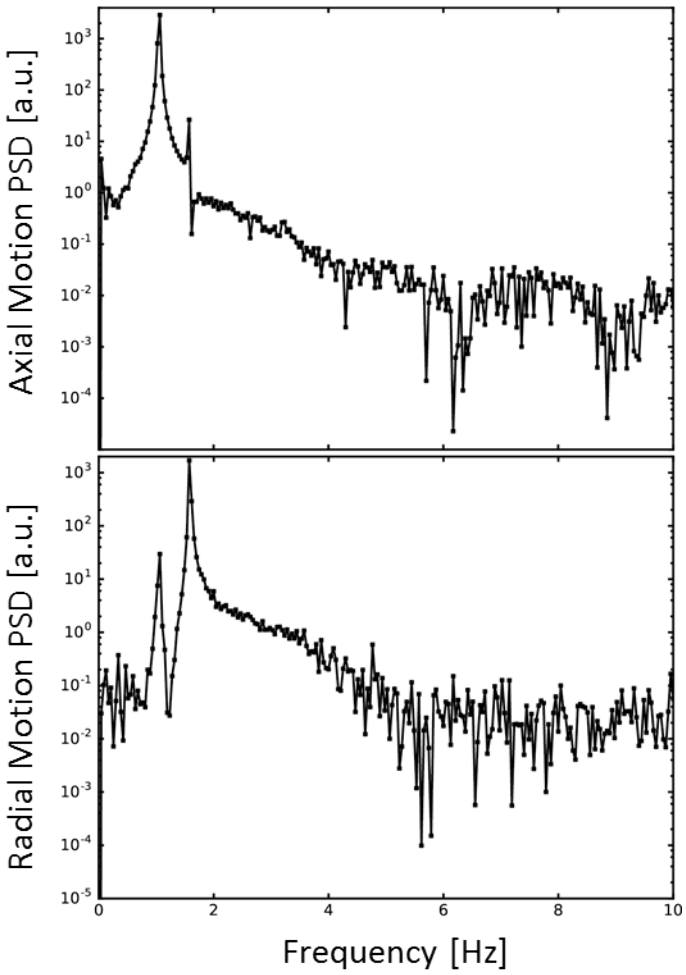

Figure 3.15: The power spectral density of the radial and axial center-of-mass motion of a trapped ^{4}He drop with $R = 272.2 \pm 0.7$ μm. The current flowing through the magnet is 115.4 A.

ferred from the number of frames in the video file, compared to 10 minutes. The effective frame rate of the videos taken with $I = \{115.4, 115.5, 115.6, 115.7, 115.8, 115.9\}$ A, was $\{20, 18, 17.252, 16.813, 17.145, 17.325\}$ FPS, respectively. Despite the decreased sampling rate of the drop's motion with increased I, the sampling was still fast enough to fully reconstruct the ~ 1 Hz harmonic motion of the levitated drop. We computed the PSDs of the COM motion data for the various I listed above, and manually extracted the COM mode frequencies with a Matlab tool, which are shown in figure 3.16. The plot shows three modes, which undergo an avoided crossing, which means the COM modes are coupled. In comparison with what is predicted by equations 2.114 and 2.115 in section 2.4.1, the measured values of the normal modes' oscillation frequencies agree to within 10%. They also show that the radial symmetry was broken, and thus we observed two nearly-degenerate oscillation modes (red and black) at lower I, where the coupling between the oscillation modes is less pronounced. This phenomenon is explained in much more detail in section 4.2, in which I discuss more accurate laser deflection measurements of the same drop's motion.

Ring-Down Measurement

In order to study the damping of a drop's COM motion, we attempted to perform a ring-down measurement. In such a measurement, the oscillator is driven to some non-zero amplitude before the drive is turned off, and the amplitude's decay is monitored. Since the COM mode frequencies are ~ 1 Hz and cell was evacuated, we expected the decay to be quite slow, so a ring-down measurement was conducted over a 20 hour period.

Before the measurement began, we gave the non-magnetic table (on which the cryostat rests) a slight bump to excite the drop's COM motion. Then, every hour, we recorded 1,200 images of the drop at 20 FPS. Figure 3.17a shows the drop at the beginning of the ring-down measurement, for which the drop had $R \approx 239$ μm. Figure 3.17b shows the same drop, but 20 hours later, with a $R \approx 224$ μm. Throughout the course of the mea-

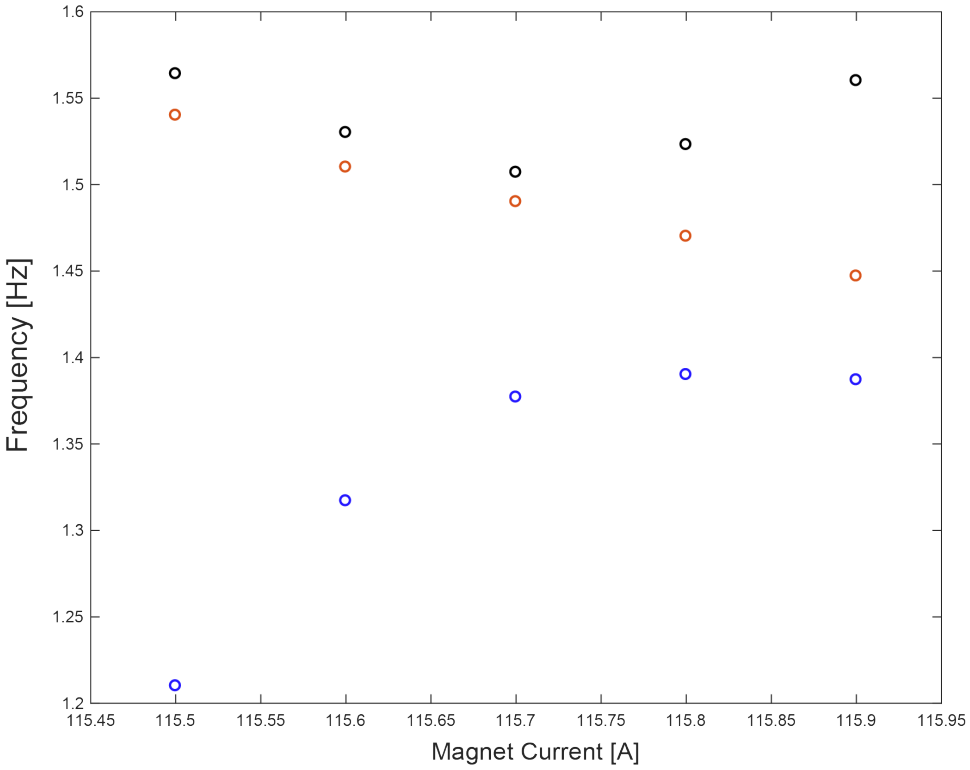

Figure 3.16: The measured COM mode frequencies versus magnet current for a trapped ^{4}He drop with $R = 272.2 \pm 0.7$ μm. At lower currents where the inter-mode coupling is less pronounced, black and red correspond to x-direction and the y-direction, whereas blue corresponds to motion in the z-direction.

surement, the drop's COM motion amplitude did not decrease to smaller values. In fact, the COM motion amplitude increased over time. This can be seen by comparing the initial radial and axial COM motion shown in figure 3.17c and figure 3.17e, respectively, to the radial and axial COM motion 20 hours later, as shown in figure 3.17d and figure 3.17f, respectively. Since the mode frequencies ~ 1 Hz, many noise sources from the environment could potentially drive the COM motion, such as seismic noise, vibrations from pumps, etc. However, because noise does not provide a coherent drive, we cannot treat the increase in the COM motion as a ring-up measurement (if we could, the ring-up measurement would give the amplitude decay rate because an oscillator's amplitude will increase at the same rate it decays when driven with a coherent tone).

3.4.3 Evaporation Measurements of Levitated ^{4}He Drops

While a levitated drop is trapped in the experimental cell, the cell is continually pumped in order to keep its pressure as low as possible. The lower the cell pressure, the less heat from the cell walls will be conducted into the drop. A drop's evaporation can be studied by analyzing the ring-down measurement in the previous section. Figure 3.17g shows the drop's radius over the entire 20 hours, with a linear fit to hours 7 through 19. The fit yields an evaporation rate $\dot{R} \approx 0.416$ Å/s over those hours. Such an evaporation corresponds to a drop temperature $T_{\rm d} \approx 330$ mK (see section 2.5.1), where I have assumed (and will continue to assume throughout this chapter, unless stated otherwise) that the accommodation coefficient $g = 1$. However, the systematic uncertainty in the drop's radius that arises via image analysis (as a result of non-perfect image cleaning and the imaging resolution) is large enough to make the systematic uncertainty in the evaporation rate large. This drop temperature is in good agreement with temperatures inferred from laser-based measurements in section 4.3.

In order to study a drop's evaporation in vacuum more in depth, we created a levitated drop, which, after the rapid evaporation period, had $R \approx 252$ μm. Immediately after the

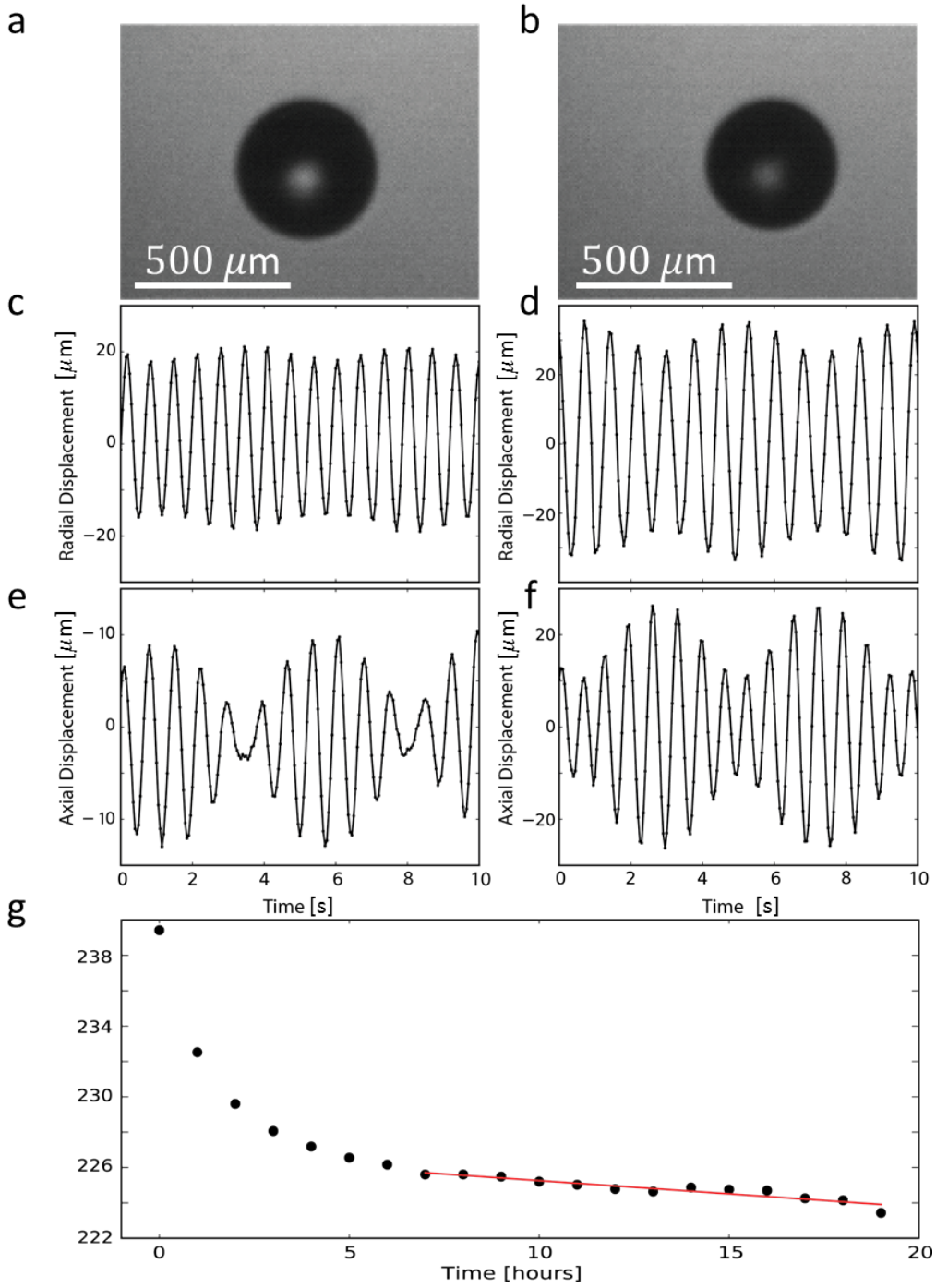

Figure 3.17: The COM motion of a levitated ^{4}He drop over 20 hours. (a) A trapped ^{4}He drop at the start of a COM motion ring-down measurement. (b) The same drop, but 20 hours later. (c) The radial and (e) the axial COM motion at the start of the measurement. (d) The radial and (f) the axial COM motion 20 hours after the start of the measurement. (g) The drop's radius over the entire 20 hours, with a linear fit to hours 7 through 19. The fit gives an evaporation rate $\dot{R} = (0.416 \pm 3.29)$ Å/s.

rapid evaporation period, we began to record images of the drop at 1 FPS for a total time of three hours. The radius data is binned in 10 minute intervals and shown in figure 3.18. Using equation 2.162 from section 2.5.1, measured values of R and the evaporation rate $\dot{R}$ are used to infer the atom flux $\dot{N}$ emanating from the drop's surface. The drops' temperatures only depend on $\dot{R}$ (see section 2.5.1), which we use to infer the temperature of the drop, as shown in figure 2.18. Plotted as a black dashed line is the theory expectation of $R(t)$, $\dot{N}$ and the drop's temperature $T(t)$ for a drop with an initial radius $R_0 = 252$ μm. The theory curves assume the drop is levitating in perfect vacuum (equation 2.164).

The fact that the measurements and the theory don't agree well makes sense because the drop is not levitated in perfect vacuum due to the finite pumping speed in the experimental cell. Residual helium gas in the system, including atoms that evaporated from the drop, is hard to remove from the cell given its 1.00" OD, and the cell walls near the drop are cryogenic. As a result, the gas in the cell is in the molecular flow regime in which an atom's mean-free-path is larger than the 1.00" OD tube of the cell body, and thus the atoms are not strongly biased to move toward the pump. In fact, the atoms have equal probability to scatter from the cell walls in any direction, as opposed to the laminar flow regime in which the atoms experiences forces toward the pump that arise due to scattering from other atoms.

Using equation 2.166, we can infer the pressure of helium gas in the experimental cell that is required to provide the measured $\dot{R}$, which is shown in figure 3.19. Here we have assumed that $\dot{R}$ has no contribution from optical absorption (see section 2.5.1). From figure 3.19 we infer that after three hours of evaporation, the cell pressure is $\sim 10^{-8}$ mbar. Also, in the first three hours of evaporation after creating the drop, its radius decreased by $\leq 5\%$.

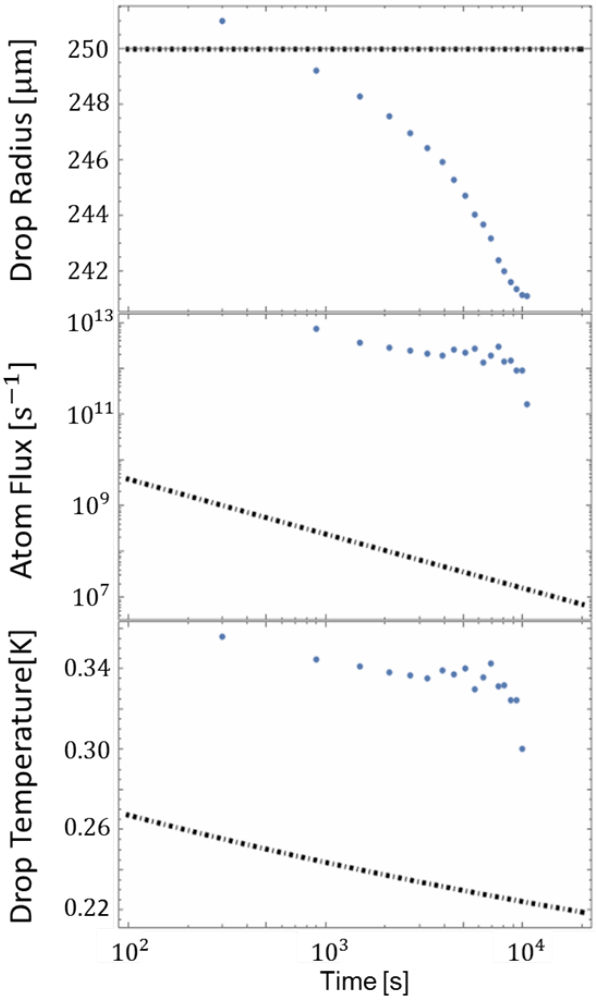

Figure 3.18: Measurements of a drop's evaporation over time. The blue circles are measurements of the drop's radius, the atom flux emanating from the drop, and the drop's temperature over time. The dashed black lines are theory curves for evaporation in perfect vacuum.

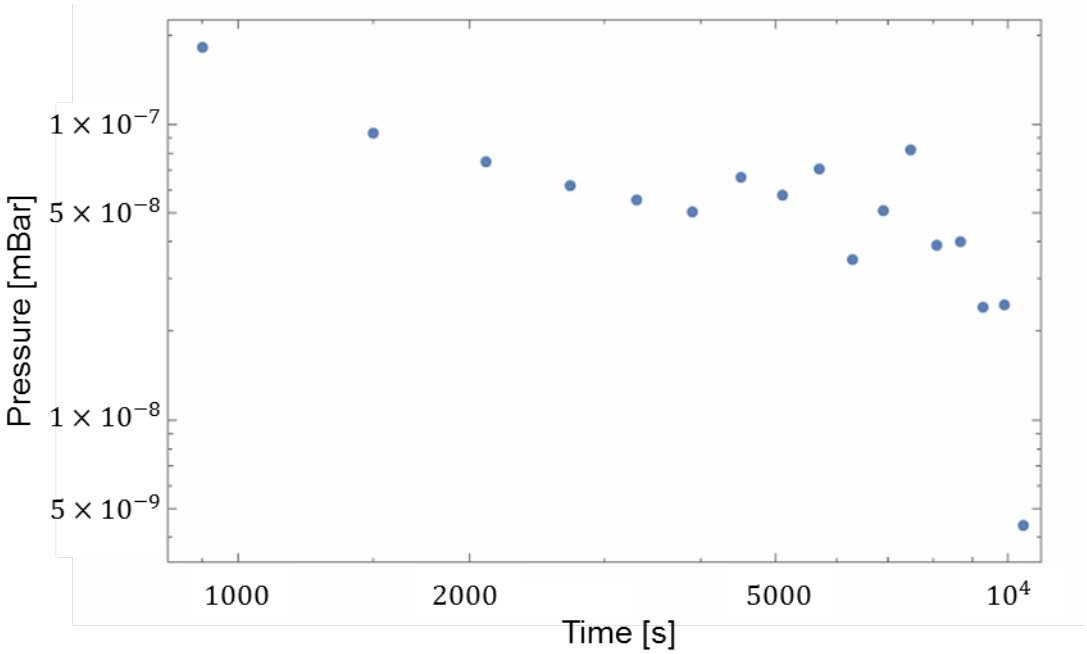

Figure 3.19: The inferred pressure of helium gas in the experimental cell during the evaporative cooling shown in figure 3.18.

Cryo-Bakeout Measurements

A trapped drop is surrounded by the cell walls, which are covered in a thin layer of liquid helium. Despite the fact that the temperature of the cell walls near the drop $T_{\text{wall}} \approx 7$ K, the van der Waals attraction of helium to the cell walls allows a thin layer of adsorbed liquid to exist. The most tightly bound layer of helium atoms (the layer that is closest to the metal walls) feels a van der Waals potential that is ≈ 40 K deep. After a few atomic layers of helium, the outer-most layer of helium feels a van der Waals potential with a depth ~ 10 K.

It was suspected that the helium film on the cell walls is constantly desorbing, and thus conducting heat into the levitated drop. It was expected that if the cell walls were raised to a high temperature ($T_{\text{wall}} \gtrsim 20$ K), then the thin film would mostly desorb from the walls. Then, after the desorption the thinner film would result in lower cell pressure after the walls cool back down. As a result, the drop's temperature would asymptote to a lower temperature due to the decreased heat load.

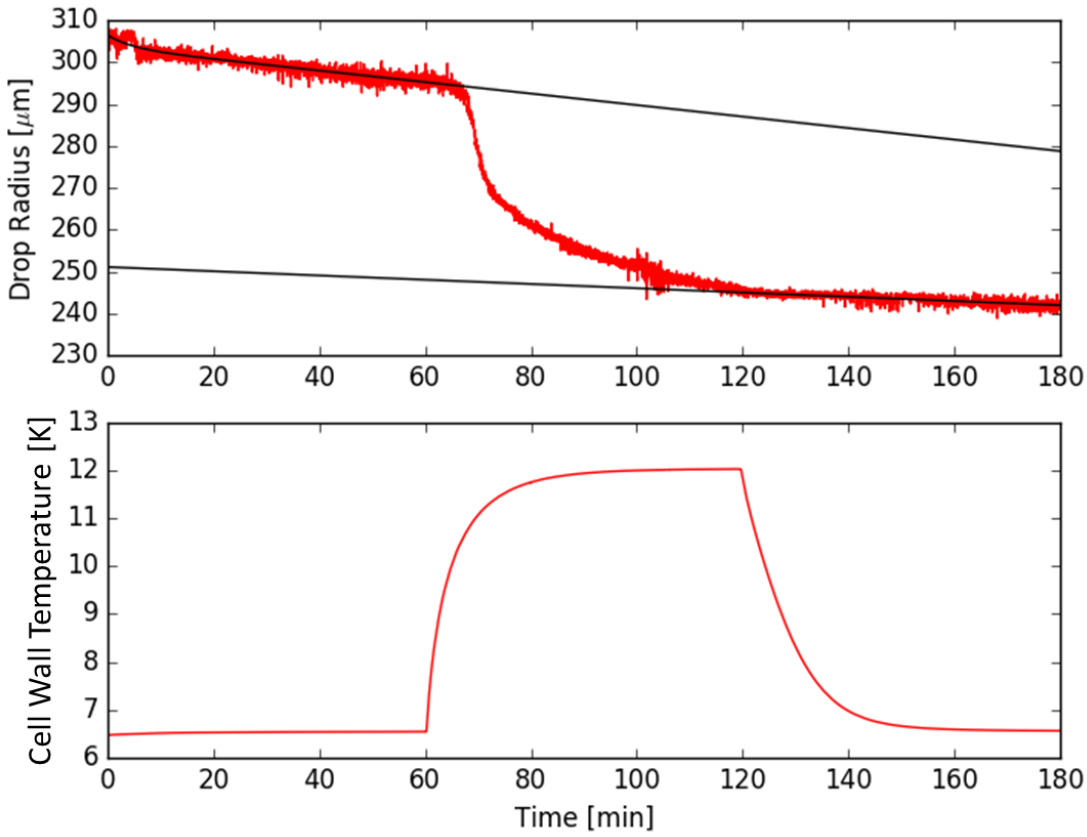

Figure 3.20: A "cryo-bakeout" measurement. Top: The drop radius measurements are red, while fits to the first and last 30 minutes of radius data are is black. Bottom: Cell wall temperature as a function of time. In the first hour the drop is freely-evaporating. At the start of the second hour a heater is turned on. At the start of the final hour the heater is turned off. For the first 30 minutes a quadratic fit gives $\dot{R} = 12.8 \pm 1.1$ μm/hour, and in the final 30 minutes a linear fit gives $\dot{R} = 3.0 \pm 0.4$ μm/hour.

Figure 3.20 shows a typical cryo-bakeout measurement, in which we allowed a drop to freely evaporate for one hour, then used a heater to increase $T_{\rm wall}$ for one hour, before turning the heater off and allowing the drop to freely evaporate for another hour. During this three hour period we recorded images of the drop at 1 FPS. In order to determine the efficacy of the cryo-bakeoout technique, the first 30 minutes of this data set are fit to a quadratic function, while the last 30 minutes of data are fit to a linear function, and we compare the extracted values of $\dot{R}$. We use a linear fit to extract the average $\dot{R}$ in the final 30 minutes because the evaporation is slow enough that high order polynomials do not yield improved fit results. These fits yield $\dot{R} \approx 12.8$ μm/hour ($T_{\rm d} \approx 400$ mK) in the first 30 minutes, while $\dot{R} \approx 3$ μm/hour ($T_{\rm d} \approx 375$ mK) in the last 30 minutes.

We conducted a systematic study of the effect of the cryo-bakeout procedure on the final temperature of a levitated drop, which is shown in figure 3.21. In figure 3.21a, we show the time evolution of the normalized radius of five different drops that experienced five different values of $T_{\rm wall}$ for one hour. All five of the drops had initial radii $\approx 260 - 280$ μm, where the data in figure 3.21a are normalized to their respective initial radii. The temperatures indicated in the legend of figure 3.21a indicate the maximum $T_{\rm wall}$ for the hour of heating. It is clear that increasing $T_{\rm wall}$ causes the drop to evaporate faster. The pressure in the cell will conduct more heat into the levitated drop if it is in contact with cell walls that have elevated $T_{\rm wall}$. The relative decrease in the R due to $T_{\rm wall} \approx 12$ K, as opposed to $T_{\rm wall} \approx 9.5$ K, suggests that at some intermediate $T_{\rm wall}$ the thin film of helium on the cell walls began to undergo a significant amount of desorption. We fit linear functions to the last 10 minutes of evaporation data from each of the traces in figure 3.21a to extract the final values of $\dot{R}$, and we infer from them the temperature of the drop.

Figure 3.21b shows the inferred $T_{\rm d}$ after the cryobake-out procedure versus the maximum $T_{\rm wall}$. $T_{\rm d}$ is shown for different values of the accommodation coefficient g (sticking probability of an atom striking the drop). In figure 3.21b, blue corresponds to $g = 1$, green corresponds to $g = 0.5$, and red corresponds to $g = 0.25$. The vertical error bars in

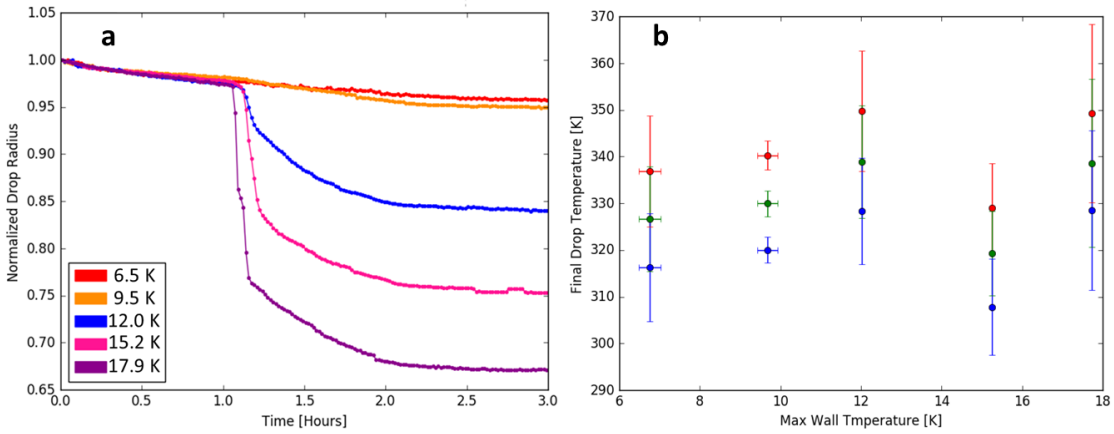

Figure 3.21: A systematic set of "cryo-bakeout" measurements with various chamber wall temperatures. (a) Five different drops undergo cryo-bakeout, with the temperatures shown being the maximum cell wall temperature during the hour-long wall heating period. (b) The final drop temperatures extracted from the data in (a), which are plotted against the maximum wall temperature during the cryo-bakeout. Blue corresponds to a sticking probability (accommodation coefficient) of 1, green corresponds to a sticking probability of 0.5, and red corresponds to a sticking probability of 0.25.

figure 3.21b come from the uncertainty in the fit used to determine $\dot{R}$. Although the uncertainty in $\dot{R}$ is quite small, the drop's temperature has a strong dependence on $\dot{R}$, which results in sizeable error bars in the temperature plot (see figure 2.18). Overall, the cryo-bakeout results suggest that allowing the drop to freely evaporate for a few hours after its creation will essentially yield the same T_{d} as implementing the cryo-bakeout procedure. This at least seems to be true for $T_{\mathrm{wall}} \leq 18$ K in the bakeout procedure. We did not increase T_{wall} further because the drop would shrink to $R \lesssim 150$ μm and escape the trap; this phenomenon is discussed in detail in section 3.4.3

Drop Size-Dependence of the Levitation Point

Both the magnetostatic and gravitational energy stored in the drop depend on its volume. As a result, the drop's axial and radial position along the magnet's symmetry axis at which the levitation condition of equation 2.106 is fulfilled should not depend on the drop's volume. Consequently, the diamagnetic levitation theory in section 2.3.4 suggests that as a

levitated drop shrinks, it should not translate in any direction. However, we have observed translation of the drop's COM as it shrinks.

Figure 3.22a shows a drop's radius over 30 minutes, during which $T_{\rm wall}$ was increased to induce evaporation. Images of the drop were recorded at 1 FPS. In the first 10 minutes, $T_{\rm wall}$ was increased to ≈ 9.5 K from ≈ 7 K. In the following 10 minutes, $T_{\rm wall}$ was increased to ≈ 12 K. For the final 10 minutes, $T_{\rm wall}$ was increased to ≈ 13.5 K. Figure 3.22b shows the drop's axial displacement and figure 3.22c shows the drop's radial displacement. From these data one can see that there was a time period from $t = 300 - 700$ s where the drop essentially stopped displacing as its size decreased. After $t = 700$ s, the radial and axial velocities are ≈ 80 nm/s and ≈ 1 μm/s, respectively. It's important to note that a positive axial displacement corresponds to motion opposite to the direction of gravity. Drops that become much smaller than what is shown in figure 3.22a will continue to move opposite to gravity until they are destroyed by crashing into some surface inside the cell; when the drop is destroyed, a pressure gauge on the cell records a temporary spike in the cell pressure to $P \sim 10^{-3}$ mbar. It is typically the case that a drop with $R \lesssim 150$ μm is lost from the trap in this manner.

In figure 3.23, the displacement of the same drop is plotted against its radius. Since the drop's position is changing as its size changes, both figure 3.23a and figure 3.23b suggest the possibility that there is a force acting on the drop which does not depend on the drop's volume. Such a force could be due to stray electric fields in the experimental cell, which apply forces to a charge on the levitated drop. Alternatively, a non-volumetric force that could result in this sort of motion is a force that depends on drop's surface area. Our experimental cell is ≈ 2.5 feet long, and in normal operation, its base is near liquid helium temperatures, whereas the top of the cell is outside the cryostat and thus at room temperature. The top of the cell is also connected to ≈ 6 feet of vacuum line, which has non-zero leak rate. One possibility is that there is a wind of impurities that originate from above – or beneath – the drop and apply forces to it. Another possibility is that there is some sort

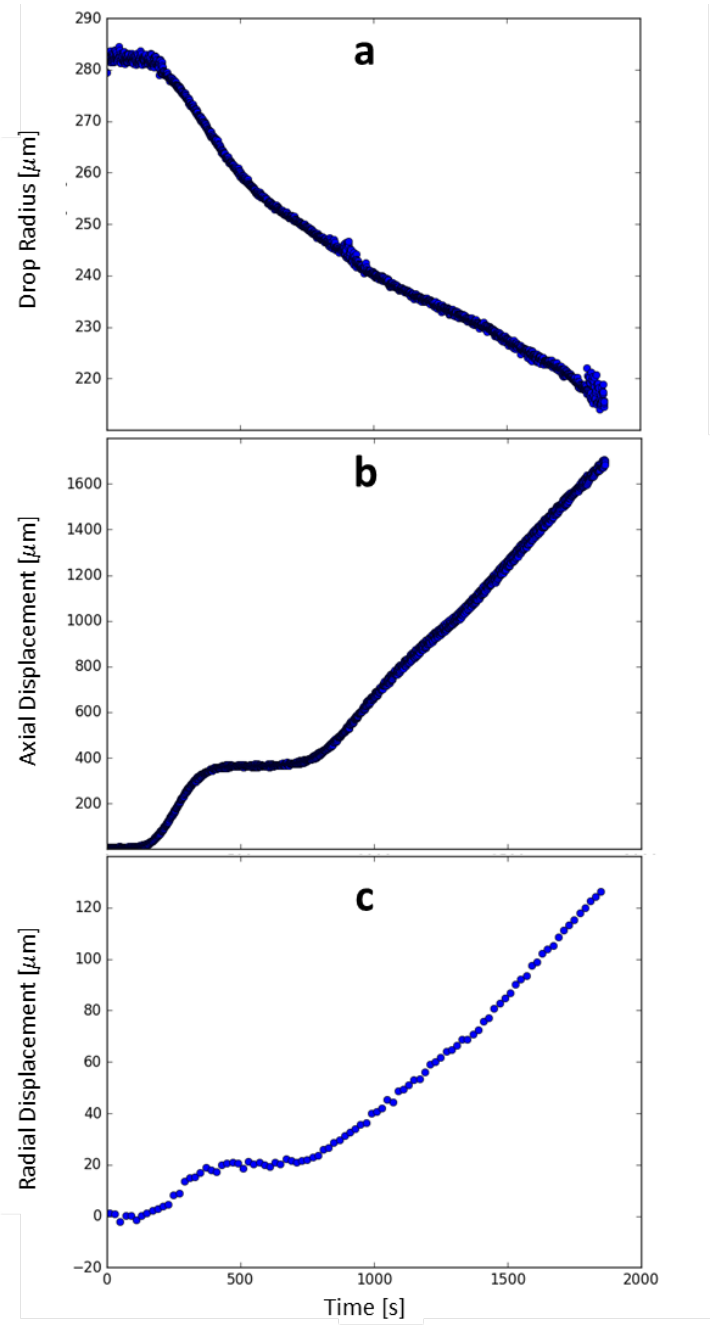

Figure 3.22: The measured displacement of a ^{4}He drop's equilibrium position. (a) The radius of the drop versus time. (b) The axial displacement of the drop's center of mass versus time. (c) The radial displacement of the drop's center of mass versus time. The drop was made to evaporate more quickly than usual by raising the temperature of the walls around it to ≈ 13.5 K.

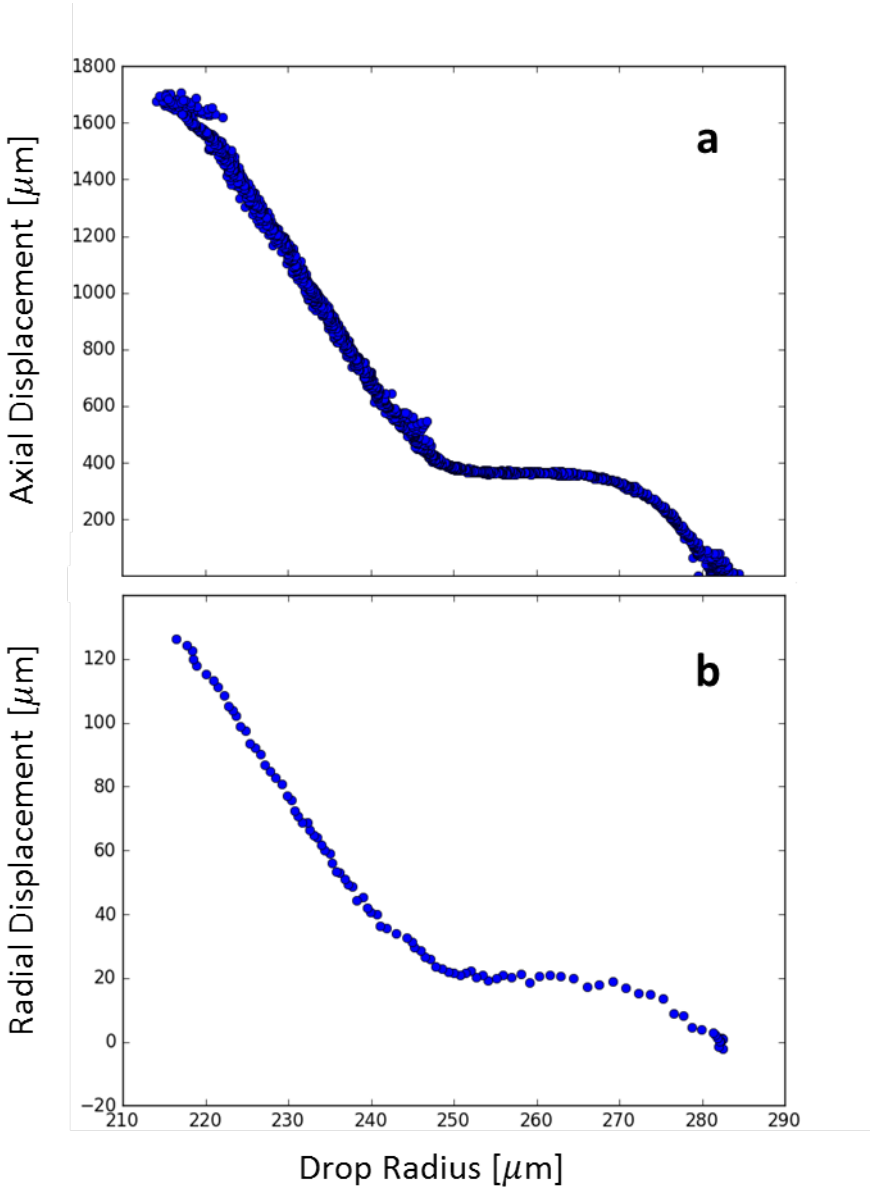

Figure 3.23: The measured displacement of a ^{4}He drop's equilibrium position. (a) The axial displacement of the drop's center of mass versus its radius. (b) The radial displacement of the drop's center of mass versus its radius. These plots are derived from the data shown in figure 3.22.

of local complex flow of the helium atoms evaporating from the drop as they eventually scatter away from it.

It is useful to note a recent change we have made to the experiment, as it has relevance here. In the past, we used slightly less pure ^{4}He gas (99.999% instead of 99.9999%) to make drops, and we did not clean the helium gas by passing it through a liquid nitrogen cold trap before allowing it to enter the cell. The measurements presented in figures 3.21, 3.24 and 3.25 used 99.9999% pure ^{4}He gas, and the gas was not cleaned with the cold trap. The measurements presented in figures 3.22 and 3.23 used 99.999% pure ^{4}He gas, and the gas was not cleaned with the cold trap. All other measurements presented in this thesis used 99.9999% pure ^{4}He gas that was cleaned with the cold trap. Over the entire measurement period, the drop described in figure 3.17 (99.9999% pure ^{4}He gas cleaned with the cold trap) displaced radially ≈ 8 μm and axially ≈ 70 μm, which is considerably less than what is found in figures 3.22 and 3.24. This suggests that the cleaner ^{4}He gas results in much less drop displacement over long periods.

On a couple of occasions when we used 99.999% pure ^{4}He gas that was not cleaned with the cold trap, we saw the sudden appearance of solid chunks in a levitated drop while we recorded video. In one particular video, we observe an asymmetric mass undergo ≈ 18 revolutions inside a drop with $R \approx 218$ μm during the 14 second video clip. We applied -300 volts to an electrode near the drop and we were unable to notice a displacement in the drop's position, so the asymmetric mass seemed to be charge neutral. Since we began using the higher purity gas, and cleaning it using the cold trap before it enters the experimental cell, we have not observed rotating solid chunks in the drops. The rotation observed in the video corresponds to an angular speed $\omega_{\rm imp}/2\pi \approx 1.3$ Hz. It's known that superfluid rotation may manifest as a lattice of uniformly distributed parallel vortices with area density [76]

$$n_{\rm v} = \frac{2\omega m}{h} \tag{3.1}$$

where m is the mass of a ^{4}He atom. Assuming the drop has rotational motion that would

correspond to an average angular speed ω, then the number of vortices $N_{\rm v}$ that may have been inside the drop is given by $N_{\rm v} = \pi R^2 n_{\rm v} = 155$ with $\omega = \omega_{\rm imp}/2\pi \approx 1.3$ Hz and $R \approx 218$ μm.

Trapping a Single ^{4}He Drop for Many Hours

We were interested to know if allowing a drop to evaporate for much more than three hours would result in the drop reaching lower $T_{\rm d}$ than we had previously measured (see section 3.4.2). Figure 3.24 shows a plot of a drop's radius and displacement over 24 hours. Figure 3.24a shows that R decreased by only 10% over this period. Interestingly, $\dot{R}$ seems to be negative from hour 11 through hour 14. $\dot{R} < 0$ was the result of systematic errors that affected extracting R from fits to drop images. Such errors could have been the result of condensation build-up on the cryostat's room temperature window, or imaging part of the drop's edge through transparent kapton tape that fell onto the sapphire window (both of these will affect the drop's apparent size). Around hour 14, the needle valve in the continuous flow line seemed to have gotten clogged, which allowed $T_{\rm wall}$ to increase to $T_{\rm wall} \gtrsim 20$ K. As a result, we observed an increased $\dot{R}$ around hour 14.

Figure 3.25 shows a plot of the inferred average temperature of the drop as a function of time, where the radius data was binned into two hour segments before the extracting the slope and converting $\dot{R}$ into $T_{\rm d}$.

As described in section 3.4.3, when a drop shrinks, its equilibrium position translates. Figure 3.24b and Figure 3.24c show the axial and radial displacement of the drop's COM, respectively. The drop's average axial velocity over 24 hours was ≈ 6 nm/s in the direction opposite of gravity, whereas its average radial velocity was ≈ 7Å/s.

Although not shown in this section, we have continually trapped a single drop for 30 hours. The trap time of 30 hours was not limited by an inherent property of the levitated drop, or evaporation. It should be possible to trap a single drop for several days.

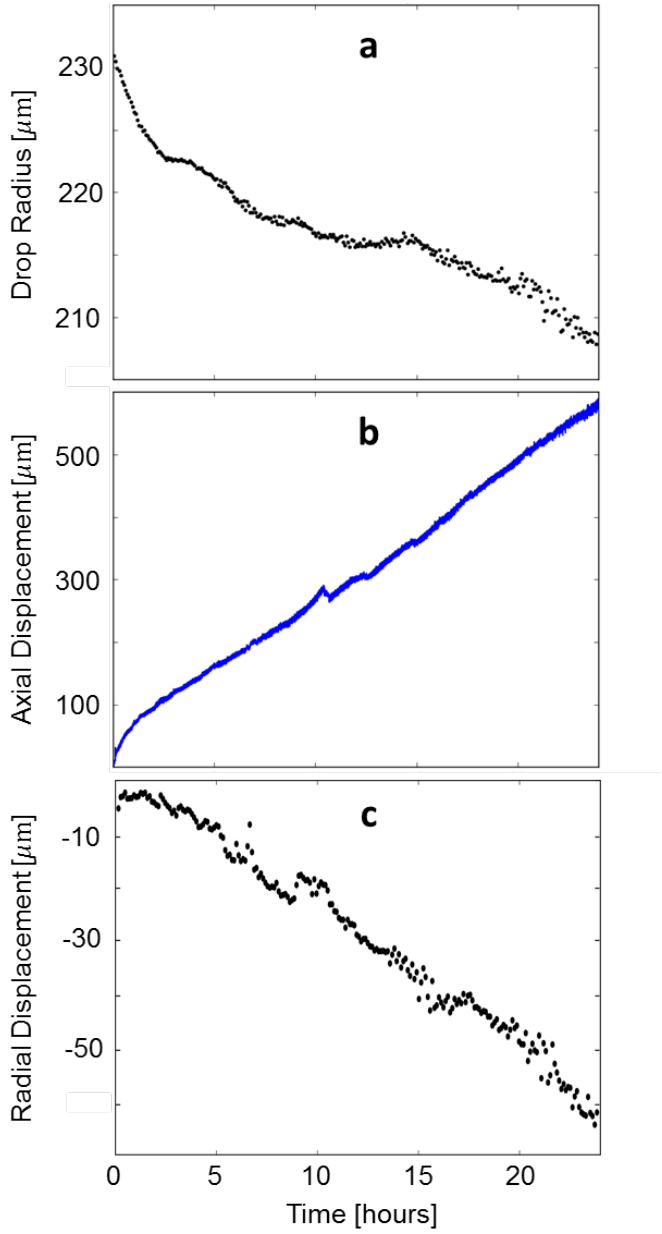

Figure 3.24: The evaporation of a ^{4}He drop over 24 hours. (a) The radius of the drop versus time. (b) The axial displacement of the drop's center of mass versus time. (c) The radial displacement of the drop's center of mass versus time.

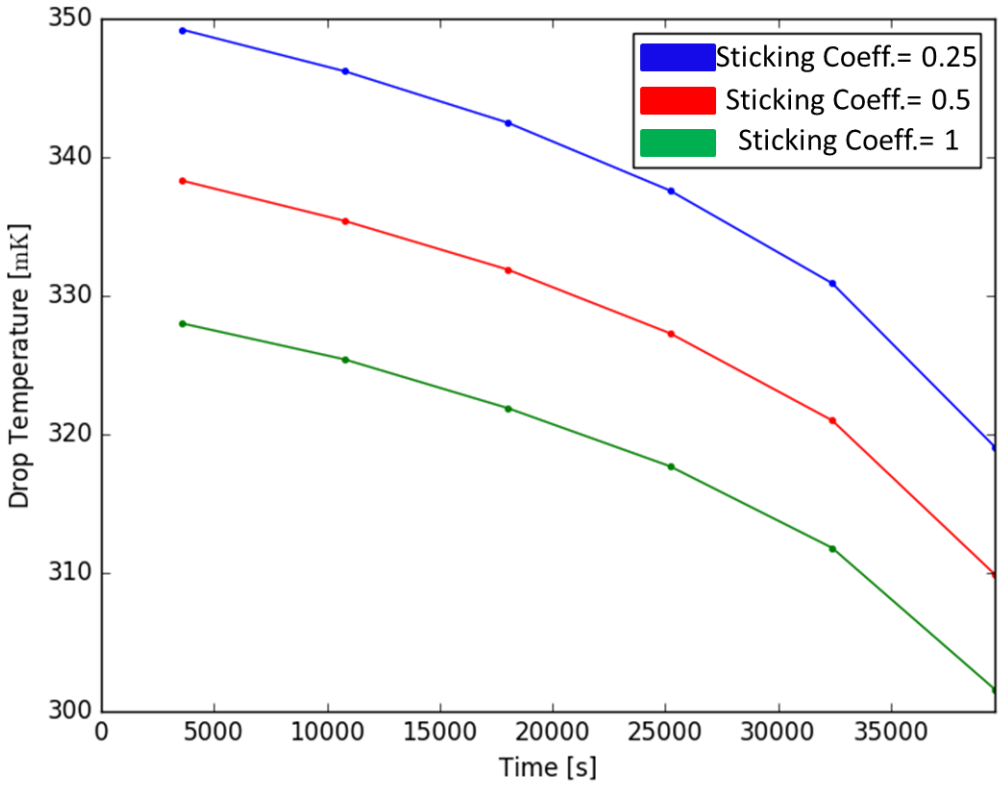

Figure 3.25: The inferred temperature of a drop as a function of time, which is plotted for different values of the sticking coefficient (accommodation coefficient). This plot was generated by extracting the evaporation rate $\dot{R}$ from the data in figure 3.24a (after binning it), and converting it into temperature.

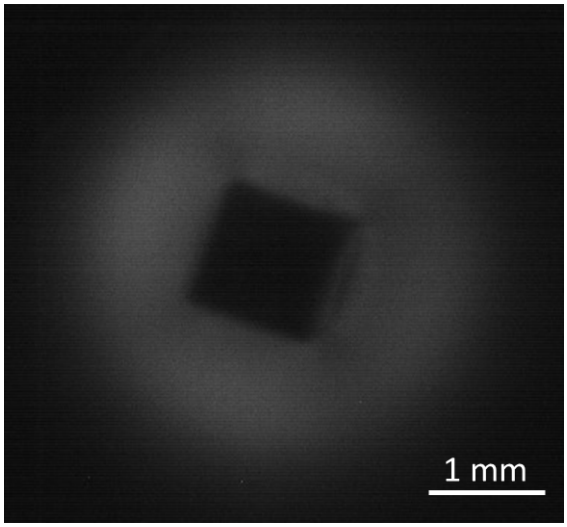

Figure 3.26: Coronal discharge in cryogenic helium gas at a pressure $P \approx 6$ mbar surrounding an electrode of square cross-section. The voltage applied to the electrode was 200 V.

3.4.4 Charged Levitated ^{4}He Drops

The dielectric breakdown strength of cold helium gas at low pressure first decreases with decreasing density of the gas, before turning around and beginning to increase as the density decreases. Work done in the early 1990's shows that the dielectric breakdown strength of helium gas can get quite low, and that with a voltage of about 1 kV, it could be possible to initiate dielectric breakdown at pressures $P \sim 1$ mbar in mm-scale gaps [156].

We first tried to initiate dielectric breakdown in helium gas with the magnetic field off. First, we evacuated the experimental cell and applied 200 V to an electrode near the levitation point. Next, we slowly filled the experimental cell with helium gas, and when the pressure reached $P \approx 6$ mbar, we observed coronal discharge, which looked like a circular glow around the electrode. Figure 3.26 shows an image of a coronal discharge halo surrounding an electrode with square cross-section. If we stopped filling the experimental cell with gas, we could sustain the coronal discharge. If we initiated the coronal discharge, then slowly reduced the cell pressure, the coronal discharge halo around the electrode would enlarge and become fainter. The coronal discharge persisted until the pressure was less than $\approx 10^{-1}$ mbar. It seems likely that the large electric fields near the sharp corners of

the electrode provide the necessary condition to initiate dielectric breakdown in the helium gas.

In order to charge a levitated drop, we followed the usual drop generation procedure, but with one small difference. When there was a puddle of liquid helium at the bottom of the cell, we applied -300 V to one of the electrodes near the levitation point. Next, we pumped on the experimental cell and created a drop. When the cell pressure reached $P \approx 9$ mbar, the electrode power supply registered a spike in current (up to 100 μA from its zero value) and coronal discharge initiated around the electrode. However, the spatial extent of the coronal discharge was quite different with the magnetic field on, compared to coronal discharge with the magnetic field off; with the magnetic field on, the coronal discharge is focused near the tip of the electrode. When the coronal discharge had initiated, there was a bright spot at the tip of the electrode, which can be seen in figure 3.27a. At the same time, there was a $\approx 5\%$ spike in P, and $T_{\rm wall}$ began to rise quickly to ≈ 20 K. Consequently, perhaps due to a combination of hotter cell walls and energetic particles bombarding the drop, the drop began to evaporate rapidly. Occasionally, if we did not shut off the power supply in time, the drop would evaporate until it was so small that it was lost from the trap entirely. On the other hand, a drop would occasionally outlive the coronal discharge; the coronal discharge stopped when the cell pressure $P \lesssim 10^{-1}$ mbar, which can be seen in figure 3.27b. In the end, the drop from figure 3.27b survived, and settled to a radius $R \approx 300$ μm. Next, we applied an AC voltage with $V_{\rm pp} = 28$ V and frequency $\omega_{\rm drive}/2\pi = 1.4$ Hz to another electrode ($\omega_{\rm drive}/2\pi = 1.4$ Hz is near the COM mode frequencies). The drop's radial and axial COM motion rang up to ≥ 2 mm, over $\approx 2 - 3$ minutes of driving. From the large response of the drop's COM motion due to the application of an AC voltage to the electrode, we could conclude that the drop was charged. Furthermore, it is interesting to note that at one point we applied -10 V to an electrode next to a charged drop. The drop moved towards the electrode, which suggests that it was positively charged due to positive helium ions bound to its surface.

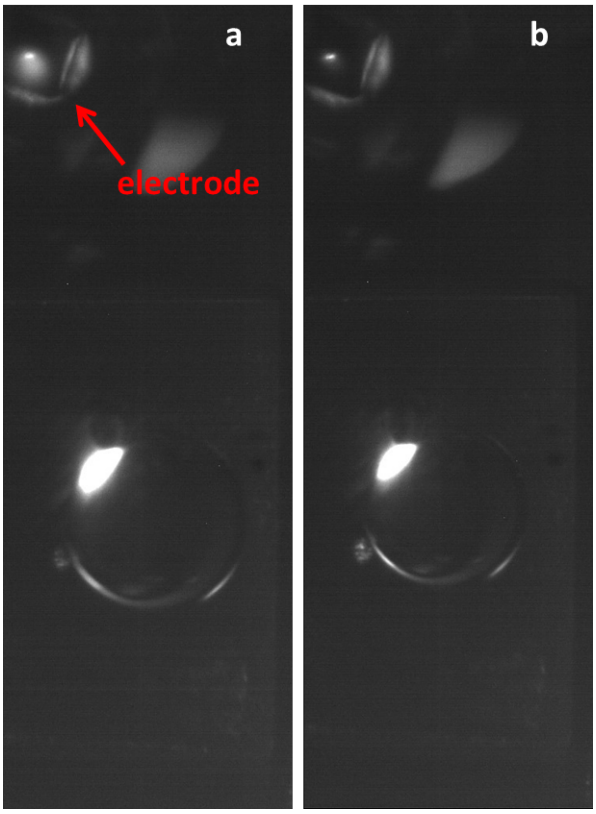

Figure 3.27: Coronal discharge in cryogenic helium gas in a large magnetic field. (a) The initiation of coronal discharge in cryogenic helium gas at a pressure of 9 mbar near the tip of an electrode with square cross-section. (b) The end of the coronal discharge due to lowered experimental cell pressure. The voltage applied to the electrode was -300 V and the helium is in a magnetic field with a magnitude ≈ 14 T.

Chapter 4

Laser-Based Measurements

In this chapter I describe the experimental setup that we used to measure levitated helium drops. We have made laser-based measurements of drops' center of mass motion, evaporation and driven surface modes. We have also measured drops' optical modes. Here I explain in detail how an optical dipole force that was generated by a focused laser was used to drive these surface modes. I also explain how a drop's motion (center of mass motion or surface mode) will steer a laser that propagates through it, and how we have used this steering to make measurements.

4.1 Measurement Setup

We used two optical tables. The first table is a standard optics table (which is magnetic) resting on vibration-dampening air legs, on which the lasers, fiber couplers and modulators reside. This table is located $\approx$ 10 ft. from the superconducting magnet in the cryostat. The second optics table, which is non-magnetic, consists of a 4 ft. $\times$ 4 ft. $\times$ 1 ft. solid block of granite that is bolted to an optical breadboard, with the granite resting on vibration-dampening air legs. An aluminum framing structure which rests on top of the non-magnetic table supports the cryostat. Laser light from the first table is coupled into optical fibers and sent to the non-magnetic table, where all of the optical components are positioned beneath

the cryostat. When the laser light reaches the non-magnetic table, it is sent back into free space, where it passes through various lenses and wave plates to control the beam size, convergence and polarization. The light is then guided by mirrors on the table and sent upward into the cryostat through its windows, and into the experimental cell through its sapphire window. The light propagates through the experimental cell and reflects from the two right-angle prism mirrors on the brass cage (described in section 3.2.3), which allow the light to interact with the drop before sending the light downward and outside of the cryostat. Once the light exits the cryostat it is guided to photodiodes, which send signals to our data acquisition system for analysis. Figure 4.1 shows the setup used to measure drops' surface modes, optical modes and evaporation rates.

4.1.1 Drop Shape Distortion Via Optical Dipole Force

The application of an electric field to a levitated helium drop provides a non-contact method to deform its shape. As a result, we used an intensity-modulated focused laser to drive drops' surface modes. Here I describe a drop's deformation due to a laser propagating through its center.

Despite the fact that liquid helium has a dielectric constant near that of vacuum, which results in weak electric polarizability, it is still a dielectric liquid that will deform itself in an applied electric field in order to minimize its total energy. In fact, a laser focused onto a levitated helium drop with a beam diameter of $2w_0$, which is less than the diameter ($2R_0$) of the drop will tend to elongate the drop in the propagation direction of the beam. To lowest order in the amplitude of elongation, the drop's deformation takes on the shape of the $Y_2^0(\theta,\phi)$ spherical harmonic with amplitude $\alpha_{2,0}$ (which corresponds to a drop's $\ell_d = 2$ surface modes – see section 2.4). Then, the drop's radius is given by $R(\theta,\phi) = R_0 + \delta R(\theta,\phi)$, with $\delta R(\theta,\phi) = R_0 \alpha_{2,0} Y_2^0(\theta,\phi)$.

The larger the laser power P_{L}, the greater the deflection amplitude. However, since the magnetostatic energy and gravitational potential energy depend on the drop's volume, and

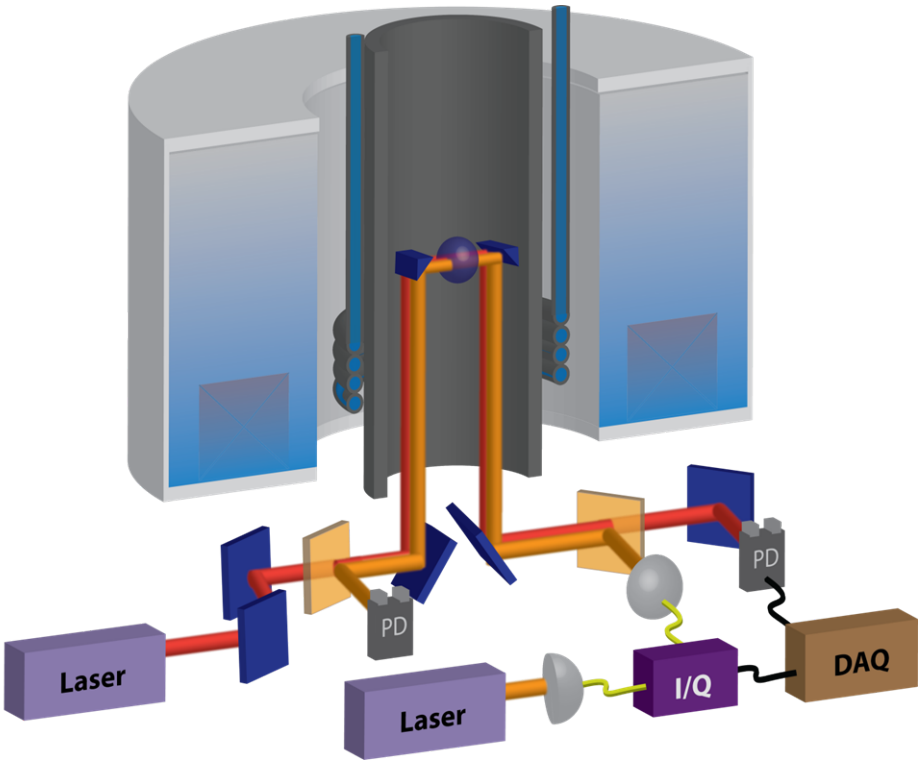

Figure 4.1: The setup used to measure the mechanical and optical modes of levitated drops. The optics rest beneath the cryostat and direct lasers (shown in red and orange) vertically into the cryostat's optical access windows to interact with the drop, before exiting the cryostat and being detected. A drop's mechanical modes were driven via an intensity-modulated laser (orange) created by the modulator (I/Q). These modes deflected a measurement laser (red), which caused the laser to sweep across a photodiode (PD). As a result, the photodiode detected intensity fluctuations at the mechanical mode frequencies and they were recorded with a data acquisition system (DAQ).

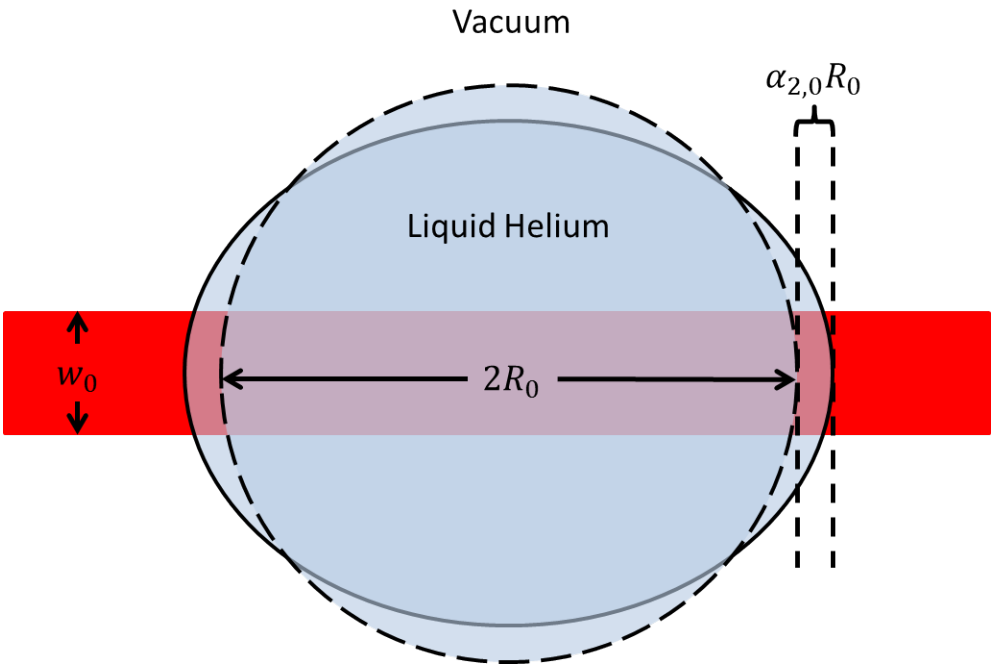

Figure 4.2: A sketch of the $Y_2^0(\theta, \phi)$ spherical harmonic deformation of a levitated helium drop due to a laser propagating through it. Red rectangle: laser beam, $\alpha_{2,0}$: magnitude of drop deformation, R_0: unperturbed drop radius.

the volume is unaffected (to lowest order) by a $Y_2^0(\theta, \phi)$ deflection, the deflection amplitude is determined by the balance between the surface tension (which depends on area, not volume) and the electrostatic energy stored within the drop. Figure 4.2 provides an illustration of the elongation of the drop along the beam propagation direction. As discussed in section 2.6.1 (equation 2.174), to lowest non-zero order in the deflection amplitude, the surface curvature energy of the drop is given by $U_{\mathrm{S}} = \pi\sigma(\alpha_{2,0}R_0)^2$, where σ is the surface tension. The time-averaged energy of the electric field U_{E} in the drop is given by $1/2(\epsilon_{\mathrm{r}} - 1)\epsilon_0 \int \mathrm{d}V|\mathbf{E}|^2$, where $|\mathbf{E}|^2 = 2P_{\mathrm{L}}/(\pi c w_0^2 \epsilon_0)$, ϵ_0 is the permittivity of free space, ϵ_{r} is the relative permittivity of helium, and c is the speed of light in vacuum. For a beam with a width that is approximately constant over the diameter of the drop (as is the case in our experiment), The electric field can be removed from the integral and the volume $V \approx 2\pi w_0^2 R_0(1 + \alpha_{2,0})$. The drop's shape is defined by minimizing the total energy $U_{\mathrm{T}} = U_{\mathrm{S}} + U_{\mathrm{E}}$ with respect to $\alpha_{2,0}$. That is, the shape of the drop is determined by the

condition that $\mathrm{d}U_{\mathrm{T}}/\mathrm{d}\alpha_{2,0} = 0$. This condition implies that

$$-\alpha_{2,0} = \frac{\epsilon_{\mathrm{r}} - 1}{\sigma \pi c R_0} P_{\mathrm{L}}. \tag{4.1}$$

For a drop with $R_0 = 250$ μm and $P_{\mathrm{L}} = 1$ mW, the drop's radial deflection at the equator $\delta R(\theta = \pi/2, \phi) = -\alpha_{2,0} R_0 Y_2^0(\theta = \pi/2, \phi) \approx 5 \times 10^{-11}$ m. Using an intensity-modulated (full modulation depth) laser with $P_{\mathrm{L}} \sim 20$ mW, oscillatory shape distortions with $\delta R(\theta = \pi/2, \phi) \sim 1$ nm can be driven. Such shape distortions are easily measurable with the technique described in section 4.4.

The focused beam in figure 4.2 generates a force that has maximal overlap with a drop's $\ell_d = 2$ surface modes. Yet, the optical force has smaller (but non-zero) overlap with surface modes with $\ell_d > 2$, so this technique can be used to excite many surface modes with various ℓ_d (see section 4.4).

4.1.2 Beam Steering

In our experiment, a levitated drop is, in effect, a ball lens that vibrates and oscillates in the path of the laser beam. Provided the beam diameter is smaller than the drop diameter, and the amplitude of the drop's center of mass (COM) motion is small enough that the beam remains entirely within the drop (i.e. no skimming), we can describe the laser using ray optics and use ABCD matrices to determine the size and location of the beam. Alternatively, one can use Snell's law to describe how the beam will refract into, and out of, the levitated drop. Figure 4.3 shows a parametric plot of five rays propagating in vacuum before striking a dielectric of circular cross-section with an index of refraction of 1.1. Snell's law is solved at the first interface, defining the propagation direction across the dielectric, and then it is solved again at the second interface, determining the propagation direction into vacuum. As shown by figure 4.3, one would then expect a beam's exit-angle (subjected to the constraints listed above) to depend on its impact parameter h relative to a diameter

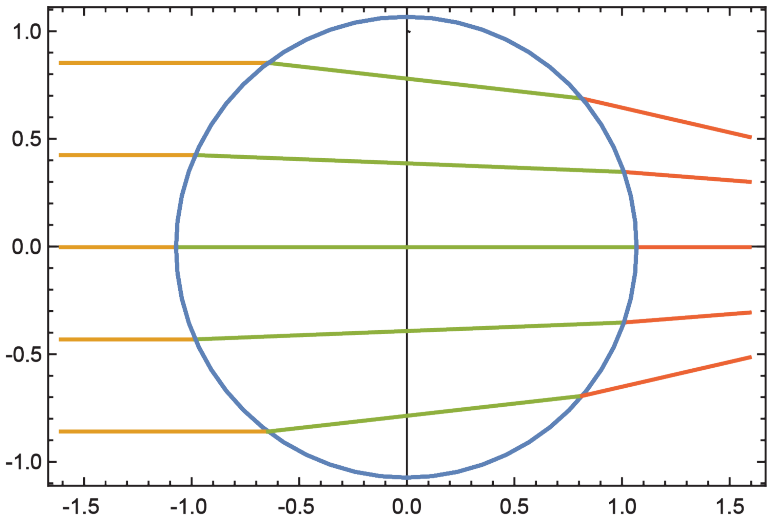

Figure 4.3: A parametric plot of five rays propagating in vacuum before striking a dielectric of circular cross-section with an index of refraction of 1.1.

line through the drop. Consequently, the displacement of the beam $s(h, z)$ from the axis coincident with the diameter line through the drop also depends on h, as shown by figure 4.4a.

Figure 4.4b shows the beam's translation $s(h, z)$ from the axis that penetrates the drop's center, as a function of the input beam impact parameter h, after the beam has propagated by one meter from the drop. This translation is given by the product of the propagation distance of the beam after the drop and $\tan(\theta_{\mathrm{f}})$, where θ_{f} is the beam's exit-angle from the drop.

As mentioned earlier, ABCD matrices are a useful tool for calculating the size and location of the beam as it propagates through a series of optical components. Under the small-angle approximation (which is equivalent to the paraxial approximation in Gaussian beam optics) the output position and propagation angle of a ray that propagates through an optical component is related to the ray position and propagation angle at the input of the component through a 2×2 matrix. Three fundamental 2×2 matrices – corresponding to ray propagation, refraction through an interface, and reflection – can be used to build up any optical system [157]. The ray propagation matrix $\mathbf{M}_{\mathrm{prop}}$, which propagates a ray by a

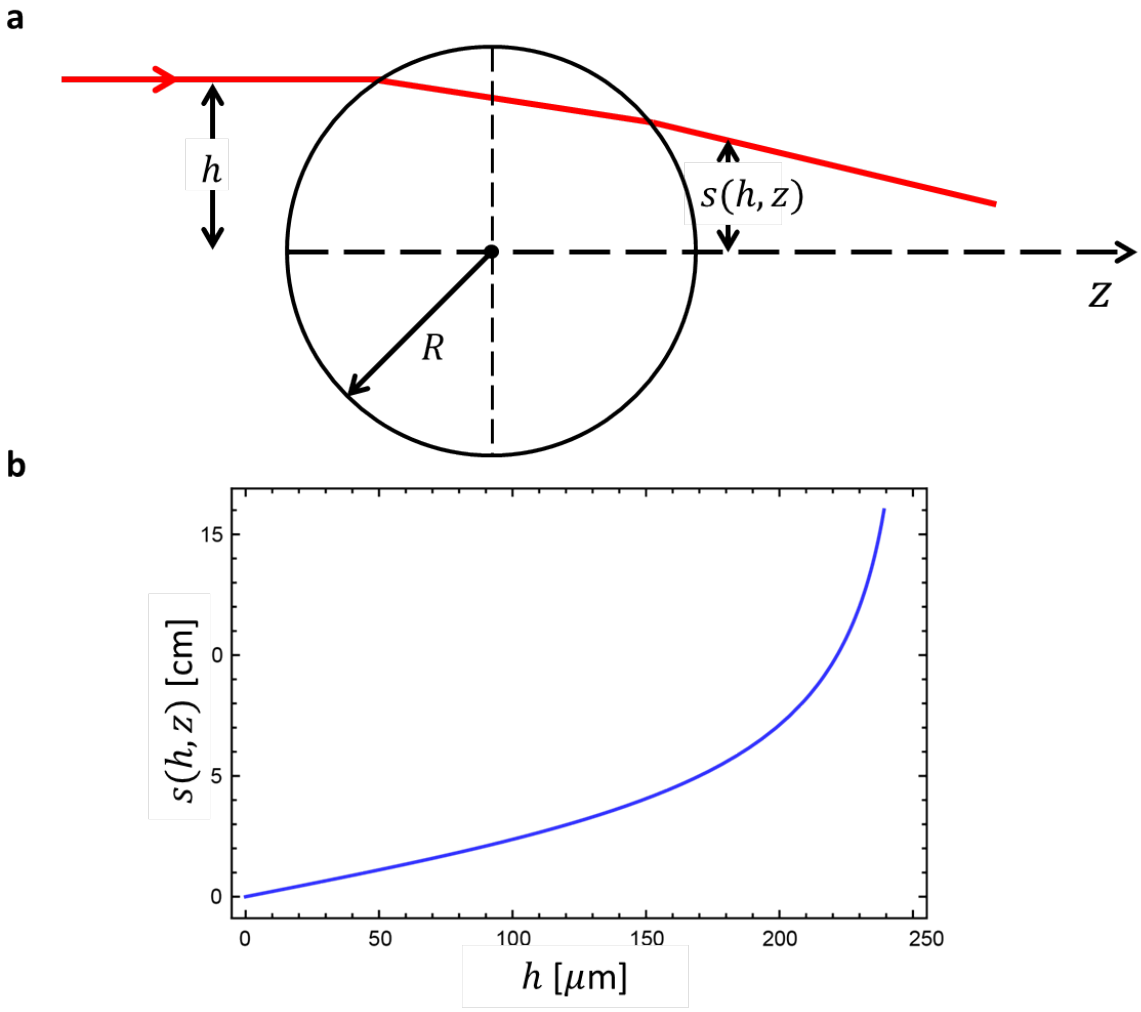

Figure 4.4: Offset ray propagation through a dielectric sphere. (a) A sketch of a beam displaced by an amount $s(h, z)$ after refraction through a drop of radius $R = 250$ μm. The input beam impinges upon the drop with an impact parameter h. (b) A plot of the displacement $s(h, z)$ (evaluated at $z = 1$ m) of a beam from the axis that passes through the center of the drop, as a function of the impact parameter h of the input beam.

distance d is given by

$$\mathbf{M}_{\text{prop}} = \begin{bmatrix} 1 & d \\ 0 & 1 \end{bmatrix}. \tag{4.2}$$

The refraction matrix $\mathbf{M}_{\text{refr}}$ for the refraction of a ray between two dielectric mediums with indices of refraction n_1 and n_2, where the interface between the two mediums has a radius of curvature R is given by

$$\mathbf{M}_{\text{refr}} = \begin{bmatrix} 1 & 0 \\ -\frac{n_2 - n_1}{n_2 R} & \frac{n_1}{n_2} \end{bmatrix}. \tag{4.3}$$

The reflection matrix $\mathbf{M}_{\text{refl}}$ for the reflection of a ray from a curved mirror, where R is the radius of curvature of the mirror is given by

$$\mathbf{M}_{\text{refl}} = \begin{bmatrix} 1 & 0 \\ \frac{2}{R} & 1 \end{bmatrix}. \tag{4.4}$$

Any number of these matrices can be multiplicatively combined to represent the entire optical chain through which a ray propagates by a single 2×2 matrix $\mathbf{M}$. Generally,

$$\mathbf{M} = \begin{bmatrix} A & B \\ C & D \end{bmatrix} \tag{4.5}$$

and it is applied to the left of a 2×1 column vector whose top and bottom entries are the ray's position and propagation angle, respectively. The matrix $\mathbf{M}$ can also be applied in Gaussian beam optics to the complex parameter q, in order to find the beam waist at any given location. As a result, the input complex beam parameter q_1 is related to the output complex beam parameter q_2 by the relationship

$$\frac{1}{q_2} = \frac{C + D/q_1}{A + B/q_1}, \tag{4.6}$$

where

$$\frac{1}{q(z)} = \frac{1}{R(z)} - \frac{\lambda}{\pi w^2(z)} i. \tag{4.7}$$

Here, λ is the wavelength of the beam, and $R(z)$ and $w(z)$ are the beam's wavefront curvature and radius respectively, at location z. The complex beam parameter can also be expressed as

$$q(z) = z + i z_{\mathrm{R}}, \tag{4.8}$$

where the Rayleigh range z_{R} is given by

$$z_{\mathrm{R}} = \frac{\pi w_0^2}{\lambda} \tag{4.9}$$

and w_0 is the radius of the beam at the beam waist.

The ABCD matrix $\mathbf{M}_{\mathrm{drop}}$ corresponding to propagation of a beam through the center of a levitated drop (or a ball lens, in general) is given by $\mathbf{M}_{\mathrm{drop}} = \mathbf{M}^{(2)}_{\mathrm{refr}} \mathbf{M}_{\mathrm{prop}} \mathbf{M}^{(1)}_{\mathrm{refr}}$, where $\mathbf{M}^{(1)}_{\mathrm{refr}}(\mathbf{M}^{(2)}_{\mathrm{refr}})$ is the refraction matrix for propagation through interface 1(2). As a result,

$$\mathbf{M}_{\mathrm{drop}} = \begin{bmatrix} -1 + \frac{2n_0}{n_1} & \frac{2n_0 R}{n_1} \\ \frac{2(n_0 - n_1)}{n_1 R} & -1 + \frac{2n_0}{n_1} \end{bmatrix}, \tag{4.10}$$

where n_0 is the index of refraction of vacuum, n_1 is the index of refraction of liquid helium, and R is the radius of the drop. The drop's focal length f is given by the negative reciprocal of matrix element (2,1) in $\mathbf{M}_{\mathrm{drop}}$. For helium drop with $n_1 = 1.028$ and $R = 250$ μm, $f \approx 9$ mm.

Figure 4.5 (orange) shows the radius $w(z)$ of a Gaussian beam which is focused such that its focal plane lies midway between the two prism mirrors on the brass cage (see section 3.2.3), but without propagating through the levitated drop. Figure 4.5 (blue) shows $w(z)$ for the same beam, but including a liquid helium drop with $R = 250$ μm at the midpoint between the two prism mirrors. It is useful to note that the origin in figure 4.5

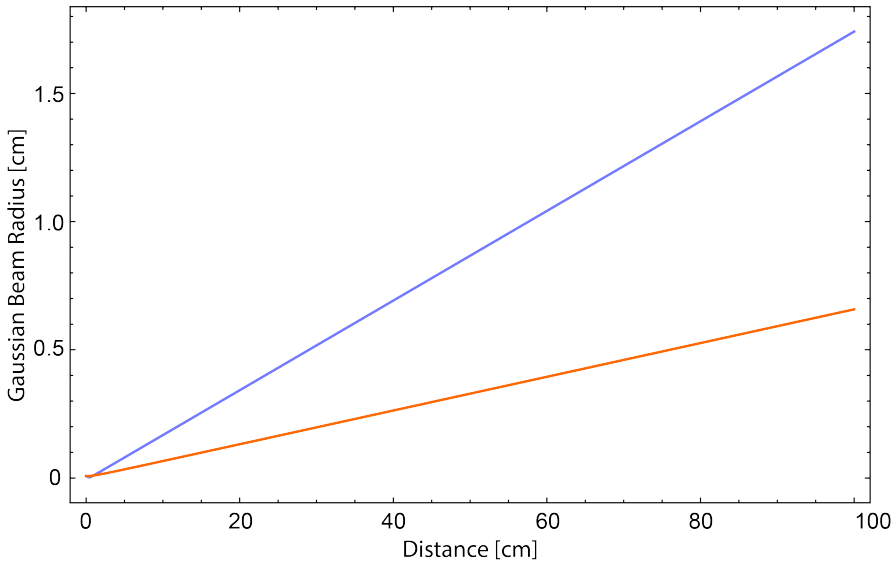

Figure 4.5: The radius of a Gaussian beam that is focused at the midpoint between the prism mirrors on the brass cage. Horizontal axis: distance from the midpoint. Orange: the radius of the beam when there is no drop present. Blue: the radius of the beam when there is a drop present.

refers to the midpoint between the two prism mirrors. If the plot is inspected closely, one may notice that the two curves do not overlap. This occurs because the drop is refractive, and so it changes the location of the Gaussian beam's waist. The drop shifts the focal plane of the beam ≈ 4 mm for a drop $R = 250$ μm. What is immediately clear from inspecting this plot is that the levitated drop's small focal length results in much faster (compared to not having a drop) beam divergence after the beam passes the midpoint between the two prism mirrors.

If a drop's shape is distorted (i.e. due to a focused laser propagating through it, as described in section 4.1.1) then it will exhibit ellipticity $e = R(\theta = 0)/R(\theta = 2\pi)$ (see figure 4.2 and section 3.4.1) and the local radius of curvature will depend on e. Furthermore, the distance the laser travels inside the drop also depends on e. In this case, in order to use ABCD matrices to describe beam propagation through the elliptical drop one can use $\mathbf{M}_{\text{refr}}$ with the local radius of curvature $R \to R(e)$. One can also use $\mathbf{M}_{\text{prop}}$ where d is parametrically defined for a beam with an arbitrary incidence angle and impact parameter. Figure 4.6 shows the displacement of a laser with $h = 240$ μm at $z = 1$ m after it propa-

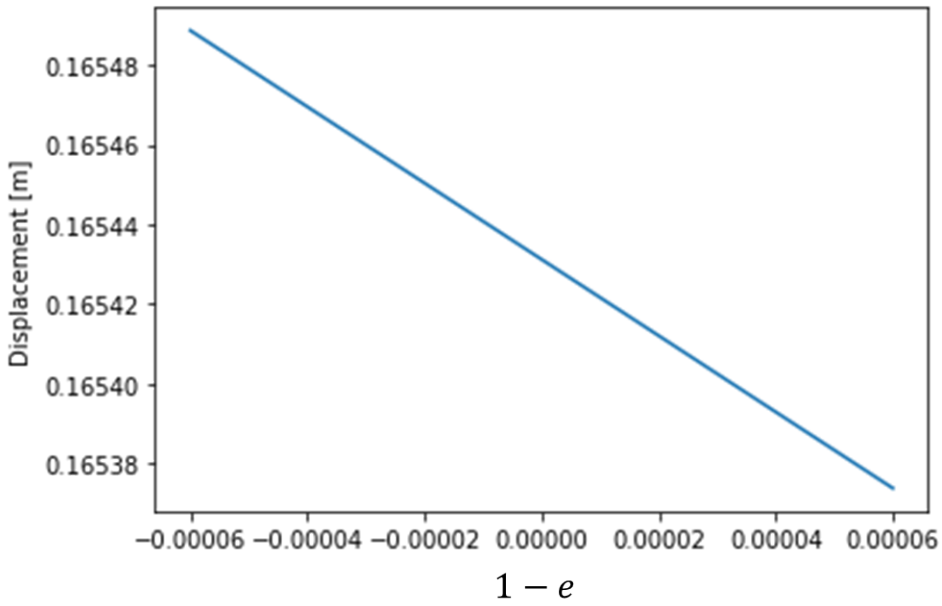

Figure 4.6: The displacement of a laser (with $h = 240$ μm at $z = 1$ m) after it propagates through a drop of ellipticity e. Here, the drop's unperturbed radius $R_0 = 250$ μm.

gates through the drop versus $1 - e$ (this is approximately how far away the photodetector is in actual measurements). The drop's cross-section is circular when $1 - e = 0$. Here, the drop's unperturbed radius $R_0 = 250$ μm.

From this section, we gather that COM modes will change h at the frequency of their motion, and thus will deflect a laser at the same frequency. As described in section 4.1.1, a focused laser can be used to drive a drop's surface modes. Driving the drop's $\ell_d = 2$ surface mode (4.2 can be conceived as a snapshot of this driving) necessarily introduces ellipticity. Figure 4.5 and figure 4.6 then suggest that a drop's surface modes will deflect and focus a laser at the surface modes' frequencies.

4.2 Center of Mass Motion of a Levitated ^{4}He Drop

In this section I describe center of mass (COM) motion measurements of magnetically levitated drops (see section 2.3.4). We have measured the drop's COM modes and found that the modes are coupled, and that an asymmetry in our trap leads to a broken degeneracy

of the drop's radial motion. We measured three normal modes of oscillation with frequencies $\sim$ 1 Hz, which are in good agreement with what was predicted in equations 2.114 and 2.115. We attempted to measure these modes' quality factor via a ring-down measurement, but we found that the amplitude of the drops' COM modes tend to grow over time; this precluded a quality factor measurement. Using a laser for measurement rather than video analysis (see section 3.4.2) allowed for more precise measurements of drops' COM motion, and thus a better characterization of the magnetic trap.

After a drop has been levitated and its radius has stabilized to a value around 250-300 μm, we allowed the drop to evaporate for some time ($\sim$30 minutes for these measurements) before allowing a laser to enter the cryostat. The prism mirrors warm slightly when laser light impinges on them, so if they are allowed to warm before the pressure in the experimental cell is very low, it can cause the gas around the drop to warm, which causes increased evaporation of the drop.

The levitated drop is positioned between the two prism mirrors so that a laser that enters the cryostat will pass through the drop. By the time the drop radius has stabilized, it typically undergoes center of mass (COM) motion with an amplitude that is smaller than the resolution of our imaging system. If desired, we apply an impulse to the levitated drop (by giving the non-magnetic table a small bump), giving it several tens of microns of COM motion. As discussed in section 4.1.2, when the drop undergoes COM motion and moves across the path of the laser beam, the beam is refracted at an angle dependent upon the drop's position relative to the beam. As a result, when the refracted laser exits the cryostat it sweeps across a photodiode in such a way that the photodiode detects an intensity proportional to the COM displacement.

Figure 4.1 illustrates the measurement set-up for COM measurements, except that the intensity-modulated laser was not used. Figure 4.7 shows a simplified illustration of the setup. The beam is guided into the cryostat (after transmitting through a dichroic mirror) with steering mirrors, and focused down to a diameter $\sim$ 190 μm at the location of the

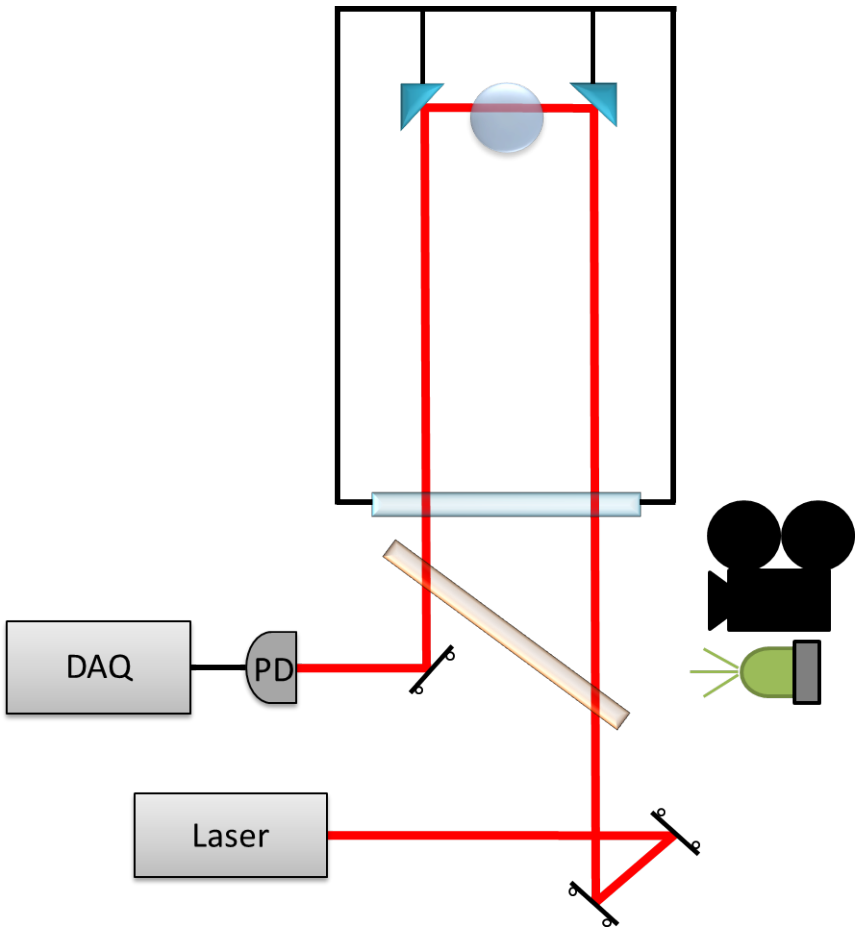

Figure 4.7: The setup used for laser-based COM motion measurements. A beam propagates into the fridge and through the drop. The drop's motion causes the beam to sweep across a photodiode (PD) outside of the fridge. The dichroic mirror (pink slab) passes red light, but reflects green. The drop is illuminated (green diode) and imaged (black camcorder) coaxially.

levitated drop, which is smaller than the drop diameter by nearly a factor of three. Beam profile measurements show that the beam diameter increases to 500 μm at 7 cm away from the focal plane, which means the beam has an approximately constant diameter throughout the drop. Like in the COM measurements taken using video analysis, in these measurements we set the magnet current to some value, wait for 5 minutes to let the magnet settle, then use a National Instruments 12-Bit DAQ card to sample the photocurrent signal from the photodiode at 20 Hz for 10 minutes, before repeating the process for multiple currents.

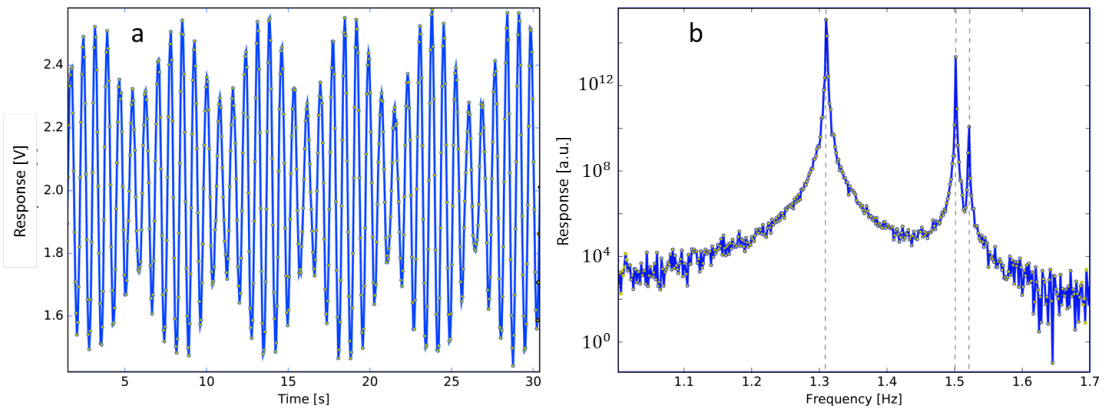

Figure 4.8: A drop's COM motion. (a) 30 seconds of laser deflection measurement of the drop's COM motion. (b) The power spectral density of this motion. The peaks in (b) correspond to the motion in x, y and z directions (x and y direction motion is nearly degenerate).

It is important to note that the beam propagation length from the drop to the photodiode is $\sim$ 1 m. As a result, the beam exiting the cryostat is $\sim$ 1 cm in visible diameter (on a detector card) at the cryostat's optical access window, and the light must be focused onto the photodiode. The beam diameter cannot be measured with a beam profiler at the window because the magnetic field is too large, which causes the profiler to malfunction.

One immediate difference between measuring COM motion with video analysis versus laser deflection is that every time the magnet current is changed, the levitation point moves, and so we must re-align the laser so that it propagates through the drop properly, while also reaching the photodetector. The measurements presented next are of the same levitated drop that is depicted in figure 3.13. Figure 4.8a shows 30 seconds of the COM motion signal of a trapped ^{4}He drop with a radius of 272.2 ± 0.7 μm, and figure 4.8b shows the power spectral density (PSD) of this signal. The magnet current was set to 115.6 A for this measurement. The most striking difference between the laser measurement and the video analysis is that we detect a third motional peak at ≈ 1.52 Hz using the laser. This peak was not detected in the video analysis measurements because it corresponds to motion along the video camera's line of sight. The peak at ≈ 1.52 Hz is distinct from the other peak at ≈ 1.50 because of a broken degeneracy of motion in the radial direction, (i.e. r-direction,

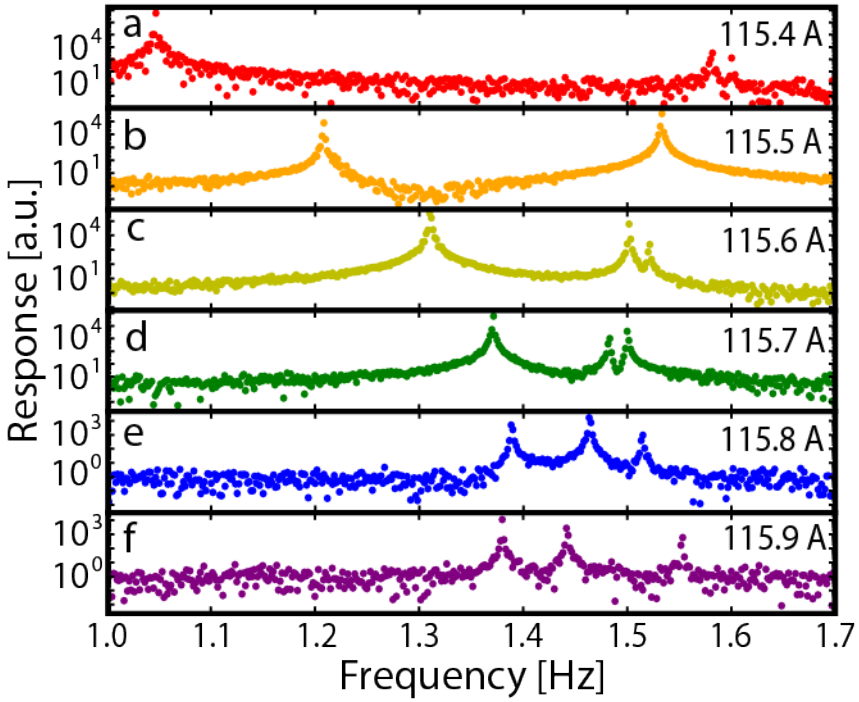

Figure 4.9: The power spectra of a drop's COM motion for various magnet currents.

$r = \sqrt{x^2 + y^2}$) into non-degenerate x-direction and y-direction motion.

Similar to the video analysis method for studying the COM motion, we have used this laser-based measurement to study the COM at various magnet currents. Figures 4.9(a-f) show the power spectral density of COM motion for levitation currents 115.4 - 115.9 A, spaced by 100 mA. Each peak in a given trace corresponds to a normal mode of COM oscillations. Near 115.4 A, the modes do not seem to be interacting significantly, so we associate them with x-direction, y-direction, and z-direction COM motion. However, as the magnet current is increased through 115.9 A, the mode frequencies initially approach each other, before undergoing an avoided crossing. The avoided crossing suggests that the modes are coupled and hybridize into a new set of normal modes of oscillation.

In order to begin to understand how a perturbation in the system could affect the COM modes, we start by defining the dynamical matrix $\mathbf{\Omega}^2(B)$ for the three components of the

COM oscillations that includes the unperturbed mode frequencies:

$$\mathbf{\Omega}^2(B) = \frac{1}{4\pi^2}\begin{pmatrix} \omega_z^2(B) & 0 & 0 \\ 0 & \omega_r^2(B) & 0 \\ 0 & 0 & \omega_r^2(B) \end{pmatrix} \tag{4.11}$$

where B is the magnetic field strength and $\omega_{\mathrm{r}}(B)$ and $\omega_{\mathrm{z}}(B)$ are given by equations 2.114 and 2.115.

We are interested in finding a matrix representation $\mathbf{\Delta}$ of a perturbation caused by an additional potential V that would cause the normal modes of COM oscillations to couple to each other. A possible cause for this coupling is a tilt of the magnet's symmetry axis relative to the direction of gravity.

Consider the unperturbed trapping potential $U = \frac{1}{2}r_i r_j U^{(2)}_{i,j} + \frac{1}{6}r_i r_j r_k U^{(3)}_{i,j,k} + \ldots$, which contains contributions from gravity and the magnetic field (as discussed in section 2.3.4 U has a minimum at $\mathbf{r} = 0$). Summation over repeated indices are assumed and $i, j, k, \in \{1, 2, 3\}$, with $r_1 = x, r_2 = y, r_3 = z$. The i, j element of the matrix $U^{(2)}_{i,j} \equiv \partial_{r_i}\partial_{r_j}U$. An arbitrary perturbing potential takes the form $V = r_j V^{(1)}_i + \frac{1}{2}r_i r_j V^{(2)}_{i,j} + \frac{1}{6}r_i r_j r_k V^{(3)}_{i,j,k} + \ldots$. The minimum of the combined potential $U + V$ occurs at a displacement $X_k = V^{(1)}_\ell \left[U^{(2)}\right]^{-1}_{k\ell}$, where $\left[U^{(2)}\right]^{-1}_{k\ell}$ is the matrix inverse of $U^{(2)}$. If we define a new coordinate system which is equal to the old coordinate system but with the origin shifted to the minimum of U + V (i.e., coordinates $y_i = r_i - X_i$), then to second order

$$\begin{aligned} U + V &= \frac{1}{2}y_i y_j \left\{ U^{(2)}_{i,j} + V^{(2)}_{i,j} + X_k \left(U^{(3)}_{i,j,k} + V^{(3)}_{i,j,k} \right) \right\} \\ &= \frac{1}{2}y_i y_j \left\{ U^{(2)}_{i,j} + V^{(2)}_{i,j} + V^{(1)}_\ell \left[U^{(2)}\right]^{-1}_{k,\ell} \left(U^{(3)}_{i,j,k} + V^{(3)}_{i,j,k} \right) \right\} \end{aligned} \tag{4.12}$$

The term in the braces represent the curvature about the new minimum. A perturbation due to the tilt of the magnet's axis relative to gravity can be described by $V = r_j V^{(1)}_i$, in which

case equation 4.12 simplifies to

$$\begin{aligned} U + V &= \frac{1}{2} y_i y_j \left\{ U^{(2)}_{i,j} + V^{(1)}_{\ell} \left[U^{(2)} \right]^{-1}_{k,\ell} U^{(3)}_{i,j,k} \right\} \\ &= \frac{1}{2} y_i y_j \left\{ U^{(2)}_{i,j} + \Delta_{i,j,k} \right\} \end{aligned} \tag{4.13}$$

The matrix elements $U^{(2)}_{i,j}$ and the tensor elements $U^{(3)}_{i,j,k}$ are obtained from fits to axial and radial magnetic field data. Using the polar angle θ (θ=0 means that the magnet's axis and gravity are perfectly aligned) and the azimuthal angle ϕ the vector $V^{(1)}_{\ell}$ can be expressed in terms of the projection of the gravitational force along the magnet's axis. In this case we find that

$$\Delta = \begin{pmatrix} 63.5(1-\cos\theta) & 37.4\sin\theta\cos\phi & 37.4\sin\theta\sin\phi \\ 37.4\sin\theta\cos\phi & -27.6(1-\cos\theta) & 0 \\ 37.4\sin\theta\sin\phi & 0 & -27.6(1-\cos\theta) \end{pmatrix} \tag{4.14}$$

We add equation 4.11 to equation 4.14 and diagonalize the result to find the new normal mode frequencies. Figure 4.10 shows the peak frequencies from figures 4.9a-f plotted versus the magnet current. When the inter-mode coupling is insignificant (near 115.4 A), the black data (circles) corresponds to z-direction motion, while the red and blue data correspond to x-direction and y-direction motion. The dotted lines are the unperturbed radial mode (purple) and axial mode (black) frequencies, which are predicted by equations 2.114 and 2.115. The solid lines are the result of a fit to the data using the new normal mode frequencies, where θ, ϕ and the molar magnetic susceptibility $\chi_{\rm mol}$ have been used as fitting parameters. The fit gives $\theta = (0.27 \pm 0.11)^\circ$, $\phi = (3 \pm 360)^\circ$, $\chi_{\rm mol} = (1.92 \pm 0.10)$ m^3/mol. The larger uncertainty in ϕ is not surprising because $\phi = 0$ is arbitrary in a system with high azimuthal symmetry. Although the fits are not excellent, the model does in fact predict the breaking of the radial degeneracy between COM modes and an avoided crossing between the COM modes. The fit quality is likely limited by our ignorance of the magnetic field

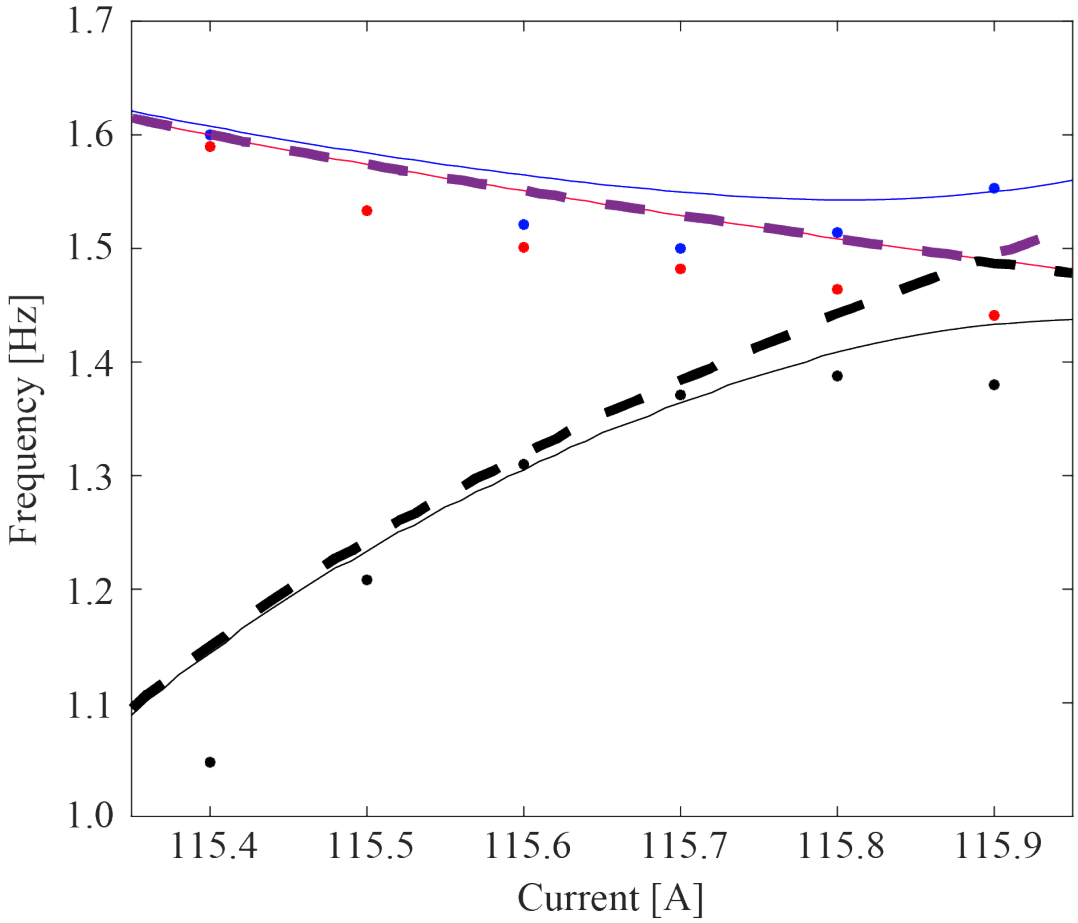

Figure 4.10: A drop's COM mode frequencies versus magnet current. Circles: measurements. Dotted lines: unperturbed radial mode (purple) and axial mode (black) frequencies, which are predicted by equations 2.114 and 2.115. Solid lines: the result of a fit that allows for inter-mode coupling due to a tilt of the magnet's axis with respect to gravity. The fit has free parameters $\theta, \phi, \chi_{\text{mol}}$ and the best fit values are $\theta = (0.27 \pm 0.11)^\circ, \phi = (3 \pm 360)^\circ, \chi_{\text{mol}} = (1.92 \pm 0.10)$ m^3/mol.

properties near the levitation point. This is because in building the experiment we have added objects (see section 3.2.3) with small (but non-zero) magnetic susceptibility near the levitation point, which will slightly alter the magnetic field.

Ring-Down Measurement

Although we tried to measure the COM motion ring-down with video analysis and found that the motion does not ring down, we also attempted to measure COM motion ring-down via laser deflection. In this measurement (like the video analysis measurement)

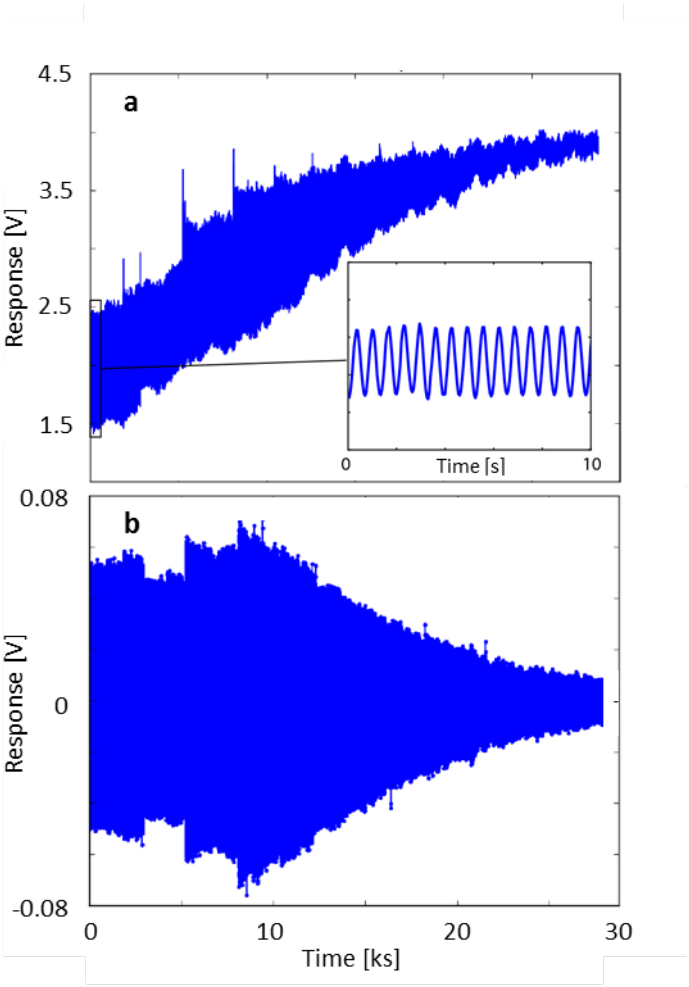

Figure 4.11: A drop's COM motion over 8 hours. (a) The laser deflection measurement of a drop's COM motion versus time. (b) The data from (a) after subtracting the DC offset and binning the data into 1 s bins.

the magnet was operated in persistent mode. We recorded video at a frame rate of 0.25 FPS for 8 hours, but the video quality is poor, so it is difficult to extract useful information from the video. However, over the course of the 8 hour measurement, the drop's equilibrium position shifted in the direction of gravity by ≈ 250 μm. It is interesting to note that over the 8 hours, the current decayed from 115.60 A to 115.48 A, which corresponds to a supercurrent decay of 0.009% per hour (approximately 33% faster decay than specified by Oxford Instruments). Alongside the video capture of the COM motion, we simultaneously used a 1550 nm laser with $P_{\mathrm{L}} \approx 3$ mW to measure the COM motion of the drop. The photodiode signal was sampled at 20 Hz for the entire 8 hours. Figure 4.11a shows the raw laser deflection data, which shows a large drift in the DC offset of the oscillations. The shift occurs because the signal depends on the location of the drop. Figure 4.11b shows the COM motion data with the DC offset over the entire data set subtracted, and after binning the data and subtracting the mean of each bin. The bin size was 0.01 minutes. There is a good-looking decaying envelope in the data, starting at 8,162 seconds, but because we know that the COM motion of the drop does not ring down, we do not attribute this decaying amplitude to a decaying COM motion amplitude. This decaying amplitude is consistent with a slow displacement of the drop's COM, which led to less laser light overlapping with the drop throughout its COM oscillations, and thus decreasing measurement sensitivity to the drop's COM modes.

In order to begin investigating the decay amplitude, the data from figure 4.11b is Hilbert transformed in order to recover the envelope from the oscillatory COM signal. The recovered amplitude is fit to a second order polynomial, and it is assumed that at the time that the data from figure 4.11b has the largest amplitude, we have the largest detection sensitivity (at 8,162 seconds). Figure 4.12a shows the extracted envelope of the COM motion plotted against time, where the envelope has been normalized by its maximum value. Under the assumption that the vertical displacement of the drop's equilibrium position was linear in time, figure 4.12b shows the detection sensitivity plotted against the displacement of the

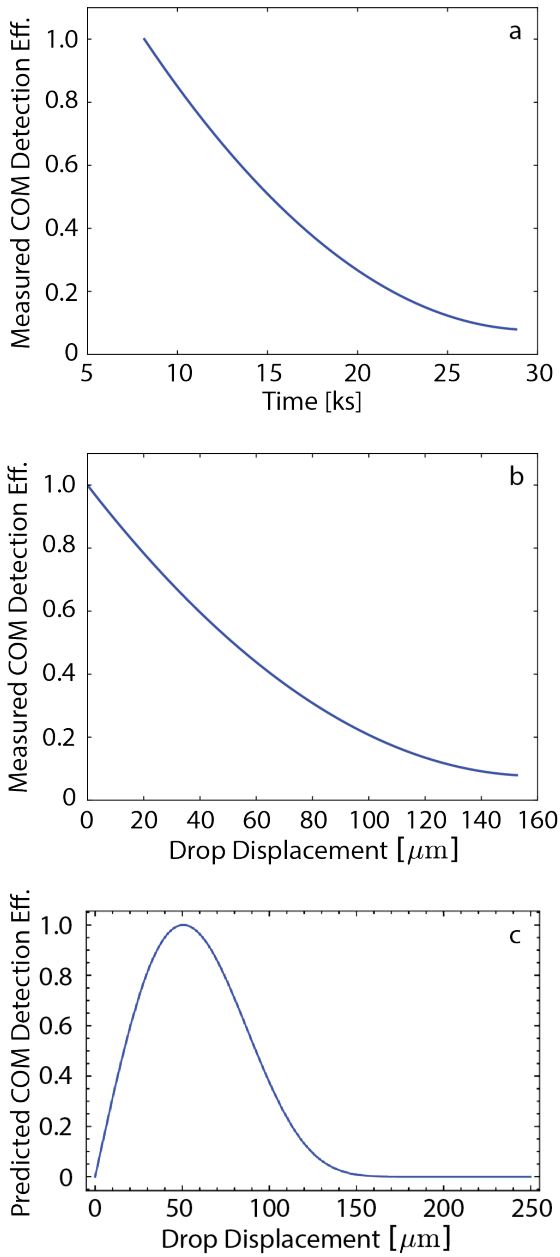

Figure 4.12: Sensitivity to a drop's COM motion. (a) The measured detection sensitivity to COM motion versus time. (b) The measured detection sensitivity to COM motion versus the drop's equilibrium displacement. (c) the predicted detection sensitivity to COM motion versus time.

levitation point. Note that figure 4.12b is a best-case-scenario, because it assumes that the COM motion of the drop did not increase over time. If the COM motion did increase, but only by a small value, then figure 4.12b should decently represent the detection sensitivity. With what we know about how the laser beam is steered as a function of h (see section 4.1.2), and how the laser beam width grows with distance after it propagates through the drop, we can predict the intensity of the beam as a function of distance away from the drop and the impact parameter h of the input beam, along the axis that is coincident with the diameter of the drop ($h = 0$). The normalized intensity along this axis is given by $I(h, z) = \exp\left(-s^2(h, z)/w^2(z)\right)$. The predicted intensity detection sensitivity to the relative position (h) between the drop and the input beam is, then, given by $\mathrm{d}I(h, z)/\mathrm{d}h$. Figure 4.12c shows the predicted intensity detection sensitivity (for a photodetector at $z = 1$ m) plotted against the displacement of the drop's equilibrium position. The detection sensitivity is maximized with ~ 50 μm of separation between the input beam and the center of the drop, and starts to quickly decrease from there. If the maximum detection sensitivity here corresponds to the maximum COM motion amplitude in figure 4.11b (at 8,162 seconds), then the predicted detection sensitivity in figure 4.12c is in good agreement with the detection sensitivity that was extracted from measurements in figure 4.12b. From figure 4.12, we gather that (given a fixed laser) the displacement of the drop's equilibrium position resulted in the decreased sensitivity to the drop's COM motion. The displacement of the drop's equilibrium position likely caused the laser to displace across the active region of the photodiode, such that the COM oscillations did not lead to sizable intensity fluctuations on the photodiode. A secondary cause of the decreased sensitivity was likely due to the decreasing overlap between the laser and the drop, such that as the drop oscillated the laser was only partially refracted.

Another effect from the displacement of the drop's equilibrium position is the COM oscillation frequencies that change as a function of time. Figure 4.13a shows the shift of one of the radial (red) and axial (blue) COM oscillation frequencies over the entire

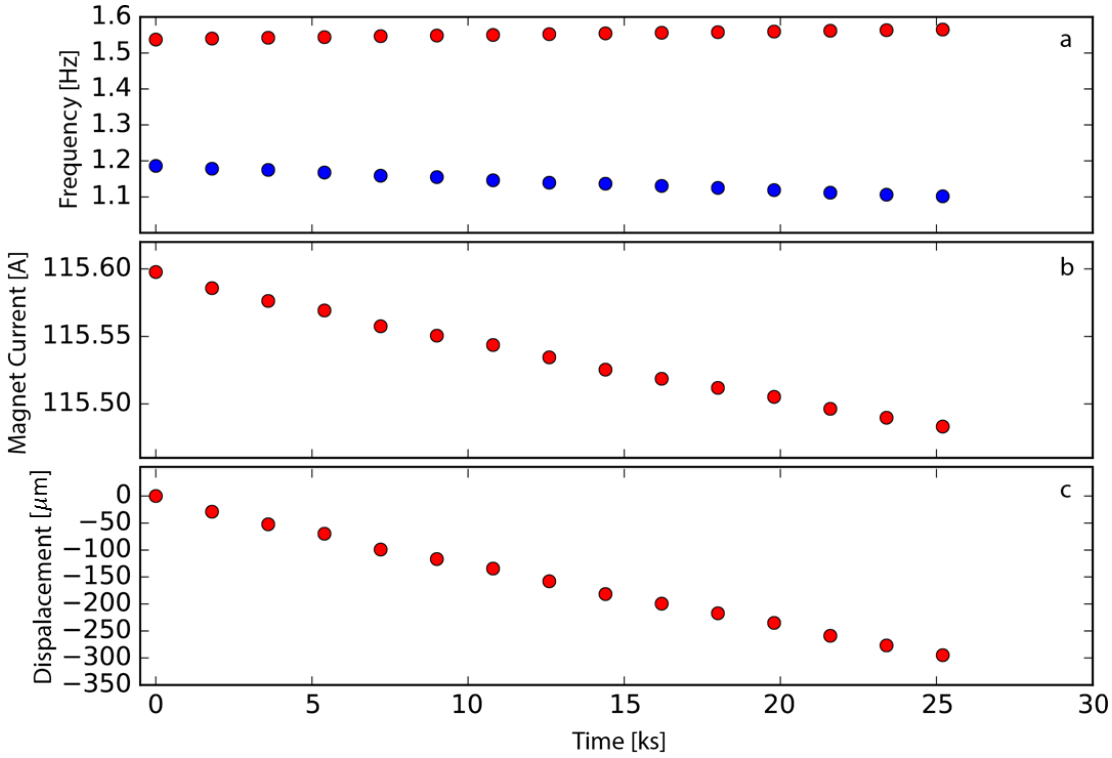

Figure 4.13: Drop displacement due to the decaying supercurrent in the levitation magnet. (a) The COM mode frequency of one of the radial directions (red) and the axial direction (blue) versus time. (b) The magnet current as inferred from the data in (a). (c) The displacement of the drop's equilibrium as inferred from the data in (b).

measurement. These data were obtained by binning the data from figure 4.11b and plotting the peak frequencies that appear in the PSDs of the bins. The magnet's current decay is shown in figure 4.13b, which was inferred from the measurements in figure 4.13a (using equation 2.114). As mentioned, there was a corresponding displacement in the drop's equilibrium position, which was inferred from figure 4.13b (using equation 2.106), and is shown figure 4.13c.

4.3 Evaporation of a Levitated ^{4}He Drop

In this section, we describe how optical modes were used to measure a levitated drop's evaporation rate, and thus its temperature. Using optical modes (described in detail in section 2.2.3), we measured changes in a drop's radius due to evaporation to be as small as ≈ 0.56 Å/s, which corresponds to a temperature ≈ 331 mK. We found that drops could be continuously illuminated with laser power $\gtrsim 10$ mW for 6 hours without suffering measurable absorptive heating.

Figure 4.1 illustrates the set-up for evaporation measurements. Section 4.5 described how we excite the optical modes of a ^{4}He drop by placing the focus of a laser at the drop's edge, and detect the laser's intensity at a photodetector. These modes are resonant in the drop when the laser's wavelength λ satisfies $\ell\lambda = 2\pi R$, where ℓ is an integer and R is the drop's radius. When this resonance condition is satisfied, the optical mode amplitude grows inside the drop, and since the electromagnetic field of these modes leaks radially around the drop's periphery, less light will impinge upon the photodetector downstream. As a result, we observe dips in the light intensity measured at the photodetector.

The levitated drop slowly evaporates, so in actuality the drop's radius $R = R(t)$. Then, the resonance condition $\ell\lambda = 2\pi n_1 R$ can be satisfied at multiple times such that $\ell\lambda = 2\pi n_1 R(t_0)$, $(\ell-1)\lambda = 2\pi n_1 R(t_1)$, $(\ell-2)\lambda = 2\pi n_1 R(t_2)$, etc. We excited the optical modes using an intensity-stabilized HeNe laser with power $P_{\rm L}^{\rm meas} = 300$ μW and $\lambda_{\rm opt} =$

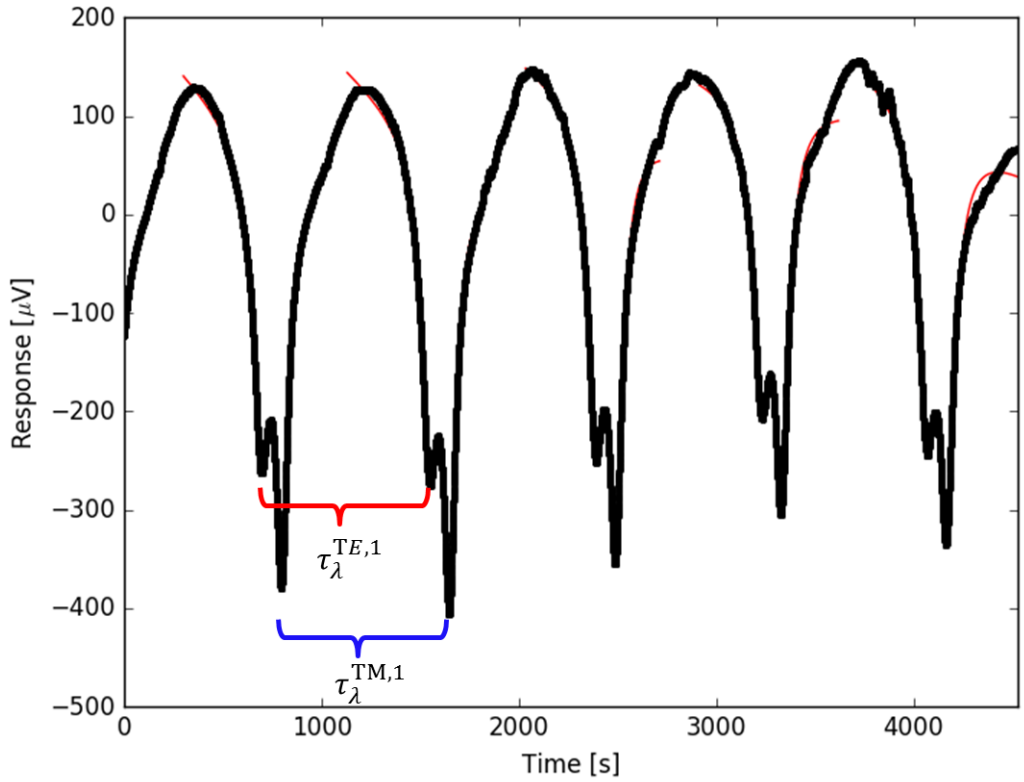

Figure 4.14: Optical modes with $\lambda_{\text{opt}} = 632.8$ nm of a levitated drop with radius $R \approx 208$ μm. Black: measurement of the drop's optical modes over time. Red: Lorentzian fits to the optical modes. The results of the fits are shown in table 4.1.

632.8 nm, whose focus (beam waist diameter $2w_0 \approx 135$ μm) was made to skim the drop's edge. While the optical modes were excited, we modulated a separate laser at frequency f_{surf}, with power $P_{\text{L}}^{\text{drive}}$, $\lambda_{\text{drive}} = 1,550$ nm and $2w_0 \approx 190$ μm, and placed its focus near the drop's center. Consequently, we drove the drop's fundamental ($\ell_d = 2$) surface mode with frequency f_{surf} (see section 4.4). As a result, the transmission of the optical mode was modulated at f_{surf}, and we detected the transmitted light with a photodetector whose photocurrent was measured using a lock-in amplifier (LA). We used the LA to demodulate the photocurrent at f_{surf}, and integrated the resulting signal. This integration provided the optical mode's transmission over time. A more detailed description of this measurement technique is given in section 4.5.

Figure 4.14 shows the optical transmission over time for a drop with $R \approx 208$ μm

and $P_{\rm L}^{\rm drive} \approx 30$ mW. We fitted the transmission dips to Lorentzians to extract the time spacing τ_λ of the modes. In this data there are a series of double dip features, which reflect the presence TE and TM optical modes. The TE and TM modes have respective time spacing $\tau_\lambda^{{\rm TE},n}$ and $\tau_\lambda^{{\rm TM},n}$, where n is an integer. In the figure, $\tau_\lambda^{{\rm TE},1} = 849.87 \pm 0.15$ s and $\tau_\lambda^{{\rm TM},1} = 849.43 \pm 0.10$ s. In $\tau_\lambda^{{\rm TE},1}$, the drop's circumference decreased by λ, which means that its radius R decreased by $\lambda/2\pi$. As a result, $\dot{R} = (\lambda/2\pi)/\tau_\lambda^{{\rm TE},1} \approx 1.185$ Å/s, which corresponds to a drop temperature $T_{\rm d} = 341.5 \pm 0.05$ mK, according to equation 2.163 in section 2.5.1. If instead $\tau_\lambda^{{\rm TM},1}$ is used to find $\dot{R}$, one finds $\dot{R} = (\lambda/2\pi)/\tau_\lambda^{{\rm TM},1} \approx 1.185$ Å/s, which corresponds to $T_{\rm d} = 341.5 \pm 0.05$ mK. The temperature measurements associated with $\tau_\lambda^{{\rm TE},n}$ and $\tau_\lambda^{{\rm TM},n}$ for $n = 1, 2, 3, 4$ are shown in table 4.1. In this table, I have only included $\dot{R}$ and $T_{\rm d}$ as calculated from $\tau_\lambda^{{\rm TE},n}$.

n	$\tau_\lambda^{\rm TE}$ [s]	$\tau_\lambda^{\rm TM}$ [s]	$\dot{R}$ [Å/s]	$T_{\rm d}$ [mK]
1	849.87	849.43	1.185	341.50 ± 0.05
2	841.77	841.97	1.196	341.67 ± 0.05
3	839.23	839.94	1.199	341.71 ± 0.05
4	835.51	835.53	1.205	341.78 ± 0.05

Table 4.1: Evaporation rates and temperatures of a drop with $R \approx 208$ μm.

The data show that $T_{\rm d}$ increased by ≈ 300 μK over $t_{\rm meas} = 4,500$ s, which we suspect to be the result of heat conduction between the drop and the cell walls (as described in section 2.3.1, the optical absorption is expected to be negligible for $P_{\rm L}^{\rm drive} \approx 30$ mW). However, when the drive laser enters the cell, the cell wall temperature $T_{\rm wall}$ can increase from ≈ 6.5 K to ≈ 10 K, depending on the laser alignment (perhaps from striking an absorptive object, such as dust). During the measurement, $T_{\rm wall}$ slightly increased, which caused a corresponding slight increase in $T_{\rm d}$. Using equation 2.166 to infer the heat load necessary to cause $T_{\rm d}$ to asymptote to ≈ 341 mK, one finds a heat load $\dot{Q} \approx 70$ pW, which would arise from a cell pressure $P_{\rm cell} \approx 6 \times 10^{-8}$ mbar.

For the same drop, we systematically studied how $\dot{R}$ varied with the total laser power $P_{\rm L}^{\rm tot} = P_{\rm L}^{\rm drive} + P_{\rm L}^{\rm meas}$ entering the cell. In order to do this, we varied $P^{\rm tot}$ and measured the

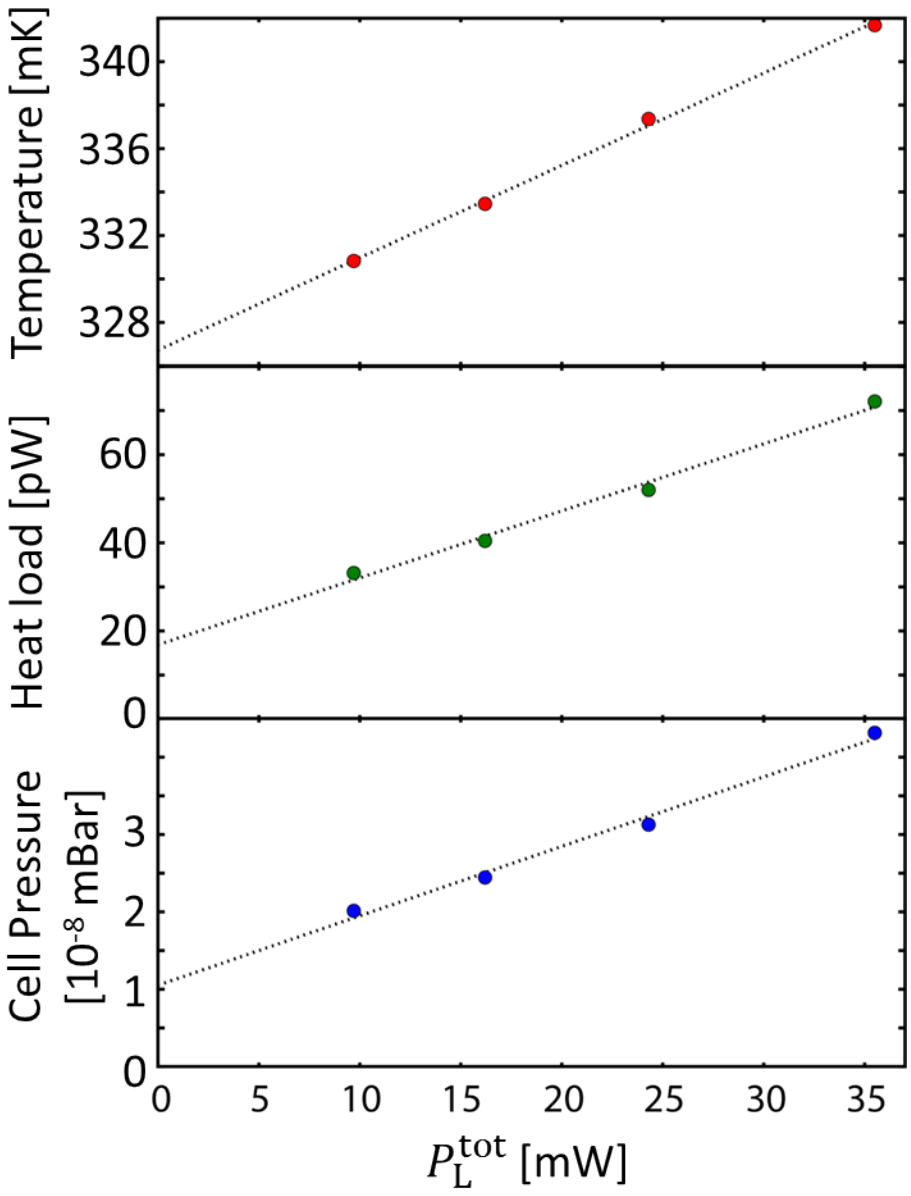

Figure 4.15: Laser power dependence of a drop's evaporation rate. Top: The temperature of a drop with $R \approx 208$ μm. Middle: The heat load on the drop. Bottom: the helium pressure required to produce the measured heat load. All three are plotted versus the total input laser power. Dotted line: Linear extrapolation to zero laser power.

optical modes that appeared in $t_{\rm meas}$. Prior to the measurement, we raised the experimental cell wall temperatures to $\approx$ 30 K for 10 minutes (removes desorbing liquid helium film from the cell walls) and we allowed the drop to evaporate for ≈ 4 hours without allowing laser light to enter the cryostat. Figure 4.15 shows the result of this measurement. The black dotted line in the figure is an extrapolation to $P_{\rm L}^{\rm tot} = 0$ mW, giving $T_{\rm d} = 326$ mK, $\dot{Q} \approx 18$ pW, and $P_{\rm cell} \approx 1 \times 10^{-8}$ mbar in the absence of heat conduction into the drop due to optically absorptive objects in the cell generating heat.

In order to check that the optical mode measurements of $\dot{R}$ were sensible, we wanted to use an independent measurement of R and compare the two measurements. We measured the drop's radius via measurement of its $\ell_d = 2$ surface mode (see section 4.4) just before and one hour after the measurements presented in figure 4.15, and found that after the total time $\Delta t \approx 5.3 t_{\rm meas} = 6.7$ hours, $\Delta R \approx 2.1$ μm. This gives an average evaporation rate $\dot{R}_{\rm avg} \approx 0.9$ Å/s, which corresponds to $T_{\rm d}^{\rm avg} \approx 337$ mK, and is in good agreement with the average of the temperature measurements in figure 4.15.

Figure 4.16 shows the theory curve that relates $T_{\rm d}$ to $\dot{R}$ (dotted line), and it is overlaid with our evaporation measurements (solid circles). The point of showing this plot is to convey that because of the non-linear relationship between $T_{\rm d}$ and $\dot{R}$, a small decrease in T (for example, realized by a small decrease in $P_{\rm cell}$) is expected to provide a significant decrease in $\dot{R}$. A decreased $T_{\rm d}$ is ideal for our purposes for a number of reasons. First, decreased $T_{\rm d}$ comes with a decreased $\dot{R}$, which will decrease the frequency sweep rate required to track the drop's optical modes (see section 2.5.1). Second, the surface mode loss $\propto T_{\rm d}^4$ (see section 2.4), and so will be strongly suppressed. Third, as described in section 2.3.1, for larger drops (future work), the dominant optical loss mechanism is expected to be scattering from thermal surface waves, so decreased $T_{\rm d}$ will suppress the optical loss.

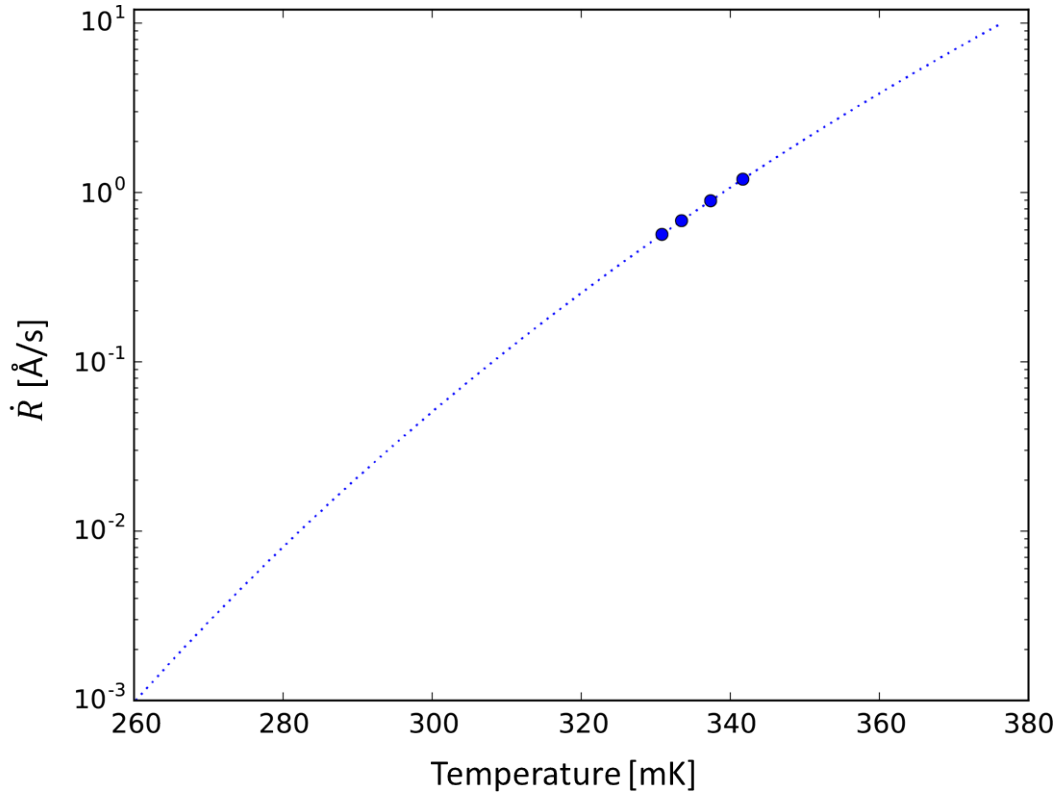

Figure 4.16: A drop's evaporation rate versus its temperature. Dotted line: the theory that relates a drop's temperature to $\dot{R}$. Circles: the drop's inferred temperature from measurements of $\dot{R}$.

4.4 Surface Modes of a Levitated ^{4}He Drop

In this section, I describe measurements of driven surface modes in levitated drops with $R \approx 175 - 300$ μm (see section 2.4 for a detail description of these modes). We found that these modes' frequencies are in good agreement with theory. We also found that these modes' decay rates are close to the predictions given by ballistic phonons damping the surface modes (see section 2.4), but that they may be slightly overestimated.

As described in section 2.4, a levitated drop's surface modes are harmonic oscillation modes that are restored by the drop's surface tension. The angular frequencies of these modes are given by equation 2.140:

$$\omega_{\ell_d} = \sqrt{\frac{\ell_d(\ell_d - 1)(\ell_d + 2)\sigma}{\rho_0 R^3}} \tag{4.15}$$

where $\ell_d \geq 2$ is the surface mode index, σ is the surface tension, ρ_0 is the mass density and R is the drop's radius. With the image analysis techniques discussed in section 3.4.1, extract R from images of a drop, then substitute it into equation 2.140 to find ω_{ℓ_d}.

In these measurements, we modulated (up to $\approx 100\%$ modulation depth) a drive laser at frequency $\omega_{\ell_d}/2\pi$, with power $P_{\mathrm{L}}^{\mathrm{drive}}$, $\lambda_{\mathrm{drive}} = 1,550$ nm and beam waist diameter $2w_0 \approx 190$ μm, and placed its focus near the drop's center. Consequently, the intensity-modulation provided a modulated optical dipole force to the liquid helium, and thus drove the drop's surface modes (see section 4.1.1). We placed the waist of a measurement laser with $P_{\mathrm{L}}^{\mathrm{meas}} \approx 3$ mW, $\lambda_{\mathrm{meas}} = 635$ nm and beam waist diameter $2w_0 \approx 135$ μm, slightly offset from the drop's center. The measurement laser was collected onto a photodiode (and filtered with a dichroic mirror to ensure the driving laser did not reach the photodiode) whose photocurrent was measured using a lock-in amplifier (LA). Because the drop's surface mode was driven, the measurement laser that propagated through it was deflected, which led to power fluctuations with frequency $\omega_{\ell_d}/2\pi$ at the photodetector. The LA's reference frequency was also used to modulate the drive laser intensity. We swept the

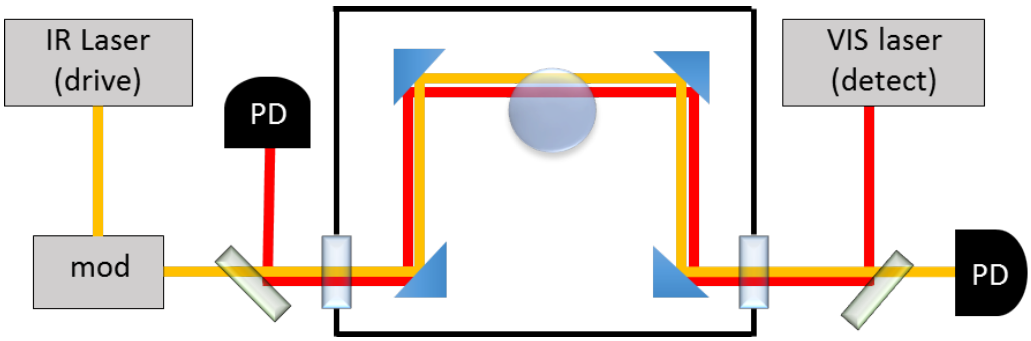

Figure 4.17: The setup used for surface mode measurements. A drive laser is intensity modulated, imparting a modulated optical dipole force on the drop. A detection laser is deflected by the drop's vibrations and detected by a photodiode.

LA's reference frequency about $\omega_{\ell_d}/2\pi$, which allowed us to drive and measure the surface mode oscillations. Figure 4.1 illustrates the set-up for surface mode measurements. However, figure 4.17 shows a simplified illustration of the setup for surface and optical mode measurements (however, in actuality the driving laser is made to strike the drop near its center).

Figure 4.18 shows a measurement (light blue) of the $\ell_d = 4$ surface mode in a drop with $R = 246 \pm 0.7$ μm, and it includes a fit to a Lorentzian lineshape (dark blue). Here, $P_{\rm L}^{\rm drive} \approx 10$ mW. The fit gives $\omega_{\ell_d=4}/2\pi = 566.585 \pm 0.014$ Hz and the linewidth $\Gamma_{\ell_d=4}/2\pi = 2.12 \pm 0.03$ Hz. We measured ω_{ℓ_d} and Γ_{ℓ_d} for surface modes of the same drop with $2 \leq \ell_d \leq 14$. The data and the corresponding theory are shown in figure 4.19 (equation 2.140). The sensitivity to the surface mode's motion depended on the measurement laser alignment, and we were unable to find good enough alignment in order to detect the $\ell_d = 9$ mode. Figure 4.19a shows the difference between the expected and measured oscillation frequencies, which along with figure 4.19b, shows that they are in good agreement.

The dominant source of surface mode damping is expected to arise from ballistic phonons (phonons with mean-free-path $L_{\rm mfp} \gg R$) scattering from the surface modes (which are also called ripplons) and carrying away energy, which is described in section 2.4. Using

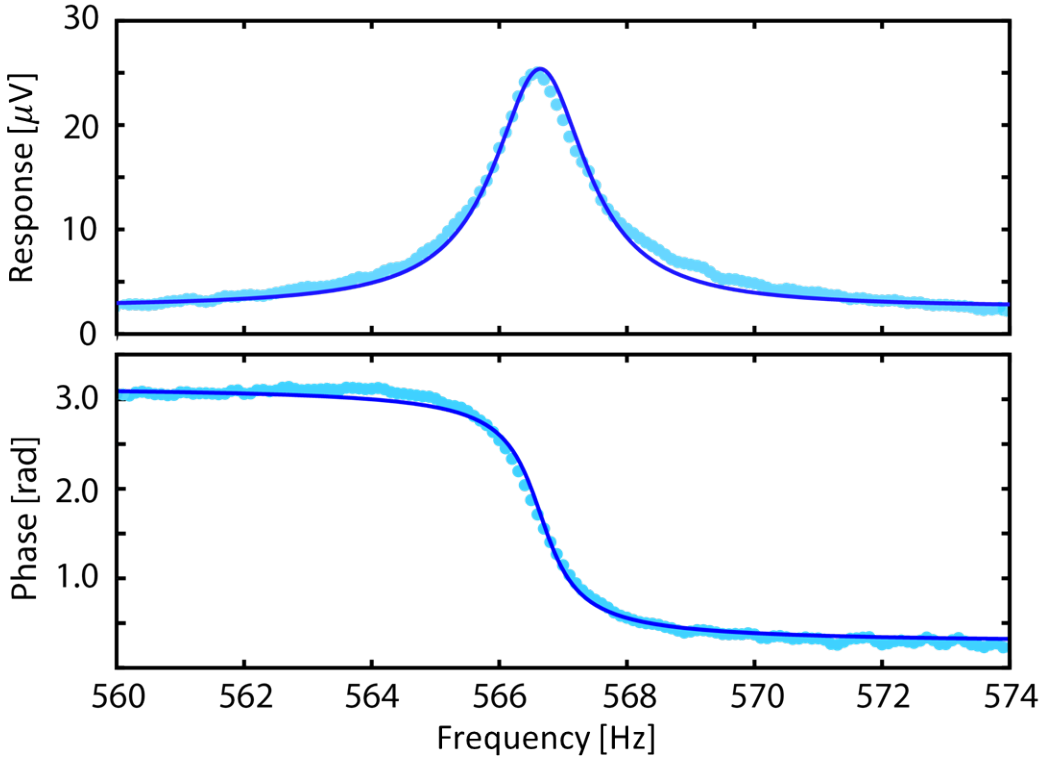

Figure 4.18: A measurement of one of a drop's surface modes. Light blue circles: a measurement of the $\ell_d = 4$ surface mode in a drop with $R = 246 \pm 0.7$ μm. Dark blue line: a Lorentzian fit. The fit gives $\omega_{\ell_d=4}/2\pi = 566.585 \pm 0.014$ Hz and the linewidth $\Gamma_{\ell_d=4}/2\pi = 2.12 \pm 0.03$ Hz

equation 2.144, this model leads to an expected surface mode decay rate

$$\frac{\Gamma_{\ell_d}^{\exp}}{2\pi} = \frac{\pi^2 \hbar \mathcal{K}}{60\rho_0} \left(\frac{k_{\mathrm{B}} T}{\hbar u_{\mathrm{c}}} \right)^4 \tag{4.16}$$

where u_{c} is the speed of sound and the surface mode wavenumber $\mathcal{K}$ is given by [83]

$$\mathcal{K} = \frac{\sqrt[3]{\ell_d(\ell_d - 1)(\ell_d + 2)}}{R} \tag{4.17}$$

We measured the $\ell_d = 2$ mode frequency in the middle, and at the end, of the measurement series shown in figure 4.19, and used it to extract the average evaporation rate $\dot{R}_{\mathrm{avg}}$. We found $\dot{R}_{\mathrm{avg}} \approx 0.5$ Å/s, which corresponds to an average drop temperature $T_d^{\mathrm{avg}} \approx 330$ mK. In figure 4.19c, equation 4.16 is plotted with $T = 330$ mK (green crosses) and $T = 310$ mK (red stars).

One observation that can be made from this plot is that the slope in the measurements and theory with ℓ_d are different from each other. The slopes match more closely with $T = 310$ mK, which has a corresponding $\dot{R} \approx 0.12$ Å/s. However, this $\dot{R}$ is nearly $5\times$ smaller than what we measured, so we do not believe this to be the actual $\dot{R}$. Another difference between the measured and expected decay rate occurs for $\ell_d = 2$. The apparent deviation between the measured $\ell_d = 2$ decay rate and the rest of the measurements is repeatable, and is not predicted by equation 4.16.

These deviations may reflect the fact that equation 4.16 assumes inelastic ripplon-phonon scattering events that each involve an independent phonon. However, a given phonon only reaches equilibrium with its bath after travelling its mean free path $L_{\mathrm{mfp}} \sim 1/T^4$, which for T = 330 mK gives $L_{\mathrm{mfp}} \approx 4.5$ mm. We note that $L_{\mathrm{mfp}} \approx 18R$, and the phonon lifetime $L_{\mathrm{mfp}}/u_{\mathrm{c}} \approx 16\ \mu\mathrm{s} \ll 2\pi/\omega_{\ell_d}$, the period of motion of the surface modes (for $2 \leq \ell_d \leq 14$). Thus, a phonon scatters many times from an effectively "frozen" surface, with the opportunity to average over the inward-moving and outward-moving portions of the drop's surface. The behavior of the surface mode decay rates have not been

calculated in this regime.

We have also studied how $\omega_{\ell_d}/2\pi$ and $\Gamma_{\ell_d}/2\pi$ change with R. Figure 4.20 shows measurements of $\omega_{\ell_d}/2\pi$ for various drops with radii $R \approx 175 - 275$ μm. Occasionally we could not find the proper laser alignment to be sensitive to all the modes, so some are missing in the plot. Again, the data (circles) shows good agreement with theory (dotted lines). Figure 4.21 shows $\Gamma_{\ell_d}/2\pi$ for the same drops. The error bars arise due to the uncertainty in R. Some error bars are bigger than others due to a low number of measurements used to determine R. Additionally, because some data points come from a single measurement of a surface mode, the drop temperatures are not known precisely so I take $T_d^{\rm avg} = 350 \pm 20$ mK. The theory curves in figure 4.21 are generated using $T = 350$ mK. Although the predictions and measurements have a relative offset, the decay rate seems to scale with $1/R$, as expected from theory.

We studied how the surface mode frequencies change over time. Again, the laser alignment effects our surface mode detection sensitivity, and it tended to be the case that if modes with even ℓ_d were easily detectable, then the modes with odd ℓ_d were more difficult to measure (and vice versa). This could be due to surface mode nodes appearing where the measurement laser strikes the drop for even or odd ℓ_d. Here, $P_{\rm L}^{\rm drive} \approx 10$ mW. For these measurements we used an automation process via a python script. First, a LA sweep measured $\omega_{\ell_d=2}$, then ω_{ℓ_d} for $2 \leq \ell_d \leq 6$ was predicted using equation 2.140. Next, in increasing order of $2 \leq \ell_d \leq 6$, the LA recorded surface mode sweeps (which took $\sim$ 10 minutes). Next, a LA sweep was used to measure $\omega_{\ell_d=2}$ again, and the entire process was repeated. Figure 4.22 and figure 4.23 show these measurements for drops with initial radii $R \approx 240$ μm and $R \approx 275$ μm, respectively. The circles are the measurements and the solid lines are the predicted frequencies. Our measurement was not sensitive to the $\ell_d = 3, 5$ modes, so they are not included. The solid curves are predictions generated by an $\omega_{\ell_d=2}$ surface mode measurement, and the circles are the measurements.

The surface mode measurements can be used to extract the drop's temperature $T_{\rm d}$. Us-

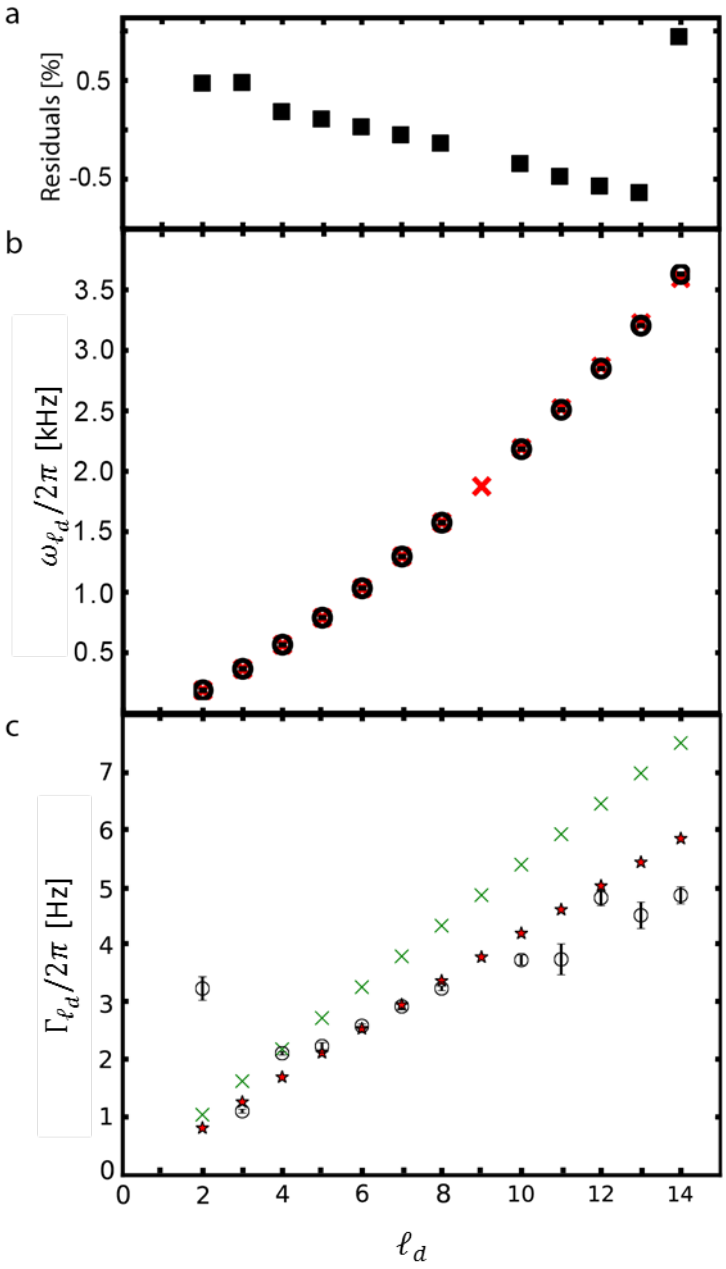

Figure 4.19: Measurements of many surface modes of a single drop. The drop's radius $R = 246 \pm 0.7$ μm. (a) The difference between the measured frequencies (circles) and predicted frequencies (crosses) in (b) versus the surface mode index ℓ_d. (b) Circles: measurements of the $2 \leq \ell_d \leq 14$ surface mode frequencies, crosses: predicted frequencies. (c) Circles: measurements of the $2 \leq \ell_d \leq 14$ surface mode linewidths, crosses: predicted linewidths for $T = 330$ mK, stars: predicted linewidths for $T = 310$ mK.

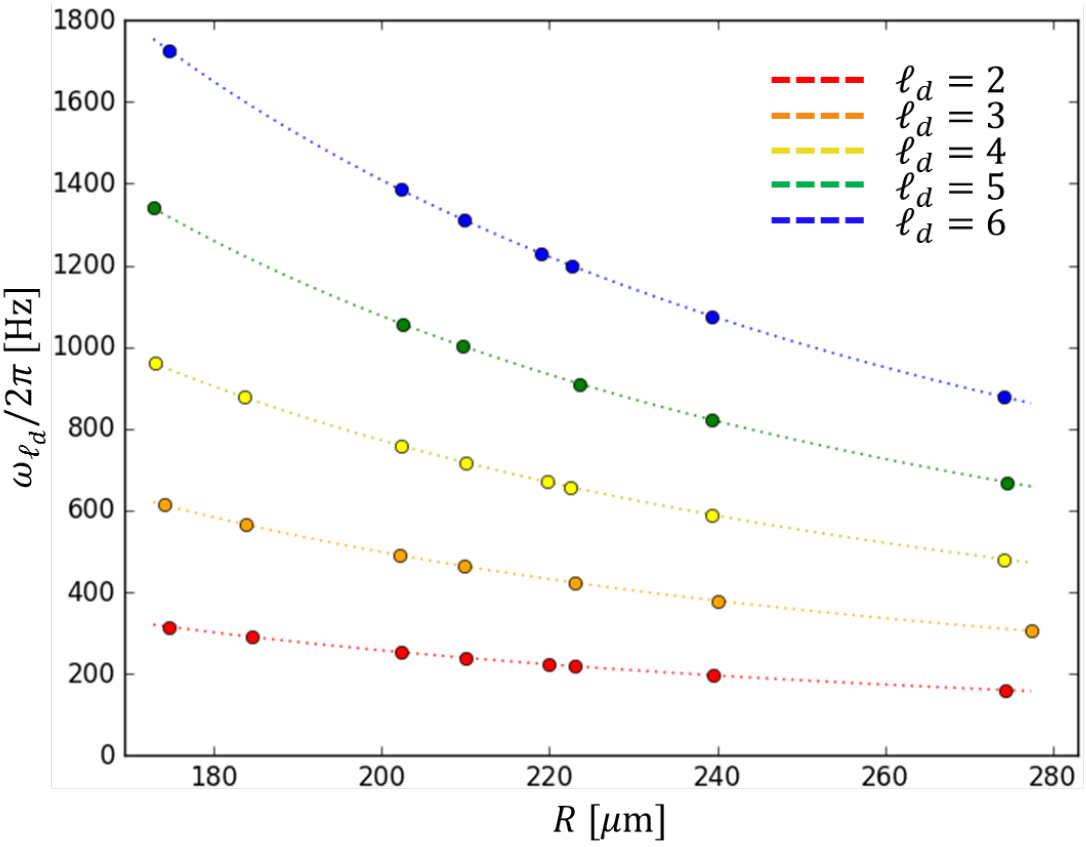

Figure 4.20: A plot of the expected (dotted lines) and measured (circles) surface mode frequencies versus the drop radius R. These surface modes were driven using laser power $P_{\mathrm{L}}^{\mathrm{drive}} \approx 10$ mW (with full modulation depth).

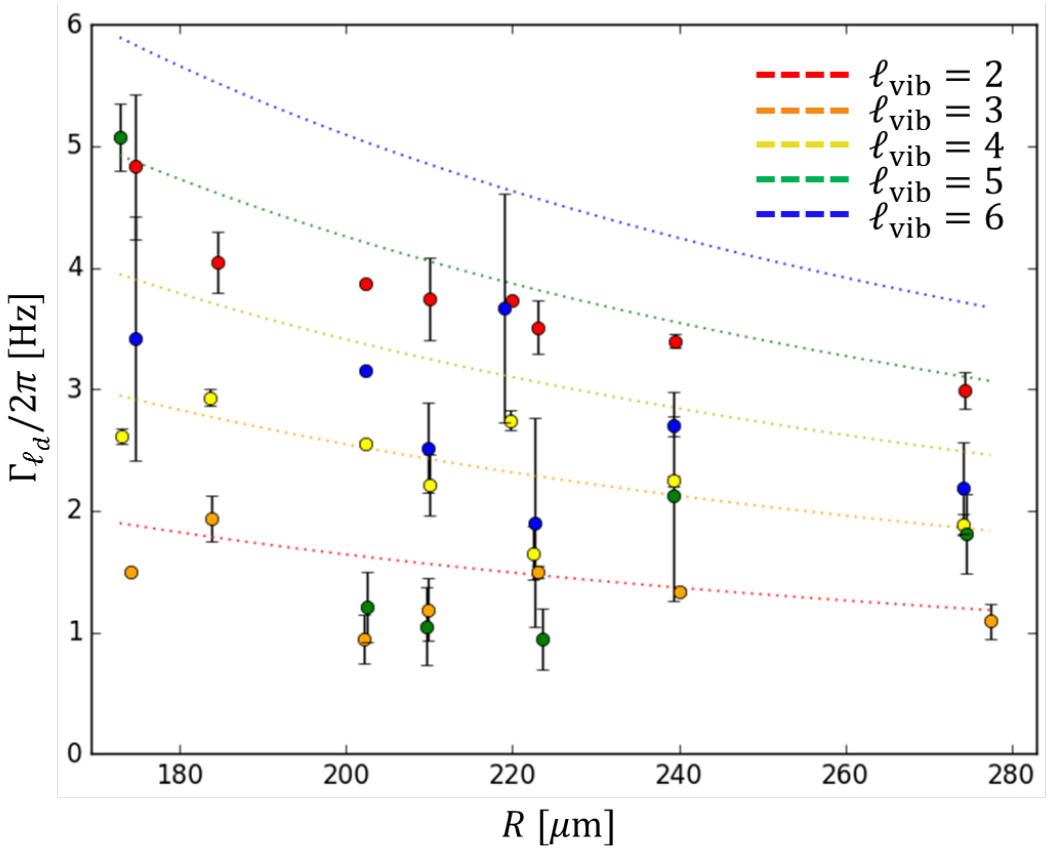

Figure 4.21: A plot of the expected (dotted lines) and measured (circles) surface mode linewidths versus the drop radius R. These surface modes were driven using laser power $P_{\mathrm{L}}^{\mathrm{drive}} \approx 10$ mW (with full modulation depth). The theory curves are plotted for $T = 350$ mK.

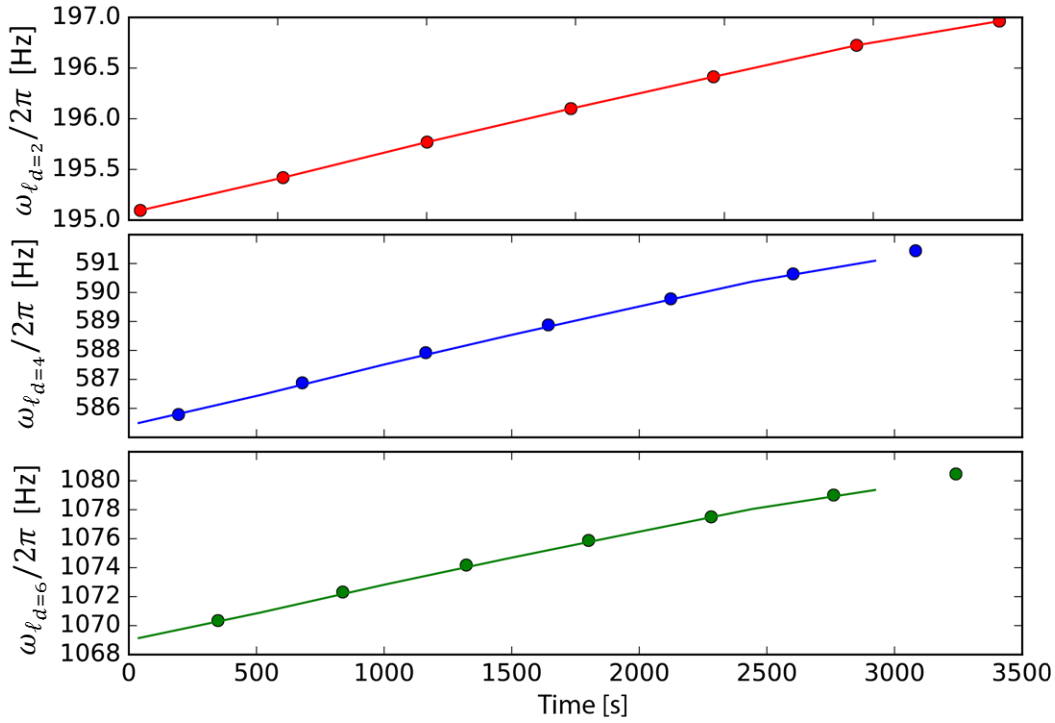

Figure 4.22: Surface mode frequency measurements plotted versus time for a drop with initial $R \approx 240$ μm. Circles: measurements. Solid lines: predictions (assuming a constant evaporation rate $\dot{R} = 4.1$ Å/s).

ing equation 2.140 and the $\omega_{\ell_d=2}$ data from figure 4.22, $\omega_{\ell_d=2}/2\pi \approx 195.1$ gives $R \approx 240.4$ μm, while $\omega_{\ell_d=2}/2\pi \approx 197$ Hz at $\delta t \approx 3,400$ s later gives $R \approx 238.9$ μm. This corresponds to an evaporation rate $\dot{R}_{\rm avg} \approx 4.1$ Å/s, which gives an average drop temperature $T_{\rm d}^{\rm avg} \approx 360$ mK. The same analysis for the drop with $R \approx 275$ μm in figure 4.23 (where I have used the first and last data points in the $\omega_{\ell_d=2}$ plot) gives $\dot{R}_{\rm avg} \approx 5.1$ Å/s, which corresponds to $T_{\rm d}^{\rm avg} \approx 365$ mK. Here, the drops are not as cold as the drops presented in section 4.3 because we did not bake the experimental cell walls, nor did we wait for many hours before starting this measurement; we allowed the drop to freely evaporate for two hours before allowing laser light into the cryostat.

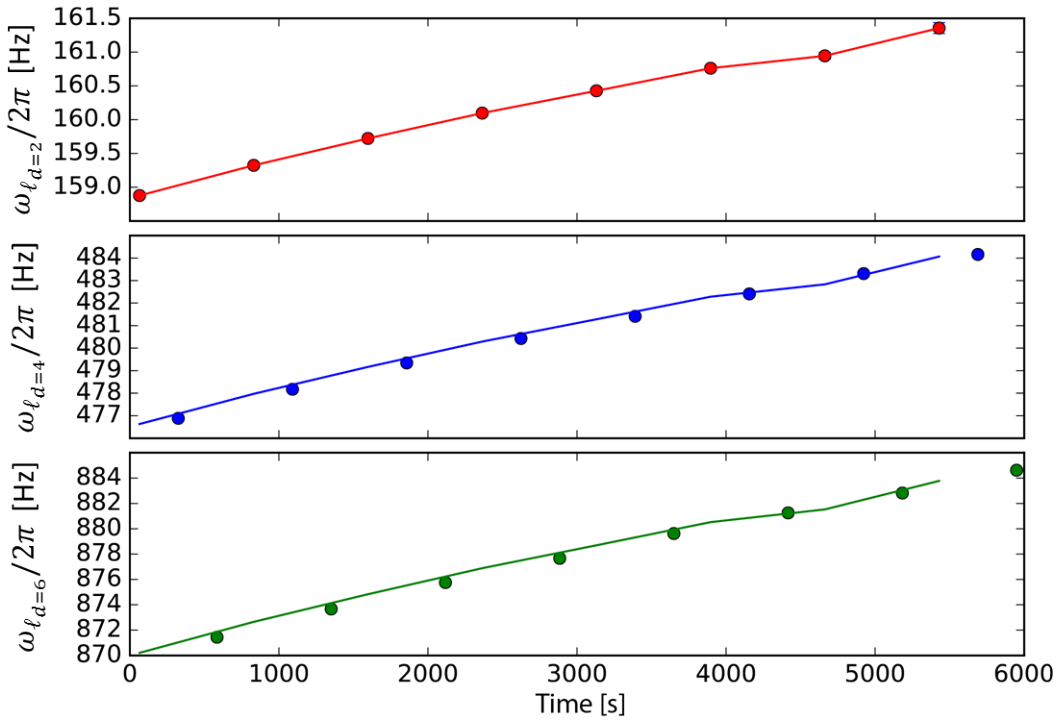

Figure 4.23: Surface mode frequency measurements plotted versus time for a drop with initial $R \approx 275$ μm. Circles: measurements. Solid lines: predictions (assuming a constant evaporation rate $\dot{R} = 5.1$ Å/s).

4.5 Optical Whispering Gallery Modes of a Levitated ^{4}He Drop

In this section we describe measurements of drops' optical modes. We found optical modes with finesse as high as $\mathcal{F} \sim 40$, which we believe to be limited by radiation loss (see sections 2.2.3 and 2.3.1) and line broadening due to ellipticity in the drops' shapes (ellipticity breaks the $(2\ell + 1)$-fold degeneracy of optical modes – see section 2.3.4). We also measured the polarization splitting between transvserse electric (TE) and transverse magnetic (TM) modes and found good agreement with predictions from analytic solutions of Maxwell's equations.

We excite an optical mode in a levitated drop by placing a focused laser's waist near the drop's edge. A small amount of the laser light couples into the optical mode and laser's intensity at a photodetector can be detected. These modes are resonant in the drop when the wavelength λ of the laser satisfies $\ell\lambda = 2\pi R$, where ℓ is an integer and R is the drop's radius. When this resonance condition is satisfied, the optical mode amplitude grows inside the drop, and since the electromagnetic field of these modes leaks radially around the drop's periphery, less light will impinge upon the photodetector downstream. As a result, we observe transmission dips in the light intensity measured at the photodetector. Figure 4.1 illustrates the set-up for optical mode measurements.

Because a levitated drop evaporates, the optical resonance condition $\ell\lambda = 2\pi n_1 R$ could be satisfied at multiple times such that $\ell\lambda = 2\pi n_1 R(t_0)$, $(\ell-1)\lambda = 2\pi n_1 R(t_1)$, $(\ell-2)\lambda = 2\pi n_1 R(t_2)$, etc.

We excited the optical modes using an intensity-stabilized HeNe laser (the measurement laser) with power $P_{\rm L}^{\rm meas} = 300$ μW and $\lambda_{\rm opt} = 632.8$ nm, whose focus (beam waist diameter $2w_0 \approx 135$ μm) was made to skim the drop's edge. At its waist, the beam diameter had a circular cross-section that was $\approx 6\times$ larger than the expected spatial extent of the optical mode inside the drop. Furthermore, as shown in section 2.2.3, the optical modes

in the drop are elliptical in cross-section. Owing to the mismatch between the size and shape of the beam and the optical mode, the amount of light coupled into the mode was low. To get a rough overestimate for the coupling efficiency (by assuming the optical mode has a circular cross-section), one can take the ratio of the beam's cross-sectional area to the optical mode's, which is $\approx (1/6)^2 \sim 10^{-2}$. But this is an overestimate so we estimate the coupling efficiency $\eta_{\text{eff}} \lesssim 10^{-2}$. Because $\eta_{\text{eff}} \ll 1$, we used a modulation technique to detect optical modes.

While the optical modes were excited, we modulated another laser (the drive laser) at frequency f_{surf}, with power $P_{\text{L}}^{\text{drive}}$, λ_{drive} and $2w_0 \approx 190$ μm, and placed its focus near the drop's center. This served to drive the drop's fundamental surface mode via the optical dipole force (see section 4.4). The resulting shape oscillations modulated the drop's radius, which is analogous to modulating the cavity length in a Fabry-Perot cavity. As a result, when the measurement laser was nearly resonant with an optical mode, the mode's transmission was modulated at f_{surf}. We measured the photocurrent using a lock-in amplifier (LA), which demodulated the photocurrent at f_{surf}. This modulation technique removed the large DC background from detecting the measurement laser, and allowed us to measure the optical modes. We could not measure η_{eff} directly because the calibration between the LA signal per surface mode displacement was unknown.

As the drop evaporated and the measurement laser intermittently became resonant with an optical mode, the photodetector detected a dip in the power with a Lorentzian lineshape of the form

$$\mathcal{L}(t) = \frac{A}{(t-t_0)^2 - \kappa^2/4} \tag{4.18}$$

where A is the feature size, t_0 is the time at which $\ell\lambda_{\text{meas}} = n_1 R(t_0)$ and κ is the mode's linewidth in units of seconds via the the drop's evaporation rate. The LA signal at f_{surf} is $\propto \dot{\mathcal{L}}(t)$. Here, $\dot{\mathcal{L}}(t)$ refers to the time derivative of $\mathcal{L}(t)$, but the derivative is with respect to $t - t_0$.

Figure 4.24 shows optical mode measurements for a drop with $R \approx 240\mu$m along with

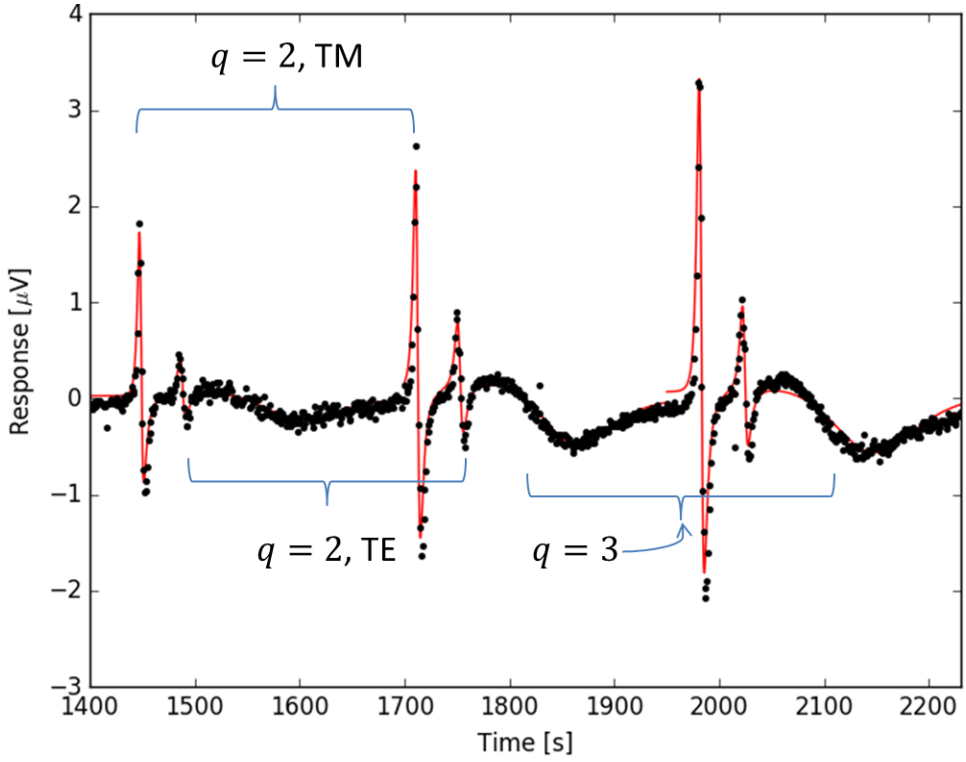

Figure 4.24: Optical modes with $\lambda \approx 632.8$ nm in a levitated drop with radius $R \approx 240\mu$m. Black: measurements of the $q = 2, 3$ TE and TM optical modes in a drop, which was excited using a laser with $\lambda = 632.8$ nm. Red: Lorentzian derivative fits to the optical modes. These fits give $\mathcal{F} = 36 \pm 2$ for the $q = 2$ TM mode, $\mathcal{F} = 30 \pm 3$ for the $q = 2$ TM mode and $\mathcal{F} = 1.9 \pm 0.1$ for the $q = 3$ mode.

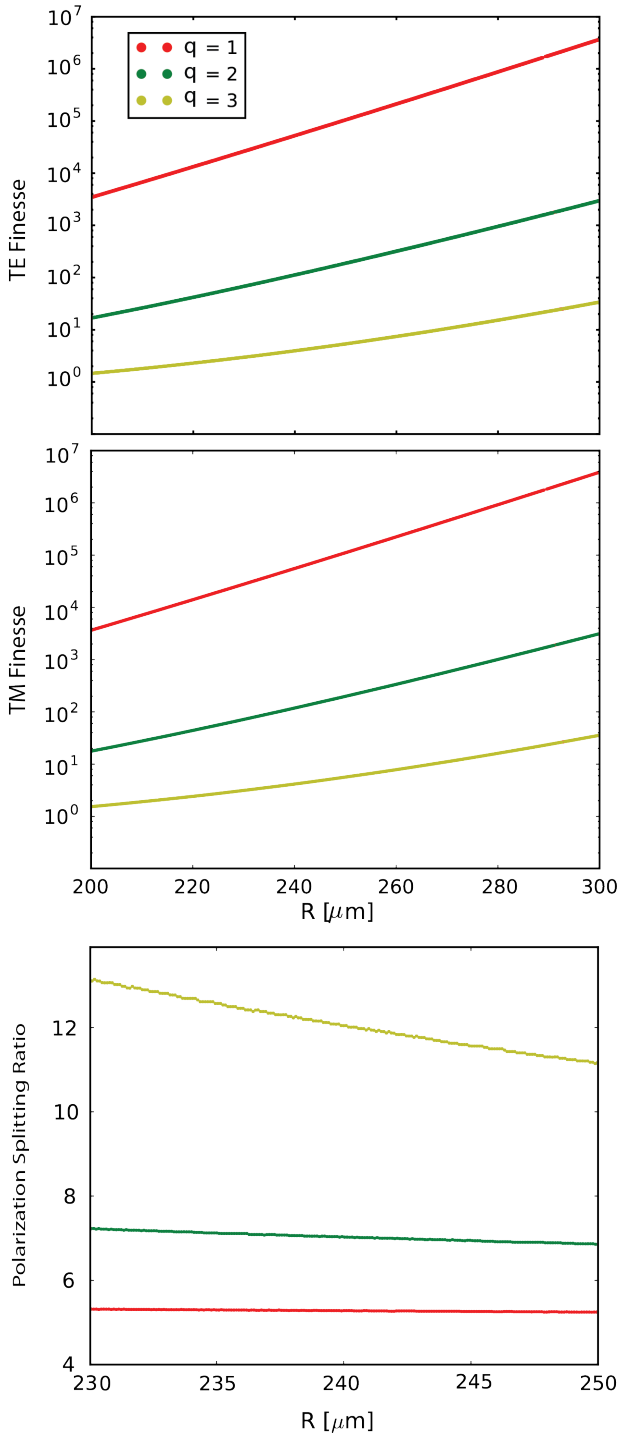

Figure 4.25: Predicted optical mode finesse versus the drop radius and q. The polarization splitting ratio is defined as the splitting between TE and TM modes, relative to the free spectral range between consecutive TE or TM modes.

fits to $\dot{\mathcal{L}}(t)$. Figure 4.25 shows the expected mode finesse for $q = 1, 2, 3$. Here, $P_{\rm L}^{\rm drive} \approx 35$ mW, and the modulation depth $\approx 64\%$. The fits give $\mathcal{F} = 36 \pm 2$ for the $q = 2$ TM mode, $\mathcal{F} = 30 \pm 3$ for the $q = 2$ TM mode and $\mathcal{F} = 1.9 \pm 0.1$ for the $q = 3$ mode. The TM modes are predicted to have slightly larger $\mathcal{F}$ than TE modes for this value of R, so it seems that the $q = 3$ mode was likely a TM mode. As shown in figure 4.25, the expected finesse values for this drop are $\mathcal{F} \approx 110$ and $\mathcal{F} \approx 4$ for the $q = 2$ and the $q = 3$ modes, respectively.

The polarization splitting ratio is the time spacing between two successive TE (or TM) modes with the same q – the free spectral range (FSR) – divided by the time spacing between a TE and TM with the same q. For $q = 2$ modes, the predicted splitting ratio ≈ 6.9, and we measured ≈ 6.7, which is in good agreement with the expected value. We did not observe the $q = 1$ modes with $\lambda_{\rm meas} = 632.8$ nm because they were likely narrow compared to our data sampling rate $t_{\rm samp} = 1$ Hz.

There are at least two reasons why the measured $\mathcal{F}$ differed from its expected value. First, we drove the drop's surface mode near resonance. Large radial deformations that modulate the optical mode frequency could have caused inhomogeneous broadening of the optical modes. Second, the drop is predicted to be non-speherical and have ellipticity e, such that $1 - e \sim 10^{-5}$ for magnet current $I = 116$ A (see section 2.3.4). This ellipticity will break the optical modes' $(2\ell+1)$-fold degeneracy and cause the modes to spread apart. The ellipticity-induced splitting between the $2\ell + 1$ different modes with index m is [158]

$$\Delta\omega_e \equiv \left|\omega_{q\ell m} - \omega_{n,\ell,m+1}\right| \approx \omega_{q\ell m} e \frac{|m| + 1/2}{\ell^2} \tag{4.19}$$

Because the measurement laser's spot size was much larger than the optical mode profile, optical modes with a wide range of m were likely excited. For $R = 240$ μm, $\ell \approx 2500$. For a mode with $\lambda = n_1 \lambda_{\rm meas}$, $\omega_{q\ell m} \approx 432$ THz, where $n_1 = 1.028$ is liquid helium's refractive index. For $m = 0$, $\Delta\omega_e/2\pi \approx 350$ Hz, but for $m = \pm 2500$, $\Delta\omega_e/2\pi \approx 1.7$ MHz.

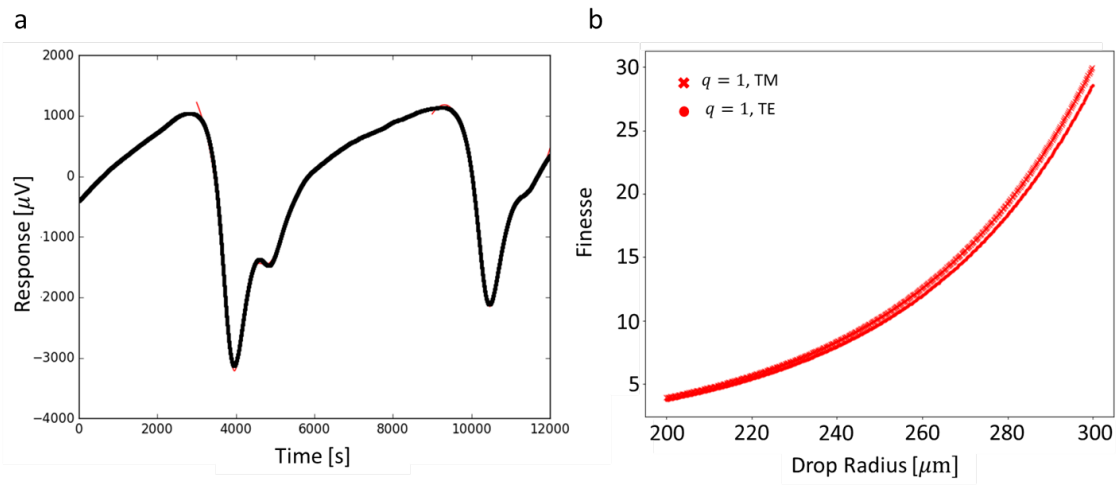

Figure 4.26: Optical modes with $\lambda \approx 1,550$ nm in a levitated drop with radius $R \approx 270$ μm. (a) Black: measurement of the $q = 1$ TE and TM optical modes in a drop. Red: Lorentzian fits to the optical modes. The fits give $\mathcal{F} = 9 \pm 1$ for the $q = 1$ optical mode. (b) The predicted finesse for the $q = 1$ TE and TM optical modes.

The $q = 2$ mode linewidth can be estimated from the measurements using $\kappa = \mathrm{FSR}/\mathcal{F}$, where $\mathrm{FSR} = c/2\pi n_1 R \approx 200$ GHz and $\mathcal{F} \approx 40$, which gives $\kappa \approx 5$ GHz. Then for all m, $\Delta\omega_e < \kappa$, so the split modes were unresolved and will have broadened the measured optical modes.

Integrating equation 4.19 with respect to m and taking the integration bounds to be ± 2500 sets the maximum size of the ellipticity-induced inhomogeneous broadening, which is $\kappa_\mathrm{e} \approx 4.3$ GHz. Then in the optical measurement above, the $q = 2$ mode finesse should be bounded above by the ellipticity-broadening finesse $\mathcal{F}_\mathrm{e} = \mathrm{FSR}/\kappa_\mathrm{e} \approx 46$. The additional mode broadening could be associated with driving large drop deformations.

We were able to measure the $q = 1$ mode with $\lambda_\mathrm{meas} = 1,550$ nm because these modes have larger linewidths (see sections 2.2.3 and 2.3.1), so we could sample them well with our data acquisition. Figure 4.26a shows a measurement of the $q = 1$ TE and TM modes in a drop with $R \approx 270$ μm, where we integrated the LA signal and fitted the measurement result to $\mathcal{L}(t)$. We measured $\mathcal{F} \approx 9$. For the $q = 1$ mode, the polarization splitting ratio was measured to be ≈ 7, while it was predicted to be ≈ 6.7. The $q = 2$ mode is predicted to have $\mathcal{F} < 1$ for $R = 270$ μm, so we did not expect to observe it. In

this measurement, $P_{\mathrm{L}}^{\mathrm{drive}} \approx 10$ mW, with $\approx 80\%$ modulation depth and $\lambda_{\mathrm{drive}} = 635$ nm. Shown in figure 4.26b is the predicted finesse for the $q = 1$ mode, which is $\mathcal{F} \approx 14$ for $R = 270$ μm.

Chapter 5

Future Work

In this chapter I first describe a re-design of the experimental cell, and the improvements it should offer over the design used for the measurements presented in this thesis. With the re-design in mind, I also describe intriguing physics that may be experimentally accessible with a levitated helium drop, such as quantum optomechanics and physics beyond the standard model.

5.1 New Experimental Cell Design

We have made several improvements to the experimental cell design. With these improvements, we aim to generate and sustain drops with larger radius R and lower temperature T, to reduce the cell pressure P, and to efficiently couple light into the high finesse $q = 1$ optical WGMs (see section 2.2.3). Furthermore, we have re-designed the electrodes that surround the levitation region, so that they should allow for the application of large electric fields to a levitated drop.

To date, the drops' initial size has been limited by its tendency to collide with the mirrors and electrodes in the cell during its initial formation (see figure 3.4). The new cell includes a flexible edge-welded bellows section that allows it to be raised and lowered by ≈ 2" so that the mirrors and electrodes can be moved away from the levitation region while

the drop is formed. We suspect that using the "fog-based" drop formation method (see section 3.3) with the mirrors and electrodes retracted should yield drops with larger R. If the "fog-based" drop formation method does not produced the desired results, we will use a capillary fill line to deliver liquid helium directly into the trap. The new experimental cell includes a ≈ 5 foot-long flexible bellows assembly that can be collapsed to a total length $\lesssim 12$", and used to guide a capillary through the cell. One end (at room temperature) of the capillary will be at room temperature, and the opposite end (cryogenic) can be positioned near the levitation region by collapsing the bellows assembly. We will pressurize the room temperature end of the capillary with high purity helium gas, which should condense and exit the opposite end as liquid. As previously demonstrated by the groups at Brown University, such a method should be able to produce drops with $R \sim 0.5$ cm [125, 126].

Reducing P will allow the drop to asymptote to lower T (see section 2.5.2). In the new cell, the liquid helium continuous flow line that is used to cool the cell walls is affixed to a segment of the cell walls that is made from brass (free-machining yellow brass), as is shown in figure 5.2. Also in the new cell, the titanium can (see section 3.2.4) has been replaced with a brass can. Because brass has larger thermal conductivity than stainless steel, the cell walls should be more efficiently cooled by the continuous flow line. With lower cell wall temperature $T_{\rm wall}$, desorption of any liquid helium film on the cell walls will be suppressed, and P should decrease. Pumping the continuous flow line could further decrease $T_{\rm wall}$ to $\sim$ 2 K, resulting in even lower P. To further decrease P we will experiment with charcoal sorbtion pumps in the cell, which are known to produce very low base pressures in chambers whose primary gas load is helium. Lower T should have three immediate effects on the drop. First, lower T will decrease the drops' evaporation rate, and thus the optical WGMs' frequency scan rate (see section 2.5.1). This should enable measurements of $q = 1$ optical WGMs with high-Q. Second, lower T is expected to decrease the damping rates of the drops' surface modes (see section 2.4). Third, lower T is expected to decrease the scattering loss from thermal surface modes, and thus the drop's optical WGMs should

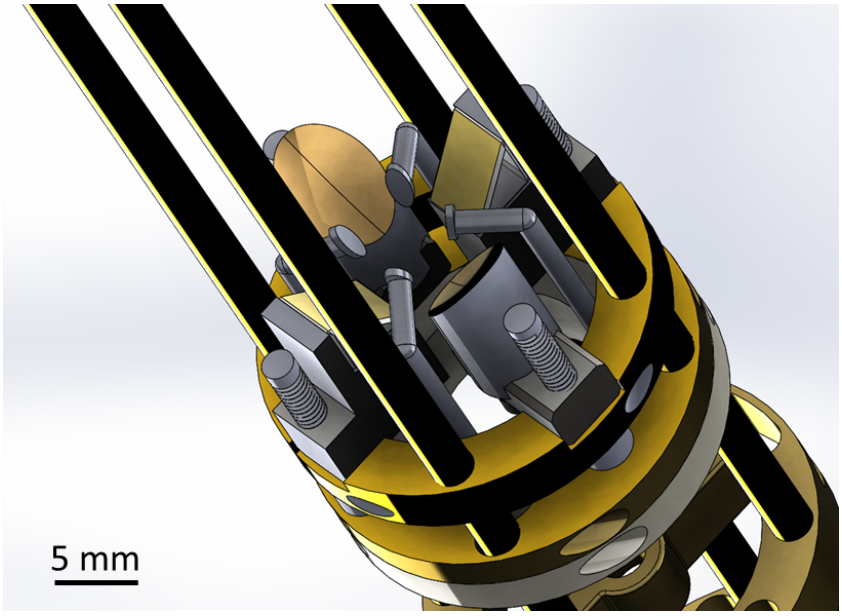

Figure 5.1: The new experimental cell's new mirror mount. The mirror mount now has a set of parabolic mirrors that will focus a laser to a width $2w \sim 10$ μm. This mount also includes angled electrodes with ellipse-shaped plates, which will be used to apply forces to a levitated drop.

have larger finesse (see section 2.3.1).

To improve the coupling of a free space laser to the drop's optical WGMs (see section 2.2.3), we have added a pair of parabolic mirrors to the mirror mount in the brass cage (see section 3.2.3), which is shown in figure 5.1. The parabolic mirrors will focus the laser to a width $2w \sim 10$ μm, which is of the same order as the $q = 1, \ell \gg 1$ optical WGMs' transverse (r, θ) extent for a drop with $R \sim 1$ μm. However, as can be seen in figures 2.5 and 2.8, the WGM transverse profile is not circular. We will prepare the laser light outside the cryostat using cylindrical optics, which in combination with the focusing provided by the parabolic mirrors should yield significantly improved mode matching. Additionally, COMSOL simulations suggest that the new electrodes could be used to feedback-cool the drops' center of mass (COM) motion. Suppressed COM motion will be useful for more efficiently coupling a free space laser to optical WGMs.

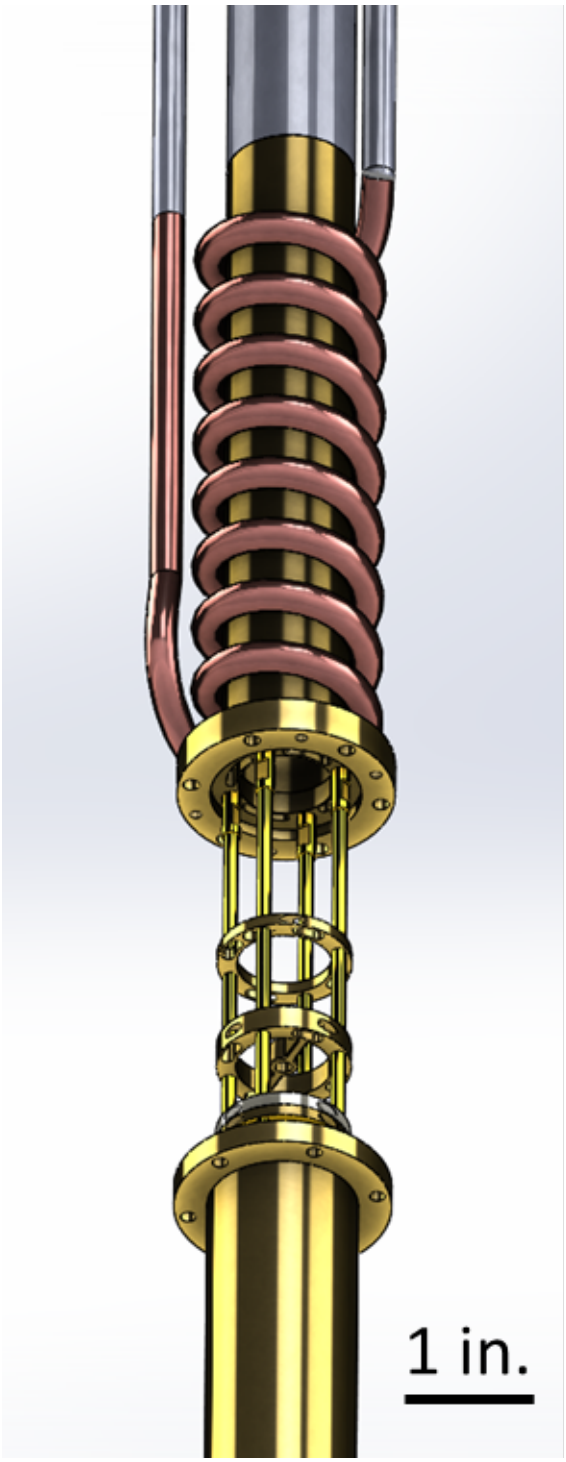

Figure 5.2: A model of the bottom of the new experimental cell. The liquid helium continuous flow line coils around a brass tube segment. The titanium can (see figure 3.2.4) has been replaced with a brass can, which mates with the brass tube segment (to which the coil is affixed) via an indium seal.

5.2 Gaussian Quantum Optomechanics

Liquid helium drops will be in an unusual regime for Gaussian quantum effects, given that they support high finesse optical WGMs and surface modes with very low stiffness. The optical spring effect (the stiffening of a mechanical mode via radiation pressure exerted on it by the optical mode) could be used to lower a surface modes' mean phonon number $n_{\rm m}$ [10]. For a drop with $R = 1$ mm and optical WGM finesse $\mathcal{F} = 10^6$, driving the WGM to intra-cavity photon number $n_{\rm circ} = 10^6$ would stiffen the $\ell_d = 2$ surface mode from $\omega_{\ell_d}/2\pi = 23$ Hz to 30 kHz. This stiffening would reduce $n_{\rm m}$ by $\sim 10^3$, and would place the surface mode near the resolved sideband regime (see section 2.1.2). A second laser that drives the WGM to $n_{\rm circ} = 10^8$ could then cool the stiffened $\ell_d = 2$ surface mode into its quantum ground state, with $n_{\rm m} \approx 0.2$.

This system could be used to study Gaussian quantum effects, such as quantum sideband asymmetry, where the effect of quantum fluctuations in radiation pressure becomes apparent in the drop's vibrational motion [37]. If the surface modes can indeed be cooled to $n_{\rm m} < 1$, they could potentially be used as starting place from which to generate non-classical states of motion, as described in section 2.1.2.

5.3 Non-Gaussian Quantum Optomechanics

As described in section 2.1.2, to access exotic non-Gaussian quantum effects in an optomechanical system it must be nonlinear at the single quantum level. Such non-Gaussian quantum effects include the negative Wigner function associated, for example, with in an excited Fock state, or a superposition. Non-classical states of motion (in particular, Fock states) have been achieved via the use of the nonlinearity inherent to single photon detection, or via the strong interaction between a mechanical oscillator and a superconducting qubit. To date, preparation of a non-classical state of a mechanical oscillator has been limited to oscillators with frequency $\omega_{\rm m}/2\pi \sim 1$ GHz, and mass $m \lesssim 10^{-14}$ kg

(see section 2.1.2). However, due to the extremely low optical loss and low stiffness of a millimeter-scale helium drop, it could be possible to use the inherent nonlinearity of the optomechanical interaction to observe non-Gaussian quantum effects in an object with mass ~ 0.5 mg. This is because for an optical WGM with $\mathcal{F} \sim 10^7$ (see section 2.2.3) in a drop with $R \sim 1$ mm, $g_0/\omega_{\ell_d=2} > 1$ while $g_0/\kappa \approx 0.04$ is non-negligbile.

If $\mathcal{F}$ is found to be $\approx 20\times$ larger (which could result from the breakdown of the "surface roughness" model described in section 2.3.1), the levitated drop will reach the single-quantum strong coupling regime in which $g_0 > \omega_{\ell_d=2}, \kappa$. In this regime it should be possible to directly measure non-classical effects, such as photon blockade and Jaynes-Cummings-like behavior [10, 159]. Reaching the single-quantum strong coupling regime remains one of the outstanding goals of quantum optomechanics.

5.4 Rotational Quantum Optomechanics

A levitated liquid helium drop could possibly be used to explore quantum rotational effects in an unprecedentedly massive object [38]. To date, all quantum optomechanics experiments have used harmonic oscillators as the mechanical element. On the other hand, free rotational motion (undergone by a rigid rotator) exhibits qualitatively different behavior in the quantum regime, as its energy eigenvalues are not evenly spaced. Additionally, a rigid rotator's angular momentum degrees of freedom $\hat{L}_x, \hat{L}_y, \hat{L}_z$ obey different commutation relations than those of a harmonic oscillator with degrees of freedom $\hat{x}$ and $\hat{p}$. The angular momentum commutation relations $[\hat{L}_i, \hat{L}_j] = i\hbar\epsilon_{ijk}\hat{L}_k$ (ϵ_{ijk} is the Levi-Civita tensor) are such that any angular momentum component can serve as a quantum non-demolition (QND) variable (e.g. measuring $\hat{L}_z$ perturbs $\hat{L}_x$ and $\hat{L}_y$, but this does not necessarily impact measurements of $\hat{L}_z$ at later times). In contrast, a measurement of a harmonic oscillator's $\hat{x}$ or $\hat{p}$ perturbs the oscillator's $\hat{p}$ or $\hat{x}$, which affects the time evolution of these degrees of freedom. Details of the proposed QND measurements of $\hat{L}$ are described in detail in

reference [38].

A levitated helium drop provides two immediate advantages over systems which explore rotational optomechanics with levitated solid objects. First, the drop's chemical and structural isotropy should provide a closer approximation to free rotation. Second, the drop's optical WGMs provide a method to realize a QND measurement of $\hat{L}$.

As described in section 2.183, the coupling between the drop's rotation and optical WGMs is not described by the standard optomechanical coupling. Instead, the optical WGM frequency shift $\Delta\omega_{\mathrm{opt}}^{(\mathrm{rot})} \propto \delta R \propto L_{\mathrm{z}}^2$, where δR is the drop's radial deflection that results from its rotation.

This optical WGM measurement approach does not depend crucially on the form of the velocity field $\mathbf{v}(\mathbf{r})$ within the drop. As a result, this method should work for levitated drops of both ^{3}He and ^{4}He. Such measurements in superfluid ^{4}He drops are especially interesting because the superfluid state requires an irrotational $\mathbf{v}(\mathbf{r})$ (see section 2.4.5). As a result, the circulation in the drop associated with $\hat{L}$ must correspond to the presence of vortex lines, and the quantum fluctuations in $\hat{L}$ correspond to the quantum fluctuations in the vortex lines' alignment with respect to the drop.

5.5 Tests of Physics Beyond the Standard Model

The standard model of particle physics accurately describes the phenomena accessible at modern particle accelerators, but it is incomplete. The standard model predicts that all stable, isolated particles have charge that is an integer multiple of the electron charge q_{e}. However, the standard model does not describe dark matter, and some dark matter models (as well as other possible extensions to the standard model) predict a violation of the usual charge quantization. As a result, researchers have studied the electrical neutrality of matter by testing the relationship $|q_{\mathrm{e}}| = \left|q_{\mathrm{p}}\right|$ (q_{p} is the proton charge). Additionally, researchers have searched for dark matter particles with "millicharge." By exploiting the

unique properties of levitated liquid helium, a levitated helium drop could possibly improve searches for beyond-standard-model (BSM) physics related to the electrical neutrality of matter and dark matter models.

5.5.1 The Electrical Neutrality of Matter

To date, all electrical neutrality measurements are consistent with the electron and proton having exactly opposite electrical charges such that $q_{\mathrm{e}} = -q_{\mathrm{p}}$, and the neutron having charge $q_{\mathrm{n}} = 0$ [160, 161]. Most experiments have tested the relationship $q_{\mathrm{e}} + q_{\mathrm{p}} = 0 = q_{\mathrm{n}}$ by measuring the electrical neutrality of macroscopic bodies (in which any imbalance between the body's electron and proton numbers were eliminated). The present limit on the electrical neutrality of matter is $(q_{\mathrm{e}} + q_{\mathrm{p}})/q_{\mathrm{e}} < 10^{-21}$ and $q_{\mathrm{n}}/q_{\mathrm{e}} < 10^{-21}$. This apparent charge symmetry is not a standard model prediction, and lacks a corresponding conservation law. This apparent symmetry is regarded as the result of some unknown fundamental symmetry at energies that are presently inaccessible, and whose connections to deeper physical principles are not yet fully understood. Consequently, measurements of electrical neutrality with enhanced precision may shed light on BSM physics.

A levitated liquid helium drop provides a nearly ideal system in which to measure electrical neutrality. The drop's chemical and structural purity (and thus its lack of electrostatic disorder) removes important backgrounds from the measurement (e.g. a drop would have no permanent electric dipole moment, unlike the solid objects used in typical levitated optomechanics experiments). Keeping a drop with $R \sim 1$ mm in mind, its large number of helium atoms would provide enhanced sensitivity to $(q_{\mathrm{e}} + q_{\mathrm{p}})/q_{\mathrm{e}}$ and $q_{\mathrm{n}}/q_{\mathrm{e}}$ (as compared to solid objects in levitated optomechanical experiments to date). One could measure the response of a drop's $\ell_d = 2$ surface modes to an applied electric field gradient that oscillates at $\omega_{\ell_d=2}$, the $\ell_d = 2$ surface mode angular frequency. This drive would resonantly excite the $\ell_d = 2$ surface modes if the drop possesses a uniform charge density due to $(q_{\mathrm{e}} + q_{\mathrm{p}})/q_{\mathrm{e}}$ or $q_{\mathrm{n}}/q_{\mathrm{e}}$. This charge density could then be extracted from measurements of this surface

mode. in addition, simultaneous measurements of the drop's other surface modes can be used to reject various background signals.

5.5.2 Searching for "Millicharged" Particles

Several proposed modifications of the standard model focus on extensions that include a dark matter particle that weakly interacts with standard model particles. Given the many standard model particles it is reasonable to ask whether a variety of dark matter particles might exist [162, 163]. For example, dark matter particles may interact with each other and still remain "dark" if there is a new gauge interaction under which dark matter carries a "dark charge," while SM particles are "dark neutral" [163]. In the case of a dark $U(1)$ gauge group, there are several processes that can lead to mixing between this group and conventional standard model electromagnetism [164]. Such mixing causes the dark matter particles to acquire a small conventional electrical charge ηq_{e}, where q_{e} is the electron charge and $\eta \ll 1$. If stable, these so-called "millicharged" particles can become bound inside conventional atoms. It is important to note that the order of magnitude of η is unknown, so the term "millicharged" is likely a misnomer.

As described in detail in section 2.1.4, some searches for millicharged particles have used optically levitated silica spheres [42]. The spheres' charge was determined by applying an electric field and measuring the spheres' resulting center of mass motion. These results were limited in part by the spheres' permanent electric dipole moment (and higher moments), which arose from the structural defects and chemical impurities in the silica. Similar to the tests of the electrical neutrality of matter described in section 5.5.1, permanent electric moments in the solid sphere produce backgrounds that can obscure the desired measurement.

A search for millicharged particles in a levitated superfluid helium drop could offer several advantages. First, a drop's chemical and structural purity (and thus its lack of electrostatic disorder) removes important backgrounds from the measurement. Additionally, a

drop with $R = 1$ mm has $\sim 10^6$ more nucleons than the spheres in reference [42] (this is important because a search for millicharged particles not only bounds η, but also the number n_χ of millicharged particles per nucleon, and more nucleons will give a larger measurement signal). A helium atom that contains a stable millicharged particle (which we label as He*) will be mobile within the superfluid drop. Consequently, an applied electric field E will cause the He* to drift across the drop until it strikes the drop's surface. By modulating E at the frequency ω_{ℓ_d} the He* will resonantly drive the drop's ℓ_d-th surface mode (see section 2.4) with a force of magnitude $F \sim \eta q_{\rm e}|E|$. Measurements of the drop's surface modes could thus be used to measure η and n_χ, and provide more precise measurements of these values. Once again, simultaneous measurements of the drop's other surface modes can be used to reject various background signals.

Chapter 6

Conclusion

In this dissertation I have reported measurements of superfluid ^{4}He drops that are magnetically levitated in vacuum. We constructed an entirely new experiment, and used it to measure drops' size, shape, evaporation and temperature, optical modes, center of mass motion and surface modes. We found excellent agreement between the measured and predicted surface mode frequencies, and found that theory slightly overestimates their decay rates. We found decent agreement between the measured and predicted center of mass mode frequencies. We found optical modes with finesse that differ from predictions by a factor ≤ 2.5.

The size and shape measurements showed that when drops were initially created they had radii $R \lesssim 1.5$ mm, but would quickly evaporate and stabilize to $R \sim 300$ μm. The drops with $R \sim 300$ μm were very spherical, with deviations from sphericity $\lesssim 10^{-3}$.

The evaporation measurements showed that the drops reached temperatures as low as $T \approx 330$ with evaporation rates as low as $\dot{R} \lesssim 0.5$ Å/s. We trapped a single drop for 24 hours, but could have trapped it for longer had we opted to. A trapped drop should remain trapped for one month or longer.

The optical mode measurements found modes with finesse as high as $\mathcal{F} \sim 40$. These modes were predicted to have $\mathcal{F} \sim 110$. The discrepancy between measurement and pre-

dictions were likely due to two causes. First, the optical modes were likely inhomogeneously broadened due to a lifted degeneracy of these modes via the drops' deviation from perfect sphericity. Second, the modulation technique used to measure these modes likely caused additional broadening.

The measurements of the center of mass motion found that the normal modes of oscillation were coupled, and underwent an avoided crossing as the trapping potential was changed. After extending the model describing the modes to include inter-mode coupling due to a tilt of the levitation magnet's axis with respect to gravity, the measured and predicted mode frequencies agreed to within 10%.

The surface mode frequency measurements showed agreement with theory to $\leq 0.5\%$. Measurements of these modes' decay rates showed values somewhat lower than predicted. This could be because our drops existed in a regime for which the damping of surface modes has not yet been calculated. In the theory, a thermal phonon is assumed to scatter and extract energy from a surface mode just once before equilibrating with its thermal bath. In contrast, in our experiments a thermal phonon has a mean free path $\approx 20\times$ the drop radius, and so will scatter from an effectively "frozen" surface mode many times (owing to the speed of sound in helium) before equilibrating. As a result, it could be interesting to extend the theory to describe the multi-scattering damping process.

There is much exciting work to be done with levitated superfluid helium drops. These drops may play an important role in the future of quantum optomechanics, as well as in studies of quantum turbulence in a fluid without contact with walls, and in searches for physics beyond the standard model.

Bibliography

[1] Albert Einstein. On the present status of the radiation problem. *Phys. Z*, 10:185–193, 1909.

[2] R. Frisch. Experimental proof of einstein's radiation recoil. *Zeitschrift Fur Physik*, 86(1-2):42–48, 1933.

[3] R. A. Beth. Mechanical detection and measurement of the angular momentum of light. *Physical Review*, 50(2):115–125, 1936.

[4] A. Ashkin. Acceleration and trapping of particles by radiation pressure. *Physical Review Letters*, 24(4):156–, 1970.

[5] E. L. Raab, M. Prentiss, A. Cable, S. Chu, and D. E. Pritchard. Trapping of neutral sodium atoms with radiation pressure. *Physical Review Letters*, 59(23):2631–2634, 1987.

[6] K. B. Davis, M. O. Mewes, M. R. Andrews, N. J. Vandruten, D. S. Durfee, D. M. Kurn, and W. Ketterle. Bose-einstein condensation in a gas of sodium atoms. *Physical Review Letters*, 75(22):3969–3973, 1995.

[7] M. H. Anderson, J. R. Ensher, M. R. Matthews, C. E. Wieman, and E. A. Cornell. Observation of bose-einstein condensation in a dilute atomic vapor. *Science*, 269(5221):198–201, 1995.

[8] E. S. Shuman, J. F. Barry, and D. DeMille. Laser cooling of a diatomic molecule. *Nature*, 467(7317):820–823, 2010.

[9] J. Chan, T. P. M. Alegre, A. H. Safavi-Naeini, J. T. Hill, A. Krause, S. Groblacher, M. Aspelmeyer, and O. Painter. Laser cooling of a nanomechanical oscillator into its quantum ground state. *Nature*, 478(7367):89–92, 2011.

[10] M. Aspelmeyer, T. J. Kippenberg, and F. Marquardt. Cavity optomechanics. *Reviews of Modern Physics*, 86(4):1391–1452, 2014.

[11] M. E. Gertsenshtein and V. I. Pustovoit. On the detection of low frequency gravitational waves. *Soviet Physics Jetp-Ussr*, 16(2):433–435, 1963.

[12] V. B. Braginskii. Gravitational radiation and prospect of its experimental discovery. *Soviet Physics Uspekhi-Ussr*, 8(4):513–+, 1966.

[13] Rainer Weiss and Dirk Muehlner. Electronically coupled broadband gravitational antenna. *Quarterly Progress Report, Research Laboratory of Electronics*, 105, 1972.

[14] R. L. Forward. Wideband laser-interferometer gravitational-radiation experiment. *Physical Review D*, 17(2):379–390, 1978.

[15] B. P. Abbott, R. Abbott, T. D. Abbott, M. R. Abernathy, F. Acernese, K. Ackley, C. Adams, T. Adams, P. Addesso, R. X. Adhikari, V. B. Adya, C. Affeldt, M. Agathos, K. Agatsuma, N. Aggarwal, O. D. Aguiar, L. Aiello, A. Ain, P. Ajith, B. Allen, A. Allocca, P. A. Altin, S. B. Anderson, W. G. Anderson, K. Arai, M. A. Arain, M. C. Araya, C. C. Arceneaux, J. S. Areeda, N. Arnaud, K. G. Arun, S. Ascenzi, G. Ashton, M. Ast, S. M. Aston, P. Astone, P. Aufmuth, C. Aulbert, S. Babak, P. Bacon, M. K. M. Bader, P. T. Baker, F. Baldaccini, G. Ballardin, S. W. Ballmer, J. C. Barayoga, S. E. Barclay, B. C. Barish, D. Barker, F. Barone, B. Barr, L. Barsotti, M. Barsuglia, D. Barta, J. Bartlett, M. A. Barton, I. Bartos, R. Bassiri, A. Basti,

J. C. Batch, C. Baune, V. Bavigadda, M. Bazzan, B. Behnke, M. Bejger, C. Belczynski, A. S. Bell, C. J. Bell, B. K. Berger, J. Bergman, G. Bergmann, C. P. L. Berry, D. Bersanetti, A. Bertolini, J. Betzwieser, S. Bhagwat, R. Bhandare, I. A. Bilenko, G. Billingsley, J. Birch, R. Birney, O. Birnholtz, S. Biscans, A. Bisht, M. Bitossi, C. Biwer, M. A. Bizouard, J. K. Blackburn, C. D. Blair, D. G. Blair, R. M. Blair, S. Bloemen, O. Bock, T. P. Bodiya, M. Boer, G. Bogaert, C. Bogan, A. Bohe, P. Bojtos, C. Bond, et al. Observation of gravitational waves from a binary black hole merger. *Physical Review Letters*, 116(6), 2016.

[16] C. M. Caves. Quantum-mechanical radiation-pressure fluctuations in an interferomer. *Physical Review Letters*, 45(2):75–79, 1980.

[17] J. D. Teufel, T. Donner, M. A. Castellanos-Beltran, J. W. Harlow, and K. W. Lehnert. Nanomechanical motion measured with an imprecision below that at the standard quantum limit. *Nature Nanotechnology*, 4(12):820–823, 2009.

[18] David Mason, Junxin Chen, Massimiliano Rossi, Yeghishe Tsaturyan, and Albert Schliesser. Continuous force and displacement measurement below the standard quantum limit. *Nature Physics*, page 1, 2019.

[19] A. D. O'Connell, M. Hofheinz, M. Ansmann, R. C. Bialczak, M. Lenander, E. Lucero, M. Neeley, D. Sank, H. Wang, M. Weides, J. Wenner, J. M. Martinis, and A. N. Cleland. Quantum ground state and single-phonon control of a mechanical resonator. *Nature*, 464(7289):697–703, 2010.

[20] M. Underwood, D. Mason, D. Lee, H. Xu, L. Jiang, A. B. Shkarin, K. Borkje, S. M. Girvin, and J. G. E. Harris. Measurement of the motional sidebands of a nanogram-scale oscillator in the quantum regime. *Physical Review A*, 92(6), 2015.

[21] S. Groblacher, K. Hammerer, M. R. Vanner, and M. Aspelmeyer. Observation of strong coupling between a micromechanical resonator and an optical cavity field. *Nature*, 460(7256):724–727, 2009.

[22] S. Bose, K. Jacobs, and P. L. Knight. Scheme to probe the decoherence of a macroscopic object. *Physical Review A*, 59(5):3204–3210, 1999.

[23] W. Marshall, C. Simon, R. Penrose, and D. Bouwmeester. Towards quantum superpositions of a mirror. *Physical Review Letters*, 91(13), 2003.

[24] S. Hong, R. Riedinger, I. Marinkovic, A. Wallucks, S. G. Hofer, R. A. Norte, M. Aspelmeyer, and S. Groblacher. Hanbury brown and twiss interferometry of single phonons from an optomechanical resonator. *Science*, 358(6360):203–+, 2017.

[25] H. Yang, H. X. Miao, D. S. Lee, B. Helou, and Y. B. Chen. Macroscopic quantum mechanics in a classical spacetime. *Physical Review Letters*, 110(17), 2013.

[26] J. J. Viennot, X. Ma, and K. W. Lehnert. Phonon-number-sensitive electromechanics. *Physical Review Letters*, 121(18), 2018.

[27] Y. W. Chu, P. Kharel, T. Yoon, L. Frunzio, P. T. Rakich, and R. J. Schoelkopf. Creation and control of multi-phonon fock states in a bulk acoustic-wave resonator. *Nature*, 563(7733):666–670, 2018.

[28] L. A. De Lorenzo and K. C. Schwab. Superfluid optomechanics: coupling of a superfluid to a superconducting condensate. *New Journal of Physics*, 16, 2014.

[29] L. A. De Lorenzo and K. C. Schwab. Ultra-high q acoustic resonance in superfluid he-4. *Journal of Low Temperature Physics*, 186(3-4):233–240, 2017.

[30] S. Singh, L. A. De Lorenzo, I. Pikovski, and K. C. Schwab. Detecting continuous gravitational waves with superfluid he-4. *New Journal of Physics*, 19, 2017.

[31] X. Rojas and J. P. Davis. Superfluid nanomechanical resonator for quantum nanofluidics. *Physical Review B*, 91(2), 2015.

[32] F. Souris, X. Rojas, P. H. Kim, and J. P. Davis. Ultralow-dissipation superfluid micromechanical resonator. *Physical Review Applied*, 7(4), 2017.

[33] G. I. Harris, D. L. McAuslan, E. Sheridan, Y. Sachkou, C. Baker, and W. P. Bowen. Laser cooling and control of excitations in superfluid helium. *Nat Phys*, advance online publication, 2016.

[34] Y. P. Sachkou, C. G. Baker, G. I. Harris, O. R. Stockdale, S. Forstner, M. T. Reeves, X. He, D. L. McAuslan, A. S. Bradley, M. J. Davis, and W. P. Bowen. Coherent vortex dynamics in a strongly-interacting superfluid on a silicon chip. *arXiv preprint arXiv:1902.04409*, 2019.

[35] A. D. Kashkanova, A. B. Shkarin, C. D. Brown, N. E. Flowers-Jacobs, L. Childress, S. W. Hoch, L. Hohmann, K. Ott, J. Reichel, and J. G. E. Harris. Superfluid brillouin optomechanics. *Nature Physics*, 13(1):74–79, 2017.

[36] A. D. Kashkanova, A. B. Shkarin, C. D. Brown, N. E. Flowers-Jacobs, L. Childress, S. W. Hoch, L. Hohmann, K. Ott, J. Reichel, and J. G. E. Harris. Optomechanics in superfluid helium coupled to a fiber-based cavity. *Journal of Optics*, 19(3), 2017.

[37] A. B. Shkarin, A. D. Kashkanova, C. D. Brown, S. Garcia, K. Ott, J. Reichel, and J. G. E. Harris. Quantum optomechanics in a liquid. *Physical Review Letters*, 122(15), 2019.

[38] L. Childress, M. P. Schmidt, A. D. Kashkanova, C. D. Brown, G. I. Harris, A. Aiello, F. Marquardt, and J. G. E. Harris. Cavity optomechanics in a levitated helium drop. *Physical Review A*, 96(6), 2017.

[39] M. Bhattacharya, A. N. Vamivakas, and P. Barker. Levitated optomechanics: introduction. *Journal of the Optical Society of America B-Optical Physics*, 34(6):L01–L2, 2017.

[40] A. A. Geraci, S. B. Papp, and J. Kitching. Short-range force detection using optically cooled levitated microspheres. *Physical Review Letters*, 105(10), 2010.

[41] G. Ranjit, M. Cunningham, K. Casey, and A. A. Geraci. Zeptonewton force sensing with nanospheres in an optical lattice. *Physical Review A*, 93(5), 2016.

[42] D. C. Moore, A. D. Rider, and G. Gratta. Search for millicharged particles using optically levitated microspheres. *Physical Review Letters*, 113(25), 2014.

[43] A. D. Rider, D. C. Moore, C. P. Blakemore, M. Louis, M. Lu, and G. Gratta. Search for screened interactions associated with dark energy below the 100 mu m length scale. *Physical Review Letters*, 117(10), 2016.

[44] F. Monteiro, S. Ghosh, A. G. Fine, and D. C. Moore. Optical levitation of 10-ng spheres with nano-g acceleration sensitivity. *Physical Review A*, 96(6), 2017.

[45] J. Millen, P. Z. G. Fonseca, T. Mavrogordatos, T. S. Monteiro, and P. F. Barker. Cavity cooling a single charged levitated nanosphere. *Physical Review Letters*, 114(12), 2015.

[46] A. T. M. A. Rahman and P. F. Barker. Laser refrigeration, alignment and rotation of levitated yb3+:ylf nanocrystals. *Nature Photonics*, 11(10):634–+, 2017.

[47] R. M. Pettit, L. P. Neukirch, Y. Zhang, and A. N. Vamivakas. Coherent control of a single nitrogen-vacancy center spin in optically levitated nanodiamond. *Journal of the Optical Society of America B-Optical Physics*, 34(6):C31–C35, 2017.

[48] E. Hebestreit, M. Frimmer, R. Reimann, and L. Novotny. Sensing static forces with free-falling nanoparticles. *Physical Review Letters*, 121(6), 2018.

[49] O. Romero-Isart, A. C. Pflanzer, F. Blaser, R. Kaltenbaek, N. Kiesel, M. Aspelmeyer, and J. I. Cirac. Large quantum superpositions and interference of massive nanometer-sized objects. *Physical Review Letters*, 107(2), 2011.

[50] B. R. Slezak, C. W. Lewandowski, J. F. Hsu, and B. D'Urso. Cooling the motion of a silica microsphere in a magneto-gravitational trap in ultra-high vacuum. *New Journal of Physics*, 20, 2018.

[51] U. Delic, M. Reisenbauer, D. Grass, N. Kiesel, V. Vuletic, and M. Aspelmeyer. Cavity cooling of a levitated nanosphere by coherent scattering. *Physical Review Letters*, 122(12), 2019.

[52] F. V. Kowalski, R. T. Hawkins, and A. L. Schawlow. Digital wavemeter for cw lasers. *Journal of the Optical Society of America*, 66(9):965–966, 1976.

[53] Michael Hercher. The spherical mirror fabry-perot interferometer. *Applied Optics*, 7(5):951–966, 1968.

[54] T. H. Maiman. Stimulated optical radiation in ruby. *Nature*, 187(4736):493–494, 1960.

[55] R Russel Austin. The use of solid etalon devices as narrow band interference filters. *Optical Engineering*, 11(3):110365, 1972.

[56] S. R. Mallinson. Wavelength-selective filters for single-mode fiber wdm systems using fabry-perot interferometers. *Applied Optics*, 26(3):430–436, 1987.

[57] G. V. Deverall, K. W. Meissner, and G. J. Zissis. Hyperfine structures of the resonance lines of indium (in-115). *Physical Review*, 91(2):297–299, 1953.

[58] J. F. Markey and R. R. Austin. High-resolution solar observations - hydrogen-alpha telescopes on skylab. *Applied Optics*, 16(4):917–921, 1977.

[59] A. D. Ludlow, M. M. Boyd, J. Ye, E. Peik, and P. O. Schmidt. Optical atomic clocks. *Reviews of Modern Physics*, 87(2):637–701, 2015.

[60] G. Rempe, R. J. Thompson, H. J. Kimble, and R. Lalezari. Measurement of ultralow losses in an optical interferometer. *Optics Letters*, 17(5):363–365, 1992.

[61] Y. Akahane, T. Asano, B. S. Song, and S. Noda. High-q photonic nanocavity in a two-dimensional photonic crystal. *Nature*, 425(6961):944–947, 2003.

[62] A. H. Safavi-Naeini, T. P. M. Alegre, M. Winger, and O. Painter. Optomechanics in an ultrahigh-q two-dimensional photonic crystal cavity. *Applied Physics Letters*, 97(18), 2010.

[63] O. Painter, R. K. Lee, A. Scherer, A. Yariv, J. D. O'Brien, P. D. Dapkus, and I. Kim. Two-dimensional photonic band-gap defect mode laser. *Science*, 284(5421):1819–1821, 1999.

[64] S. Noda, A. Chutinan, and M. Imada. Trapping and emission of photons by a single defect in a photonic bandgap structure. *Nature*, 407(6804):608–610, 2000.

[65] R. Riedinger, S. Hong, R. A. Norte, J. A. Slater, J. Y. Shang, A. G. Krause, V. Anant, M. Aspelmeyer, and S. Groblacher. Non-classical correlations between single photons and phonons from a mechanical oscillator. *Nature*, 530(7590):313–+, 2016.

[66] I. Marinkovic, A. Wallucks, R. Riedinger, S. Hong, M. Aspelmeyer, and S. Groblacher. Optomechanical bell test. *Physical Review Letters*, 121(22), 2018.

[67] John William Strutt Baron Rayleigh. *The theory of sound*, volume 2. Macmillan, 1896.

[68] M. Cai, O. Painter, and K. J. Vahala. Observation of critical coupling in a fiber taper to a silica-microsphere whispering-gallery mode system. *Physical Review Letters*, 85(1):74–77, 2000.

[69] D. K. Armani, T. J. Kippenberg, S. M. Spillane, and K. J. Vahala. Ultra-high-q toroid microcavity on a chip. *Nature*, 421(6926):925–928, 2003.

[70] A. A. Savchenkov, A. B. Matsko, V. S. Ilchenko, and L. Maleki. Optical resonators with ten million finesse. *Optics Express*, 15(11):6768–6773, 2007.

[71] J. Z. Zhang, D. H. Leach, and R. K. Chang. Photon lifetime within a droplet - temporal determination of elastic and stimulated raman-scattering. *Optics Letters*, 13(4):270–272, 1988.

[72] S. Uetake, M. Katsuragawa, M. Suzuki, and K. Hakuta. Stimulated raman scattering in a liquid-hydrogen droplet. *Physical Review A*, 61(1):art. no.–011803, 2000.

[73] Keqian Zhang, Dejie Li, Keqian Chang, K Zhang, and D Li. *Electromagnetic theory for microwaves and optoelectronics*. Springer, 1998.

[74] A. N. Oraevsky. Whispering-gallery waves. *Quantum Electronics*, 32(5):377–400, 2002.

[75] G. A. Williams and R. E. Packard. Photographs of quantized vortex lines in rotating he ii. *Physical Review Letters*, 33(5):280–283, 1974.

[76] L. F. Gomez, K. R. Ferguson, J. P. Cryan, C. Bacellar, R. M. P. Tanyag, C. Jones, S. Schorb, D. Anielski, A. Belkacem, C. Bernando, R. Boll, J. Bozek, S. Carron, G. Chen, T. Delmas, L. Englert, S. W. Epp, B. Erk, L. Foucar, R. Hartmann, A. Hexemer, M. Huth, J. Kwok, S. R. Leone, J. H. S. Ma, F. R. N. C. Maia, E. Malmerberg, S. Marchesini, D. M. Neumark, B. Poon, J. Prell, D. Rolles, B. Rudek, A. Rudenko, M. Seifrid, K. R. Siefermann, F. P. Sturm, M. Swiggers, J. Ullrich, F. Weise, P. Zwart, C. Bostedt, O. Gessner, and A. F. Vilesov. Shapes and vorticities of superfluid helium nanodroplets. *Science*, 345(6199):906–909, 2014.

[77] G. Baym, C. Pethick, and D. Pines. Superfluidity in neutron stars. *Nature*, 224(5220):673–, 1969.

[78] P. W. Anderson and N. Itoh. Pulsar glitches and restlessness as a hard superfluidity phenomenon. *Nature*, 256(5512):25–27, 1975.

[79] N. Chamel. Superfluidity and superconductivity in neutron stars. *Journal of Astrophysics and Astronomy*, 38(3), 2017.

[80] Subrahmanyan Chandrasekhar. The stability of a rotating liquid drop. *Proceedings of the Royal Society of London. Series A. Mathematical and Physical Sciences*, 286(1404):1–26, 1965.

[81] R. A. Brown and L. E. Scriven. The shape and stability of rotating liquid-drops. *Proceedings of the Royal Society of London Series a-Mathematical Physical and Engineering Sciences*, 371(1746):331–357, 1980.

[82] V. Cardoso and L. Gualtieri. Equilibrium configurations of fluids and their stability in higher dimensions. *Classical and Quantum Gravity*, 23(24):7151–7198, 2006.

[83] Rico Mayro P Tanyag, Curtis F Jones, Charles Bernando, Sean MO O'Connell, Deepak Verma, and Andrey F Vilesov. Experiments with large superfluid helium nanodroplets. *Cold chemistry: molecular scattering and reactivity near absolute zero*, 11:389, 2017.

[84] Anthony James Leggett. *Quantum liquids: Bose condensation and Cooper pairing in condensed-matter systems*. Oxford university press, 2006.

[85] John Wilks. The properties of liquid and solid helium. 1967.

[86] David R Lide. *CRC handbook of chemistry and physics*, volume 85. CRC press, 2004.

[87] Lev Davidovich Landau, JS Bell, MJ Kearsley, LP Pitaevskii, EM Lifshitz, and JB Sykes. *Electrodynamics of continuous media*, volume 8. elsevier, 2013.

[88] G. M. Seidel, R. E. Lanou, and W. Yao. Rayleigh scattering in rare-gas liquids. *Nuclear Instruments Methods in Physics Research Section a-Accelerators Spectrometers Detectors and Associated Equipment*, 489(1-3):189–194, 2002.

[89] H. Z. Cummins and R. W. Gammon. Rayleigh and brillouin scattering in liquids - landau-placzek ratio. *Journal of Chemical Physics*, 44(7):2785–, 1966.

[90] J. S. Brooks and R. J. Donnelly. Calculated thermodynamic properties of superfluid he-4. *Journal of Physical and Chemical Reference Data*, 6(1):51–104, 1977.

[91] T. J. Greytak and J. Yan. Light scattering from rotons in liquid helium. *Physical Review Letters*, 22(19):987–, 1969.

[92] K. Onnes. *Communications from the Kamerlingh Onnes Laboratory of the University of Leiden*, volume 105,108. Kamerlingh Onnes Laboratorium, Rijksuniversiteit., 1908.

[93] H. Buchenau, E. L. Knuth, J. Northby, J. P. Toennies, and C. Winkler. Mass-spectra and time-of-flight distributions of helium cluster beams. *Journal of Chemical Physics*, 92(11):6875–6889, 1990.

[94] J. Braun, P. K. Day, J. P. Toennies, G. Witte, and E. Neher. Micrometer-sized nozzles and skimmers for the production of supersonic he atom beams. *Review of Scientific Instruments*, 68(8):3001–3009, 1997.

[95] J. P. Toennies, A. F. Vilesov, and K. B. Whaley. Superfluid helium droplets: An ultracold nanolaboratory. *Physics Today*, 54(2):31–37, 2001.

[96] J. P. Toennies and A. F. Vilesov. Superfluid helium droplets: A uniquely cold nanomatrix for molecules and molecular complexes. *Angewandte Chemie-International Edition*, 43(20):2622–2648, 2004.

[97] A. Kautsch, M. Koch, and W. E. Ernst. Photoinduced molecular dissociation and photoinduced recombination mediated by superfluid helium nanodroplets. *Physical Chemistry Chemical Physics*, 17(18):12310–12316, 2015.

[98] P. Thaler, A. Volk, D. Knez, F. Lackner, G. Haberfehlner, J. Steurer, M. Schnedlitz, and W. E. Ernst. Synthesis of nanoparticles in helium droplets-a characterization comparing mass-spectra and electron microscopy data. *Journal of Chemical Physics*, 143(13), 2015.

[99] E. W. Becker, R. Klingelhofer, and P. Lohse. Strahlen aus kondensiertem helium im hochvakuum. *Zeitschrift Fur Naturforschung Part a-Astrophysik Physik Und Physikalische Chemie*, 16(11):1259–1259, 1961.

[100] E. W. Becker, P. Lohse, and R. Klingelhofer. Strahlen aus kondensiertem wasserstoff, kondensiertem helium und kondensiertem stickstoff im hochvakuum. *Zeitschrift Fur Naturforschung Part a-Astrophysik Physik Und Physikalische Chemie*, A 17(5):432–, 1962.

[101] J. Gspann. Atomic impact experiments with free he-3 and he-4 clusters. *Zeitschrift Fur Physik B-Condensed Matter*, 98(3):405–411, 1995.

[102] A. Scheidemann, J. P. Toennies, and J. A. Northby. Capture of neon atoms by he-4 clusters. *Physical Review Letters*, 64(16):1899–1902, 1990.

[103] A. Scheidemann, B. Schilling, J. P. Toennies, and J. A. Northby. Capture of foreign atoms by helium clusters. *Physica B*, 165:135–136, 1990.

[104] J. Harms and J. P. Toennies. Observation of anomalously low momentum transfer in the low energy scattering of large he-4 droplets from he-4 and he-3 atoms. *Journal of Low Temperature Physics*, 113(3-4):501–508, 1998.

[105] S. Goyal, D. L. Schutt, and G. Scoles. Infrared-spectroscopy of sf6 attached to classical and quantum clusters (finite size particles attaining bulk-like properties). *Physics and Chemistry of Finite Systems : From Clusters to Crystals, Vols 1 and 2*, 374:85–91, 1992.

[106] M. Hartmann, R. E. Miller, J. P. Toennies, and A. Vilesov. Rotationally resolved spectroscopy of sf6 in liquid-helium clusters - a molecular probe of cluster temperature. *Physical Review Letters*, 75(8):1566–1569, 1995.

[107] J. Gspann and G. Krieg. Reflection of ionized hydrogen clusters at polished stainless-steel. *Zeitschrift Fur Naturforschung Section a-a Journal of Physical Sciences*, A 29(10):1501–1503, 1974.

[108] J. Gspann and H. Vollmar. Metastable excitations of large clusters of he-3, he-4 or ne atoms. *Journal of Chemical Physics*, 73(4):1657–1664, 1980.

[109] J. Gspann. Electron-impact on helium clusters - metastable excitation, ionization, and charged mini-cluster ejection. *Surface Science*, 106(1-3):219–224, 1981.

[110] J. Gspann and H. Vollmar. Ejection of positive cluster ions from large electron-bombarded he-3 or he-4 clusters. *Journal of Low Temperature Physics*, 45(3-4):343–355, 1981.

[111] J. Gspann. Negatively charged he-4 clusters. *Physica B*, 169(1-4):519–520, 1991.

[112] C. C. Grimes. Electrons in surface-states on liquid-helium. *Surface Science*, 73(1):379–395, 1978.

[113] M. V. R. Krishna and K. B. Whaley. Excess-electron surface-states of helium clusters. *Physical Review B*, 38(16):11839–11842, 1988.

[114] J. A. Northby and C. Kim. Lifetime of an electron on the liquid-helium surface in the presence of an electric-field. *Physica B*, 194:1229–1230, 1994.

[115] T. Jiang and J. A. Northby. Fragmentation clusters formed in supercritical expansions of he-4. *Physical Review Letters*, 68(17):2620–2623, 1992.

[116] C. G. Kuper. Theory of negative ions in liquid helium. *Physical Review*, 122(4):1007–, 1961.

[117] T. Jiang, C. Kim, and J. A. Northby. Electron-attachment to helium microdroplets - creation induced magic. *Physical Review Letters*, 71(5):700–703, 1993.

[118] J. A. Northby, C. Kim, and T. Jiang. Negatively charged helium microdroplets. *Physica B*, 197(1-4):426–434, 1994.

[119] C. Kim and J. A. Northby. Infrared induced electron detachment from negatively charged helium nanodroplets. *Czechoslovak Journal of Physics*, 46:375–376, 1996.

[120] C. Kim, S. Yurgenson, and J. A. Northby. Spontaneous and infrared induced electron detachment from negatively charged helium nanodroplets. *Zeitschrift Fur Physik D-Atoms Molecules and Clusters*, 40(1-4):119–122, 1997.

[121] W. Schollkopf and J. P. Toennies. Nondestructive mass selection of small van-der-waals clusters. *Science*, 266(5189):1345–1348, 1994.

[122] E. Lugovoj, J. P. Toennies, and A. Vilesov. Manipulating and enhancing chemical reactions in helium droplets. *Journal of Chemical Physics*, 112(19):8217–8220, 2000.

[123] J. J. Niemela. Electrostatic charging and levitation of helium ii drops. *Journal of Low Temperature Physics*, 109(5-6):709–732, 1997.

[124] M. A. Weilert, D. L. Whitaker, H. J. Maris, and G. M. Seidel. Laser levitation of superfluid helium. *Journal of Low Temperature Physics*, 98(1):17–35, 1995.

[125] M. A. Weilert, D. L. Whitaker, H. J. Maris, and G. M. Seidel. Magnetic levitation and noncoalescence of liquid helium. *Physical Review Letters*, 77(23):4840–4843, 1996.

[126] M. A. Weilert, D. L. Whitaker, H. J. Maris, and G. M. Seidel. Magnetic levitation of liquid helium. *Journal of Low Temperature Physics*, 106(1-2):101–131, 1997.

[127] D. L. Whitaker, C. Kim, C. L. Vicente, M. A. Weilert, H. J. Maris, and G. M. Seidel. Shape oscillations in levitated he ii drops. *Journal of Low Temperature Physics*, 113(3-4):491–499, 1998.

[128] D. L. Whitaker, M. A. Weilert, C. L. Vicente, H. J. Maris, and G. M. Seidel. Oscillations of charged helium ii drops. *Journal of Low Temperature Physics*, 110(1-2):173–178, 1998.

[129] W. M. Fairbank, W. B. Ard, and G. K. Walters. Fermi-dirac degeneracy in liquid he3 below 1-degree-k. *Physical Review*, 96(3):846–846, 1954.

[130] L. Goldstein. Paramagnetism of liquid helium 3. *Physical Review*, 133(1a):A52–A68, 1964.

[131] H. A. Schwettman and H. E. Rorschach. Nuclear paramagnetism of helium-3-helium-4 solutions above o.9 degrees k. *Physical Review*, 144(1):133–+, 1966.

[132] Aage Bohr and Ben R Mottelson. Nuclear structure: Volume ii: Nuclear deformations.

[133] L. D. Landau and E. M. Lifshitz. *Fluid Mechanics*. 1987.

[134] R. W. Whitworth. Experiments on the flow of heat in liquid helium below 0.7-degree-k. *Proceedings of the Royal Society of London Series a-Mathematical and Physical Sciences*, 246(1246):390–405, 1958.

[135] H. J. Maris. Phonon-phonon interactions in liquid-helium. *Reviews of Modern Physics*, 49(2):341–359, 1977.

[136] P. Roche, M. Roger, and F. I. B. Williams. Interpretation of the low damping of subthermal capillary waves (ripplons) on superfluid he-4. *Physical Review B*, 53(5):2225–2228, 1996.

[137] Milton Abramowitz and Irene A Stegun. Handbook of mathematical functions with formulas, graphs, and mathematical tables. national bureau of standards applied mathematics series 55. tenth printing. 1972.

[138] J Plateau. Annual report of the board of regents of the smithsonian institution. *Smithsonian Institution, Washington*, pages 270–285, 1863.

[139] C. J. Heine. Computations of form and stability of rotating drops with finite elements. *Ima Journal of Numerical Analysis*, 26(4):723–751, 2006.

[140] E. J. Yarmchuk and R. E. Packard. Photographic studies of quantized vortex lines. *Journal of Low Temperature Physics*, 46(5-6):479–515, 1982.

[141] O. V. Lounasmaa and E. Thuneberg. Vortices in rotating superfluid he-3. *Proceedings of the National Academy of Sciences of the United States of America*, 96(14):7760–7767, 1999.

[142] H. Kojima, W. Veith, S. J. Putterman, E. Guyon, and I. Rudnick. Vortex-free landau state in rotating superfluid helium. *Physical Review Letters*, 27(11):714–+, 1971.

[143] G. H. Bauer, R. J. Donnelly, and W. F. Vinen. Vortex configurations in a freely rotating superfluid drop. *Journal of Low Temperature Physics*, 98(1-2):47–65, 1995.

[144] D. M. Brink and S. Stringari. Density of states and evaporation rate of helium clusters. *Zeitschrift Fur Physik D-Atoms Molecules and Clusters*, 15(3):257–263, 1990.

[145] R. J. Donnelly and C. F. Barenghi. The observed properties of liquid helium at the saturated vapor pressure. *Journal of Physical and Chemical Reference Data*, 27(6):1217–1274, 1998.

[146] D. S. Greywall. Specific-heat of normal liquid-he-3. *Physical Review B*, 27(5):2747–2766, 1983.

[147] E. C. Kerr. Orthobaric densities of he-3 1.3-degrees-k to 3.2-degrees-k. *Physical Review*, 96(3):551–554, 1954.

[148] Y. H. Huang and G. B. Chen. A practical vapor pressure equation for helium-3 from 0.01 k to the critical point. *Cryogenics*, 46(12):833–839, 2006.

[149] A. L. Fetter. Light scattering in liquid helium. *Journal of Low Temperature Physics*, 6(5-6):487–504, 1972.

[150] H. Gang, A. H. Krall, and D. A. Weitz. Thermal fluctuations of the shapes of droplets in dense and compressed emulsions. *Physical Review E*, 52(6):6289–6302, 1995.

[151] H. M. Lai, P. T. Leung, K. Young, P. W. Barber, and S. C. Hill. Time-independent perturbation for leaking electromagnetic modes in open systems with application to resonances in microdroplets. *Physical Review A*, 41(9):5187–5198, 1990.

[152] David M Pozar. Microwave engineering, john willey son. *INC, 3rd Editon*, 2005.

[153] Laura Anne De Lorenzo. *Optomechanics with superfluid helium-4*. Thesis, 2016.

[154] Lawrence E Kinsler, Austin R Frey, Alan B Coppens, and James V Sanders. Fundamentals of acoustics. *Fundamentals of Acoustics, 4th Edition, by Lawrence E. Kinsler, Austin R. Frey, Alan B. Coppens, James V. Sanders, pp. 560. ISBN 0-471-84789-5. Wiley-VCH, December 1999.*, page 560, 1999.

[155] E. W. Collings and S. C. Hart. Low-temperature magnetic-susceptibility and magnetization studies of some commercial austenitic stainless-steels. *Cryogenics*, 19(9):521–530, 1979.

[156] M. Irmisch, A. Ulbricht, V. Zwecker, R. Badent, A. Hinderer, J. Olbrisch, and M. Jaarah. Breakdown characteristics of he gas at cryogenic temperature and low-pressure. *Ieee Transactions on Electrical Insulation*, 28(4):507–511, 1993.

[157] R. C. Gauthier, M. Friesen, T. Gerrard, W. Hassouneh, P. Koziorowski, D. Moore, K. Oprea, and S. Uttamalingam. Self-centering of a ball lens by laser trapping: fiber-ball-fiber coupling analysis. *Applied Optics*, 42(9):1610–1619, 2003.

[158] Tobias Jan August Kippenberg. *Nonlinear optics in ultra-high Q whispering-gallery optical microcavities*. Thesis, 2004.

[159] A. Nunnenkamp, K. Borkje, and S. M. Girvin. Single-photon optomechanics. *Physical Review Letters*, 107(6), 2011.

[160] C. S. Unnikrishnan and G. T. Gillies. The electrical neutrality of atoms and of bulk matter. *Metrologia*, 41(5):S125–S135, 2004.

[161] G. Bressi, G. Carugno, F. Della Valle, G. Galeazzi, G. Ruoso, and G. Sartori. Testing the neutrality of matter by acoustic means in a spherical resonator. *Physical Review A*, 83(5), 2011.

[162] J. Jaeckel and A. Ringwald. The low-energy frontier of particle physics. *Annual Review of Nuclear and Particle Science, Vol 60*, 60:405–437, 2010.

[163] S. Andreas, M. D. Goodsell, and A. Ringwald. Dark matter and dark forces from a supersymmetric hidden sector. *Physical Review D*, 87(2), 2013.

[164] B. Holdom. 2 u(1)s and epsilon-charge shifts. *Physics Letters B*, 166(2):196–198, 1986.